Water Harvesting by Adsorption Based Processes on MOFs

Dissertation presented to Faculty of Engineering of University of Porto for the PhD degree in Chemical and Biological Engineering
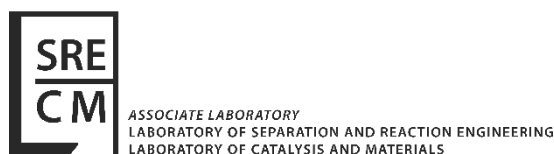
by

Márcia Patrícia Cardoso da Silva

<u>Supervisor</u>
Doctor Alexandre Filipe Porfírio Ferreira

<u>Co-supervisors:</u>
Professor Alírio Egídio Rodrigues
Doctor Ana Mafalda Almeida Peixoto Ribeiro

ACKNOWLEDGMENTS

Começo por expressar a minha gratidão ao meu orientador Alexandre Ferreira, por todo o apoio e acompanhamento ao longo do meu percurso pela FEUP. Obrigada por todos os ensinamentos, e por teres sempre uma visão otimista e prática.

Aos meus co-orientadores, Ana Mafalda Ribeiro e Professor Alírio Rodrigues quero agradecer todo o acompanhamento e suporte no decorrer do meu percurso.

Ao Professor José Miguel Loureiro, agradeço a boa disposição e estórias, assim como todos os ensinamentos partilhados.

À Cláudia Gomes da Silva, quero agradecer toda a ajuda e disponibilidade, bem como a partilha de conhecimentos.

Ao Idelfonso, quero agradecer a ajuda nas simulações e por toda a paciência na resposta às minhas dúvidas.

O meu muito obrigada a todos os meus colegas do LSRE-LCM, em especial à Maria João, pela ajuda no laboratório e pela partilha de frustrações quando o ESA teimava em não colaborar.

Um agradecimento ao laboratório associado LSRE-LCM, que foi a minha segunda casa nestes últimos anos, e que contribuiu para a minha evolução profissional e pessoal.

Às minhas companheiras dos almoços e pausas do café, o meu muito obrigada pelo apoio genuíno, palhaçadas, e por serem muitas vezes um balão de oxigénio nos dias mais cinzentos. Obrigada Andreia, Filipa, Isabel, Margarida, e Yaidelin.

Às meninas do grupo CC&MM (Catarina, Carina e Maria João), que de colegas se tornaram a boas amigas, agradeço a amizade e todas as partilhas ao longo destes anos. Venham mais Almoços 21!

Aos meus amigos próximos, agradeço toda a preocupação e compreensão pelas minhas ausências. Mesmo distantes fizeram-se notar e ouvir as minhas inquietações. Em breve retomaremos os nossos lanchinhos!

Aos meus pais e irmão, agradeço por estarem sempre presentes, pelo apoio incondicional e por sempre me impulsionarem a continuar. Sou-vos eternamente grata.

Por último, mas não menos importante, quero agradecer a ti, Rui, pelo teu sentido crítico, e por me fazeres sair da minha zona de conforto. Quero também agradecer as correções dos capítulos feitas às pinguinhas ☺

"O sucesso nasce do querer, da determinação e persistência em se chegar a um objetivo. Mesmo não atingindo o alvo, quem busca e vence obstáculos, no mínimo fará coisas admiráveis."

José de Alencar

ABSTRACT

This thesis main objective is to design an efficient adsorptive process to extract water from thin air using MOFs as adsorbents and solar energy to regenerate the adsorptive bed. MOFs are promising materials in water adsorption-related processes. Five MOFs were selected, namely Aluminum Fumarate, CAU-10, MIL-160(Al), MIL-100(Fe), and MIL-125(Ti)_NH_2. The samples were provided by the Korean Research Institute of Chemical Technology (KRICT) through a partnership with LA/LSRE-LCM. MOFs were characterized employing different techniques (*e.g.,* SEM, XRD, N_2 adsorption at 77 K, and TGA). Adsorption equilibrium and dynamic behavior were assessed, and a mathematical model was developed, using the adsorption equilibrium isotherms and fixed-bed experiments to validate it. The model is able of describing the experimental dynamic behavior of the fixed-bed in the bench scale unit.

Adsorption equilibrium isotherms were measured in a temperature range between 283 and 343 K, and pressure between 0 and 6 bar, employing a gravimetric method. CO_2, N_2, and O_2 adsorption equilibrium isotherms were measured on MIL-160(Al), MIL-100(Fe), and MIL-125(Ti)_NH_2. Indeed, CO_2 is the gas that presents a higher affinity towards MOFs. H_2O vapor adsorption equilibrium was studied on all MOFs and obtained data were regressed against adsorption equilibrium isotherm models (Cooperative Multimolecular Sorption model, Langmuir model, Dual Ising-Single Langmuir model, and Polanyi's potential theory). All the water adsorption equilibrium isotherms exhibit a step-like shape (S-shaped isotherms). Type IV isotherm is shown on Al-Fum, CAU-10, and MIL-125(Ti)_NH_2, while MIL-160(Al) and MIL-100(Fe) follow a Type V and Type VI isotherm, respectively. The MOFs presented themselves suitable for water harvesting in arid regions ($P/P_o < 0.3$), except Al-Fum, which presented a steep step between 25 % and 38.5 %. MIL-100(Fe) presented two steps ($0.21 < P/P_o < 0.30$ and $0.36 < P/P_o < 0.40$) due to the presence of two different cavities (25 and 29 Å) on its structure.

Water adsorption dynamic behavior was studied through breakthrough curves for a single component (H_2O, CO_2, and N_2), and multicomponent. The breakthrough experiments were conducted in a fixed-bed bench-scale unit at 1.0 bar and 298 K. The water adsorption dynamic behavior was in agreement with the expected from the water vapor adsorption equilibrium isotherms for all MOFs. This fact leads to conclude that only adsorption equilibrium contributes

to the dynamic response on water adsorption, under the experimental conditions. Water co-adsorption with CO_2 or N_2 presented similar behavior as water vapor adsorption against an inert background, allowing us to conclude that these gases do not have a significant impact on H_2O adsorption. Additionally, the fixed-bed model developed does not consider any competition between H_2O and the permanent gases, and even then is capable to predict well the water adsorption dynamic behavior.

Adsorption of CO_2 and H_2O and its co-adsorption were studied on MIL-160(Al), MIL-100(Fe), and MIL-125(Ti)_NH$_2$, by Diffuse Reflectance Infrared Fourier Transform (DRIFT) measurements. The interactions of CO_2 and H_2O with the MOF's structure (organic ligands, metal cluster, and functional groups) under the controlled *in situ* DRIFT cell environment were studied, as well as the stability of MOF structures after adsorption/desorption cycles and exposure at different temperatures. For the three studied MOFs, Diffuse Reflectance Infrared Fourier Transform Spectroscopy (DRIFTS) analysis revealed a high capability of regeneration during the adsorption/desorption cycles, and the structure remains stable during the water vapor contact and after exposed at different temperatures.

To define the best-operating conditions for regeneration with solar energy, the effect of irradiation power and solid temperature were studied on MIL-125(Ti)_NH$_2$. The experiments were performed under laboratory-controlled conditions using a solar simulator where the adsorbent bed is irradiated under simulated solar light.

A water harvesting process from thin air by adsorption and its posterior condensation from the regeneration outlet stream was designed. The cyclic adsorption process is composed of two co-current steps, feed and purge. On MIL-125(Ti)_NH$_2$, the highest productivity was achieved on the TSA design process against the PTSA or PTSA coupled with a buffer tank process. TSA process (column volume – 0.98 m^3) allowed to achieve maximum H_2O productivity of 111 l·day^{-1} for MIL-125(Ti)_NH$_2$ and MIL-160(Al), while for CAU-10 and MIL-100(Fe) one can harvest 84.0 and 79.8 l·day^{-1}, respectively (regeneration temperature – 373 K, condensation temperature – 283 K, and flowrate – 0.30 m^3·s^{-1}).

RESUMO

O primordial objetivo desta tese corresponde ao desenho de um processo adsortivo eficiente, com a finalidade de extração de água a partir da atmosfera, usando estruturas metal-orgânicas (MOFs) como adsorventes, e recorrendo à energia solar para regeneração do leito adsortivo. Os MOFs são materiais auspiciosos em processos relacionados à adsorção de água. Cinco MOFs foram selecionados para o estudo, sendo eles o alumínio fumarato, CAU-10, MIL-160(Al), MIL-100(Fe) e MIL-125(Ti)_NH$_2$. As amostras foram fornecidas pelo KRICT, através de uma parceria com o LA/LSRE-LCM. Os MOFs foram caracterizados recorrendo a diferentes técnicas (por exemplo, SEM, XRD, adsorção de N$_2$ a 77 K e TGA). O equilíbrio de adsorção e o comportamento dinâmico foram avaliados, bem como foi desenvolvido um modelo matemático, usando as isotérmicas de equilíbrio de adsorção e experiências em leito fixo para a sua validação. O modelo é capaz de descrever o comportamento dinâmico do leito fixo obtido experimentalmente.

As isotérmicas de equilíbrio de adsorção foram medidas, através do método gravimétrico, na gama de temperaturas entre 283 e 343 K e a pressões compreendidas entre 0 e 6 bar. As isotérmicas de equilíbrio de adsorção de CO$_2$, N$_2$ e O$_2$ foram medidas no MIL-160(Al), MIL-100(Fe) e MIL-125(Ti)_NH$_2$. O CO$_2$ é o gás que apresenta maior afinidade para com os MOFs. O equilíbrio de adsorção de vapor H$_2$O foi estudado em todos os MOFs e, aos dados obtidos, foram aplicados modelos de equilíbrio de adsorção (Cooperative Multimolecular Sorption, Langmuir, Dual Ising-Single Langmuir e Teoria do Potencial de Polanyi). Todas as isotérmicas de equilíbrio de adsorção de água exibem uma forma semelhante a um degrau (isotérmicas em forma de S). As isotérmicas do tipo IV são observadas no CAU-10, Al-Fum, e MIL-125(Ti)_NH$_2$, enquanto que o MIL-160(Al) e MIL-100(Fe) seguem uma isotérmica do Tipo V e Tipo VI, respectivamente. Os MOFs apresentaram-se adequados para captação de água em regiões áridas (P/P$_o$ < 0.3), exceptuando o Al-Fum pois apresentou degrau acentuado entre 25% e 38.5%. O MIL-100 (Fe) apresentou dois degraus (0.21 < P/P$_o$ < 0.30 e 0.36 < P/P$_o$ < 0.40) devido à presença de duas cavidades diferentes na sua estrutura (25 e 29 Å).

O comportamento dinâmico da adsorção de água foi estudado através de curvas de ruptura para um único componente (H$_2$O, CO$_2$ e N$_2$) e com multicomponentes. As experiências foram conduzidas numa coluna de leito fixo, à escala laboratorial, a 1.0 bar e 298 K. O comportamento dinâmico de adsorção de água estava de acordo com o esperado a partir das isotérmicas de

equilíbrio de adsorção de vapor de água para todos os MOFs. Esse fato leva a concluir que, nas condições experimentais, apenas o equilíbrio de adsorção contribui para a resposta dinâmica na adsorção de água. A co-adsorção de água com CO_2 ou N_2 apresentou comportamento semelhante à adsorção de vapor de água em fundo inerte, permitindo concluir que esses gases não têm impacto significativo na adsorção de H_2O. Adicionalmente, o modelo de leito fixo desenvolvido não considera qualquer competição entre H_2O e os gases permanentes, e mesmo assim, é capaz de prever bem o comportamento dinâmico de adsorção de água.

A adsorção de CO_2 e H_2O, bem como a sua co-adsorção, foram estudadas no MIL-160(Al), MIL-100(Fe) e MIL-125(Ti)_NH_2, recorrendo a medições por reflectância difusa por transformada de Fourier (DRIFT). As interações de CO_2 e H_2O com a estrutura do MOF (ligantes orgânicos, aglomerados metálicos e grupos funcionais) foram estudadas em ambiente controlado *in situ* na célula de DRIFT, bem como foi realizado o estudo da estabilidade das estruturas do MOF após os ciclos de adsorção/dessorção e exposição a diferentes temperaturas. A análise através da espectroscopia de infravermelhos de reflectância difusa por transformada de Fourier (DRIFTS) nos três MOFs revelou uma alta capacidade de regeneração durante os ciclos de adsorção/dessorção, permanecendo estável a estrutura dos MOFs durante o contacto com vapor de água e após exposta em diferentes temperaturas.

O efeito da potência de irradiação e a temperatura do sólido foram estudados no MIL-125 (Ti) _NH_2 com o intuito de definir as melhores condições de operação para a regeneração com energia solar. As experiências foram realizadas no simulador solar, em condições controladas laboratorialmente, em que o leito adsorvente é irradiado sob luz solar simulada.

Um processo de captação de água a partir do ar por adsorção foi desenhado, ocorrendo condensação da água através da regeneração da corrente de saída. O processo de adsorção cíclica é composto por duas etapas em co-corrente, sendo elas a alimentação e purga. Com MIL-125(Ti)_NH_2, a produtividade mais alta foi alcançada no processo de TSA, em oposição ao PTSA e PTSA acoplado a um tanque de reserva. O processo de TSA (volume da coluna - 0,98 m³) permitiu atingir a produtividade máxima de H_2O de 111 l·dia^{-1} para MIL-125(Ti)_NH_2 e MIL-160(Al), enquanto para o CAU-10 e MIL-100(Fe) é possível coletar 84.0 e 79.8 l·dia^{-1}, respetivamente (temperatura de regeneração - 373 K, temperatura de condensação - 283 K e caudal – 0.30 m³·s^{-1}).

TABLE OF CONTENTS

LIST OF FIGURES

xviii

xxii

LIST OF TABLES

1 RELEVANCE AND MOTIVATION

1.1 Global water crisis

The water crisis is one of the primary global risks based on its societal impact, particularly the access to safe drinking water (H_2O) in regions with a dry (arid) or mainly dry (semi-arid) climate [1]. The World Economic Forum considers water crisis as one of the world´s global risks of society and industry [2]. Currently, the emerging markets of countries such as China, India, and Indonesia, are affected by water scarcity [3]. Indeed, according to the Food Agriculture Organization of the United Nations (FAO), water scarcity is defined as "an excess of water demand over available supply" [4]. Availability of water supply is dependent on natural and anthropogenic factors, while water demand is only dependent on anthropogenic factors by nature [4]. Malin Falkenmark, from Stockholm's Natural Science Research Council, points the aridity, drought, and water stress as the causes for the water scarcity [5].

Several factors, such as the increase of world population and the improvement of living standards, and expansion of irrigated agricultural lands, contribute to the rise of water demand [6, 7]. Indeed, the agriculture sector is the largest global water consumer (69% of annual water withdrawals) [8] against industry (19%) and domestics sectors (12%) [9].

More than 40% of the present world population has lack of water [10]. Over the past decades, the rate of demand for water is two times higher than the population growth rate [11, 12]. About 66% of the world population (4 billion) faced water scarcity episode for at least one month a year [13].

In 2015, about 159 million people collected directly drinking water from surface water, wherein 59% of them lived in sub-Saharan Africa [14, 15]. According to the FAO, in 2010, at least 50% of drinking water is provided from groundwater [16] (Figure 1.1). Indeed, in 2012, 2.5 billion people used only groundwater for their basic daily needs [17].
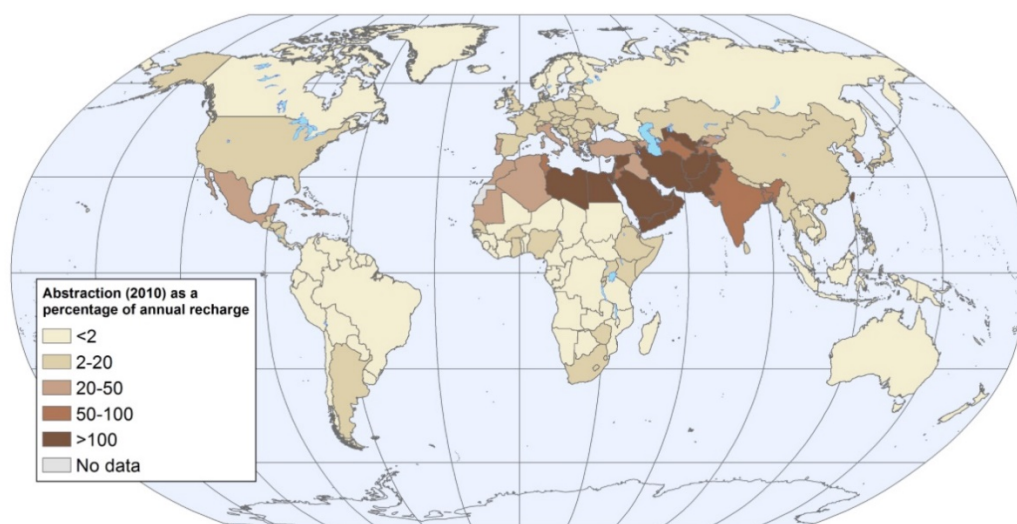
Figure 1.1. Groundwater development stress [18].

It is expected an increase in physical water stress due to climate change and the increase of the world population and consequently, their water demands (Figure 1.2) [19].
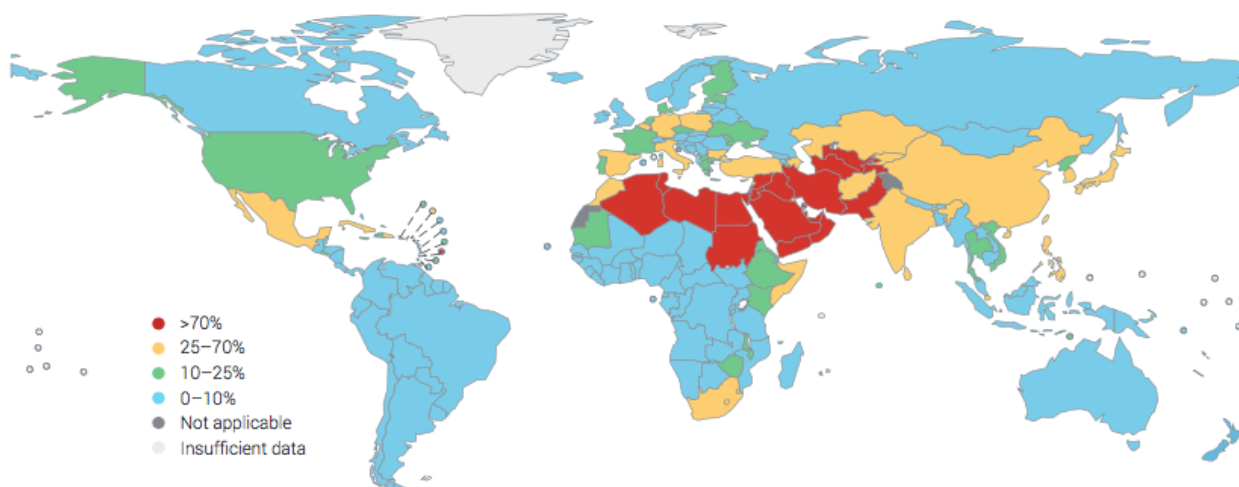
Figure 1.2. Levels of global water stress - the ratio of total freshwater withdrawn annually by all major sectors [9].

Climate change leads to an increase in the severity and frequency of extreme weather episodes [8]. Figure 1.3 presents the occurrence of floods and droughts for the period of 1996 to 2015.
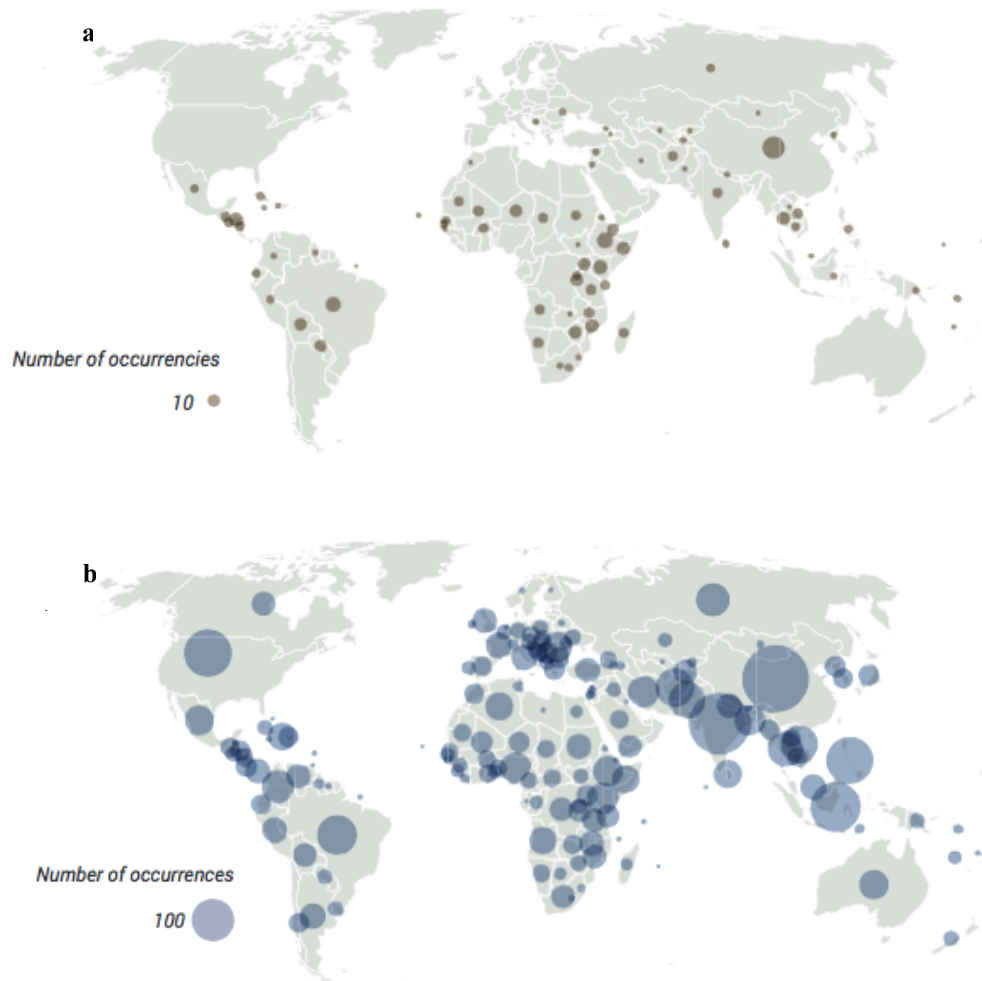
Figure 1.3. Country-level overview of the occurrence of droughts (a) and floods (b) between 1996 and 2015 [20].

1.2 Portugal water crisis

1.2.1 Water demand

In Portugal, daily water consumption per person is about 192 L [21]. This consumption is fulfilled by national resources (surface and groundwater) [21]. Agriculture is the sector with the highest water consumption in terms of volume (> 80%) [22]. Water distribution, in terms of sectors, is very variable along river basins as shown in Table 1.1. Alentejo is the region with the highest water consumption in the agriculture sector, while for North region the water consumption is higher in the urban sector.

Table 1.1. Water consumed by the main sectors in the hydrographic regions of Portugal [23].

Main sectors	Hydrographic Regions (ARH)				
	Norte	Centro	Tejo	Alentejo	Algarve
Urban supply	51.7	25.9	27.2	10.8	27.8
Agriculture	na	55.3	65.4	83.2	57.0
Livestock	na	0.6	0.5	na	na
Industry	44.6	17.9	6.5	4.6	4.0
Tourism	2.2	na	na	1.0	11.2
Golf	1.5	0.3	0.4	na	na
Energy	na	na	na	0.4	na

1.2.2 Climatology

In mainland Portugal, the frequency of extreme climatic phenomena occurrences is increasing, particularly drought situations, in the last decades (Figure 1.4), and mainly from February to April [24-26]. Due to the geographic location, mainland Portugal is prone to occur regular drought episodes, particularly in its Southern regions [26, 27].
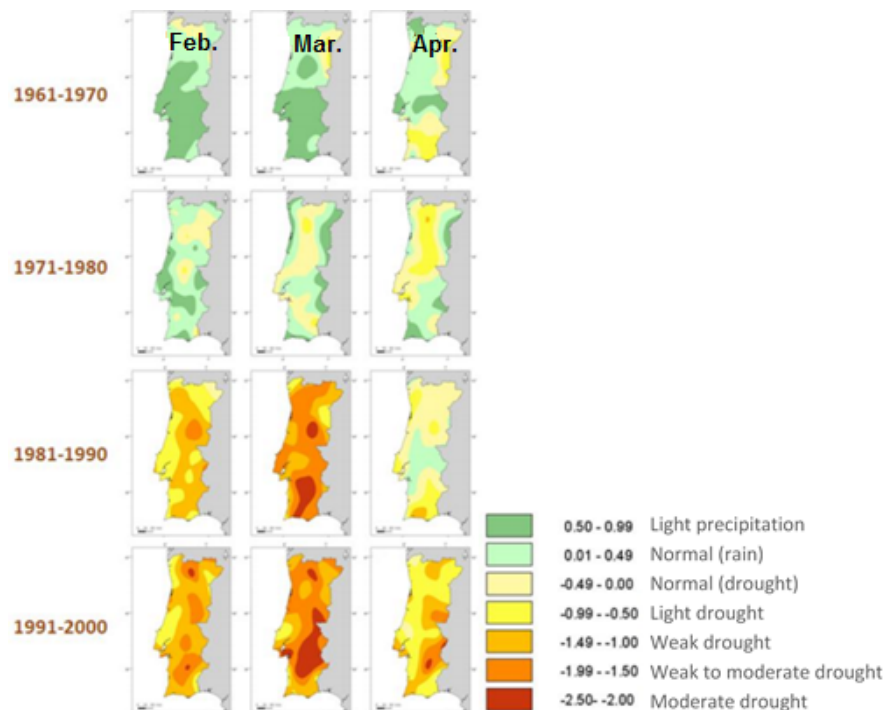
Figure 1.4. PDSI[1] monthly average in the decades 1961-1970, 1971-1980, 1981-1990, and 1991-2000 in mainland Portugal [28].

---

[1] *Palmer Drought Severity Index* (PDSI) - detects and classify dry periods accordingly with their intensity.

Figure 1.5 presents the number of consecutive months, which recorded the severe or extreme droughts of 1944-1945, 1948-1949, 1964-1965, 1974-1976, 1980-1983, 1990-1992, 1994-1995, and 2004-2006. From 2004 through 2006, 100% of mainland Portugal suffered periods of severe and extreme drought, and in some regions, these periods lasted between seven and nine months [10, 26]. The winter of 2019 was considered by the Portuguese Institute for Sea and Atmosphere (IPMA, IP) as a very dry and hot winter [29]. Indeed, the 2019's winter ended with all of the Portuguese mainland affected by drought (Figure 1.6) [30].
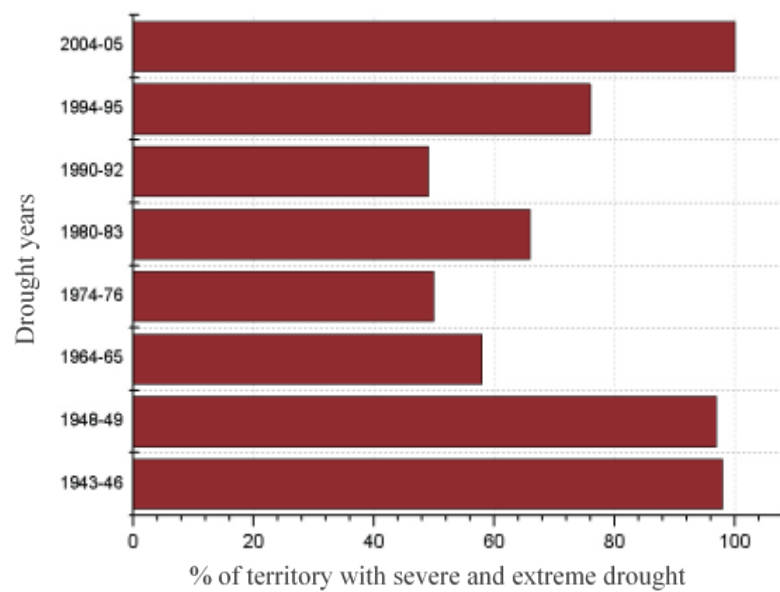
Figure 1.5. Percentage of the Portuguese territory affected by severe and extreme drought situations in the period of 1941 to 2006 [10].
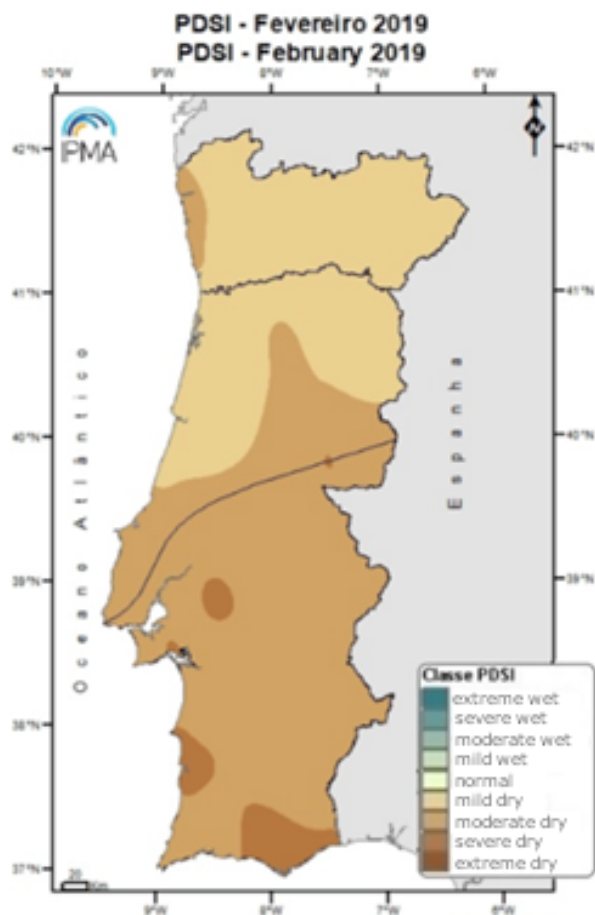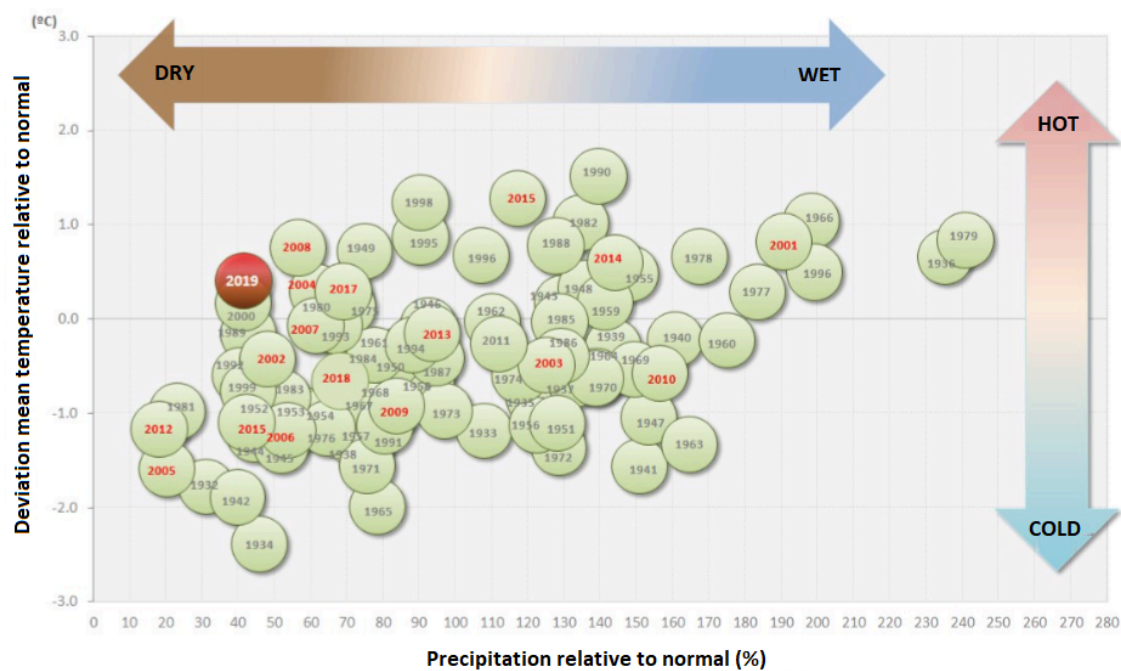
Figure 1.6. Climate classification per year (January and February 2019 – very dry and very hot), PDSI February 2019 [29, 30].

In consequence, the mainland Portugal arid area increased from 58% (1980 to 2010) to 63%, in the 2010 decade (Figure 1.7) [31].
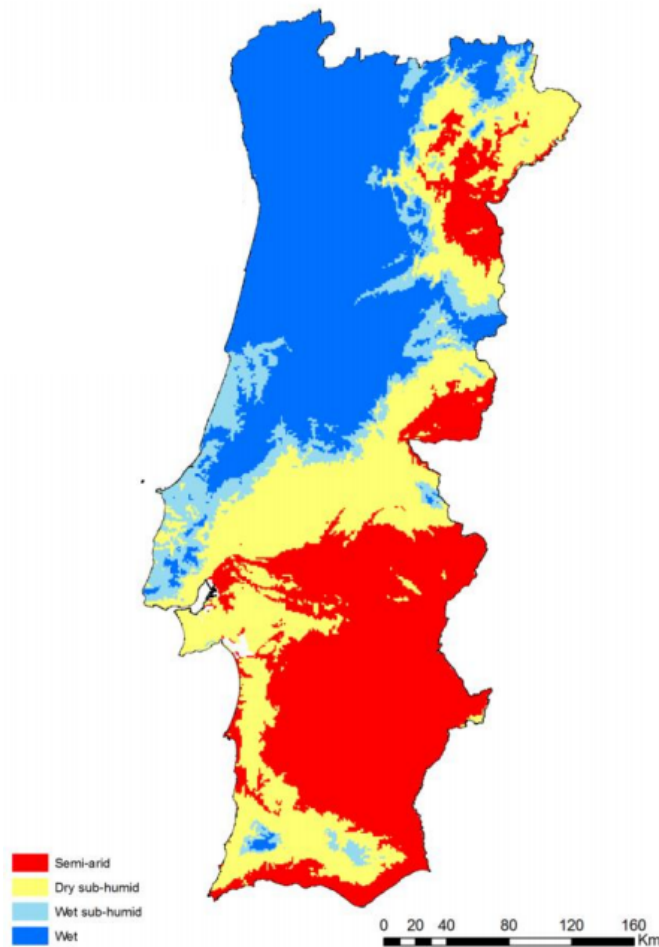
Figure 1.7. Spatial representation of the aridity index[2] [31].

1.3   European water policies

The access to water is a human right; therefore, policies and targets are being developed to attend this goal. In 2000, the Member States of the United Nations defined the Millennium Development Goals (MDGs) after the sign of the Millennium Declaration [15]. The seventh

---

[2] *Aridity Index* (AI) – ratio between the local precipitation (P) and the potential evaporation (ETP) from 1980 to 2010, classified as

Semi-arid: 0.20 – 0.50

Dry sub-humid: 0.50 – 0.65

Wet sub-humid: 0.65 – 1.00

Wet: > 1.00

goal aimed to ensure environmental sustainability with a target of 88% availability of drinking water sources, by 2015 [15]. This goal was established in 2010 (Figure 1.8); yet, in 2015, about 32% of the 215 countries still did not achieve such a goal (Figure 1.9).
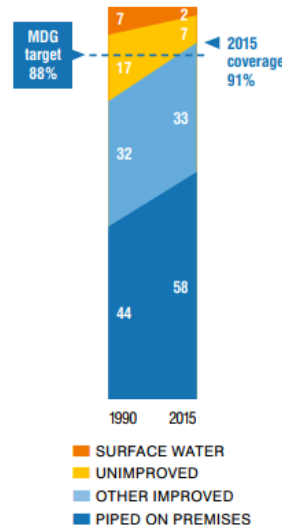
Figure 1.8. Global drinking water coverage and MDG target trends (%), 1990–2015 [15].
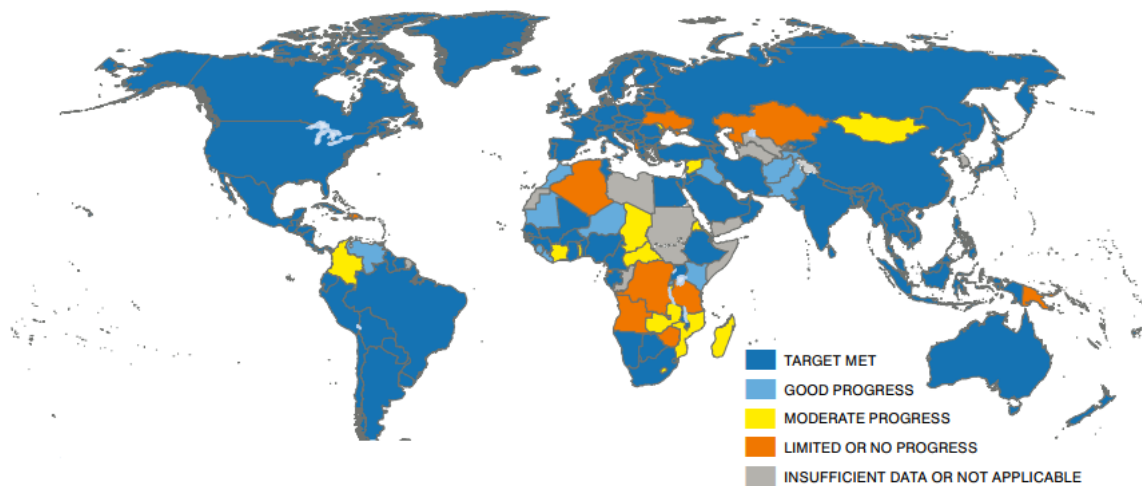
Figure 1.9. MDG target achievement for drinking water [15].

On September 2015, the Member States of the United Nations approved the 2030 Agenda for Sustainable Development covering 17 Sustainable Development Goals (SDG) (Figure 1.10) [15]. Goal 6 of this ambitious agenda, embraces to "Ensure availability and sustainable management of water and sanitation for all" [15].

Figure 1.10. Sustainable Development Goals [32].

This goal has eight specific targets to address all aspects of the freshwater cycle [15]:

6.1) safe drinking water;

6.2) adequate sanitation and hygiene;

6.3) water quality and wastewater;

6.4) water use and scarcity;

6.5) water resources management;

6.6) ecosystems;

6a) international cooperation;

6b) stakeholder participation.

Indeed, the European Commission has established water as one of the main focus areas of the "Climate action, environment, resource efficiency, and raw materials challenge" in the Horizon 2020 programme.

Portugal does not have a national policy or plan with the aim of drought mitigation [33]. Indeed, drought management is dispersed in several regulations of the sectors affected, as well as in municipal contingency plans (Table 1.2).

Table 1.2. Management instruments for drought planning in Portugal [33-36].

Year	Instrument	Scale
1998	Convention on cooperation for the protection and sustainable use of Portuguese-Spanish river basins	Iberian Peninsula
2001	River Basin Plans	River basins - Regional
2002	National Water Plan	National
2005	National Water Law	National
2005, 2012	Drought Commissions	National
2001	National Program for Efficient Water Use (PNUEA)	National
2010	National Strategy for Climate Change adaptation (ENAAC)	National
2011-2012	River Basin Management Plans	River basins - Regional
-	Specific Water Management Plans (PEGA)	Local
-	Municipal contingency plans	Local
-	Regulations for irrigated areas	Local
2000 - 2006 **2007 - 2013**	Strategic Plan for water supply and treatment of wastewater (PEAASAR)	National

1.4 Future perspectives

In 2050, the worldwide population is expected to grow by about 2 billion people relatively with 2019 (7.6 billion) [37], with about 2.4 billion people living in Sub-Saharan Africa [38]. This population increase will lead to an expected global water demand about 20 to 30% higher than the actual [39]. Indeed, according to the International Water Management Institute (IWMI), it is expected to increase about 40% by 2030 [40].

Figure 1.11 indicates the countries most affected by extreme water stress, which are mainly located in Asia, North Africa, and Middle East.

Water Stress by Country: 2040

ratio of withdrawals
to supply

Low (< 10%)
Low to medium (10-20%)
Medium to high (20-40%)
High (40-80%)
Extremely high (> 80%)
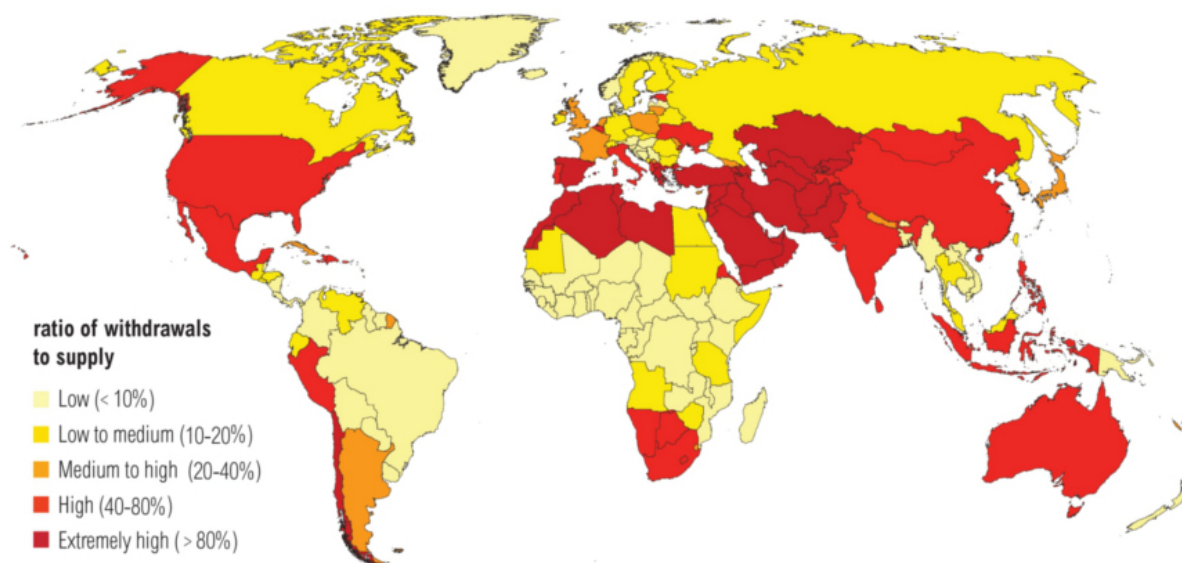
Figure 1.11. Global water stress forecast for 2040 [41].

In 2050, it is expected that about 1.8 billion people will be affected by water stress, with 80% of them living in developing countries [40, 42].

1.5   Objectives and Outline

With this dramatic scenario for water demand shortly, it is the main objective of this thesis to develop an efficient technology that allows water harvesting from air. This technology will be adsorption based and will exploit the potential of new emerging materials to act as water sponges, such as the Metal-Organic Frameworks (MOFs). For this purpose, adsorption equilibrium isotherms of pure component (carbon dioxide (CO_2), nitrogen (N_2), oxygen (O_2), and H_2O vapor) were measured at different temperatures. Breakthrough experiments were performed under different conditions to evaluate the dynamic behavior of adsorbents in fixed-bed experiments. The interactions between the adsorbates (*e.g.*, H_2O, CO_2) and the adsorbents, the stability of the shaped adsorbents regarding water vapor exposure, and the adsorption kinetics over/within in MOFs powder/crystals, was assessed by vibrational spectroscopy, namely by using an experimental reaction set-up equipped for in situ Diffuse Reflectance Infrared Fourier Transform Spectroscopy (DRIFTS) analyses. These results were essential for the mathematical modelling of the adsorptive process and model validation. The study of

regeneration of the adsorbent bed was performed in a solar simulator and allowed to assess the effect of operating conditions (*e.g.* irradiation intensity) on the efficiency of the regeneration step.

The thesis is divided into eight chapters described below.

Chapter 1 provides a vision of the water demand all over the world and the projections for the future. **Chapter 2** focuses on the most relevant studies, and main results in the field of water generation technologies, as well as the adsorbent materials applied, namely the MOFs. Also, a brief overview of energy involving global consumption trends and renewable energies is presented. In **Chapter 3** a detailed description of methodology and equipment is provided. An overview of selected adsorbents and the reasons for their choice is reported. Additionally, characterization techniques are presented. A complete explanation of the mathematical model developed to describe the adsorption dynamic behavior in an adsorber (fixed bed and Temperature Swing Adsorption (TSA)) is presented in **Chapter 4**. This chapter also includes the adsorption equilibrium models and the theoretical isosteric heat of adsorption. In **Chapter 5**, **Chapter 6**, and **Chapter 7**, the main results for each adsorbent material are reported, including the selected experimental conditions. The textural, morphologic and crystallographic properties of each adsorbent were evaluated by using classical characterization techniques, such as N_2 adsorption at 77 K, Scanning Electron Microscopy (SEM), and X-ray diffraction (XRD). Adsorption equilibrium and adsorption kinetics were assessed for the five selected materials. Studies related to bed regeneration with solar energy are also reported in this chapter. Finally, the design of TSA processes for water production was performed, for each adsorbent, the employed methodology is described, including the optimization of the operating conditions. **Chapter 8** summarizes the main achievements and conclusions obtained during this work and presents suggestions for future work.

References

1.   Balon, M. and F. Dehnad. *Water crisis in arid and semi-arid regions- an international challenge.* 2006. Tehran (Iran).

2.   World Economic Forum, *The Global Risks Report 2019*. 2019.

3.   World Water Assessment Programme, *Water in a changing world: the United Nations world water development report 3*. 2009, UNESCO: earthscan.

4.   Food and Agriculture Organization of the United Nations (FAO), *Coping With Water Scarcity: An Action Framework For Agriculture And Food Security: No 38* FAO Water Reports, Editor. 2012.

5.   Clarke, R., *Water: The international Crisis*, ed. Routledge. 1992.

6.   Vörösmarty, C.J., P. Green, J. Salisbury, and R.B. Lammers, *Global Water Resources: Vulnerability from Climate Change and Population Growth.* Science, 2000. **289**(5477): p. 284-288.

7.   Ercin, A.E. and A.Y. Hoekstra, *Water footprint scenarios for 2050: A global analysis.* Environment International, 2014. **64**: p. 71-82.

8.   World Water Assessment Programme, *The United Nations world water development report 2019 - leaving no one behind*. 2019, UNESCO.

9.   Food and Agriculture Organization of the United Nations (FAO). *Water uses*. 2016; Available from: http://www.fao.org/nr/water/aquastat/water_use/index.stm.

10.   Pires, V., *Análise das secas em Portugal Continental*. 2008, Instituto de Meteorologia. p. 15.

11.   Shiklomanov, I.A., *World Water Resources: A new appraisal and assessment for the 21st century*. 1998: United Nations Educational, Scientific and Cultural Organization (UNESCO), .

12.   Pazwash, H., *Urban Storm Water Management*. 2016: CRC Press

13.   Mekonnen, M.M. and A.Y. Hoekstra, *Four billion people facing severe water scarcity*. Science Advances, 2016. **2**(2).

14.   United Nations Children's Fund (UNICEF) and World Health Organization (WHO), *Progress on drinking water, sanitation and hygiene: 2017 update and SDG baselines*. 2017, World Health Organization (WHO) and the United Nations Children's Fund (UNICEF): Geneva. p. 110.

15.   United Nations Children's Fund (UNICEF) and World Health Organization (WHO), *Progress on Sanitation and Drinking Water: 2015 update and MDG assessment*. 2015, United Nations Children's Fund (UNICEF) and World Health Organization (WHO): Geneva.

16.   Winpenny, J., I. Heinz, S. Koo-Oshima, M. Salgot, J. Collado, F. Hernandez, and R. Torricelli, *The Wealth of Waste: The economics of wastewater use in agriculture*. 2010.

17.   UNESCO, *World's groundwater resources are suffering from poor governance*. 2012.

18.   International Groundwater Resources Assessment Center (IGRAC). *Groundwater Development Stress Map*. 2010   06.09.2017]; Available from: https://www.un-igrac.org/resource/groundwater-development-stress-map.

19.   United Nations (UN), *Sustainable Development Goal 6: Synthesis Report 2018 on Water and Sanitation*. 2018.

20.   Ligtvoet, W., A. Bouwman, J. Knoop, S. de Bruin, K. Nabielek, H. Huitzing, J. Janse, J. van Minne, D. Gernaat, P. van Puijenbroek, J. de Ruiter, and H. Visser, *The geography of future water challenges* 2018.

21.   Entidade Reguladora dos Serviços de Água e Resíduos (ERSAR). Available from: http://www.ersar.pt/pt.

22.   Agência Portuguesa do Ambiente (APA), *Programa nacional para o uso eficiente da água- Implementação 2012 - 2020*. 2012.

23.   Agência Portuguesa do Ambiente (APA), *Regional hydrographic management plans. Final Technical Report. Part 4 – Prospective scenarios MAMAOT*. 2012.

24.   Silva, Á., I. De Lima, and V. Pires, *Assessing changes in drought and wetness episodes in drainage basins using the Standardized Precipitation Index.* Bodenkultur, 2014. **65**: p. 31-37.

25.   Vicente-Serrano, S., J.I. López-Moreno, S. Beguería, J. Lorenzo-Lacruz, A. Sanchez-Lorenzo, J.M. García-Ruiz, C. Azorin-Molina, E. Morán-Tejeda, J. Revuelto, R. Trigo, M.F. Coelho, and F. Espejo, *Evidence of Increasing Drought Severity Caused by Temperature Rise in Southern Europe.* Environmental Research Letters, 2014. **9**.

26.   Pires, V.C., Á. Silva, and L. Mendes, *Riscos de secas em Portugal Continental.* Territorium: Revista Portuguesa de riscos, prevenção e segurança, 2010(17).

27.   Santos, J.F., I. Pulido-Calvo, and M.M. Portela, *Spatial and temporal variability of droughts in Portugal.* Water Resources Research, 2010. **46**(3).

28.   Pires, V., *Frequência e Intensidade de Fenómenos meteorológicos extremos associados a precipitação*. 2003, University of Lisbon. p. 98.

29.   Instituto Português do Mar e da Atmosfera (IPMA), *Boletim Climatológico Sazonal – Inverno de 2018/19* 2019.

30.   Instituto Português do Mar e da Atmosfera (IPMA), *Boletim Climatológico - Fevereiro 2019, Portugal Continental* 2019.

31.   *Plano de Prevenção, Monitorização e Contingência para situações de seca*. 2012, República Portuguesa.

32.   World Health Organization (WHO). *UN Sustainable Development Summit 2015*. 2015   06.09.2017];   Available   from:

http://www.who.int/mediacentre/events/meetings/2015/un-sustainable-development-summit/en/.

33. Iglesias, A., D. Assimacopoulos, and H.A.J. Van Lanen, *Drought: Science and Policy*. 2018: Wiley-Blackwell.

34. Do Ó, A. and M. Roxo, *Drought response and mitigation in Mediterranean irrigation agriculture.* WIT Transactions on Ecology and the Environment, 2009. **125**: p. 515-524.

35. Fidelis, T. and P. Roebeling, *Water resources and land use planning systems in Portugal—Exploring better synergies through Ria de Aveiro.* Land Use Policy, 2014. **39**: p. 84-95.

36. Costa, F., *Water policy(ies) in Portugal: Inertia and challenges within the European framework.* Méditerranée, 2018.

37. United Nations (UN), *World Population Prospects 2019: Highlights*, P.D. Department of Economic and Social Affairs, Editor. 2019.

38. United Nations (UN), *World Population Prospects: The 2012 Revision*. 2013: New York.

39. Burek, P., Y. Satoh, G. Fischer, M.T. Kahil, A. Scherzer, S. Tramberend, L.F. Nava, Y. Wada, S. Eisner, M. Flörke, N. Hanasaki, P. Magnuszewski, B. Cosgrove, and D. Wiberg, *Water Futures and Solution*. 2016: IIASA, Laxenburg, Austria.

40. Schlosser, C.A., K. Strzepek, X. Gao, C. Fant, É. Blanc, S. Paltsev, H. Jacoby, J. Reilly, and A. Gueneau, *The future of global water stress: An integrated assessment.* Earth's Future, 2014. **2**(8): p. 341-361.

41. Luo, T., R. Young, and P. Reig. *Aqueduct projected water stress country rankings.* 2015 [cited 2019 01.08]; Available from: https://www.visualcapitalist.com/extreme-water-shortages-are-expected-to-hit-these-countries-by-2040/.

42.   Floerke, M., C. Schneider, and R. McDonald. *Climate change and urban growth will pose a major challenge to urban water supply*. in *20th EGU General Assembly, EGU2018*. 0472018. Vienna, Austria.

2 STATE OF THE ART

2.1 Water harvesting

According to FAO, water harvesting (WH) corresponds to "collection of runoff for its productive use" [1]. Water harvesting techniques have been used throughout thousands of years [1, 2]. In the Negev Desert of Israel, WH schemes with 4000 years or more were discovered [3]. These schemes present irrigation systems using walls to channelize and collect floodwaters [3]. Babylon, Israel, Tunisia, China, Africa, and North and South America's regions are some examples where ancient WH structures were implemented centuries ago [4-11]. However, only in the 1970s and 1980s, the interest for water harvesting techniques increased due to widespread droughts in Africa [1, 12]. Rainwater collection, terracing, small dams, runoff enhancement, runoff collection, flood spreading, water holes and ponds, are some examples of the practiced WH [13].

The climate change and the world's population growth are factors that origin water stress [14]. To cover the lack of potable water, several techniques are being developed along with the traditional water sources. Nontraditional water sources such as seawater, fog and dew, and atmospheric water vapor are being considered to produce potable water [15].

2.1.1 Water extraction techniques

Desalination is one of the solutions that contributes to diminishing water scarcity [16, 17]. In this technique, the dissolved salts present in saline water are removed converting it to drinking water [18]. Desalination is an ancient technique; indeed it was discovered a description from Alexander of Aphrodisias (200 AD) in which sailors boiled seawater in a bronze vessel and the steam was then adsorbed by large sponges located in the mouth of the vessel resulting potable water [18, 19]. Distillation, dew evaporation, reverse osmosis, electrodialysis, and electrosorption are current water desalination methods [20, 21]. This technology has been developed in the past five decades [22] and the first systems presented high energy demand and high costs of implementation and process [21]. Minimization of energy utilization is one of the concerns related to this technology [23]. Nowadays, the use of renewable energy (solar, wind, and geothermal), and strategies for reducing energy-consumption are being developed and implemented [24-26].

Over the past two decades, the production of water for domestic and industrial use by this technology has substantially increased [18, 27]. Although in 2004, only 0.4% of the water use

was achieved by desalination (approximately 14 km³·year⁻¹), it is expected that by 2025 its contribution will double [28, 29]. In March of 2019 was estimated 15906 desalination plants across 177 countries, reaching approximately 95.4 million m³·day⁻¹ (34.8 km³·year⁻¹) worldwide desalination capacity [30]. Until 2030 is expected an increase of 9% or more per year of the desalination plants global capacity [18]. Worldwide desalination plants are mainly concentrated in the coastline, and these are larger than the ones present inland (Figure 2.1).
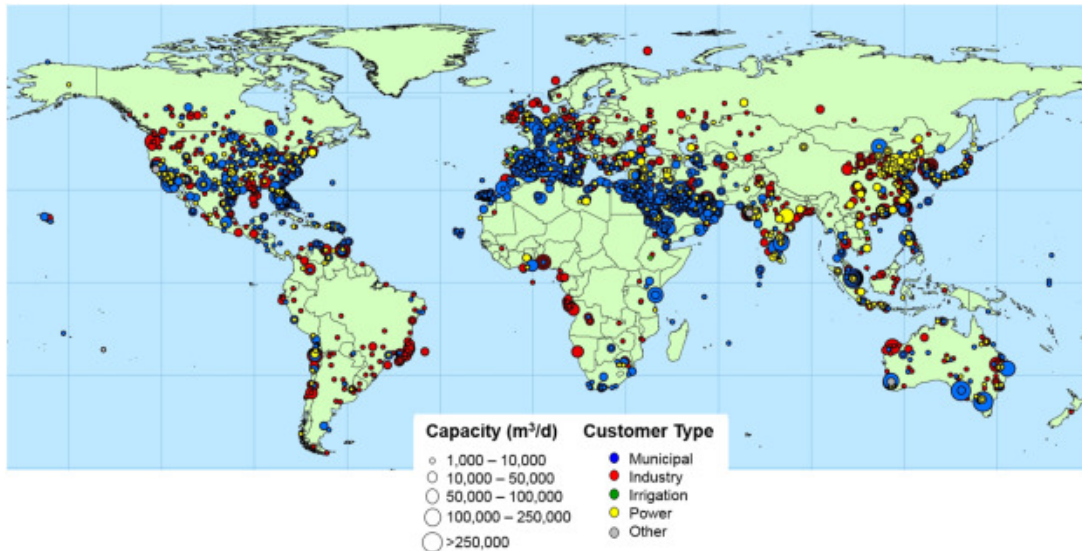
Figure 2.1. Worldwide distribution of operational desalination facilities and capacities (>1000 m³·day⁻¹) according to water-consuming sector [30].

In non-coastal arid regions, this technique is not suitable to be applied due to the nonexistence of saline water resources [31].

In areas where no viable liquid water source is available, such as arid regions, war zones, natural calamity areas, heavily chemically/biologically contaminated water supply areas, water in the atmospheric air can be considered as a possible water source. Indeed, on Earth, while the surface freshwater sources (rivers and lakes) only sum up to 1200 km³, there are 14,000 km³ of water in the air [32]. Water harvesting from the air provides water with sufficient quality for drinking [33], does not have spatial limitations and can be powered by renewable energies [34]. Besides, the capture of water from the air does not influence the hydrological cycle neither removes water from critical sources nearby, contrariwise to desalination [35].

The moist from atmospheric air can be extracted by different Atmospheric Water Vapour Processing (AWVP) technologies, which are divided into three categories, according to Wahlgren [36] (Figure 2.2) classification:
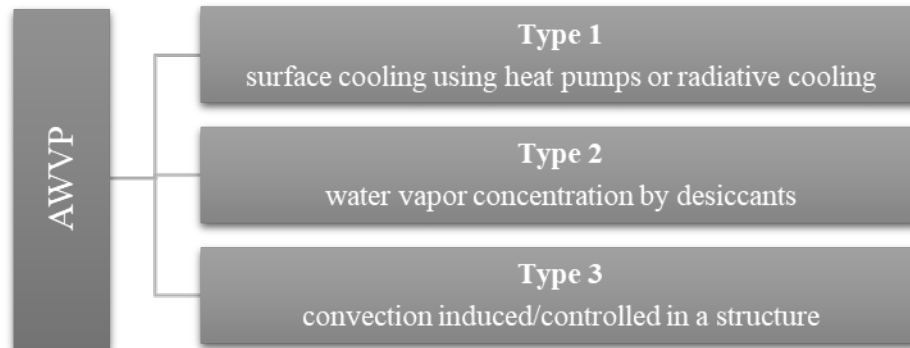
Figure 2.2. AWVP technologies for the extraction of moisture from atmospheric air.

Tu and his co-workers [37] present a similar categorization of **Atmospheric Water Generators (AWG) technologies**, dividing them in three major classes: integrated systems, vapor concentration, and direct harvesting (Figure 2.3). Direct harvesting and vapor concentration can be subdivided according to the need for an external power or not [37]. Furthermore, Milani *et al.* [38] classified moist air dehumidification technologies into two dehumidification strategies: via cooling surfaces and via desiccants (Figure 2.4). The choice for the best extraction method depends on the atmospheric and meteorological conditions, as well as on the economic factors [31].
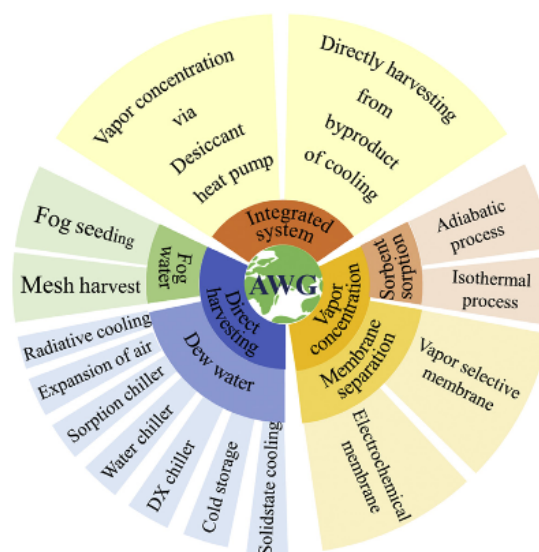
Figure 2.3. Atmospheric water generators classification [37].
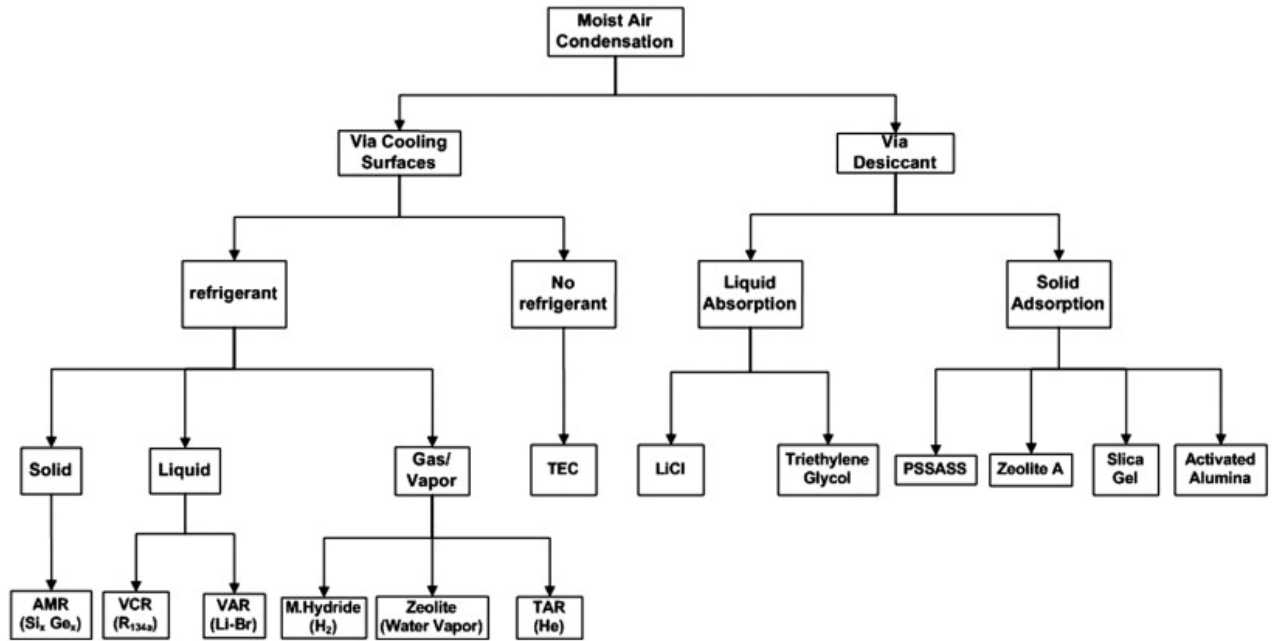
Figure 2.4. Air dehumidification methods classification and main materials. (AMR – active magnetic regenerator, M.Hydride – metal hydride systems, TAR – thermoacoustic refrigeration, TEC – thermoelectric cooler, VAR – vapor absorption refrigeration, VCR – vapor compression refrigeration, PSSASS – polystyrenesulfonic acid sodium salt) [38].

Water collection from **fog** is a technique practiced for a long time. Reports about fog drip from trees in California were recorded at the beginning of the 1890s [39], and at early 1900s, projects to collect water from fog started in South Africa (Table Mountain) [39, 40]. Other studies (*e.g.* Nagel study [41] and Kerfoot study [42]) followed this aim of water collection from fog; however, most of them were not successful due to the lack of knowledge about physics involved in the process of water collection [39]. In 1987 started a new era of fog collectors with the development of the second larger operational fog-water collection project (large fog collectors) in Chile, by a collaboration between researchers from Chile and Canada [39, 43]. The 100 fog collectors (each 12 m long by 4 m high) allowed a maximum production of 20 $l \cdot m^{-2} \cdot day^{-1}$ [33].

Table 2.1 summarizes some of fog water harvesting potential worldwide, presenting the location of the fog harvester, the operation period, number of fog days per year, the water amount obtained, and the study reference. From the list of works presented, it is possible to observe a significant variability in the amount of water captured (range of 0.93 – 41.8 $l \cdot day^{-1} \cdot m^{-2}$) depending on the local, the number of fog days during the period of the study, and relative humidity (RH).

Table 2.1. Summary of literature review of fog collectors implemented worldwide.

Country	Site	Operation period	Fog (days·year^{-1})	Fog water collection (L·day^{-1}·m^{-2})	Reference
Canary Islands	Tenerife (Anaga)	2006–2010	354	10	[33, 44, 45]
Cape Verde	Serra Malagueta	2003	365	12	[33, 45]
Chile	Alto Patache	1997–2010	365	7.8	[33, 45, 46]
	Cerro Guatalaya	1997–2001	-	0.93	
	Cerro Moreno	1999–2001	-	8.26	
	Paposo	1999–2001	-	3.36	
	Falda Verde	1998–2000	-	1.43	
	El Tofo (Chungungo)	1987–2002	365	2.98	
Colombia	Andes Mountain	May 2008 – Feb. 2009	210	2.0	[33, 47]
Ecuador	Pachamama Grande	1995–1997	210	4	[33, 48]
Guatemala	Tojquia	2006–2010	210	6	[49]
India	Coimbatore	-	-	7.7	[50]
Namibia	Central Namib Desert	1996–1997	-	2.4	[51]
Nepal	Naya Bazar	Feb. 1998–Apr. 2000	-	1.4 – 33.0	[52]
	Megma	May 2000 –Sep. 2000	-	17.4 – 41.8	
Peru	Mejia	1995–1999	210	11.8	[33, 45]
South Africa	Lepelfontein	1999–2001	~ 188	4.6	[33, 53]
	Soutpansberg		200	2	
Spain	Valencia	2007–2010	142	3.3	[33, 54, 55]
Yemen	Hajja	2003–2005	-	4.5	[33, 56]

The collection of fog droplets depends on the diameter of the droplets, the fog-laden wind speed, and the nature of the collection surface (area and mesh efficiency) [57, 58]. Fog collectors can operate in regions with less than 1 mm of rain per year [14]. The most common method of fog collection is using a vertical mesh, perpendicular to wind direction, allowing to trap fog droplets (Figure 2.5) [37, 59]. Then, the condensed water is drained to a collector by gravity [37, 59, 60].

Figure 2.5. Typical fog water collector with fog harvester arranged in the perpendicular direction of the wind [59].

According to Schemenaeur and co-workers [58], for a fog collector to be efficient it is necessary to fulfill three criteria in terms of location: (i) located in regions with frequent fog events; (ii) positioned in high-elevation areas (*e.g.*, mountains); and (iii) windy places. The constant need for high relative humidities in the air (about 100%) is a restriction in its application on sites with typically low RH [14]. Another problem is the uncertainty of climate change in the long term, with Johnstone and Dawson [61] suggesting a significant reduction in fog frequency in the Pacific basin, while Haensler and his co-workers predict a rise in the Atlantic areas [62].

One of the first studies dealing with water extraction from atmospheric air was patented in the former USSR as early as in 1947 [63]. The invention consists of a vertical system and inclined channels in the soil which collects water by cooling moist air to a temperature below its dew point. **Dew harvesting** is a renewable process of producing a significant amount of water in isolated or arid regions [64-66]. The methodology of collecting fresh water from dew in deserts has been practiced since ancient times [66]. It is believed that Ancient Greeks, who founded Theodosia (6th century BC), used dew collectors to fulfill their water demand [67, 68]. Radiative (also known as passive) and active condensers are the two main types of dew condensers (Figure 2.6) [69].
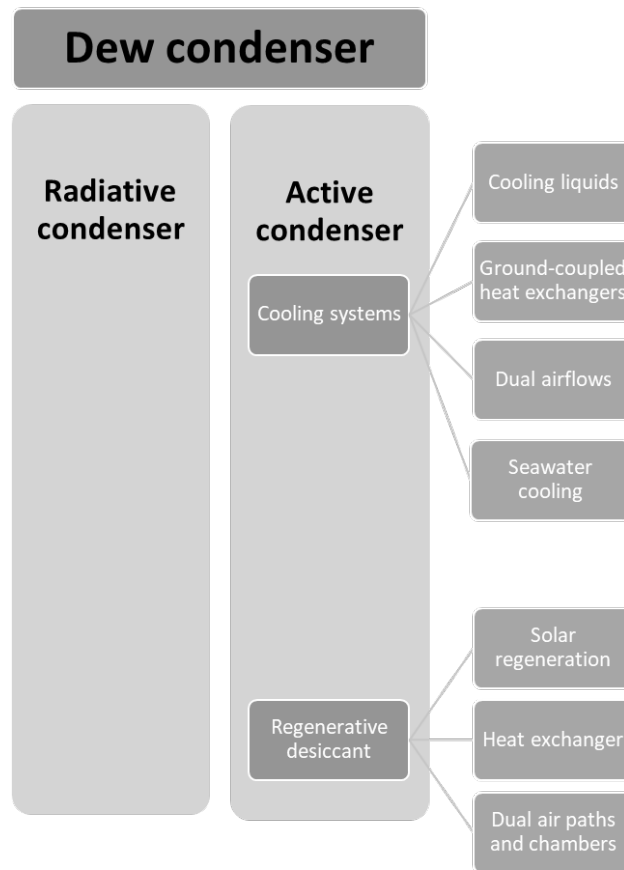
Figure 2.6. Dew condenser technologies (adapted from [69]).

Passive dew condenser (PDC) is dependent on the physical process responsible for dew collection and does not rely upon any energy input [69]. It is one of the most promising and most accessible technologies to collect water from the atmosphere [70, 71]. This technology recorded its highest yield in a range of $0.3 - 0.6$ L·day^{-1}·m^{-2} in regions facing water scarcity (arid and semi-arid regions) [71-73]. Nevertheless, radiative condensers are affected by several factors that limit their application (Figure 2.7).
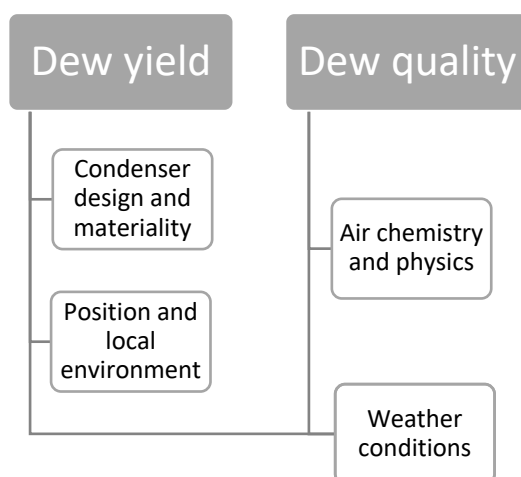
Figure 2.7. Factors that affect dew collection and water quality of a passive dew condenser (adapted from [74]).

Table 2.2 reports some examples of the potential radiative condensers supports during dew seasons worldwide, using different methodologies or combinations of methodologies, shapes, and materials.

Table 2.2. PDC types implemented worldwide.
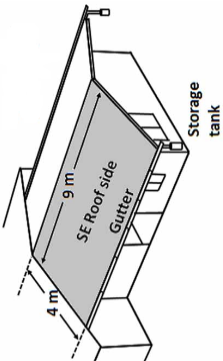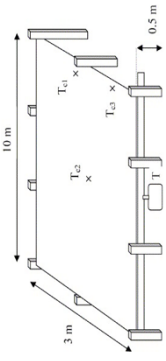
Country	Site	Structure	Material	Water collection ($l \cdot m^{-2} \cdot day^{-1}$)	Reference
Chile	Combarbalá		Condenser-on-roof (aluminosilicate minerals)	**0.05**	[74]
Croatia	Dalmatian Coast		Condensing foil (TiO_2 and $BaSO_4$ microspheres embedded in a matrix of low-density polyethylene (LDPE))	**0.06 (Zadar)** **0.03 (Komiža)**	[72]
France	Ajaccio		Condensing foil (TiO_2 and $BaSO_4$ microspheres embedded in a matrix of LDPE)	**0.12 – 0.8**	[75]
India	Gujarat		Condenser-on-ground (foamed polystyrene insulation)	**0.06**	[65]
India	Kothara	–	Condenser-on-roof (corrugated galvanized iron)	**0.09**	[76]

Table 2.2. PDC types implemented worldwide (cont.).

Country	Site	Structure	Material	Water collection (L·m⁻²·day⁻¹)	Reference
Israel	Revivim desert Eshtaol sub-humid hills Rehovot semi-arid plain		Polyethylene (PE) foil	**0.03 – 0.12**	[77]
Kenia	Maktau		PE foil and polyvinyl chloride (PVC) foil	**0.052 – 0.069 (night)**	[78]
Spain	Cartagena		Black PE foil (BF) White PE standard foil (WSF)	**0.12 (BF) 0.10 (WSF)**	[71]
Sweden	Kungsbacka	–	PE foil	**0.08**	[79]
Tanzania	Dodoma	–	PE foil	**0.06**	[79]
The Netherlands	Haarweg Station		PE foil and PVC foil	**0.18**	[80]

Active dew condensers (ADC) are an innovative alternative to produce higher yields of water by using additional energy inputs [69]. Although relative humidity also influences their efficiency, other weather conditions (*e.g.* sky emissivity, wind speed, and topography) don't have much impact contrariwise to radiative condensers [81]. Though the earliest active dew condensers were developed in the 1930s, only after the 1980s the interest on them has increased, due to the commercialization of mechanical refrigeration [36, 37]. They are a tool for water management in areas with water quality or quantity deficit [37]. The water yield is dependent on the active condenser design and can vary between 20 l·day^{-1} (small portable drinking water unit) up to more than 200,000 l·day^{-1} (agricultural water devices) [82]. Design is the principal factor that affects energy consumption and recently, active condensers are designed to minimize the consumption of energy or use renewable energy to power the unit (*e.g.*, solar energy) [37, 69, 82, 83]. Artificial **cooling systems** are based on a refrigerant fluid circulating by a compressor through the condenser [82]. Then, an expansion valve leads the refrigerant to the evaporator which allows cooling of the surrounding air to its dew point leading the condensation of water vapor on its surface (Figure 2.8) [82]. A water reservoir, purification and a filtration system are coupled to the active condenser, excepting for agriculture purposes where purification and filtration may not be required [82]. The rate of water generation depends on ambient air temperature, size of the compressor, and relative humidity [84].
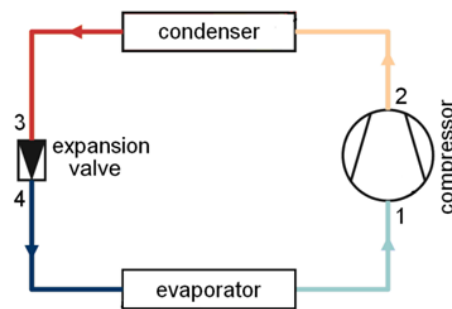
Figure 2.8. Scheme of a typical single-stage compression refrigeration system (adapted from [85]).

Low maintenance and operation costs and low initial investment are some of the advantages of active condenser using cooling condensation mechanism [69]. The ability of water condensation, even when the ambient temperature is higher than dew point temperature, makes this technology more efficient than radiative condensers [69]. The possibility of freezing the

evaporator coils and the probability of low water production-effectiveness during the low airflow periods are some disadvantages addressed to this method [69].

Water capture by desiccants (liquid or solid) through adsorption processes is the most common type of active dew condenser [69, 82]. The desiccant (*e.g.*, silica and zeolite) is exposed to moist air and then, the water is removed by a stimulus source (heat) and collected (Figure 2.9) [69]. The most common desiccants such as alumina, zeolite, and silica gel, although present high water vapor adsorption capacity, demand high temperatures (> 160°C) to perform water desorption efficiently [86]. Metal-organic frameworks, nanoporous inorganic materials, and composite materials are some examples of desiccant materials that present high water-uptake performances (Figure 2.10) [37]. The capacity of hygroscopic materials to extract and retain water, makes this technology more efficient than radiative dew condenser [69]. Besides the need for energy input, the high initial costs of desiccant materials and the need to be replaced periodically are some other disadvantages of regenerative desiccant technologies [69].
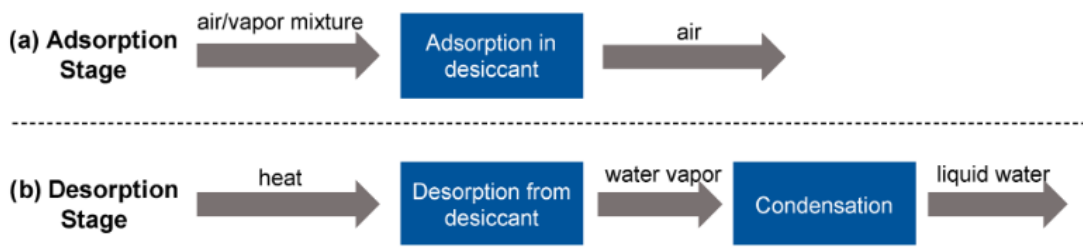
Figure 2.9. Basic water harvesting by sorption-based process: (a) moist air adsorption on desiccant; (b) desorption of water by applying heat to the desiccant with subsequent condensation [87].
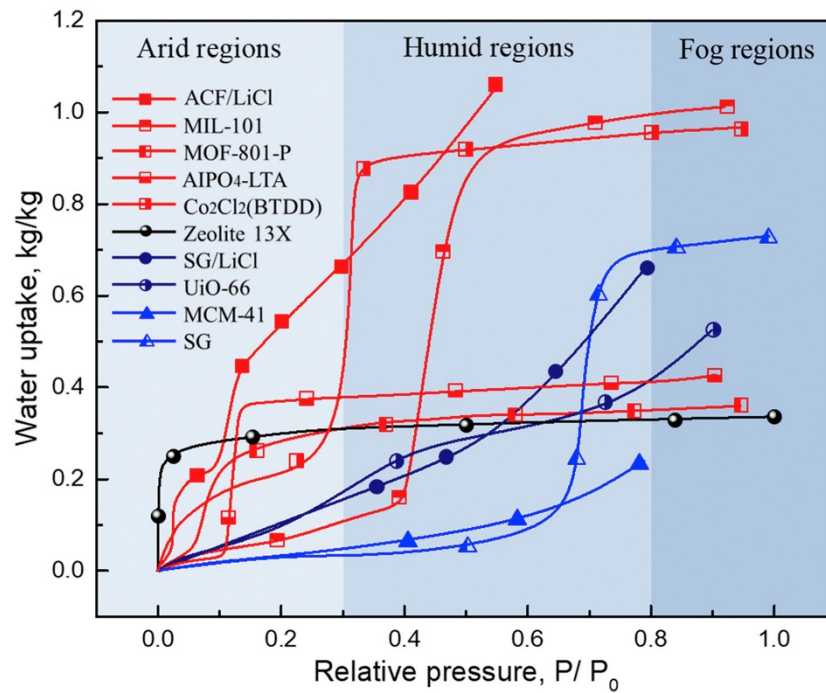
Figure 2.10. Desiccant materials with high potential for water-harvesting systems applications [37].

The performance and efficiency of water capture by sorption-based processes are dependent on heat and mass transport properties, mainly material and component-level properties (Figure 2.11) [87].
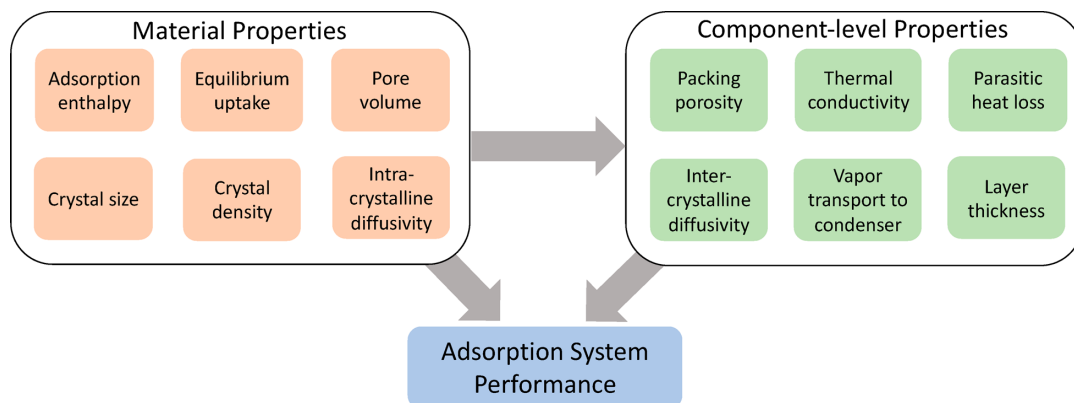
Figure 2.11. Factors that influence the adsorption water system performance [87].

In sorption-based processes, a cyclic scheme must be designed to regenerate the adsorbent in order to operate it continuously. The regeneration of the adsorbent can be done by increasing the temperature in a process termed Temperature Swing Adsorption (TSA). According to Furukawa *et al.* study [88] exist three essential requirements in all sorption-based system with

porous material: (i) water stability and high cycling performance; (ii) water adsorption isotherm should exhibit a steep uptake ("S" - shaped isotherm), with the pore filling or condensation into the pores occurring at low relative pressures; and (iii) high water vapor adsorption capacity [88].

Regarding the regeneration step, solar-thermal-driven water harvesting can be a promising renewable energy process and solar energy can be used in its direct or indirect forms [89]. In arid regions with low humidity, there is an excellent sunlight availability (> 7 kWh·m^{-2}·day^{-1}, which is equivalent to 7 hours of 1 sun (1 kW·m^{-2}) per day) [90]. The main advantage of the solar air heating system is that the necessary energy for the endothermic desorption process is provided by an inexhaustible natural resource (sun), which will lead to a significant reduction in energy costs. Recently, the scientific community started to use solar energy to powered AWGs by **sorption-regeneration-condensation** method, and dew water harvesting by **sorption chiller** [91, 92].
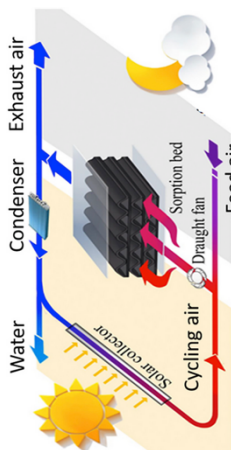
Table 2.3 presents three basic configurations of sorption-regeneration-condensation systems (glass-covered greenhouse sorber, sandwich plate sorber, and packed columns sorber) [37]. The information included in the table covers the configuration type and its structure, material used and its composition (Comp.), operating conditions (temperature (T), relative humidity, pressure (P)), water production (experimental and/or simulation), and reference (Ref.). Solar-powered sorption-based systems with an active condenser (*e.g.*, packed columns sorber [93, 94]) present high potentiality to be applied in compact systems, providing efficiency and wide adaptability [37].

Dew water harvesting by sorption chiller systems provides a continuous production if coupled with a heat storage system [37]. Further tests are necessary since some scientific studies reported that this system might not be efficient due to its complexity and expensive development; however, these assumptions are only based on the results obtained in the simplest adsorption chillers [92].

Table 2.3. Water extraction by sorption-based AWGs.

Configuration	Structure	Material	Comp.	Operating conditions	Water production Experimental	Water production Simulation	Ref.
		Calcium chloride (CaCl$_2$) and 1 kg of saw wood	10% CaCl$_2$	T=299–346K	76mL·kg⁻¹·day⁻¹(max)	–	[37, 95]
			20% CaCl$_2$	T=304–352K	82mL·kg⁻¹·day⁻¹(max)	–	
			30% CaCl$_2$	T=307–361K	100mL·kg⁻¹·day⁻¹(max)	–	
			40% CaCl$_2$	T=302–353K	110mL·kg⁻¹·day⁻¹(max)	–	
			50% CaCl$_2$	T=306–361K	144mL·kg⁻¹·day⁻¹(max)	–	
Glass-covered greenhouse sorber – PDC			60% CaCl$_2$	T=310–368K	180mL·kg⁻¹·day⁻¹(max)	–	
		Zeolite 13X	0.5 kg		12-32 g·kg⁻¹	–	[37, 96]
			1.65 kg	30-50%RH T=291–298K	15-39 g·kg⁻¹	–	
		MOF 801/G	0.825 kg		45-95 g·kg⁻¹	–	
			0.412 kg		63-87 g·kg⁻¹	–	
			0.600 kg	35%RH T=288K	47 g·kg⁻¹	–	
					100 g·kg⁻¹	–	
		MOF 303/G	0.600 kg	30-50%RH T=291–298K	100-175 g·kg⁻¹	–	
Sandwich plate sorber – PDC		MOF-801	–	T=298–338K RH=20% (T=298K) P>0.6kPa	0.24L·kg⁻¹·cycle⁻¹	0.25L·kg⁻¹·cycle⁻¹	[37, 97]

Table 2.3. Water extraction by sorption-based AWGs (cont.).

| Configuration | Structure | Material | Comp. | Operating conditions | Water production | | Ref. |
					Experimental	Simulation	
Packed column sorber - ADC		Active Carbon Felt with Lithium chloride (LiCl)	30% LiCl	20%RH T=350K	0.65g· g^{-l}	–	[37, 94]
			2.1 g	70%RH T=298-353K P=22.2mbar	2.9 g· g^{-l}	–	[93]
				20%RH T=298-353K P=6.3mbar	1.2 g· g^{-l}	–	

The **performance of AWGs** can be evaluated by three parameters: (i) moisture recovery ratio (RR); (ii) the specific energy consumption (SEC); and (iii) the specific water production (SWP) which corresponds to the water collected per day per unit collector area [37]. Passive condensers are usually evaluated by SWP, while RR and SEC (equations 2.1 and 2.2, respectively) are used to assess the water productivity of active condensers [37, 98]. The following equations can evaluate water harvesting by direct cooling

$$RR = \varepsilon_d \left(1 - \frac{d_{cond}}{d_i}\right) \tag{2.1}$$

$$SEC = \frac{Q_{cond}}{m_{H_2O}} \approx C_p \left(\frac{\varepsilon_T}{\varepsilon_d}\right) \left(\frac{T_i - T_{cond}}{d_i - d_{cond}}\right) + h_{fg} \tag{2.2}$$

with T_i and T_{cond} representing operating/feed temperature and condensation temperature, respectively; ε_d and ε_T are the mass and heat-exchange effectiveness of the condenser, respectively; d_i and d_{cond} corresponding to saturated humidity ratio at temperature of inlet air (T_i) and condensation temperature (T_{cond}), respectively; C_p is the specific heat capacity and m_{H_2O} is the moisture harvested per unit mass of dry air; h_{fg} is the enthalpy of condensation and Q_{cond} correspond to the total cooling load of the air, resulted by the sum of sensible heat load (temperature change of moist air) and the latent heat load, related to h_{fg} [37, 99]. Gido and his co-workers defined a similar index to assess the process efficiency, which is the Moisture Harvesting Index (MHI) [100] and is defined as

$$MHI = \frac{h_{fg}}{SEC} \tag{2.3}$$

PDC and passive sorption-based AWGs present low SWP due to inefficient radiative cooling capacity and low RR, respectively [69, 101]. Solar-powered sorption-based systems with active condenser present high potential, as mentioned before, although some challenges for its performance should be overcome: (i) inadequate design leading to heat losses and/or no reuse of heat before and after the condensing step; (ii) disregard possible kinetic limitations in terms of adsorbent selection and adsorber design; (iii) ineffective application of energy on adsorbents during water production; and (iv) lack of cost-effective heat sinks to obtain maximum water production [37].

2.2 Adsorbents and water adsorption

Adsorption is a surface phenomenon based on the exposure of a solid surface (adsorbent) to a gas or liquid (adsorbate) [102-104]. The earliest known use of adsorption corresponds to the manufacture of bronze by the Egyptians and Sumerians in 3750 BC, who used charcoal (activated carbon) for the reduction of copper, zinc, and tin ores [103]. However, only in 1881, the designation of "adsorption" as defined by the physicist Heinrich Kayser appeared in the literature [103]. Adsorption processes can be employed in separation [105, 106], purification [107, 108], or storage [105, 106] techniques, and is based in two steps (adsorption and desorption). Activated carbon, silica gel, activated alumina, and zeolites are some of the most common commercial adsorbents.

The type of bond formed in the adsorption process leads to its classification as chemisorption, physisorption, or electrostatic sorption [102-104]. Chemisorption involves the formation of a strong or even not reversible chemical bonding between adsorbent and adsorbate, while physisorption results from the establishment of a weaker and unstable bond yet reversible, including the Van der Waals forces [103, 109]. Table 2.4 presents the most significant differences between the two types of sorption identified by Inglezakis and Králik [103, 110].

Table 2.4. Main divergent characteristics between chemisorption and physisorption [103, 110].

	Chemisorption	Physisorption
Bonding forces	Chemical bond	Van der Waals
Adsorption temperature	Usually high temperatures	Low temperatures
Adsorption enthalpy	High enthalpy values (typically 40–800 kJ/mol)	Low enthalpy values (typically 5–40 kJ·mol^{-1})
Reversibility	Dissociative and irreversible	Nondissociative and fully reversible
Saturation uptake	Monolayer adsorption	Multilayer adsorption
Kinetics of adsorption	Very variable	Fast
Multilayers	No	Yes

The electrostatic sorption, also known as ion exchange, involves the bonding of ions with charged functional groups through Coulomb attractive forces [103].

Adsorption equilibrium and adsorption kinetics are essential phenomena that affect the capacity of adsorption and diffusional resistance, respectively, and are important tools to understand the adsorption itself [111]. Ideal adsorbent should present a good balance between sorption capacity and kinetics. Accordingly with Do, the porous solid adsorbent should present a large surface area or micropore volume, as well a large pore network with the aim of molecules transportation into the adsorbent interior [111]. Likewise proposed that a "good adsorbent" must present a combination of micropores (diameter < 2 nm) and macropores (diameter > 50 nm) [111].

Adsorption equilibrium isotherms allow to quantify the adsorption capacity of the adsorbent and provide information about adsorbent and adsorbate properties. In 1985, physisorption isotherms were divided into six types by the International Union of Pure and Applied Chemistry (IUPAC) [112]; however, the emergence of new typologies of adsorption equilibrium isotherms due to new pore structures led to an updated classification by IUPAC in 2015 [113]. Figure 2.12 presents the actual IUPAC isotherm classifications. Type I isotherms are associated with microporous adsorbents displaying small relative external surface area comparatively to the pore surface area [113, 114]. Type I(a) isotherms are related to narrow microporous (width <~ 1 nm), while for Type I(b) isotherms result from larger micropores and possibly narrow mesopores (<~ 2.5 nm) [113]. Type II isotherms are given by nonporous or macroporous adsorbents exhibiting monolayer (until near the inflection point - B) and multilayer adsorption [115, 116]. Type III also results from nonporous or macroporous adsorbents; however, it presents weaker adsorbent-adsorbate interactions with no discernable inflection point [113, 116, 117]. Type IV isotherms result usually from mesoporous adsorbents (> 20 Å diameter) showing an inflection point occurring near the completion of monolayer followed by pore condensation [113, 115, 116, 118]. What distinguishes Type IV(a) from Type IV(b) is the presence of capillary condensation accompanied by hysteresis [113, 116]. As in Type IV isotherms, Type V is given by mesoporous adsorbents with adsorbate–adsorbent interactions [115, 116]. In the case of Type VI isotherms, also called stepped isotherms, they are associated with multi-layer adsorption on uniform nonporous surfaces [113, 115].
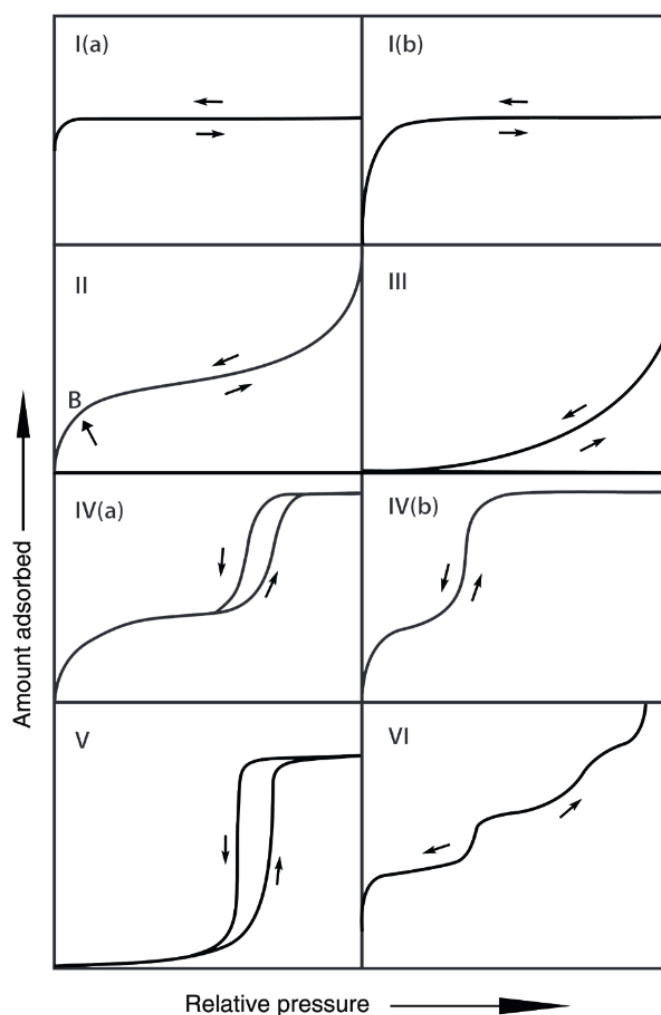
Figure 2.12. IUPAC classification of physisorption equilibrium isotherms [113].

Besides the knowledge of adsorption equilibria, the understanding of adsorption kinetics is crucial because it provides critical information to design an efficient adsorber [111, 119]. Adsorption kinetics is affected by transport mechanisms and the diffusivity of the gases.

2.2.1 MOFs

MOFs or porous coordination polymers (PCPs) are porous crystalline hybrid materials [120]. These porous crystalline structures result from the connection between inorganic clusters, also known as secondary building units (SBUs), by organic ligands in one, two, or three dimensions creating open crystalline frameworks with permanent porosity [121, 122]. These different possible connexions lead to a large diversity of topologies, resulting in a great variety of porosity and surface area [123, 124]. Additionally, the inherent tunability by the interaction of the organic ligands with functional moieties increases the diversity of potential materials

exponentially [125-129]. In the 2000s, thousands of new structures were developed, and in mid-2000s, these materials gain the status of a new class of adsorbents grouped alongside activated carbons and zeolite [116]. The number of MOF materials has increased significantly in the past decade, recording in 2016 ca. of 70,000 materials [130]. MOFs have potential for numerous applications in different areas, such as in hydrogen storage [131], catalysis [132], heat pumps [133, 134], sensing [135], drug delivery [136, 137], and adsorption/separation [138, 139]. Recently, the interest of MOFs for water vapor capture increased (Figure 2.13) [37, 87, 98, 140-142]. Indeed, a few recent publications demonstrated the great potential of robust MOFs in water adsorption related processes, being stable during several water adsorption/desorption cycles [143-147]. Design of any adsorption-based process requires the adsorption equilibrium and kinetic data for the adsorbate-adsorbent pair to be employed.
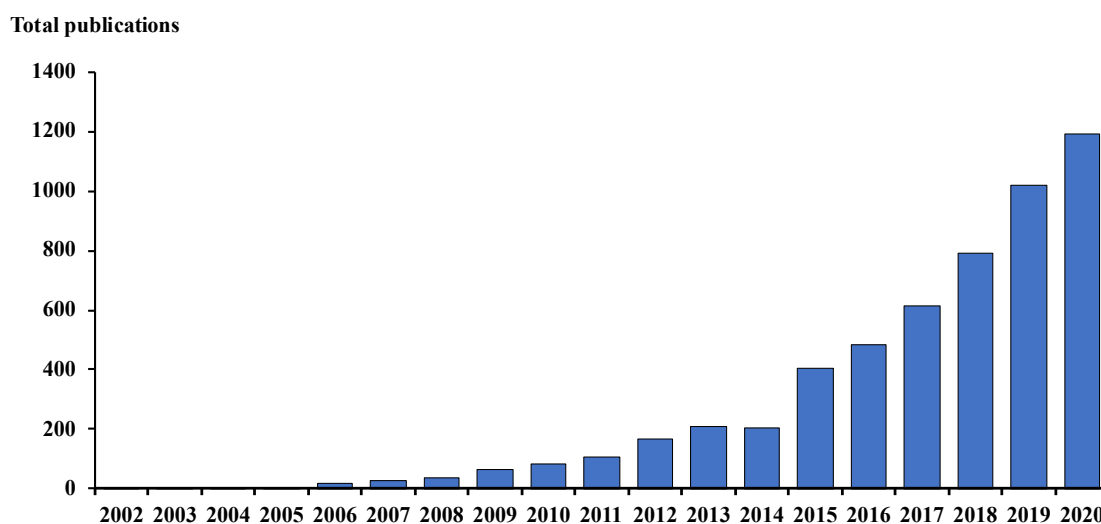
Figure 2.13. Number of publications per year (topics: water adsorption and metal-organic framework(s)) [148].

Water sorption-based applications require that the MOF must be hydrolytic stable, present high adsorption capacity, and high selectivity towards water [14]. The hydrolytic stability (thermodynamic and kinetic) is based on the MOF structural properties [14, 116]. MOFs thermodynamically stable present an inert metal cluster that avoids irreversible hydrolysis, providing structural stability upon exposure to water vapor and liquid water [116, 118]. Thermodynamic stability is affected by the strength of the metal-ligand bond, and by the energetic position of frontier orbitals of metal [14]. The strength of the metal-ligand bond is ruled by the acidity of metal ion and the basicity of protonated linker [14]. The knowledge of

pK_a values is a valuable tool to design thermodynamically stable MOFs [140]. MOFs with highly charged metals (*e.g.* Ti^{4+}, Zr^{4+}, and Hf^{4+}) tend to present high stability towards water (Figure 2.14) [88, 149, 150].
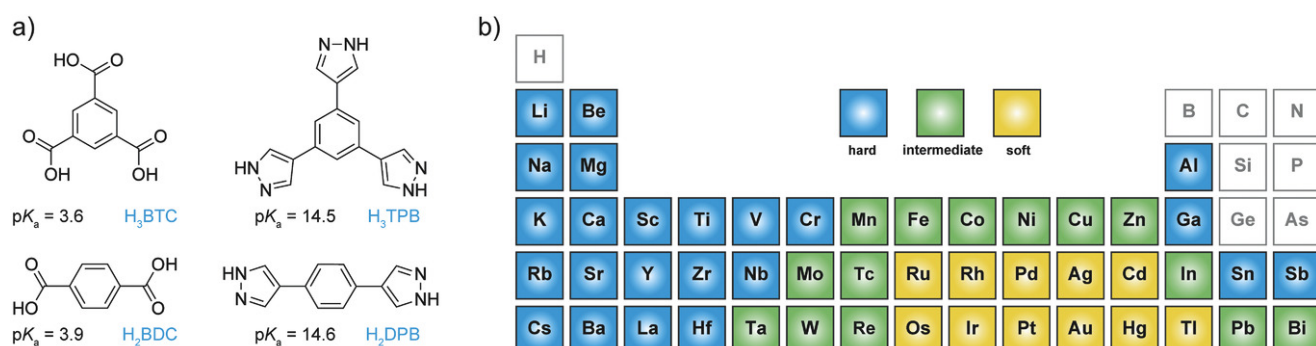
Figure 2.14. Strength of metal-ligand bond: a) pK_a values comparison between carboxylic acid (H_3BTC and H_2BDC) and pyrazole linkers (H_3TPB and H_2DPB); b) Periodic table divided according to three categories: blue – hard acid, green – intermediate acid, and yellow – soft acid [140].

Kinetic stability of the framework requires more complex parameters than thermodynamic stability, such as steric hindrance, the rigidity of SBU and/or linker, and the electronic configuration of the metal [116, 140, 151]. Hydrophobicity and steric factors are the two major structural properties that characterize the kinetic stability of MOFs [116].

Burtch *et al.* [118] developed a conceptual flowchart (Figure 2.15) to establish the stability mechanism, thermodynamic or kinetic stability; and defined criteria to classify MOFs in terms of water stability (Table 2.5).
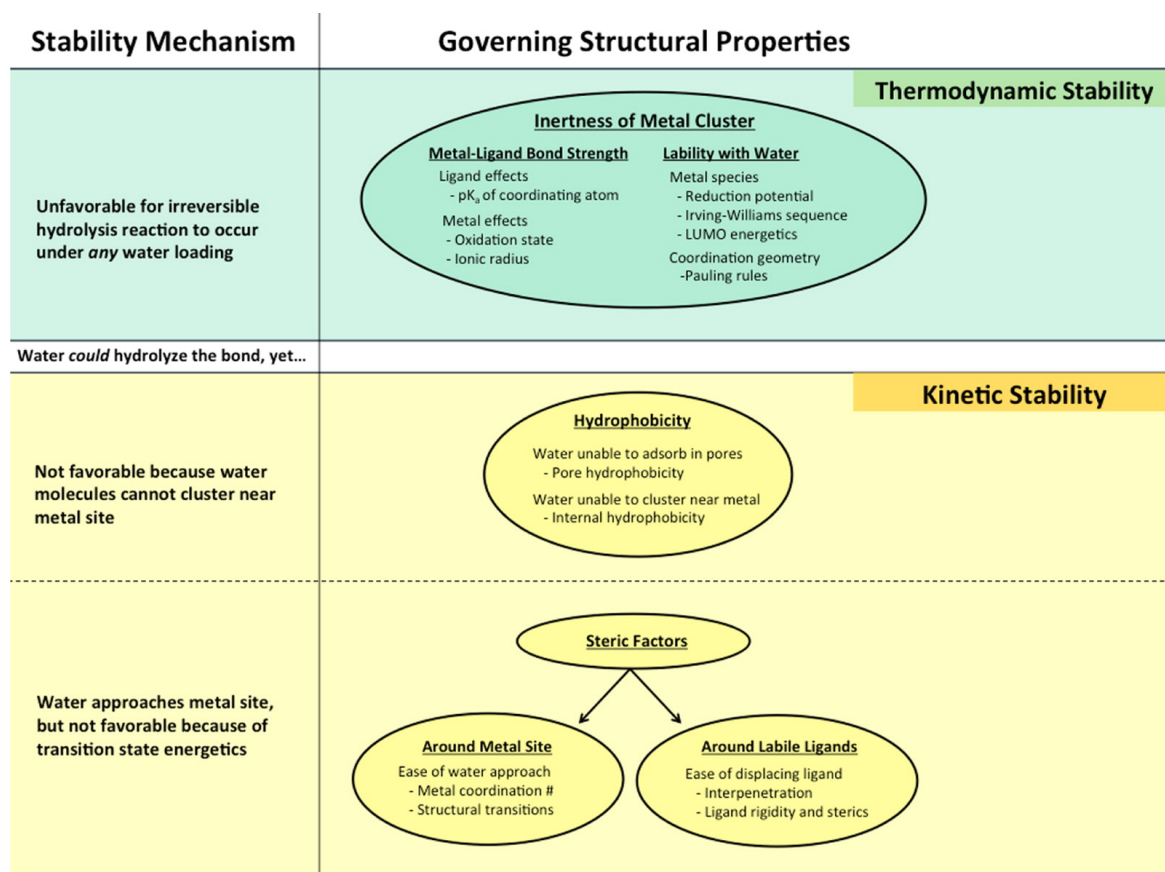
Figure 2.15. Stability mechanism factors that govern water stability in MOFs [118].

Table 2.5. Criteria for water stability classification of MOFs (adapted from [116]).

Stability Mechanism	Determining Factors	Applications
Thermodynamically stable	Stable after long-term exposure to aqueous solutions: day(s) in pure water; day(s) in acid-base or boiling conditions	Adsorbent or catalyst under wide range of conditions; aqueous and vapor phase
High kinetic stability	Stable after exposure to high humidity (> 80% RH); decomposes after short exposure times in liquid water	Industrial applications with high humidity streams
Low kinetic stability	Stable under low humidity exposure (< 40% RH)	Processes with pre-dried gas conditions
Unstable	Degradation occurs after any moisture exposure	Mild separations under moisture free conditions

Hydrophobic-hydrophilic properties of MOFs are related to the shape of the water adsorption equilibrium isotherms (Figure 2.16) [14, 116]. Figure 2.16 presents the relation between the hydrophobic-hydrophilic properties of MOFs and isotherms shape [14, 116].
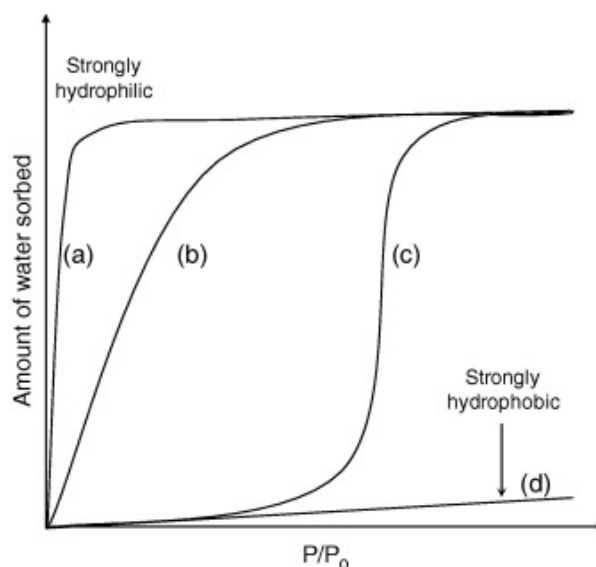
Figure 2.16. Different typologies of isotherm shapes according to its character hydrophilic and/or hydrophobic [152].

A characteristic Type I isotherm is presented as (a) with lower water adsorption at low relative pressures quickly reaching the maximum uptake [14, 118]. Isotherm (b) can represent Type II or Type IV isotherm, presenting less hydrophilic nature than the previous isotherm due to its small slope at low relative pressures [14]. Isotherm (c) corresponds to a Type V isotherm with low loadings at low relative pressures due to the formation of clusters instead of a monolayer [14]. This isotherm could reach the same maximum capacity than in (a) and (b) but at higher relative pressures, indicating the existence of a hydrophobic pore system [14]. Isotherm (d) corresponds to a strongly hydrophobic adsorbent, only with increasing water uptake at higher relative pressures [118]. It is worth noting that the comparison between relative hydrophobic and hydrophilic is only applicable for pore systems with identical pore size and dimensionality [14].

The main three mechanisms for water adsorption in MOFs are (i) chemisorption on open metal sites; (ii) reversible cluster formation; and (iii) capillary condensation.

(i) Chemisorption on open sites is a mechanism where the first coordination sphere of the metal ion is modified, by the adsorption on open-metal coordination sites, leading to a global or local deformation of MOFs structure [14, 151]. The strong water-open metal sites interaction due to chemical bonding (*e.g.*, hydrogen bond) results in water uptake at very low relative pressures (Type I isotherm) and in large Henry's constant (K_H) [14, 97, 153];

(ii) Reversible cluster formation is a mechanism that usually occurs in porous carbons [14]. A similar adsorption mechanism was recorded in microporous MOFs (*e.g.*, MOF-801 [154]). This phenomena only occur in materials with pore diameters smaller than the critical pore diameter for capillary condensation (*Dc*) [14];

(iii) Capillary condensation is observed in MOFs with pore diameters larger than *Dc* [14, 153]. This mechanism in mesoporous MOFs results in Type IV and Type V isotherms with hysteresis loop (*e.g.* MIL-100(Al)) [14, 153].

Wang and his co-workers presented one of the first water adsorption equilibrium isotherm in MOFs, namely in HKUST-1 [155]. In Teo and Chakraborty study MIL-101(Cr), alkali metal (Li^+, Na^+) doped MIL-101(Cr), aluminum fumarate, and CAU-10 were used as adsorbents to evaluate the effect of material properties on water adsorption behavior [156]. In Küsgens *et al.* study, different MOFs (HKUST-1, ZIF-8, MIL-101(Cr), MIL-100(Fe), DUT-4) were tested to select the most promising candidate(s) for water adsorption applications [157]. According to water stability, hydrophilic mesoporous adsorbents MIL-101(Cr) and MIL-100(Fe) were the selected ones [157]. On the other hand, ZIF-8 proved to be a highly hydrophobic microporous material [157]. Intending to study water adsorption in porous materials, Furukawa *et al.* selected 23 materials, which 20 of them were MOFs [88]. Due to their adsorption properties, two of these materials were highlighted: MOF-801, as a promising adsorbent for advanced thermal batteries; and MOF-841 as a suitable candidate for water capture in arid areas [88]. A review article by Canivet and his co-workers reported more than 60 types of MOFs used in studies related to water adsorption, concluding that most of them are good candidates to use in heat pumps and chiller applications [151]. In another review, Kalmutzki *et al.* compared the potential of selected MOFs for water harvesting from the air and concluded that these materials have great potential, albeit there is a gap in the development of technologies for the cyclic adsorption processes [140]. Kim *et al.*, designed an ecological device with MOF-801 as an adsorbent to capture of water from the atmosphere [90, 141]. Indeed, at 20% of relative humidity, it can harvest 2.8 L of water per kilogram of MOF [90]. More recently, it was reported an aluminum-

based MOF 303 which is capable of retaining about twice much water [142]. Rieth *et al.* studied the capture of water from the atmosphere with low relative humidity of 30% [158]. The sorbent presented is capable of harvesting 0.82 $g_{H_2O} \cdot g_{MOF}^{-1}$ [158]. Water adsorption properties in different porous materials, including ZIFs and MOFs, were also investigated using molecular simulations [159]. The main conclusion of this study was that the prediction of water adsorption in MOFs with open-metal sites is particularly sensitive to the selected water molecular model [159]. There is also an increasing interest in the application of MOFs in heat transformation processes like thermally driven heat pumps or adsorption chillers. In Henninger *et al.* study, the MOF ISE-1 was evaluated and presented a large loading spread (210 $g \cdot kg^{-1}$) being a potential adsorbent heat transformation [160]. de Lange and his co-workers studied the potential of 18 MOFs for application in adsorption-driven heat pumps/chillers (AHPs/ACs) using methanol and ethanol as working fluid [161]. Based in adsorption measurements and thermodynamic efficiencies, UiO-67, CAU-3, and ZIF-8 presented most suitable for both working fluids [161]. Furthermore, in the extensive review performed by de Lange *et al.*, the potential of MOFs in AHP/ACs were evaluated, giving a particular focus to water as a working fluid [134]. Some recent publications demonstrated the enormous potential of robust MOFs in water adsorption related processes, being stable during water adsorption/desorption cycles [143-147, 162-168]. Additionally, these materials are capable of adsorbing more water and requiring lower regeneration temperatures compared to other adsorbents (*e.g.* zeolite and silica gel) [141].

In the Associate Laboratory LSRE-LCM, some research on gas adsorption on MOFs has been developed since 2008, including water vapor in the more recent years (Table 2.6). Table 2.7 presents some examples of H_2O adsorption capacity on MOFs, as well as their structure information (surface area, pore-volume, pore size, and SEM images).

Table 2.6. Studies published by LSRE-LCM researchers in the field of gas adsorption on MOFs.

MOF	Gases	Ref.
Al(OH)-fumarate	CO_2, and **H_2O**	[169]
	CO_2, N_2, methane (CH_4) and **H_2O**	[170]
HKUST-1	Propylene (C_3H_6), propane (C_3H_8) and isobutene (C_4H_8)	[171]
	C_3H_8 and C_3H_6	[172]
	C_3H_6, C_3H_8 and isobutane (C_4H_{10})	[173]
	C_3H_6 and C_3H_8	[174]
	C_3H_6	[175]
	CO_2 and CH_4	[176]
	Hydrogen (H_2), CO_2, CO, CH_4, and N_2	[177]
	C_3H_8, C_3H_6, ethane (C_2H_6), and ethylene (C_2H_4)	[178]
	CO_2 and N_2	[179]
	C_2H_6 and C_2H_4	[180]
	CO_2, and CH_4	[181]
	CO_2 and H_2	[182]
	C_2H_6, C_2H_4 and C_3H_8	[183]
MIL-53(Al)	xylene isomers	[184]
	ortho-xylene	[185]
	CO_2 and CH_4	[186]
MIL-53(Fe)-(CF_3)$_2$	hexane isomers	[187]
MIL-100(Cr)	hexane isomers	[188]
MIL-100(Fe)	C_3H_8 and C_3H_6	[189]
	C_3H_8, C_3H_6 and C_4H_{10}	[190]
	N_2 and C_3H_6	[191]
	H_2, CH_4 and C_2H_6	[192]
	C_3H_6 and N_2	[193]
MIL-125(Ti)_NH$_2$	xylene isomers	[194]
	xylene isomers and ethylbenzene (C_8H_{10})	[195]
	xylene isomers	[196]
	hexane isomers	[188]
	CO_2, CO, N_2, CH_4, and H_2	[186]
MIL-127(Fe)	hexane isomers	[188]
MOF 1	xylene isomers	[197]
MOF-508b	CO_2, N_2, and CH_4	[198]
	CO_2, N_2, and CH_4	[199]
UiO-66	hexane and xylene isomers	[200]
	xylene isomers	[201]
	xylene isomers	[202]
UiO-66(Zr)_(COOH)$_2$	CO_2, CO, N_2, CH_4, and H_2	[203]
ZIF-8	hexane isomers	[204]
	hexane isomers	[205]
	hexane isomers	[206]
	hexane isomers	[207]
	C_2H_6 and C_2H_4	[208]
Zn(BDC)(Dabco)$_{0.5}$	xylene isomers and C_8H_{10}	[209]

Table 2.7. H_2O vapor adsorption capacity on MOFs, and their main properties.
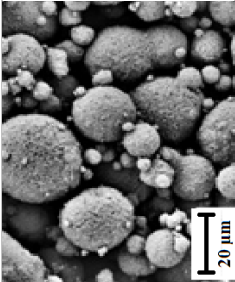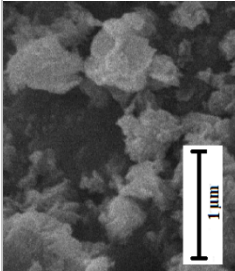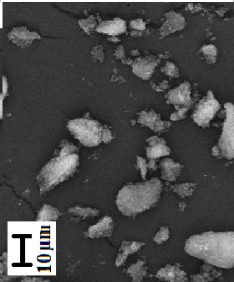
MOF	Surface area $(m^2 \cdot g^{-1})$	Pore volume $(cm^3 \cdot g^{-1})$	Pore size (Å)	SEM images	Max P/Po	T (K)	Maximum water uptake $(g \cdot g^{-1})$	Ref.
Al(OH)(1,4-NDC)·2H₂O	–	–	9	–	1.0	298	0.16	[210]
	792	0.93	6	–	0.9	298	0.47	[211]
	–	–	–		0.9	298	0.42	[212]
	–	–	–	–	0.9	298	0.53 (experimental) 0.51 (simulated)	[164]
	1021	0.48	–	–	0.8	298	0.45	[213]
Aluminium Fumarate	792	0.93	10.91		0.9	298	0.48	[214]
	1033	–	–		0.9	293	0.30	[215]
Basolite A300	1660	0.82	24.6; 31.0	–	0.9	298	0.66	[88]
Basolite F300	1300-1600	0.35	–	–	0.9	298	0.32	[216]

Table 2.7. H$_2$O vapor adsorption capacity on MOFs, and their main properties (cont.).
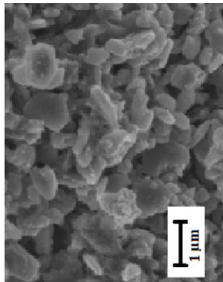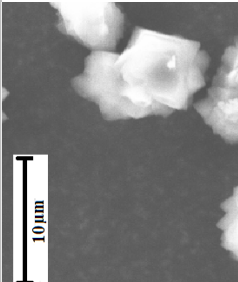
MOF	Surface area (m$^2 \cdot$g^{-1})	Pore volume (cm$^3 \cdot$g^{-1})	Pore size (Å)	SEM images	Max P/P$_0$	T (K)	Maximum water uptake (g·g^{-1})	Ref.
BIT-72	1618	0.78	–	–	1.0	283	0.61	[217]
BIT-73	1511	0.70	–	–	1.0	283	0.52	[217]
BIT-74	1394	0.67	–	–	1.0	283	0.47	[217]
CAU-1	1255	0.63	–	–	1.0	283	0.43	[217]
	760	0.34	9.1	–	0.9	298	0.31	[88]
CAU-6	620	0.25	5 to 10		0.9	298	0.39	[218]
	553	0.25	6.0	–	0.9	298	0.31	[211]
CAU-10	600	0.26	5.6	–	0.9	298	0.29	[88]
	660	0.28	–	–	0.9	298	0.37	[147]
	713	0.43	–	–	1.0	300	0.35	[219]
CH$_3$-CAU-10	–	–	–		0.8	298	0.18	[220]
Furan-CAU-10	776	0.45	–	–	1.0	300	0.38	[219]

Table 2.7. H_2O vapor adsorption capacity on MOFs, and their main properties (cont.).
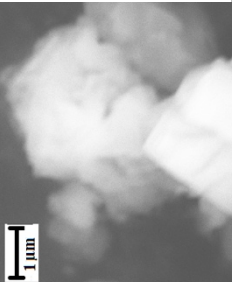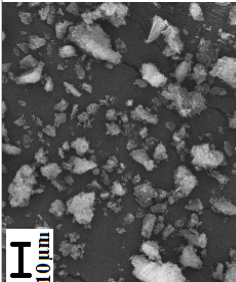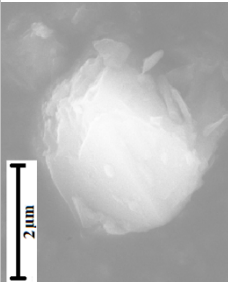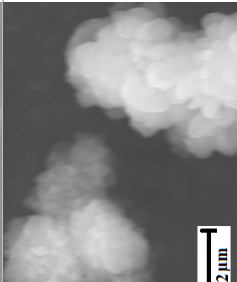
MOF	Surface area ($m^2 \cdot g^{-1}$)	Pore volume ($cm^3 \cdot g^{-1}$)	Pore size (Å)	SEM images	Max P/P_0	T (K)	Maximum water uptake ($g \cdot g^{-1}$)	Ref.
H-CAU-10	635	0.25	–		1.0	298	0.38	[220]
	–	–	–	–	0.8	–	0.37	[221]
	415–484	0.25–0.27	–		0.9	293	0.26	[215]
	525	0.27	–	–	0.9	298	0.37	[222]
NH₂-CAU-10	–	–	–		0.7	298	0.23	[220]
NO₂-CAU-10	440	0.18	–		0.5	298	0.18	[220]

Table 2.7. H_2O vapor adsorption capacity on MOFs, and their main properties (cont.).
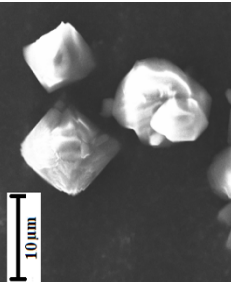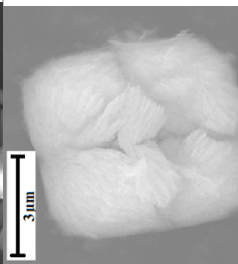
MOF	Surface area $(m^2 \cdot g^{-1})$	Pore volume $(cm^3 \cdot g^{-1})$	Pore size (Å)	SEM images	Max P/P_0	T (K)	Maximum water uptake $(g \cdot g^{-1})$	Ref.
OCH₃-CAU-10	–	–	–		0.5	298	0.09	[220]
OH-CAU-10	–	–	–		0.9	298	0.31	[220]
Pyrazine-CAU-10	810	0.42	–	–	1.0	300	0.42	[219]
Pyridine-CAU-10	732	0.43	–	–	1.0	300	0.39	[219]
Pyrrole-CAU-10	780	0.45	–	–	1.0	300	0.42	[219]
Thiophene-CAU-10	861	0.47	–	–	1.0	300	0.43	[219]
[Cu₂(pzdc)₂(bpe)]·5H₂O	–	–	6x11	–	0.7	303	0.27	[223]
[Cu₂(pzdc)₂(bpy)]·4H₂O	–	–	6x9	–	0.9	303	0.17	[223]
[Cu₂(pzdc)₂(pyz)]·2H₂O	–	–	6x4	–	0.7	303	0.11	[223]
DMOF	16980	0.75	–	–	0.4	298	0.08	[224]
A-DMOF	760	0.33	–	–	0.8	298	0.29	[224]
Br-DMOF	1315	0.53	–	–	0.8	298	0.05	[224]
Cl₂-DMOF	1175	0.45	–	–	0.8	298	0.07	[224]
N-DMOF	1420	0.57	–	–	0.7	298	0.02	[224]

Table 2.7. H₂O vapor adsorption capacity on MOFs, and their main properties (cont.).

MOF	Surface area $(m^2 \cdot g^{-1})$	Pore volume $(cm^3 \cdot g^{-1})$	Pore size (Å)	SEM images	Max P/P₀	T (K)	Maximum water uptake $(g \cdot g^{-1})$	Ref.
NH₂-DMOF-1	2010	0.58	7.5×7.5 4.8×3.2	–	0.8	298	0.11	[225]
NO₂-DMOF	1310	0.53	–	–	0.8	298	0.13	[224]
OH-DMOF	1130	0.54	–	–	0.8	298	0.09	[224]
TM1-DMOF	1210	0.53	–	–	0.7	298	0.27	[224]
TM2-DMOF	1050	0.51	–	–	0.8	298	0.35	[224]
	1050	0.51		–	0.7	298	0.27	[226]
Zn-DMOF	1794	0.65	7.5×7.5 4.8×3.2	–	0.04	298	0.52	[227]
DMOF-1	1960	0.58	7.5×7.5 4.8×3.2	–	0.9	298	0.05	[225]
DUT-4	1360	0.79	8.5	–	1.0	298	0.53	[157]
DUT-51(Zr)	2335	1.08	15.6; 18.8	–	1.0	298	0.70	[228]
DUT-52(Zr)	1399	0.60	4.35 to 8.59	–	1.0	298	0.30	[229]
DUT-53(Hf)	782	0.35	8.48 to 11.2	–	1.0	298	0.22	[229]
DUT-67	1560	0.60	16.6; 8.8	–	0.9	298	0.50	[88]
DUT-68	891	0.41	13.9; 12.5; 8	–	1.0	298	0.36	[149]
DUT-69	560	0.31	5	–	1.0	298	0.26	[149]
DUT-84(Zr)	637	0.31	7.57 to 11.1	–	1.0	298	0.14	[229]
	1340	0.72	9; 6	–	1.0	298	0.65	[157]
HKUST-1	1270	0.62	9; 6	–	0.9	298	0.58	[225]
	–	–	–	–	0.9	298	0.38	[212]
	–	–	–	–	0.9	298	0.69	[216]

Table 2.7. H_2O vapor adsorption capacity on MOFs, and their main properties (cont.).
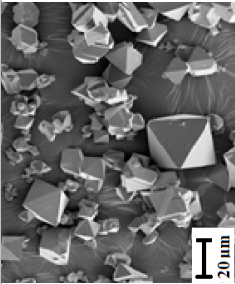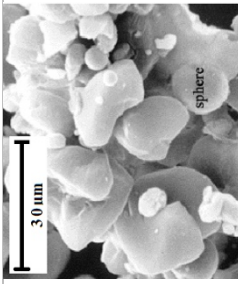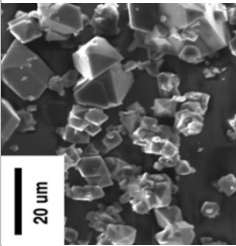
MOF	Surface area (m²·g⁻¹)	Pore volume (cm³·g⁻¹)	Pore size (Å)	SEM images	Max P/P₀	T (K)	Maximum water uptake (g·g⁻¹)	Ref.
	921	0.49	21		1.0	298	0.74	[230]
	1470	0.56	11.1; 6.3; 5.6	–	0.9	298	0.56	[88]
	1571	0.79	9	–	1.0	298	0.77	[231]
	1755	0.70	–	–	0.9	298	0.63	[232]
HKUST-1	195	–	7 to 8		0.1	298	0.06	[155]
	2200	0.81	10; 12	–	1.0	298	0.53	[233]
	1296	0.69	–		0.7	298	0.28	[234]
ISE-1	–	–	–	–	0.4	–	0.44	[216]
ISE-2	–	–	–	–	0.4	–	0.37	[216]
ISE-3	–	–	–	–	0.5	–	0.41	[216]

Table 2.7. H₂O vapor adsorption capacity on MOFs, and their main properties (cont.).
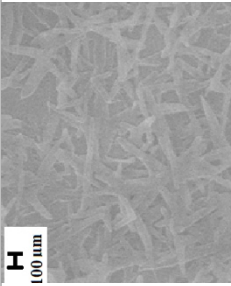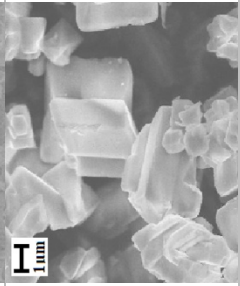
MOF	Surface area (m²·g⁻¹)	Pore volume (cm³·g⁻¹)	Pore size (Å)	SEM images	Max P/P₀	T (K)	Maximum water uptake (g·g⁻¹)	Ref.
MAF-47-0.23	–	–	–	–	1.0	298	0.45	[235]
MAF-47-0.49	–	–	–	–	1.0	298	0.44	[235]
MAF-47-0.76	–	–	–	–	1.0	298	0.44	[235]
MIL-53(Al)	870	0.36	6.9	–	0.9	298	0.20	[88]
	1040	0.51	7-13	–	0.9	298	0.10	[236]
	–	–	–	–	0.9	298	0.42	[216]
MIL-53(Al)it	1031	0.72	8.3; 34		1.0	298	0.18	[237]
MIL-53(Al)ht	1489	0.56	8.5		1.0	298	0.07	[237]
NH₂-MIL-53(Al)	940	0.37	7-13	–	0.9	298	0.09	[236]
MIL-53(Ga)	1230	0.47	8-20	–	0.9	298	0.07	[236]
NH₂-MIL-53(Ga)	210	–	8-20	–	0.9	298	0.18	[236]
MIL-68(In)	1100	0.42	6; 16	–	0.9	298	0.30	[236]
NH₂-MIL-68(In)	850	0.30	6; 16	–	0.9	298	0.34	[236]
MIL-100(Al)	1814	1.14	25; 29	–	0.9	298	0.52	[143]

Table 2.7. H_2O vapor adsorption capacity on MOFs, and their main properties (cont.).
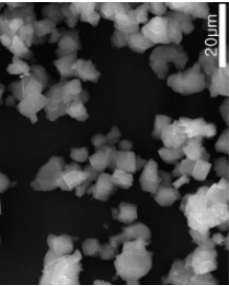
MOF	Surface area (m²·g⁻¹)	Pore volume (cm³·g⁻¹)	Pore size (Å)	SEM images	Max P/P₀	T (K)	Maximum water uptake (g·g⁻¹)	Ref.
MIL-100(Cr)	1330	0.77	25; 29	–	0.9	293	0.40	[238]
	1560	0.85	25; 29	–	0.9	298	0.57	[239]
	1790	0.78	25; 29	–	0.9	298	0.61	[233]
Cl-MIL-100(Cr)	1522	–	25; 29	–	0.6	298	0.51	[240]
DEG-MIL-100(Cr)	580	0.50	12; 15; 19; 26	–	0.9	293	0.42	[238]
EG-MIL-100(Cr)	710	0.47	12; 15; 19	–	0.9	293	0.43	[238]
EN-MIL-100(Cr)	640	0.42	12; 15; 19; 23; 26	–	0.9	293	0.37	[238]
F-MIL-100(Cr)	1517	–	25; 29	–	1.0	298	0.85	[240]
TEG-MIL-100(Cr)	680	0.53	12; 15; 19	–	0.9	293	0.33	[238]
SO₄-MIL-100(Cr)	1456		25; 29	–	0.6	298	0.49	[240]
	1549	0.82	25; 29	–	0.9	298	0.84	[157]
	1917	1.00	25; 29	–	0.9	298	0.77	[143]
	2200	0.94	25; 29	–	0.9	423	0.80	[239]
	–	–	–	–	0.7	293	0.45	[216]
	2300	–	–	–	0.6	343	0.25	[241]
MIL-100(Fe)	2050	1.08	–		1.0	303	0.85	[242]

Table 2.7. H₂O vapor adsorption capacity on MOFs, and their main properties (cont.).
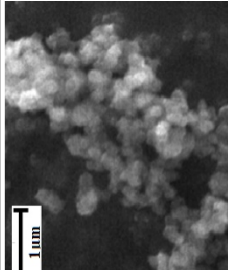
MOF	Surface area (m²·g⁻¹)	Pore volume (cm³·g⁻¹)	Pore size (Å)	SEM images	Max P/P₀	T (K)	Maximum water uptake (g·g⁻¹)	Ref.
MIL-101(Cr)	3017	1.61	29; 34	–	0.9	298	1.28	[157]
	3403	1.59	16	–	0.9	298	1.00	[211]
	2059	1.10	34	–	0.9	298	1.01	[243]
	3124	1.58	29; 34	–	0.6	298	1.30	[244]
	2500	1.22	29; 34	–	0.9	298	0.88	[236]
	3070	1.64	29; 34	–	0.9	298	1.29	[245]
	2452	1.30	–	–	0.9	298	1.47	[164]
	3060	1.45	29; 34	–	0.9	298	0.94	[239]
	–	–	–	–	0.9	298	1.43	[216]
	4150	–	–	–	1.0	303	1.71	[241]
	2931	1.45	–		0.7	298	0.43	[234]
NH₂-MIL-101(Cr)	2509	1.27	–	–	0.6	298	0.93	[244]
	2690	1.44	29; 34	–	1.0	293	0.96	[144]
	1790	0.97	29; 34	–	0.9	293	0.91	[236]
	2890	1.45	–	–	0.9	298	0.81	[245]
pNH₂-MIL-101(Cr)	2495	1.33	29; 34	–	0.9	293	1.10	[144]
pNO₂-MIL-101(Cr)	2195	1.03	29; 34	–	1.0	293	0.44	[144]
pCOOH-MIL-101(Cr)	2380/2110	1.26/1.18	–	–	0.9	298	1.02/0.91	[245]

Table 2.7. H_2O vapor adsorption capacity on MOFs, and their main properties (cont.).
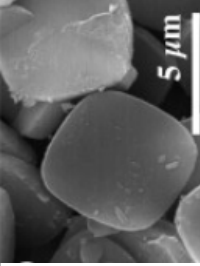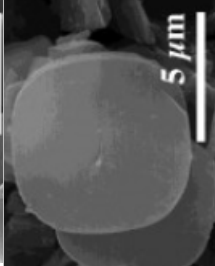
MOF	Surface area $(m^2 \cdot g^{-1})$	Pore volume $(cm^3 \cdot g^{-1})$	Pore size (Å)	SEM images	Max P/P_0	T (K)	Maximum water uptake $(g \cdot g^{-1})$	Ref.
pMal-MIL-101(Cr)	1670	0.89	–	–	0.9	298	0.71	[245]
pUR₂-MIL-101(Cr)	1330	0.64	–	–	0.9	298	0.55	[245]
p3SO₃H-MIL-101(Cr)	1020	0.71	–	–	0.9	298	0.70	[245]
	2146	1.19	–	–	0.6	293	0.94	[244]
NO₂-MIL-101(Cr)	1245	0.58	29; 34	–	1.0	293	0.40	[144]
	2040	0.95	29; 34	–	0.9	293	0.79	[236]
SO₃H-MIL-101(Cr)	1920	0.94	–	–	0.6	298	0.68	[244]
Li-MIL-101(Cr)	2054	0.94	18.5; 23.1	–	0.9	298	0.70	[211]
Na-MIL-101(Cr)	2001	0.91	18.5; 23.1	–	0.9	298	0.81	[211]
	1160	0.47	6; 12	–	0.9	298	0.40	[236]
MIL-125(Ti)	1510	0.68	6; 12.5		1.0	298	0.30	[246]
	1492	0.66	6; 12.5		1.0	298	0.53	[246]
NH₂-MIL-125(Ti)	1220	0.51	6; 12.5	–	0.9	298	0.40	[145]
	1230	0.51	6; 12	–	0.9	298	0.45	[236]
	1300	0.56	–	–	0.5	292/383	0.45	[247]

Table 2.7. H_2O vapor adsorption capacity on MOFs, and their main properties (cont.).
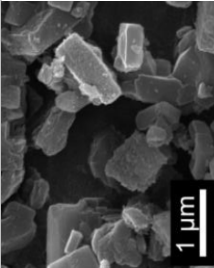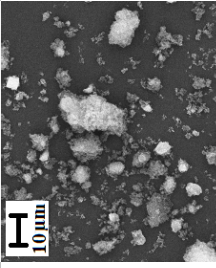
MOF	Surface area $(m^2 \cdot g^{-1})$	Pore volume $(cm^3 \cdot g^{-1})$	Pore size (Å)	SEM images	Max P/P_0	T (K)	Maximum water uptake $(g \cdot g^{-1})$	Ref.
MIL-160(Al)	1000	0.44	5		0.5	303	0.34	[248]
	1098	0.41	5.5		0.9	303	0.35	[249]
	1178	0.42	–	–	0.9	293	0.35	[215]
MOF-14	1398	0.57	5.2; 16.4	–	0.9	298	0.15	[250]
Co-MOF-74	1130	0.49	11.1	–	0.9	298	0.51	[88]
	1372	0.52	–	–	0.9	295	0.56	[251]
	1250	0.53	11.1	–	0.9	298	0.60	[88]
Mg-MOF-74	1400	0.65	11	–	0.9	298	0.66	[225]
	1607	0.69	–	–	0.8	295	0.64	[251]
	1790	0.89	–	–	0.9	298	0.37	[232]
Ni- MOF-74	1226	0.50	12.1	–	0.9	298	0.46 (simulated) 0.49 (experimental)	[164]

Table 2.7. H₂O vapor adsorption capacity on MOFs, and their main properties (cont.).
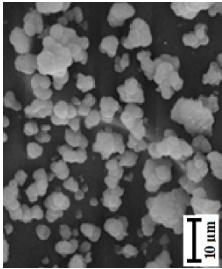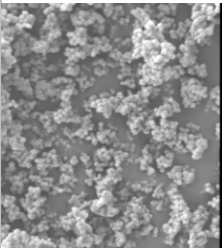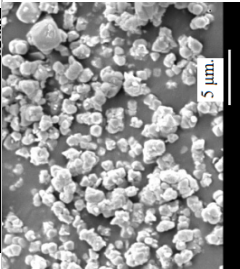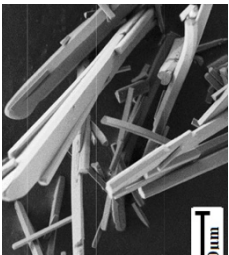
MOF	Surface area ($m^2 \cdot g^{-1}$)	Pore volume ($cm^3 \cdot g^{-1}$)	Pore size (Å)	SEM images	Max P/P_0	T (K)	Maximum water uptake ($g \cdot g^{-1}$)	Ref.
Ni-MOF-74	639	0.36	23		1.0	298	0.58	[230]
MOF-177	3100	1.58	10.6	—	0.06	298	0.10	[252]
MOF-508	800	0.42	4x4	—	0.9	298	0.05	[253]
TM-MOF-508	1330	0.56	3.5; 8x10	—	0.8	298	0.14	[253]
	—	—	—		0.1	339	0.05	[90]
					0.7	298	0.35	[90]
					0.2	308	0.25 (simulated)	[90]
MOF-801(Zr)	—	0.34	—		0.4	298	0.28 (simulated)	[141]
	990	0.45	7.4; 5.6: 4.8	—	0.9	298	0.36 (powder)	[88]
	690	0.27	7.4; 5.6: 4.8	—	0.9	298	0.28 (single crystal)	[88]
MOF-802(Zr)	<20	<0.01	5.6	—	0.9	298	0.09	[88]
MOF-804(Zr)	1145	0.46	7.2; 6.8	—	0.9	298	0.23	[88]

Table 2.7. H₂O vapor adsorption capacity on MOFs, and their main properties (cont.).

MOF	Surface area (m²·g⁻¹)	Pore volume (cm³·g⁻¹)	Pore size (Å)	SEM images	Max P/P₀	T (K)	Maximum water uptake (g·g⁻¹)	Ref.
MOF-805(Zr)	1230	0.48	9.5; 8.6	–	0.9	298	0.33	[88]
MOF-806(Zr)	2220	0.85	12.6; 10.1	–	0.9	298	0.34	[88]
MOF-808(Zr)	2060	0.84	18.4	–	0.9	298	0.59	[88]
MOF-841(Zr)	1390	0.53	9.2	–	0.9	298	0.51	[88]
MOFF-1	580	–	–	–	0.9	293	0.14	[254]
MOFF-2	444	–	–	–	0.9	293	0.01	[254]
MOFF-3	–	–	–	–	0.9	293	0.04	[254]
[Ni₈(L5)₆]	2215	–	–	–	1.0	298	1.13	[255]
[Ni₈(L5-CF₃)₆]	2195	–	–	–	1.0	298	0.86	[255]
[Ni₈(L5-CH₃)₆]	1985	–	–	–	1.0	298	0.64	[255]
[Ni(L)₂]·4H₂O}ₙ	–	–	–	–	1.0	298	0.12	[256]
PIZOF-2	2080	0.88	17.6	–	0.9	298	0.68	[88]
SIM-1	570	0.30	6.5	–	0.9	298	0.15	[236]
SNU-80	456	0.18	5.2; 7.5	–	1.0	298	0.02	[257]
UiO-66(Zr)	1290	0.49	8.4; 7.4	–	0.9	298	0.43	[88]
	1160	0.52	~6	–	0.9	298	0.45	[225]
	1032	0.52	7.5, 12	–	0.9	298	0.53	[145]
	1030	0.40	7.5; 11	–	0.9	298	0.35	[236]
	1283	–	–	–	1.0	298	0.32 (simulated)	[258]
	–	–	–	–	1.0	353	0.37	[259]
	963	0.43	–	–	0.9	298	0.36	[232]

Table 2.7. H_2O vapor adsorption capacity on MOFs, and their main properties (cont.).

MOF	Surface area ($m^2 \cdot g^{-1}$)	Pore volume ($cm^3 \cdot g^{-1}$)	Pore size (Å)	SEM images	Max P/P₀	T (K)	Maximum water uptake ($g \cdot g^{-1}$)	Ref.
NH₂-UiO-66(Zr)	1040	0.57	<6	–	0.9	298	0.40	[225]
	1328	0.59	7.5, 12	–	0.9	298	0.46	[145]
	830	0.35	7.5; 11	–	0.9	298	0.37	[236]
	1123	0.52	–	–	0.9	298	0.38	[126]
NO₂-UiO-66(Zr)	792	0.40	–	–	0.9	298	0.40	[126]
1,4-Naphyl-UiO-66(Zr)	757	0.42	–	–	0.9	298	0.30	[126]
2,5-(OMe)₂-UiO-66(Zr)	868	0.38	–	–	0.9	298	0.47	[126]
UiO-67	2064	0.87	12, 16	–	0.9	298	0.20	[145]
	1255	0.64	11.6; 3.4	–	1.0	298	0.12	[157]
ZIF-8	1530	0.48	11	–	0.9	298	0.02	[236]
	1873	0.68	11.4	–	1.0	298	0.03	[235]
ZIF-90	1874	0.67	11.2	–	1.0	298	0.45	[235]
Zn(NDI–H)	1460	–	~16	–	0.9	293	0.36	[260]
Zn(NDI–NHEt)	1236	–	~16	–	0.9	293	0.30	[260]
Zn(NDI–SEt)	888	–	~16	–	0.9	293	0.20	[260]
Zn(NDI–SOEt)	927	–	~16	–	0.9	293	0.30	[260]
Zn(NDI–SO₂Et)	764	–	~16	–	0.9	293	0.23	[260]
[La(pyzdc)1.5(H₂O)₂]·0.5 H₂O	–	–	3.6		1.0	473	0.02	[146]
Zn₂(BTC)(OH)(H₂O)·1.67H₂O	–	–	5	–	1.0	303	0.22	[261]

2.2.2 Other adsorbents

Activated carbon (AC) is one of the most common adsorbents presenting great versatility due to its high surface area (BET area range of 300 to 4000 $m^2 \cdot g^{-1}$), variable characteristics of surface chemistry, and a high degree of surface reactivity [119, 262, 263]. This material is widely applied in liquid water purification and gaseous waste streams [103, 264, 265]. AC is a member of a family of carbons with a wide range of amorphous carbonaceous materials such as carbon black (CB) and carbon nanotubes (CNTs) [262, 266, 267]. AC can be obtained by pyrolysis, physical and chemical activation process, or carbonization and steam activation of different raw materials (*e.g.*, lignite, charcoal, and coconut shell) leading to the great variability of structures (*e.g.*, powder, granulates, and extruded) [268, 269]. Pore diameter varies from 10 to 25 Å in carbons for gas-phase applications, and near 30 Å for carbons that find their application in liquid-phase processes [263]. AC carbons surface is nonpolar or with low polarity; however, the presence of water in adsorption processes is one crucial issue [263, 270]. Water vapor adsorption on AC can be correlated with pore size distribution once water vapor adsorption follows a Type V isotherm with a sigmoidal or S-shaped curve in microporous AC, while meso- and macroporous AC present Type III isotherms, according to IUPAC classification [271]. The water vapor uptake at low relative pressures ($P/P_o > 0.4$) is very low or even non-existent, however at high relative humidity conditions, it is high enough to compete with other adsorbents [271, 272]. Hydrophilic functional groups on the AC surface play an important role in primary adsorption (low RH) due to the hydrogen bond formation with adsorbed molecules [271, 273]. The increase of water vapor pressure leads to the formation of clusters around the primary adsorption centers [274]. Table 2.8 presents some examples of H_2O adsorption capacity on different typologies of ACs.

Table 2.8. H_2O adsorption capacity on ACs.

AC	Surface area (m²·g⁻¹)	Pore volume (cm³·g⁻¹)	Max P/P$_0$	T (K)	Maximum water uptake (g·g⁻¹)	Ref
pitch-based AC fiber	-	-	0.9	293	1.03	[275]
AC-1	2500	1.25	1.0	298	1.08	[276]
AC-2	2030	0.95	1.0	298	0.81	[276]
AC fiber – A7	1020	0.28	0.9	298	0.29	[277]
AC fiber – A10	1210	0.43	1.0	298	0.51	[277]
AC fiber – A20	1770	0.90	0.9	298	1.00	[277]
bamboo-based AC	-	0.51 (micropores) 0.26 (mesopores)	0.9	293	0.73	[278]

Silica gel is integrated into the group of synthetic amorphous silica and results from the aggregation of spherical colloidal silica particles (range size of 2 to 20 nm) [103, 279, 280]. BET surface area is typically between 250 and 1000 m²·g⁻¹ and pore diameters range of 22–150 Å [103, 263, 279]. The strong hydrophilicity of silica gel surface (water adsorption capacity ~ 35-40% by weight) led to be widely used in industry for water removal (*e.g.*, drying of industrial gas streams) [111, 263, 281]. Silica gel is often used in adsorption cooling systems as adsorption working pair with water [282, 283]. Some examples in the field of water adsorption onto silica gel are presented in Table 2.9.

Table 2.9. Summary of H_2O adsorption capacity on silica gel.

Silica gel	Surface area (m²·g⁻¹)	Pore volume (cm³·g⁻¹)	Max P/P$_0$	T (K)	Maximum water uptake (g·g⁻¹)	Ref
grade 40	952	0.32 (micropore)	0.8	293	0.31	[168]
Type 3A	606	0.45	0.5	303-423	0.27	[284]
Type A⁺⁺	864	0.48	1.0	298	0.43	[285]
Type-A5BW	769	0.45	1.0	298	0.44	[285]
Type-RD	828	0.46	0.9	303-423	0.47	[286]
Type-RD	650	0.35	0.7	303-423	0.36	[284]
Type-RD 2060	686	0.34	0.9	303-423	0.38	[286]
Type-RD 2560	636	0.31	1.0	298	0.37	[285]

Activated alumina is amorphous or crystalline alumina material which can be used in industry as a desiccant for drying gas streams or vapors recovery [103, 111, 263]. This adsorbent can be produced by calcination of hydrated alumina ($Al_2O_3.nH_2O$, where n =1~3) [287]. Activated alumina surface is highly porous with high functional group density providing active sites for polar molecules [111, 288]. Table 2.10 presents a summary of the H_2O adsorption in some types of activated alumina, reported in the literature.

Table 2.10. H_2O adsorption in activated alumina materials.

Activated alumina	Surface area ($m^2 \cdot g^{-1}$)	Pore volume ($cm^3 \cdot g^{-1}$)	Max P/P$_o$	T (K)	Maximum water uptake ($g \cdot g^{-1}$)	Ref
-	-	-	0.9	300	0.28	[289]
AA-300	330	0.44	0.9	303	0.39	[290]
Al_2O_3	340	0.14 (micropore)	0.9	298	0.24	[168]
F-1	260	0.40	0.9	303	0.19	[290]
F-200	360	0.50	0.9	298	0.47	[291]
H-156	350	0.43	0.9	303	0.34	[290]

Zeolites are microporous crystalline aluminosilicates, and belong to a class of metal oxides, and are composed of TO_4 tetrahedra (T = Si, Al) [111, 292]. The aluminosilicate skeletal structures themselves have a porosity between 0.2 and 0.5 [293] and are highly hydrophilic [152]. The ability for adsorption of zeolites is strongly related to the Si/Al ratio, and it is inversely proportional to it [293, 294]. They present great variability of structures with 40 types of natural zeolites and about 150 types of zeolites artificially synthesized (*e.g.*, type A, type X, and type Y) [293]. Artificially manufactured zeolites present higher bulk specific weight and higher performance in the heat transfer applications than natural zeolites [293]. Zeolites are widely used in adsorption heat pumps and cooling systems, as a working-pair with water. Besides the Si/Al ratio, the framework structure type and the ionic are some factors which affect the adsorption in zeolites [294]. One disadvantage of water adsorption on zeolites is the need for high temperatures (>200°C) in the desorption step [152]. Table 2.11 presents a summary of water adsorption on different zeolites.

Table 2.11. Some examples of H_2O adsorption in zeolites.

Zeolite	Surface area (m^2·g^{-1})	Pore volume (cm^3·g^{-1})	Max P/P$_o$	T (K)	Maximum water uptake (g·g^{-1})	Ref
13 X	-	-	1.0	293	0.37	[295]
AIPO-17	-	-	1.0	293	0.17	[295]
AIPO-18	-	-	1.0	293	0.23	[295]
AIPO-25	-	-	1.0	293	0.17	[295]
AIPO-53	-	-	1.0	293	0.15	[295]
GME	-	-	-	-	0.19	[296]
Mordenite	-	-	1.0	298	0.15	[152]

References

1. Critchley, W., K. Siegert, C. Chapman, Food, A.O.o.t.U. Nations, and M. Finkel, *Water Harvesting: A Manual for the Design and Construction of Water Harvesting Schemes for Plant Production*. 1991: FAO.

2. Bruins, H.J., M. Evenari, and U. Nessler, *Rainwater-harvesting agriculture for food production in arid zones: the challenge of the African famine.* Applied Geography, 1986. **6**(1): p. 13-32.

3. Evenari, M., L. Shanan, N. Tadmor, and Y. Aharoni, *Ancient Agriculture in the Negev.* Science, 1961. **133**(3457): p. 979-996.

4. Caran, S.C. and J.A. Neely, *Hydraulic engineering in prehistoric Mexico.* Sci Am, 2006. **295**(4): p. 78-85.

5. Zaunderer, J. and C.F. Hutchinson, *A review of water harvesting techniques of the Arid Southwestern U.S. and North Mexico*. 1988, World Bank's Sub-Saharan Water Harvesting Study.

6. Ouessar, M., M. Sghaier, N. Mahdhi, F. Abdelli, J. De Graaff, H. Chaieb, H. Yahyaoui, and D. Gabriels, *An Integrated Approach for Impact Assessment of Water Harvesting Techniques in Dry Areas: The Case of Oued Oum Zessar Watershed (Tunisia).* Environmental Monitoring and Assessment, 2004. **99**(1): p. 127-140.

7. Li , X.-Y., *Soil and Water Conservation in Arid and Semiarid Areas: The Chinese Experience.* Annals of Arid Zone 2000. **39**(4): p. 1-18.

8. Boers, T.M. and J. Ben-Asher, *A review of rainwater harvesting.* Agricultural Water Management, 1982. **5**(2): p. 145-158.

9. Frasier, G.W., *Harvesting water for agricultural, wildlife, and domestic uses.* Journal of Soil & Water Conservation, 1980. **35**(3): p. 125-128.

10. Myers, L.E. *Water Harvesting - 2000 B.C. to 1974 A.D. .* in *Water Harvesting Symposium*. 1974. Phoenix, Arizona.

11.   Gould, J. and E. Nissen-Petersen, *Rainwater Catchment Systems for Domestic Supply: Design, Construction and Implementation* 1999.

12.   Paulos , C., *Innovative Water Resource Use and Management for Poverty Reduction in Sub-Saharan Africa: An Anthology* 2014 African Books Collective.

13.   Pereira, L.S., I. Cordery, and I. Iacovides, *Surface Water Use and Harvesting*, in *Coping with Water Scarcity: Addressing the Challenges*. 2009, Springer Netherlands: Dordrecht. p. 99-132.

14.   Yaghi, O.M., M.J. Kalmutzki, and C.S. Diercks, *Water Sorption Applications of MOFs*, in *Introduction to Reticular Chemistry*. 2019. p. 395-427.

15.   Pereira, L.S., I. Cordery, and I. Iacovides, *Using Non-conventional Water Resources*, in *Coping with Water Scarcity: Addressing the Challenges*. 2009, Springer Netherlands: Dordrecht. p. 175-220.

16.   Herrera-León, S., F. Lucay, A. Kraslawski, L.A. Cisternas, and E.D. Gálvez, *Optimization Approach to Designing Water Supply Systems in Non-Coastal Areas Suffering from Water Scarcity.* Water Resources Management, 2018. **32**(7): p. 2457-2473.

17.   Manju, S. and N. Sagar, *Renewable energy integrated desalination: A sustainable solution to overcome future fresh-water scarcity in India.* Renewable and Sustainable Energy Reviews, 2017. **73**: p. 594-609.

18.   Proskynitopoulou, V. and I.A. Katsoyiannis, *Review of recent desalination developments for more efficient drinking water production across the world.* New Materials, Compounds and Applications, 2018. **2**(2): p. 179-195.

19.   Forbes, R.J., *A Short History of the Art of Distillation: from the Beginnings Up to the Death of Cellier Blumenthal*. 1948, Leiden: Brill.

20.   Bao, W., X. Tang, X. Guo, S. Choi, C. Wang, Y. Gogotsi, and G. Wang, *Porous Cryo-Dried MXene for Efficient Capacitive Deionization.* Joule, 2018. **2**(4): p. 778-787.

21.   Gude, V.G., *Desalination and sustainability – An appraisal and current perspective.* Water Research, 2016. **89**: p. 87-106.

22.   Semiat, R., *Present and Future.* Water International, 2000. **25**(1): p. 54-65.

23.   Subramani, A., M. Badruzzaman, J. Oppenheimer, and J.G. Jacangelo, *Energy minimization strategies and renewable energy utilization for desalination: A review.* Water Research, 2011. **45**(5): p. 1907-1920.

24.   Charcosset, C., *A review of membrane processes and renewable energies for desalination.* Desalination, 2009. **245**(1): p. 214-231.

25.   Kalogirou, S.A., *Seawater desalination using renewable energy sources.* Progress in Energy and Combustion Science, 2005. **31**(3): p. 242-281.

26.   Abdelkareem, M.A., M. El Haj Assad, E.T. Sayed, and B. Soudan, *Recent progress in the use of renewable energy sources to power water desalination plants.* Desalination, 2018. **435**: p. 97-113.

27.   Delyannis, E., *Historic background of desalination and renewable energies.* Solar Energy, 2003. **75**(5): p. 357-366.

28.   Maurel, A., *Dessalement de L'eau de Mer et des Eaux Saumâtres: et Autres Procédés Non Conventionneles d'approvisionnement en Eau Douce*. 2001: Lavoisier TEC & DOC.

29.   United Nations World Water Assessment Programme (UN WWAP). *The United Nations World Water Development Report 3: Water in a Changing World*. 2009: Paris: UNESCO, and London: Earthscan.

30.   Jones, E., M. Qadir, M.T.H. van Vliet, V. Smakhtin, and S.-m. Kang, *The state of desalination and brine production: A global outlook.* Science of The Total Environment, 2019. **657**: p. 1343-1356.

31.   Hamed, A.M., A.A. Aly, and E.B. Zeidan, *Application of Solar Energy for Recovery of Water from Atmospheric Air in Climatic Zones of Saudi Arabia* Natural Resources, 2011. **2**(1): p. 8-17.

32.   Obrezkova, V.E., *Hydro-energy*, in *Energoatomezdat*. 1988: Moscow.

33.   Fessehaye, M., S.A. Abdul-Wahab, M.J. Savage, T. Kohler, T. Gherezghiher, and H. Hurni, *Fog-water collection for community use.* Renewable and Sustainable Energy Reviews, 2014. **29**: p. 52-62.

34.   Kogan, B. and A. Trahtman, *The moisture from the air as water resource in arid region: hopes, doubts and facts.* Journal of Arid Environments, 2003. **53**(2): p. 231-240.

35.   Nikolayev, V.S., D. Beysens, A. Gioda, I. Milimouka, E. Katiushin, and J.P. Morel, *Water recovery from dew.* Journal of Hydrology, 1996. **182**(1): p. 19-35.

36.   Wahlgren, R.V., *Atmospheric water vapour processor designs for potable water production: a review.* Water Research, 2001. **35**(1): p. 1-22.

37.   Tu, Y., R. Wang, Y. Zhang, and J. Wang, *Progress and Expectation of Atmospheric Water Harvesting.* Joule, 2018. **2**(8): p. 1452-1475.

38.   Milani, D., A. Abbas, A. Vassallo, M. Chiesa, and D.A. Bakri, *Evaluation of using thermoelectric coolers in a dehumidification system to generate freshwater from ambient air.* Chemical Engineering Science, 2011. **66**(12): p. 2491-2501.

39.   Cech, T.V., *Principles of water resources: history, development, management and policy*. Vol. 28. 2002, New York: John Wiley and Sons.

40.   Lightfoot, D.R., *The Nature, History, and Distribution of Lithic Mulch Agriculture: An Ancient Technique of Dryland Agriculture.* The Agricultural History Review, 1996. **44**(2): p. 206-222.

41.   Nagel, J.F., *Fog precipitation on table mountain.* Quarterly Journal of the Royal Meteorological Society, 1956. **82**(354): p. 452-460.

42. Kerfoot, O., *Mist precipitation on vegetation.* Forestry Abstracts 1968. **29**: p. 8–20.

43. Schemenauer, R.S., H. Fuenzalida, and P. Cereceda, *A Neglected Water Resource: The Camanchaca of South America.* Bulletin of the American Meteorological Society, 1988. **69**(2): p. 138-147.

44. Marzol, M.V., J.L. Sánchez, and A. Yanes, *Meteorological patterns and fog water collection in Morocco and The Canary Islands.* Erdkunde, 2011. **65**(3): p. 291-303.

45. Sabino, A. *Fog collection in the natural park of Serra Malagueta. An alternative source of water for the communities.* in *4th international conference on fog, fog collection and dew.* 2007.

46. Larrain, H., F. Velásquez, P. Cereceda, R. Espejo, R. Pinto, P. Osses, and R.S. Schemenauer, *Fog measurements at the site "Falda Verde" north of Chañaral compared with other fog stations of Chile.* Atmospheric Research, 2002. **64**(1): p. 273-284.

47. Escobar, C.M., A. Lopez, H.F. Aristizabal, and J.M. Molina. *Operational fog collection and its role in environmental education and social reintegration: A case study in Colombia.* in *5th International Conference on Fog, Fog Collection and Dew.* 2010. Münster (Germany).

48. Henderson, B. and D. Falk. *Fog-water collection in Ecuador: an appropriate technology for the rural poor?* in *2nd international conference on fog and fog collection.* 2001.

49. Schemenauer, R.S., M. Rosato, and V.C. Gamberini, *Fog collection projects in Tojquia and La Ventosa, Guatemala.* 2007.

50. Abhiram, M., N.D. Priya, and P. Geetha, *Fog harvesting — A wind flow perspective in Western Ghats, Coimbatore, Tamil Nadu.* Indian Journal of Science and Technology,, 2015. **8**(28).

51.   Shanyengana, E.S., J.R. Henschel, M.K. Seely, and R.D. Sanderson, *Exploring fog as a supplementary water source in Namibia.* Atmospheric Research, 2002. **64**(1): p. 251-259.

52.   MacQuarrie, K.I.A., A. Pokhrel, Y. Shrestha, P. Osses, R.S. Schemenauer, F. Vitez, K. Kowalchuk, and R. Taylor. *Results from a High Elevation Fog Water Supply Project in Nepal*. in *2nd Int. Conf. on Fog and Fog Collection*. 2001. Vancouver, St. John's, Newfoundland (Canada).

53.   Olivier, J. and C.J. de Rautenbach, *The implementation of fog water collection systems in South Africa.* Atmospheric Research, 2002. **64**(1): p. 227-238.

54.   Estrela, M.J., J.A. Valiente, D. Corell, D. Fuentes, and A. Valdecantos, *Prospective use of collected fog water in the restoration of degraded burned areas under dry Mediterranean conditions.* Agricultural and Forest Meteorology, 2009. **149**(11): p. 1896-1906.

55.   Estrela, M.J., J.A. Valiente, D. Corell, and M.M. Millán, *Fog collection in the western Mediterranean basin (Valencia region, Spain).* Atmospheric Research, 2008. **87**(3): p. 324-337.

56.   Schemenauer, R.S., P. Osses, and M. Leibbrand. *Fog collection evaluation and operational projects in the Hajja Governorate, Yemen*. in *3rd International Conference on Fog, Fog Collection and Dew*. 2004. Cape Town.

57.   Schemenauer , R.S. and P. Cereceda, *Fog-water collection in arid coastal locations.* AMBIO (Royal Swedish Academy of Science), 1992. **20**(7): p. 303-308.

58.   Schemenauer, R.S., P. Cereceda, and P. Pablo Osses. *The complementary aspects of projects to collect rain, fog and dew*. in *11th Intl. Rainwater Catchment Systems Assoc. meeting*. 2003. Texcoco (Mexico).

59.   Pandey, A.K., S.K. Srivastava, and K.K. Tiwari, *Fog water harvesting.* Everyman's Science, 2007. **XLII**(4).

60. Rivera, J.d.D., *Aerodynamic collection efficiency of fog water collectors.* Atmospheric Research, 2011. **102**(3): p. 335-342.

61. Johnstone, J.A. and T.E. Dawson, *Climatic context and ecological implications of summer fog decline in the coast redwood region.* Proceedings of the National Academy of Sciences, 2010. **107**(10): p. 4533-4538.

62. Haensler, A., J. Cermak, S. Hagemann, and D. Jacob, *Will the southern African west coast fog be affected by future climate change? Results of an initial fog projection using a regional climate model.* Erdkunde, 2011. **65**(3): p. 261-275

63. Tygarinov, V.V., *An equipment for collecting water from air.* 1947: Russia.

64. TechSci Research. *Saudi Arabia Air Conditioners Market Forecast & Opportunities, 2018*. 2014 [cited 2018 11 June]; Available from: http://www.techsciresearch.com/2664.

65. Sharan, G., O. Clus, S. Singh, M. Muselli, and D. Beysens, *A very large dew and rain ridge collector in the Kutch area (Gujarat, India).* Journal of Hydrology, 2011. **405**(1): p. 171-181.

66. Prinz, D., *The Role of Water Harvesting in Alleviating Water Scarcity in Arid Areas*, in *International Conference on Water Resources Management in Arid Regions*. 2002, Kuwait Institute for Scientific Research: Kuwait.

67. Hitier, H., *Condensateurs des vapeurs atmosphériques dans l'Antiquité*. 1925: Compte rendu des séances de l'Académie d'agriculture de France. p. 679-683.

68. Gioda, A. and A.N.A. Baladon, *Les puits aériens de Théododia, Montpellier et Trans.* Sécheresse 1991. **2**(3).

69. Khalil, B., J. Adamowski, A. Shabbir, C. Jang, M. Rojas, K. Reilly, and B. Ozga-Zielinski, *A review: dew water collection from radiative passive collectors to recent developments of active collectors.* Sustainable Water Resources Management, 2016. **2**(1): p. 71-86.

70. Beysens, D., M. Muselli, V. Nikolayev, R. Narhe, and I. Milimouk, *Measurement and modelling of dew in island, coastal and alpine areas.* Atmospheric Research, 2005. **73**(1): p. 1-22.

71. Maestre-Valero, J.F., V. Martínez-Alvarez, A. Baille, B. Martín-Górriz, and B. Gallego-Elvira, *Comparative analysis of two polyethylene foil materials for dew harvesting in a semi-arid climate.* Journal of Hydrology, 2011. **410**(1): p. 84-91.

72. Muselli, M., D. Beysens, M. Mileta, and I. Milimouk, *Dew and rain water collection in the Dalmatian Coast, Croatia.* Atmospheric Research, 2009. **92**(4): p. 455-463.

73. Lekouch, I., K. Lekouch, M. Muselli, A. Mongruel, B. Kabbachi, and D. Beysens, *Rooftop dew, fog and rain collection in southwest Morocco and predictive dew modeling using neural networks.* Journal of Hydrology, 2012. **448-449**: p. 60-72.

74. Carvajal, D., J.-G. Minonzio, E. Casanga, J. Muñoz, A. Aracena, S. Montecinos, and D. Beysens, *Roof-integrated dew water harvesting in Combarbalá, Chile.* Journal of Water Supply: Research and Technology-Aqua, 2018. **67**(4): p. 357-374.

75. Muselli, M., D. Beysens, J. Marcillat, I. Milimouk, T. Nilsson, and A. Louche, *Dew water collector for potable water in Ajaccio (Corsica Island, France).* Atmospheric Research, 2002. **64**(1): p. 297-312.

76. Sharan, G., D. Beysens, and I. Milimouk-Melnytchouk, *A study of dew water yields on Galvanized iron roofs in Kothara (North-West India).* Journal of Arid Environments, 2007. **69**(2): p. 259-269.

77. Gindel, I., *Irrigation of Plants with Atmospheric Water within the Desert.* Nature, 1965. **207**(5002): p. 1173-1175.

78. Tuure, J., A. Korpela, M. Hautala, M. Hakojärvi, H. Mikkola, M. Räsänen, J. Duplissy, P. Pellikka, T. Petäjä, M. Kulmala, and L. Alakukku, *Comparison of surface foil materials and dew collectors location in an arid area: a one-year field experiment in Kenya.* Agricultural and Forest Meteorology, 2019. **276-277**: p. 107613.

79. Nilsson, T., *Initial experiments on dew collection in Sweden and Tanzania.* Solar Energy Materials and Solar Cells, 1996. **40**(1): p. 23-32.

80. Jacobs, A.F.G., B.G. Heusinkveld, and S.M. Berkowicz, *Passive dew collection in a grassland area, The Netherlands.* Atmospheric Research, 2008. **87**(3): p. 377-385.

81. Peters, G.M., N.J. Blackburn, and M. Armedion, *Environmental assessment of air to water machines—triangulation to manage scope uncertainty.* The International Journal of Life Cycle Assessment, 2013. **18**(5): p. 1149-1157.

82. Khalil, B., J. Adamowski, M. Rojas, and K. Reilly, *Towards an independent dew water irrigation system for arid or insular areas*, in *2014 Montreal, Quebec Canada July 13 – July 16, 2014*. 2014, ASABE: St. Joseph, MI. p. 1.

83. Bundschuh, J. and J. Hoinkins, *Renewable energy applications for freshwater production*. 2012, Florida: CRC Press.

84. Vinay, M.V., A. Suman, and R. Shadakshari, *Dehumidification of Atmospheric Air for Water Production.* International Journal of Innovative Research in Science, Engineering and Technology, 2018 **7**(4).

85. Sarbu, I. and C. Sebarchievici, *Using Ground-Source Heat Pump Systems for Heating/Cooling of Buildings, Advances in Geothermal Energy*, in *Advances in Geothermal Energy*, B.I. Ismail, Editor. 2016, IntechOpen.

86. Boriskina, S.V., A. Raza, T. Zhang, P. Wang, L. Zhou, and J. Zhu, *Nanomaterials for the water-energy nexus.* MRS Bulletin, 2019. **44**(1): p. 59-66.

87. LaPotin, A., H. Kim, S.R. Rao, and E.N. Wang, *Adsorption-Based Atmospheric Water Harvesting: Impact of Material and Component Properties on System-Level Performance.* Accounts of Chemical Research, 2019. **52**(6): p. 1588-1597.

88. Furukawa, H., F. Gándara, Y.-B. Zhang, J. Jiang, W.L. Queen, M.R. Hudson, and O.M. Yaghi, *Water Adsorption in Porous Metal–Organic Frameworks and Related Materials.* Journal of the American Chemical Society, 2014. **136**(11): p. 4369-4381.

89.   Reif, J.H. and W. Alhalabi, *Solar-thermal powered desalination: Its significant challenges and potential.* Renewable and Sustainable Energy Reviews, 2015. **48**: p. 152-165.

90.   Kim, H., S. Yang, S.R. Rao, S. Narayanan, E.A. Kapustin, H. Furukawa, A.S. Umans, O.M. Yaghi, and E.N. Wang, *Water harvesting from air with metal-organic frameworks powered by natural sunlight.* Science, 2017. **356**(6336): p. 430-434.

91.   Edmund, A., *Method for gaining water out of the atmosphere. US patent.* 1938.

92.   Scrivani, A. and U. Bardi, *A study of the use of solar concentrating plants for the atmospheric water vapour extraction from ambient air in the Middle East and Northern Africa region.* Desalination, 2008. **220**(1): p. 592-599.

93.   Entezari, A., M. Ejeian, and R.Z. Wang, *Extraordinary air water harvesting performance with three phase sorption.* Materials Today Energy, 2019. **13**: p. 362-373.

94.   Wang, J.Y., J.Y. Liu, R.Z. Wang, and L.W. Wang, *Experimental research of composite solid sorbents for fresh water production driven by solar energy.* Applied Thermal Engineering, 2017. **121**: p. 941-950.

95.   Kumar, M. and A. Yadav, *Experimental investigation of design parameters of solar glass desiccant box type system for water production from atmospheric air.* Journal of Renewable and Sustainable Energy, 2015. **7**(3): p. 033122.

96.   Fathieh, F., M.J. Kalmutzki, E.A. Kapustin, P.J. Waller, J. Yang, and O.M. Yaghi, *Practical water production from desert air.* Science Advances, 2018. **4**(6): p. eaat3198.

97.   Kim, H., *Development of adsorption-based atmospheric water harvesting and thermal energy storage technologies*, in *Massachusetts Institute of Technology. Department of Mechanical Engineering.* 2018, Massachusetts Institute of Technology.

98. Wang, J.Y., R.Z. Wang, Y.D. Tu, and L.W. Wang, *Universal scalable sorption-based atmosphere water harvesting.* Energy, 2018. **165**: p. 387-395.

99. ASHRAE, *2013 ASHRAE Handbook - Fundamentals* Vol. . 2013: American Society of Heating, Refrigerating and Air-Conditioning Engineers, Inc. (ASHRAE).

100. Gido, B., E. Friedler, and D.M. Broday, *Assessment of atmospheric moisture harvesting by direct cooling.* Atmospheric Research, 2016. **182**: p. 156-162.

101. William, G.E., M.H. Mohamed, and M. Fatouh, *Desiccant system for water production from humid air using solar energy.* Energy, 2015. **90**: p. 1707-1720.

102. Skoulikides, T.N., *Physical Chemistry I 1.2*. 1989, Athens, Greece: Symetria Editions.

103. Inglezakis, V.J. and S.G. Poulopoulos, *Adsorption, Ion Exchange, and Catalysis*, in *Adsorption, Ion Exchange and Catalysis*, V.J. Inglezakis and S.G. Poulopoulos, Editors. 2006, Elsevier: Amsterdam.

104. McCabe, W., J.C. Smith, and P. Harriott, *Unit Operations of Chemical Engineering*. 5th ed. 1993, New York: McGraw-Hill.

105. Perez, L.E., P. Sarkar, and A. Rajendran, *Experimental validation of multi-objective optimization techniques for design of vacuum swing adsorption processes.* Separation and Purification Technology, 2019. **224**: p. 553-563.

106. Peredo-Mancilla, D., I. Ghouma, C. Hort, D. Bessieres, and C.M. Ghimbeu, *9 - Gas storage*, in *Char and Carbon Materials Derived from Biomass*, M. Jeguirim and L. Limousy, Editors. 2019, Elsevier. p. 341-382.

107. Wang, L., N. Boussetta, N. Lebovka, and E. Vorobiev, *Ultrasound assisted purification of polyphenols of apple skins by adsorption/desorption procedure.* Ultrasonics Sonochemistry, 2019. **55**: p. 18-24.

108. Ligotski, R., U. Sager, U. Schneiderwind, C. Asbach, and F. Schmidt, *Prediction of VOC adsorption performance for estimation of service life of activated carbon based filter*

media for indoor air purification. Building and Environment, 2019. **149**: p. 146-156.

109.   Rouquerol, F., J. Rouquerol, and K. Sing, *CHAPTER 1 - Introduction*, in *Adsorption by Powders and Porous Solids*, F. Rouquerol, J. Rouquerol, and K. Sing, Editors. 1999, Academic Press: London. p. 1-26.

110.   Králik, M., *Adsorption, chemisorption, and catalysis.* Chemical Papers, 2014. **68**(12): p. 1625-1638.

111.   Do, D.D., *Adsorption Analysis: Equilibria and Kinetics*. Adsorption Analysis: Equilibria and Kinetics. 1998, Imperial College Press.

112.   Sing, K.S.W., D.H. Everett, R.A.W. Haul, L. Moscou, R.A. Pierotti, J. Rouquérol, and T. Siemieniewska, *Reporting Physisorption Data for Gas/Solid Systems With Special Reference to the Determination of Surface Area and Porosity.* Pure Appl. Chem., 1985. **57**(4): p. 603-619.

113.   Thommes, M., K. Kaneko, V. Neimark Alexander, P. Olivier James, F. Rodriguez-Reinoso, J. Rouquerol, and S.W. Sing Kenneth, *Physisorption of gases, with special reference to the evaluation of surface area and pore size distribution (IUPAC Technical Report)*, in *Pure and Applied Chemistry*. 2015. p. 1051.

114.   Yaghi, O.M., M.J. Kalmutzki, and C.S. Diercks, *Determination and Design of Porosity*, in *Introduction to Reticular Chemistry*. 2019. p. 29-56.

115.   Somasundaran, P. and A.T. Hubbard, *Encyclopedia of surface and colloid science*. 2006 Boca Raton: Taylor & Francis.

116.   Glover, T. and B. Mu, *Gas Adsorption in Metal-Organic Frameworks*. 2018, Boca Raton: CRC Press. 542.

117.   Fraissard, J. and C.W. Corner, *Physical Adsorption: Experiment, Theory and Applications*. 1 ed. Nato Science Series C. 1997: Kluwer Academic Publisher. 619.

118.   Burtch, N.C., H. Jasuja, and K.S. Walton, *Water Stability and Adsorption in Metal–Organic Frameworks.* Chemical Reviews, 2014. **114**(20): p. 10575-10612.

119.   Islam, M.A., M.M.R. Khan, and M.S.I. Mozumder, *Adsorption Equilibrium and Adsorption Kinetics: A Unified Approach.* Chemical Engineering & Technology, 2004. **27**(10): p. 1095-1098.

120.   Ferey, G., *Hybrid porous solids: past, present, future.* Chemical Society Reviews, 2008. **37**(1): p. 191-214.

121.   Kitagawa, S., R. Kitaura, and S.-i. Noro, *Functional Porous Coordination Polymers.* Angewandte Chemie International Edition, 2004. **43**(18): p. 2334-2375.

122.   Furukawa, H., K.E. Cordova, M. O'Keeffe, and O.M. Yaghi, *The Chemistry and Applications of Metal-Organic Frameworks.* Science, 2013. **341**(6149): p. 1230444.

123.   Furukawa, H., N. Ko, Y.B. Go, N. Aratani, S.B. Choi, E. Choi, A.Ö. Yazaydin, R.Q. Snurr, M. O'Keeffe, J. Kim, and O.M. Yaghi, *Ultrahigh Porosity in Metal-Organic Frameworks.* Science, 2010. **329**(5990): p. 424-428.

124.   Farha, O.K., I. Eryazici, N.C. Jeong, B.G. Hauser, A.A. Sarjeant, S.T. Nguyen, and A.O. Yazaydin, *Metal-Organic Framework Materials with Ultrahigh Surface Areas: Is the Sky the Limit?* J. Am. Chem. Soc.. 2012. **134**: p. 15016-15021.

125.   Yang, Q., A.D. Wiersum, P.L. Llewellyn, V. Guillerm, C. Serre, and G. Maurin, *Functionalizing porous zirconium terephthalate UiO-66(Zr) for natural gas upgrading: a computational exploration.* Chemical Communications, 2011. **47**(34): p. 9603-9605.

126.   Cmarik, G.E., M. Kim, S.M. Cohen, and K.S. Walton, *Tuning the Adsorption Properties of UiO-66 via Ligand Functionalization.* Langmuir, 2012. **28**(44): p. 15606-15613.

127.   Tanabe, K.K., Z. Wang, and S.M. Cohen, *Systematic functionalization of a metal-organic framework via a postsynthetic modification approach.* J. Am. Chem. Soc., 2008. **130**(26): p. 8508-8517.

128.   Kim, M., J.F. Cahill, Y. Su, K.A. Prather, and S.M. Cohen, *Postsynthetic ligand exchange as a route to functionalization of 'inert' metal-organic frameworks.* Chemical Science, 2012. **3**(1): p. 126-130.

129.   Goesten, M.G., J. Juan-Alcañiz, E.V. Ramos-Fernandez, K.B. Sai Sankar Gupta, E. Stavitski, H. van Bekkum, J. Gascon, and F. Kapteijn, *Sulfation of metal–organic frameworks: Opportunities for acid catalysis and proton conductivity.* Journal of Catalysis, 2011. **281**(1): p. 177-187.

130.   Moghadam, P.Z., A. Li, S.B. Wiggin, A. Tao, A.G.P. Maloney, P.A. Wood, S.C. Ward, and D. Fairen-Jimenez, *Development of a Cambridge Structural Database Subset: A Collection of Metal–Organic Frameworks for Past, Present, and Future.* Chemistry of Materials, 2017. **29**(7): p. 2618-2625.

131.   Gygi, D., E.D. Bloch, J.A. Mason, M.R. Hudson, M.I. Gonzalez, R.L. Siegelman, T.A. Darwish, W.L. Queen, C.M. Brown, and J.R. Long, *Hydrogen Storage in the Expanded Pore Metal–Organic Frameworks M2(dobpdc) (M = Mg, Mn, Fe, Co, Ni, Zn).* 2016. **28**(4): p. 1128–1138.

132.   Zhu, L., X.-Q. Liu, H.-L. Jiang , and L.-B. Sun, *Metal–Organic Frameworks for Heterogeneous Basic Catalysis.* Chem. Rev., 2017. **117** (12): p. 8129–8176.

133.   Jeremias, F., D. Frohlich, C. Janiak, and S.K. Henninger, *Water and methanol adsorption on MOFs for cycling heat transformation processes.* New Journal of Chemistry, 2014. **38**(5): p. 1846-1852.

134.   de Lange, M.F., K.J.F.M. Verouden, T.J.H. Vlugt, J. Gascon, and F. Kapteijn, *Adsorption-Driven Heat Pumps: The Potential of Metal–Organic Frameworks.* Chem. Rev., 2015. **115** (22): p. 12205–12250.

135.   Lustig, W.P., S. Mukherjee, N.D. Rudd, A.V. Desai, J. Li, and S.K. Ghosh, *Metal–organic frameworks: functional luminescent and photonic materials for sensing applications.* Chemical Society Reviews, 2017. **46**(11): p. 3242-3285.

136. Horcajada, P., R. Gref, T. Baati, P.K. Allan, G. Maurin, P. Couvreur, G. Férey, R.E. Morris, and C. Serre, *Metal–Organic Frameworks in Biomedicine.* Chemical Reviews, 2012. **112**(2): p. 1232-1268.

137. Li, B., H.-M. Wen, Y. Cui, W. Zhou, G. Qian, and B. Chen, *Emerging Multifunctional Metal–Organic Framework Materials.* Advanced Materials, 2016. **28**(40): p. 8819-8860.

138. Youssef, P.G., H. Dakkama, S.M. Mahmoud, and R.K. Al-Dadah, *Experimental investigation of adsorption water desalination/cooling system using CPO-27Ni MOF.* Desalination, 2017. **404**: p. 192-199.

139. Lee, S.-J., K.C. Kim, T.-U. Yoon, M.-B. Kim, and Y.-S. Bae, *Selective dynamic separation of Xe and Kr in Co-MOF-74 through strong binding strength between Xe atom and unsaturated Co2+ site.* Microporous and Mesoporous Materials, 2016. **236**: p. 284-291.

140. Kalmutzki, M.J., C.S. Diercks, and O.M. Yaghi, *Metal–Organic Frameworks for Water Harvesting from Air.* Advanced Materials, 2018. **30**(37): p. 1704304.

141. Kim, H., S.R. Rao, E.A. Kapustin, L. Zhao, S. Yang, O.M. Yaghi, and E.N. Wang, *Adsorption-based atmospheric water harvesting device for arid climates.* Nature Communications, 2018. **9**(1): p. 1191.

142. Fathieh, F., M.J. Kalmutzki, E.A. Kapustin, P.J. Waller, J. Yang, and O.M. Yaghi, *Practical water production from desert air.* Science Advances, 2018. **4**(6).

143. Jeremias, F., A. Khutia, S.K. Henninger, and C. Janiak, *MIL-100(Al, Fe) as water adsorbents for heat transformation purposes-a promising application.* Journal of Materials Chemistry, 2012. **22**(20): p. 10148-10151.

144. Khutia, A., H.U. Rammelberg, T. Schmidt, S. Henninger, and C. Janiak, *Water Sorption Cycle Measurements on Functionalized MIL-101Cr for Heat Transformation Application.* Chemistry of Materials, 2013. **25**(5): p. 790-798.

145.   Jeremias, F., V. Lozan, S.K. Henninger, and C. Janiak, *Programming MOFs for water sorption: amino-functionalized MIL-125 and UiO-66 for heat transformation and heat storage applications.* Dalton Transactions, 2013. **42**(45): p. 15967-15973.

146.   Plessius, R., R. Kromhout, A.L. Ramos, M. Ferbinteanu, M.C. Mittelmeijer-Hazeleger, R. Krishna, G. Rothenberg, and S. Tanase, *Highly selective water adsorption in a lanthanum metal-organic framework.* Chemistry, 2014. **20**(26): p. 7922-7925.

147.   Cadiau, A., J.S. Lee, D. Damasceno Borges, P. Fabry, T. Devic, M.T. Wharmby, C. Martineau, D. Foucher, F. Taulelle, C.H. Jun, Y.K. Hwang, N. Stock, M.F. De Lange, F. Kapteijn, J. Gascon, G. Maurin, J.S. Chang, and C. Serre, *Design of hydrophilic metal organic framework water adsorbents for heat reallocation.* Adv Mater, 2015. **27**(32): p. 4775-80.

148.   *Web of Science.* 27/08/2019]; Available from: https://apps.webofknowledge.com/CitationReport.do?product=UA&search_mode=CitationReport&SID=D11tJummBODhuTPZnkG&page=1&cr_pqid=59&viewType=summary.

149.   Bon, V., I. Senkovska, I.A. Baburin, and S. Kaskel, *Zr- and Hf-Based Metal–Organic Frameworks: Tracking Down the Polymorphism.* Crystal Growth & Design, 2013. **13**(3): p. 1231-1237.

150.   Sohail, M., Y.N. Yun, E. Lee, S.K. Kim, K. Cho, J.N. Kim, T.W. Kim, J.H. Moon, and H. Kim, *Synthesis of Highly Crystalline NH2-MIL-125 (Ti) with S-Shaped Water Isotherms for Adsorption Heat Transformation.* Crystal Growth & Design, 2017. **17**(3): p. 1208-1213.

151.   Canivet, J., A. Fateeva, Y. Guo, B. Coasne, and D. Farrusseng, *Water adsorption in MOFs: fundamentals and applications.* Chemical Society Reviews, 2014. **43**(16): p. 5594-5617.

152.   Ng, E.-P. and S. Mintova, *Nanoporous materials with enhanced hydrophilicity and high water sorption capacity.* Microporous and Mesoporous Materials, 2008. **114**(1): p. 1-26.

153. Jia, Z., *Metal-Organic Frameworks for Water Adsorption*, in *Metal-Organic Framework Composites.* 2019, Materials Research Foundations. p. 170-176.

154. Bagheri, F., *Performance investigation of atmospheric water harvesting systems.* Water Resources and Industry, 2018. **20**: p. 23-28.

155. Wang, Q.M., D. Shen, M. Bülow, M.L. Ling Lau, S. Deng, F.R. Fitch, N.O. Lemcoff, and J. Semanscin, *Metallo-organic molecular sieve for gas separation and purification.* Microporous and Mesoporous Materials, 2002. **55**(2): p. 217-230.

156. Teo, H.W.B. and A. Chakraborty, *Water Adsorption on Various Metal Organic Framework.* IOP Conference Series: Materials Science and Engineering, 2017. **272**(1): p. 012019.

157. Küsgens, P., M. Rose, I. Senkovska, H. Fröde, A. Henschel, S. Siegle, and S. Kaskel, *Characterization of metal-organic frameworks by water adsorption.* Microporous and Mesoporous Materials, 2009. **120**(3): p. 325-330.

158. Rieth, A.J., S. Yang, E.N. Wang, and M. Dincă, *Record Atmospheric Fresh Water Capture and Heat Transfer with a Material Operating at the Water Uptake Reversibility Limit.* ACS Central Science, 2017. **3**(6): p. 668-672.

159. Peng, X., L.-C. Lin, W. Sun, and B. Smit, *Water adsorption in metal–organic frameworks with open-metal sites.* AIChE Journal, 2015. **61**(2): p. 677-687.

160. Henninger, S.K., H.A. Habib, and C. Janiak, *MOFs as Adsorbents for Low Temperature Heating and Cooling Applications.* J. Am. Chem. Soc., 2009. **131**(8): p. 2776–2777.

161. de Lange, M.F., B.L. van Velzen, C.P. Ottevanger, K.J.F.M. Verouden, L.-C. Lin, T.J.H. Vlugt, J. Gascon, and F. Kapteijn, *Metal–Organic Frameworks in Adsorption-Driven Heat Pumps: The Potential of Alcohols as Working Fluids.* Langmuir, 2015. **31**(46): p. 12783-12796.

162. Wöllner, M., N. Klein, and S. Kaskel, *Measuring water adsorption processes of metal-organic frameworks for heat pump applications via optical calorimetry.* Microporous and Mesoporous Materials, 2019. **278**: p. 206-211.

163.   Towsif Abtab, S.M., D. Alezi, P.M. Bhatt, A. Shkurenko, Y. Belmabkhout, H. Aggarwal, Ł.J. Weseliński, N. Alsadun, U. Samin, M.N. Hedhili, and M. Eddaoudi, *Reticular Chemistry in Action: A Hydrolytically Stable MOF Capturing Twice Its Weight in Adsorbed Water.* Chem, 2018. **4**(1): p. 94-105.

164.   Elsayed, E., R. Al-Dadah, S. Mahmoud, P.A. Anderson, A. Elsayed, and P.G. Youssef, *CPO-27(Ni), aluminium fumarate and MIL-101(Cr) MOF materials for adsorption water desalination.* Desalination, 2017. **406**: p. 25-36.

165.   Kim, S.-I., T.-U. Yoon, M.-B. Kim, S.-J. Lee, Y.K. Hwang, J.-S. Chang, H.-J. Kim, H.-N. Lee, U.H. Lee, and Y.-S. Bae, *Metal–organic frameworks with high working capacities and cyclic hydrothermal stabilities for fresh water production.* Chemical Engineering Journal, 2016. **286**: p. 467-475.

166.   Janiak, C. and S.K. Henninger, *Porous coordination polymers as novel sorption materials for heat transformation processes.* Chimia, 2013. **67**(6): p. 419-424.

167.   Ernst, S.-J., M. Baumgartner, D. Fröhlich, H.-J. Bart, and S.K. Henninger, *Adsorbentien für sorptionsgestützte Klimatisierung, Entfeuchtung und Wassergewinnung.* Chemie Ingenieur Technik, 2017. **89**(12): p. 1650-1660.

168.   Kim, J.-H., C.H. Lee, W.-S. Kim, J.-S. Lee, J.-T. Kim , J.-K. Suh, and J.-M. Lee, *Adsorption Equilibria of Water Vapor on Alumina, Zeolite 13X, and a Zeolite X/Activated Carbon Composite.* J. Chem. Eng. Data, 2002. **48**(1): p. 137–141.

169.   Coelho, J.A., A.M. Ribeiro, A.F.P. Ferreira, S.M.P. Lucena, A.E. Rodrigues, and D.C.S. De Azevedo, *Stability of an Al-Fumarate MOF and Its Potential for CO2 Capture from Wet Stream.* Industrial and Engineering Chemistry Research, 2016. **55**(7): p. 2134-2143.

170.   Coelho, J.A., A.E.O. Lima, A.E. Rodrigues, D.C.S. de Azevedo, and S.M.P. Lucena, *Computer simulation of adsorption and sitting of CO2, N2, CH4 and water on a new Al(OH)-fumarate MOF.* Adsorption, 2017. **23**(2-3): p. 423-431.

171. Lamia, N., M. Jorge, M.A. Granato, F.A. Almeida Paz, H. Chevreau, and A.E. Rodrigues, *Adsorption of propane, propylene and isobutane on a metal-organic framework: Molecular simulation and experiment.* Chemical Engineering Science, 2009. **64**(14): p. 3246-3259.

172. Jorge, M., N. Lamia, and A.E. Rodrigues, *Molecular simulation of propane/propylene separation on the metal–organic framework CuBTC.* Colloids and Surfaces A: Physicochemical and Engineering Aspects, 2010. **357**(1): p. 27-34.

173. Ferreira, A.F.P., J.C. Santos, M.G. Plaza, N. Lamia, J.M. Loureiro, and A.E. Rodrigues, *Suitability of Cu-BTC extrudates for propane–propylene separation by adsorption processes.* Chemical Engineering Journal, 2011. **167**(1): p. 1-12.

174. Plaza, M.G., A.F.P. Ferreira, J.C. Santos, A.M. Ribeiro, U. Müller, N. Trukhan, J.M. Loureiro, and A.E. Rodrigues, *Propane/propylene separation by adsorption using shaped copper trimesate MOF.* Microporous and Mesoporous Materials, 2012. **157**(Supplement C): p. 101-111.

175. Plaza, M.G., A.M. Ribeiro, A. Ferreira, J.C. Santos, U.H. Lee, J.-S. Chang, J.M. Loureiro, and A.E. Rodrigues, *Propylene/propane separation by vacuum swing adsorption using Cu-BTC spheres.* Separation and Purification Technology, 2012. **90**(Supplement C): p. 109-119.

176. Asadi, T., M.R. Ehsani, A.M. Ribeiro, J.M. Loureiro, and A.E. Rodrigues, *CO2/CH4 Separation by Adsorption using Nanoporous Metal Organic Framework Copper-benzene-1,3,5-tricarboxylate Tablet.* Chemical Engineering Technology, 2013.

177. Silva, B., I. Solomon, A.M. Ribeiro, U.H. Lee, Y.K. Hwang, J.S. Chang, J.M. Loureiro, and A.E. Rodrigues, *H2 purification by pressure swing adsorption using CuBTC.* Separation and Purification Technology, 2013. **118**: p. 744-756.

178. Jorge, M., M. Fischer, J.R.B. Gomes, C. Siquet, J.C. Santos, and A.E. Rodrigues, *Accurate model for predicting adsorption of olefins and paraffins on MOFs with open metal sites.* Industrial and Engineering Chemistry Research, 2014. **53**(40): p. 15475-15487.

179.   Rios, R.B., L.S. Correia, M. Bastos-Neto, A.E.B. Torres, S.A. Hatimondi, A.M. Ribeiro, A.E. Rodrigues, C.L. Cavalcante, and D.C.S. de Azevedo, *Evaluation of carbon dioxide–nitrogen separation through fixed bed measurements and simulations.* Adsorption, 2014. **20**(8): p. 945-957.

180.   Martins, V.F.D., A.M. Ribeiro, A. Ferreira, U.H. Lee, Y.K. Hwang, J.S. Chang, J.M. Loureiro, and A.E. Rodrigues, *Ethane/ethylene separation on a copper benzene-1,3,5-tricarboxylate MOF.* Separation and Purification Technology, 2015. **149**: p. 445-456.

181.   Cavenati, S., C.A. Grande, A.E. Rodrigues, C. Kiener, and U. Müller, *Metal organic framework adsorbent for biogas upgrading.* Industrial and Engineering Chemistry Research, 2008. **47**(16): p. 6333-6335.

182.   Jamali, S., M. Mofarahi, and A.E. Rodrigues, *Investigation of a novel combination of adsorbents for hydrogen purification using Cu-BTC and conventional adsorbents in pressure swing adsorption.* Adsorption, 2018. **24**(5): p. 481-498.

183.   Martins, V.F.D., A.M. Ribeiro, J.-S. Chang, J.M. Loureiro, A. Ferreira, and A.E. Rodrigues, *Towards polymer grade ethylene production with Cu-BTC: gas-phase SMB versus PSA.* Adsorption, 2018. **24**(2): p. 203-219.

184.   Moreira, M.A., J.C. Santos, A.F.P. Ferreira, J.M. Loureiro, and A.E. Rodrigues, *Influence of the Eluent in the MIL-53(Al) Selectivity for Xylene Isomers Separation.* Ind. Eng. Chem. Res., 2011. **50** (12): p. 7688–7695.

185.   Moreira, M.A., J.C. Santos, A.F.P. Ferreira, U. Müller, N. Trukhan , J.M. Loureiro, and A.E. Rodrigues, *Selective Liquid Phase Adsorption and Separation of orthoXylene with the Microporous MIL-53(Al),.* Separation Science and Technology, 2011. **46**(13): p. 1995-2003.

186.   Regufe, M.J., J. Tamajon, A.M. Ribeiro, A. Ferreira, U.H. Lee, Y.K. Hwang, J.S. Chang, C. Serre, J.M. Loureiro, and A.E. Rodrigues, *Syngas Purification by Porous Amino-Functionalized Titanium Terephthalate MIL-125.* Energy and Fuels, 2015. **29**(7): p. 4654-4664.

187. Mendes, P.A.P., P. Horcajada, S. Rives, H. Ren, A.E. Rodrigues, T. Devic, E. Magnier, P. Trens, H. Jobic, J. Ollivier, G. Maurin, C. Serre, and J.A.C. Silva, *A complete separation of hexane isomers by a functionalized flexible metal organic framework.* Advanced Functional Materials, 2014. **24**(48): p. 7666-7673.

188. Mendes, P., A. Rodrigues, P. Horcajada, J. Eubank, T. Devic, C. Serre, and J. Silva, *Separation of hexane isomers on rigid porous metal carboxylate-based metal-organic frameworks.* Adsorption Science and Technology, 2014. **32**(6): p. 475-488.

189. Yoon, J.W., Y.-K. Seo, Y.K. Hwang, J.-S. Chang, H. Leclerc, S. Wuttke, P. Bazin, A. Vimont, M. Daturi, E. Bloch, P.L. Llewellyn, C. Serre, P. Horcajada, J.-M. Grenèche, A.E. Rodrigues, and G. Férey, *Controlled Reducibility of a Metal–Organic Framework with Coordinatively Unsaturated Sites for Preferential Gas Sorption.* Angewandte Chemie International Edition, 2010. **49**(34): p. 5949-5952.

190. Plaza, M.G., A.M. Ribeiro, A. Ferreira, J.C. Santos, Y.K. Hwang, Y.K. Seo, U.H. Lee, J.S. Chang, J.M. Loureiro, and A.E. Rodrigues, *Separation of C3/C4 hydrocarbon mixtures by adsorption using a mesoporous iron MOF: MIL-100(Fe).* Microporous and Mesoporous Materials, 2012. **153**: p. 178-190.

191. Ribeiro, A.M., M.C. Campo, G. Narin, J.C. Santos, A. Ferreira, J.-S. Chang, Y.K. Hwang, Y.-K. Seo, U.H. Lee, J.M. Loureiro, and A.E. Rodrigues, *Pressure swing adsorption process for the separation of nitrogen and propylene with a MOF adsorbent MIL-100(Fe).* Separation and Purification Technology, 2013. **110**: p. 101-111.

192. Okada, M., A. Ferreira, A.M. Ribeiro, U.H. Lee, Y.K. Hwang, J.S. Chang, and A.E. Rodrigues. *Pressure swing adsorption process for the separation of hydrogen, methane and ethane with the MOF.* in *Separations Division 2013 - Core Programming Area at the 2013 AIChE Annual Meeting: Global Challenges for Engineering a Sustainable Future.* 2013.

193. Narin, G., A.M. Ribeiro, A. Ferreira, Y.K. Hwang, U.H. Lee, J.M. Loureiro, J.S. Chang, and A.E. Rodrigues, *Propylene/nitrogen separation in a by-stream of the polypropylene production: From pilot test and model validation to industrial scale*

process design and optimization. Industrial and Engineering Chemistry Research, 2014. **53**(22): p. 9199-9213.

194.   Moreira, M.A., J.C. Santos, A.F.P. Ferreira, J.M. Loureiro, F. Ragon, P. Horcajada, P. Yot, C. Serre, and A.E. Rodrigues, *Toward understanding the influence of ethylbenzene in p-xylene selectivity of the porous titanium amino terephthalate MIL-125(Ti): adsorption equilibrium and separation of xylene isomers.* Langmuir, 2012 **28**(7): p. 3494-502.

195.   Moreira, M.A., J.C. Santos, A.F.P. Ferreira, J.M. Loureiro, F. Ragon, P. Horcajada, P.G. Yot, C. Serre, and A.E. Rodrigues, *Effect of ethylbenzene in p-xylene selectivity of the porous titanium amino terephthalate MIL-125(Ti)_NH2.* Microporous and Mesoporous Materials, 2012. **158**: p. 229-234.

196.   Moreira, M.A., M.P.S. Santos, C.G. Silva, J.M. Loureiro, J.-S. Chang, C. Serre, A.F.P. Ferreira, and A.E. Rodrigues, *Adsorption equilibrium of xylene isomers and ethylbenzene on MIL-125(Ti)_NH2: the temperature influence on the para-selectivity.* Adsorption, 2018. **24**(8): p. 715-724.

197.   Bárcia, P.S., M.P.M. Nicolau, J.M. Gallegos, B. Chen, A.E. Rodrigues, and J.A.C. Silva, *Modeling adsorption equilibria of xylene isomers in a microporous metal–organic framework.* Microporous and Mesoporous Materials, 2012. **155**: p. 220-226.

198.   Bárcia, P.S., L. Bastin, E.J. Hurtado, J.A.C. Silva, A.E. Rodrigues, and B. Chen, *Single and multicomponent sorption of CO2, CH4 and N2 in a microporous metal-organic framework.* Separation Science and Technology, 2008. **43**(13): p. 3494-3521.

199.   Bastin, L., P.S. Bárcia, E.J. Hurtado, J.A.C. Silva, A.E. Rodrigues, and B. Chen, *A microporous metal-organic framework for separation of CO 2/N2 and CO2/CH4 by fixed-bed adsorption.* Journal of Physical Chemistry C, 2008. **112**(5): p. 1575-1581.

200.   Bárcia, P.S., D. Guimarães, P.A.P. Mendes, J.A.C. Silva, V. Guillerm, H. Chevreau, C. Serre, and A.E. Rodrigues, *Reverse shape selectivity in the adsorption of hexane and xylene isomers in MOF UiO-66.* Microporous and Mesoporous Materials, 2011. **139**(1): p. 67-73.

201.   Granato, M.A., V.D. Martins, A.F.P. Ferreira, and A.E. Rodrigues, *Adsorption of xylene isomers in MOF UiO-66 by molecular simulation.* Microporous and Mesoporous Materials, 2014. **190**: p. 165-170.

202.   Moreira, M.A., J.C. Santos, A.F.P. Ferreira, J.M. Loureiro, F. Ragon, P. Horcajada, K.-E. Shim, Y.-K. Hwang, U.-H. Lee, J.-S. Chang, C. Serre, and A.E. Rodrigues, *Reverse Shape Selectivity in the Liquid-Phase Adsorption of Xylene Isomers in Zirconium Terephthalate MOF UiO-66* Langmuir : the ACS journal of surfaces and colloids, 2012. **28** (13): p. 5715–5723.

203.   Moreira, M.A., R.O.M. Dias, U.H. Lee, J.-S. Chang, A.M. Ribeiro, A.F.P. Ferreira, and A.E. Rodrigues, *Adsorption Equilibrium of Carbon Dioxide, Methane, Nitrogen, Carbon Monoxide, and Hydrogen on UiO-66(Zr)_(COOH)2.* Journal of Chemical & Engineering Data, 2019.

204.   Mendes, P.A.P., A.E. Rodrigues, P. Horcajada, C. Serre, and J.A.C. Silva, *Single and multicomponent adsorption of hexane isomers in the microporous ZIF-8.* Microporous and Mesoporous Materials, 2014. **194**: p. 146-156.

205.   Ferreira, A.F.P., M.C. Mittelmeijer-Hazeleger, M.A. Granato, V.F.D. Martins, A.E. Rodrigues, and G. Rothenberg, *Sieving di-branched from mono-branched and linear alkanes using ZIF-8: Experimental proof and theoretical explanation.* Physical Chemistry Chemical Physics, 2013. **15**(22): p. 8795-8804.

206.   Henrique, A., A.E. Rodrigues, and J.A.C. Silva, *Separation of Hexane Isomers in ZIF-8 by Fixed Bed Adsorption.* Industrial & Engineering Chemistry Research, 2019. **58**(1): p. 378-394.

207.   Mendes, P.A.P., A.E. Rodrigues, J.P. Almeida, and J.A.C. Silva. *Dynamics of a fixed bed adsorption column in the kinetic separation of hexane isomers in MOF ZIF-8*. in *Springer Proceedings in Mathematics and Statistics*. 2018.

208.   Martins, V.F.D., A.M. Ribeiro, P. Kortunov, A. Ferreira, and A.E. Rodrigues, *High purity ethane/ethylene separation by gas phase simulated moving bed using ZIF-8 adsorbent.* AIChE Journal, 2019. **65**(8): p. e16619.

209. Nicolau, M.P.M., P.S. Bárcia, J.M. Gallegos, J.A.C. Silva, A.E. Rodrigues, and B. Chen, *Single- and multicomponent vapor-phase adsorption of xylene isomers and ethylbenzene in a microporous metal-organic framework.* Journal of Physical Chemistry C, 2009. **113**(30): p. 13173-13179.

210. Comotti, A., S. Bracco, P. Sozzani, S. Horike, R. Matsuda, J. Chen, M. Takata, Y. Kubota, and S. Kitagawa, *Nanochannels of Two Distinct Cross-Sections in a Porous Al-Based Coordination Polymer.* Journal of the American Chemical Society, 2008. **130**(41): p. 13664-13672.

211. Teo, H.W.B. and A. Chakraborty, *Water Adsorption on Various Metal Organic Framework.* IOP Conference Series: Materials Science and Engineering, 2017. **272**: p. 012019.

212. Gaab, M., N. Trukhan, S. Maurer, R. Gummaraju, and U. Müller, *The progression of Al-based metal-organic frameworks – From academic research to industrial production and applications.* Microporous and Mesoporous Materials, 2012. **157**: p. 131-136.

213. Jeremias, F., D. Fröhlich, C. Janiak, and S.K. Henninger, *Advancement of sorption-based heat transformation by a metal coating of highly-stable, hydrophilic aluminium fumarate MOF.* RSC Advances, 2014. **4**(46): p. 24073-24082.

214. Teo, H.W.B., A. Chakraborty, Y. Kitagawa, and S. Kayal, *Experimental study of isotherms and kinetics for adsorption of water on Aluminium Fumarate.* International Journal of Heat and Mass Transfer, 2017. **114**: p. 621-627.

215. Tannert, N., C. Jansen, S. Nießing, and C. Janiak, *Robust synthesis routes and porosity of the Al-based metal–organic frameworks Al-fumarate, CAU-10-H and MIL-160.* Dalton Transactions, 2019. **48**(9): p. 2967-2976.

216. Henninger, S.K., F. Jeremias, H. Kummer, and C. Janiak, *MOFs for Use in Adsorption Heat Pump Processes.* European Journal of Inorganic Chemistry, 2012. **2012**(16): p. 2625-2634.

217. Li, H., X. Feng, D. Ma, M. Zhang, Y. Zhang, Y. Liu, J. Zhang, and B. Wang, *Stable Aluminum Metal–Organic Frameworks (Al-MOFs) for Balanced CO2 and Water Selectivity.* ACS Applied Materials & Interfaces, 2018. **10**(4): p. 3160-3163.

218. Reinsch, H., B. Marszałek, J. Wack, J. Senker, B. Gil, and N. Stock, *A new Al-MOF based on a unique column-shaped inorganic building unit exhibiting strongly hydrophilic sorption behaviour.* Chemical Communications, 2012. **48**(76): p. 9486-9488.

219. Borges, D.D., M. Guillaume , and D.S. Galvão, *Design of Porous Metal-Organic Frameworks for Adsorption Driven Thermal Batteries.* MRS Advances, 2017. **2**(9): p. 519–524.

220. Reinsch, H., M.A. van der Veen, B. Gil, B. Marszalek, T. Verbiest, D. de Vos, and N. Stock, *Structures, Sorption Characteristics, and Nonlinear Optical Properties of a New Series of Highly Stable Aluminum MOFs.* Chemistry of Materials, 2013. **25**(1): p. 17-26.

221. Fröhlich, D., E. Pantatosaki, P.D. Kolokathis, K. Markey, H. Reinsch, M. Baumgartner, M.A. van der Veen, D.E. De Vos, N. Stock, G.K. Papadopoulos, S.K. Henninger, and C. Janiak, *Water adsorption behaviour of CAU-10-H: a thorough investigation of its structure–property relationships.* Journal of Materials Chemistry A, 2016. **4**(30): p. 11859-11869.

222. Fröhlich, D., S.K. Henninger, and C. Janiak, *Multicycle water vapour stability of microporous breathing MOF aluminium isophthalate CAU-10-H.* Dalton Transactions, 2014. **43**(41): p. 15300-15304.

223. Kondo, A., T. Daimaru, H. Noguchi, T. Ohba, K. Kaneko, and H. Kanoh, *Adsorption of water on three-dimensional pillared-layer metal organic frameworks.* Journal of Colloid and Interface Science, 2007. **314**(2): p. 422-426.

224. Jasuja, H., Y.-g. Huang, and K.S. Walton, *Adjusting the Stability of Metal–Organic Frameworks under Humid Conditions by Ligand Functionalization.* Langmuir, 2012. **28**(49): p. 16874-16880.

225. Schoenecker, P.M., C.G. Carson, H. Jasuja, C.J.J. Flemming, and K.S. Walton, *Effect of Water Adsorption on Retention of Structure and Surface Area of Metal–Organic Frameworks.* Industrial & Engineering Chemistry Research, 2012. **51**(18): p. 6513-6519.

226. Jasuja, H., N.C. Burtch, Y.-g. Huang, Y. Cai, and K.S. Walton, *Kinetic Water Stability of an Isostructural Family of Zinc-Based Pillared Metal–Organic Frameworks.* Langmuir, 2013. **29**(2): p. 633-642.

227. Lee, J.Y., D.H. Olson, L. Pan, T.J. Emge, and J. Li, *Microporous Metal–Organic Frameworks with High Gas Sorption and Separation Capacity.* Advanced Functional Materials, 2007. **17**(8): p. 1255-1262.

228. Bon, V., V. Senkovskyy, I. Senkovska, and S. Kaskel, *Zr(iv) and Hf(iv) based metal–organic frameworks with reo-topology.* Chemical Communications, 2012. **48**(67): p. 8407-8409.

229. Bon, V., I. Senkovska, M.S. Weiss, and S. Kaskel, *Tailoring of network dimensionality and porosity adjustment in Zr- and Hf-based MOFs.* CrystEngComm, 2013. **15**(45): p. 9572-9577.

230. Liu, J., Y. Wang, A.I. Benin, P. Jakubczak, R.R. Willis, and M.D. LeVan, *CO2/H2O Adsorption Equilibrium and Rates on Metal–Organic Frameworks: HKUST-1 and Ni/DOBDC.* Langmuir, 2010. **26**(17): p. 14301-14307.

231. Liang, Z., M. Marshall, and A.L. Chaffee, *CO2 Adsorption-Based Separation by Metal Organic Framework (Cu-BTC) versus Zeolite (13X).* Energy & Fuels, 2009. **23**(5): p. 2785-2789.

232. DeCoste, J.B., G.W. Peterson, B.J. Schindler, K.L. Killops, M.A. Browe, and J.J. Mahle, *The effect of water adsorption on the structure of the carboxylate containing metal–organic frameworks Cu-BTC, Mg-MOF-74, and UiO-66.* Journal of Materials Chemistry A, 2013. **1**(38): p. 11922-11932.

233. Pirngruber, G.D., L. Hamon, S. Bourrelly, P.L. Llewellyn, E. Lenoir, V. Guillerm, C. Serre, and T. Devic, *A Method for Screening the Potential of MOFs as CO2 Adsorbents in Pressure Swing Adsorption Processes.* ChemSusChem, 2012. **5**(4): p. 762-776.

234. Li, Y. and R.T. Yang, *Hydrogen storage in metal-organic and covalent-organic frameworks by spillover.* AIChE Journal, 2008. **54**(1): p. 269-279.

235. Zhang, J.-P., A.-X. Zhu, R.-B. Lin, X.-L. Qi, and X.-M. Chen, *Pore Surface Tailored SOD-Type Metal-Organic Zeolites.* Advanced Materials, 2011. **23**(10): p. 1268-1271.

236. Canivet, J., J. Bonnefoy, C. Daniel, A. Legrand, B. Coasne, and D. Farrusseng, *Structure–property relationships of water adsorption in metal–organic frameworks.* New Journal of Chemistry, 2014. **38**(7): p. 3102-3111.

237. Liu, J., F. Zhang, X. Zou, G. Yu, N. Zhao, S. Fan, and G. Zhu, *Environmentally friendly synthesis of highly hydrophobic and stable MIL-53 MOF nanomaterials.* Chemical Communications, 2013. **49**(67): p. 7430-7432.

238. Wickenheisser, M., F. Jeremias, S.K. Henninger, and C. Janiak, *Grafting of hydrophilic ethylene glycols or ethylenediamine on coordinatively unsaturated metal sites in MIL-100(Cr) for improved water adsorption characteristics.* Inorganica Chimica Acta, 2013. **407**: p. 145-152.

239. Wickenheisser, M., A. Herbst, R. Tannert, B. Milow, and C. Janiak, *Hierarchical MOF-xerogel monolith composites from embedding MIL-100(Fe,Cr) and MIL-101(Cr) in resorcinol-formaldehyde xerogels for water adsorption applications.* Microporous and Mesoporous Materials, 2015. **215**: p. 143-153.

240. George, A., M. Ryotaro, and K. Susumu, *Highly Porous and Stable Coordination Polymers as Water Sorption Materials.* Chemistry Letters, 2010. **39**(4): p. 360-361.

241. Seo, Y.-K., J.W. Yoon, J.S. Lee, Y.K. Hwang, C.-H. Jun, J.-S. Chang, S. Wuttke, P. Bazin, A. Vimont, M. Daturi, S. Bourrelly, P.L. Llewellyn, P. Horcajada, C. Serre, and G. Férey, *Energy-Efficient Dehumidification over Hierachically Porous Metal–Organic*

Frameworks as Advanced Water Adsorbents. Advanced Materials, 2012. **24**(6): p. 806-810.

242. Mileo, P.G.M., K. Ho Cho, J. Park, S. Devautour-Vinot, J.-S. Chang, and G. Maurin, *Unraveling the Water Adsorption Mechanism in the Mesoporous MIL-100(Fe) Metal–Organic Framework.* The Journal of Physical Chemistry C, 2019. **123**(37): p. 23014-23025.

243. Ehrenmann, J., S.K. Henninger, and C. Janiak, *Water Adsorption Characteristics of MIL-101 for Heat-Transformation Applications of MOFs.* European Journal of Inorganic Chemistry, 2011. **2011**(4): p. 471-474.

244. Akiyama, G., R. Matsuda, H. Sato, A. Hori, M. Takata, and S. Kitagawa, *Effect of functional groups in MIL-101 on water sorption behavior.* Microporous and Mesoporous Materials, 2012. **157**: p. 89-93.

245. Ko, N., P.G. Choi, J. Hong, M. Yeo, S. Sung, K.E. Cordova, H.J. Park, J.K. Yang, and J. Kim, *Tailoring the water adsorption properties of MIL-101 metal–organic frameworks by partial functionalization.* Journal of Materials Chemistry A, 2015. **3**(5): p. 2057-2064.

246. Kim, S.-N., J. Kim, H.-Y. Kim, H.-Y. Cho, and W.-S. Ahn, *Adsorption/catalytic properties of MIL-125 and NH2-MIL-125.* Catalysis Today, 2013. **204**: p. 85-93.

247. Gordeeva, L.G., M.V. Solovyeva, and Y.I. Aristov, *NH2-MIL-125 as a promising material for adsorptive heat transformation and storage.* Energy, 2016. **100**: p. 18-24.

248. Permyakova, A., O. Skrylnyk, E. Courbon, M. Affram, S. Wang, U.-H. Lee, A.H. Valekar, F. Nouar, G. Mouchaham, T. Devic, G. De Weireld, J.-S. Chang, N. Steunou, M. Frère, and C. Serre, *Synthesis Optimization, Shaping, and Heat Reallocation Evaluation of the Hydrophilic Metal–Organic Framework MIL-160(Al).* ChemSusChem, 2017. **10**(7): p. 1419-1426.

249. Wahiduzzaman, M., D. Lenzen, G. Maurin, N. Stock, and M.T. Wharmby, *Rietveld Refinement of MIL-160 and Its Structural Flexibility Upon H2O and N2 Adsorption.* European Journal of Inorganic Chemistry, 2018. **2018**(32): p. 3626-3632.

250. Karra, J.R., B.E. Grabicka, Y.-G. Huang, and K.S. Walton, *Adsorption study of CO2, CH4, N2, and H2O on an interwoven copper carboxylate metal–organic framework (MOF-14).* Journal of Colloid and Interface Science, 2013. **392**: p. 331-336.

251. Jiao, Y., C.R. Morelock, N.C. Burtch, W.P. Mounfield, J.T. Hungerford, and K.S. Walton, *Tuning the Kinetic Water Stability and Adsorption Interactions of Mg-MOF-74 by Partial Substitution with Co or Ni.* Industrial & Engineering Chemistry Research, 2015. **54**(49): p. 12408-12414.

252. Li, Y. and R.T. Yang, *Gas Adsorption and Storage in Metal–Organic Framework MOF-177.* Langmuir, 2007. **23**(26): p. 12937-12944.

253. Jasuja, H. and K.S. Walton, *Effect of catenation and basicity of pillared ligands on the water stability of MOFs.* Dalton Transactions, 2013. **42**(43): p. 15421-15426.

254. Chen, T.-H., I. Popov, O. Zenasni, O. Daugulis, and O.Š. Miljanić, *Superhydrophobic perfluorinated metal–organic frameworks.* Chemical Communications, 2013. **49**(61): p. 6846-6848.

255. Padial, N.M., E. Quartapelle Procopio, C. Montoro, E. López, J.E. Oltra, V. Colombo, A. Maspero, N. Masciocchi, S. Galli, I. Senkovska, S. Kaskel, E. Barea, and J.A.R. Navarro, *Highly Hydrophobic Isoreticular Porous Metal–Organic Frameworks for the Capture of Harmful Volatile Organic Compounds.* Angewandte Chemie International Edition, 2013. **52**(32): p. 8290-8294.

256. Hou, C., Q. Liu, P. Wang, and W.-Y. Sun, *Porous metal–organic frameworks with high stability and selective sorption for CO2 over N2.* Microporous and Mesoporous Materials, 2013. **172**: p. 61-66.

257. Xie, L.-H. and M.P. Suh, *Flexible Metal–Organic Framework with Hydrophobic Pores.* Chemistry – A European Journal, 2011. **17**(49): p. 13653-13656.

258. Ghosh, P., Y.J. Colón, and R.Q. Snurr, *Water adsorption in UiO-66: the importance of defects.* Chemical Communications, 2014. **50**(77): p. 11329-11331.

259. Wiersum, A.D., E. Soubeyrand-Lenoir, Q. Yang, B. Moulin, V. Guillerm, M.B. Yahia, S. Bourrelly, A. Vimont, S. Miller, C. Vagner, M. Daturi, G. Clet, C. Serre, G. Maurin, and P.L. Llewellyn, *An Evaluation of UiO-66 for Gas-Based Applications.* Chemistry – An Asian Journal, 2011. **6**(12): p. 3270-3280.

260. Wade, C.R., T. Corrales-Sanchez, T.C. Narayan, and M. Dincă, *Postsynthetic tuning of hydrophilicity in pyrazolate MOFs to modulate water adsorption properties.* Energy & Environmental Science, 2013. **6**(7): p. 2172-2177.

261. Čelič, T.B., M. Mazaj, N. Guillou, E. Elkaïm, M. El Roz, F. Thibault-Starzyk, G. Mali, M. Rangus, T. Čendak, V. Kaučič, and N. Zabukovec Logar, *Study of Hydrothermal Stability and Water Sorption Characteristics of 3-Dimensional Zn-Based Trimesate.* The Journal of Physical Chemistry C, 2013. **117**(28): p. 14608-14617.

262. Bansal, R.C. and M. Goyal, *Activated carbon adsorption*. 2005, Boca Raton: CRC Press.

263. Yang, R.T., *Adsorbents: Fundamentals and Applications*. 2003: John Wiley & Sons, Inc.

264. Zuo, Q., Y. Zhang, H. Zheng, P. Zhang, H. Yang, J. Yu, J. Tang, Y. Zheng, and J. Mai, *A facile method to modify activated carbon fibers for drinking water purification.* Chemical Engineering Journal, 2019. **365**: p. 175-182.

265. Oh, J.-Y., Y.-W. You, J. Park, J.-S. Hong, I. Heo, C.-H. Lee, and J.-K. Suh, *Adsorption characteristics of benzene on resin-based activated carbon under humid conditions.* Journal of Industrial and Engineering Chemistry, 2019. **71**: p. 242-249.

266. Kwiatkowski, J.F., *Activated Carbon: Classifications, Properties and Applications*. 2012: Nova Science Publishers,. 555.

267. Marsh, H. and F. Rodríguez-Reinoso, *Activated Carbon*. 2006: Elsevier Science & Technology Books.

268. Tadda, M.A., A. Ahsan, A. Shitu, M. ElSergany, T. Arunkumar, J. Bipin, M.A. Razzaque, and N.N. Daud, *A review on activated carbon: process, application and prospects.* Journal of Advanced Civil Engineering Practice and Research, 2016. **2**(1): p. 7-13.

269. Koehlert, K. *Activated Carbon: Fundamentals and New Applications.* 2017. 40.

270. Yao, X.-l., L.-q. Li, H.-l. Li, and W.-w. Ma, *A simplified adsorption model for water vapor adsorption on activated carbon.* Journal of Central South University, 2014. **21**(4): p. 1434-1440.

271. Alcañiz-Monge, J., A. Linares-Solano, and B. Rand, *Water Adsorption on Activated Carbons: Study of Water Adsorption in Micro- and Mesopores.* The Journal of Physical Chemistry B, 2001. **105**(33): p. 7998-8006.

272. Salame, I.I. and T.J. Bandosz, *Experimental Study of Water Adsorption on Activated Carbons.* Langmuir, 1999. **15**(2): p. 587-593.

273. Xiao, J., S. Sitamraju, and M.J. Janik, *CO2 Adsorption Thermodynamics over N-Substituted/Grafted Graphanes: A DFT Study.* Langmuir, 2014. **30**(7): p. 1837-1844.

274. Foley, N.J., K.M. Thomas, P.L. Forshaw, D. Stanton, and P.R. Norman, *Kinetics of Water Vapor Adsorption on Activated Carbon.* Langmuir, 1997. **13**(7): p. 2083-2089.

275. Ohba, T., H. Kanoh, and K. Kaneko, *Cluster-Growth-Induced Water Adsorption in Hydrophobic Carbon Nanopores.* The Journal of Physical Chemistry B, 2004. **108**(39): p. 14964-14969.

276. Naono, H., M. Hakuman, M. Shimoda, K. Nakai, and S. Kondo, *Separation of Water and Ethanol by the Adsorption Technique: Selective Desorption of Water from Micropores of Active Carbon.* Journal of Colloid and Interface Science, 1996. **182**(1): p. 230-238.

277. Ito, H., T. Iiyama, and S. Ozeki, *Kinetics of Cluster-Mediated Filling of Water Molecules into Carbon Micropores.* The Journal of Physical Chemistry C, 2015. **119**(8): p. 4118-4125.

278. Horikawa, T., N. Sakao, and D.D. Do, *Effects of temperature on water adsorption on controlled microporous and mesoporous carbonaceous solids.* Carbon, 2013. **56**: p. 183-192.

279. Küsgens, P., *Metal-organic frameworks for water adsorption applications in the automotive filtration industry* in *Fakultat Mathematik und Naturwissenschaften.* 2010, Technische Universität Dresden. p. 123.

280. Lagaly, G., *K. K. Unger: Porous Silica — its properties and use as support in column liquid chromatography. Elsevier Scientific Publishing Co., Amsterdam, Oxford, New York 1979. 226 Seiten, Preis: $ 46.25.* Berichte der Bunsengesellschaft für physikalische Chemie, 1980. **84**(1): p. 111-111.

281. Ng, K.C., H.T. Chua, C.Y. Chung, C.H. Loke, T. Kashiwagi, A. Akisawa, and B.B. Saha, *Experimental investigation of the silica gel–water adsorption isotherm characteristics.* Applied Thermal Engineering, 2001. **21**(16): p. 1631–1642.

282. Sah, R.P., B. Choudhury, and R.K. Das, *A review on adsorption cooling systems with silica gel and carbon as adsorbents.* Renewable and Sustainable Energy Reviews, 2015. **45**: p. 123-134.

283. Wang, D., J. Zhang, X. Tian, D. Liu, and K. Sumathy, *Progress in silica gel–water adsorption refrigeration technology.* Renewable and Sustainable Energy Reviews, 2014. **30**: p. 85-104.

284. Ng, K.C., H.T. Chua, C.Y. Chung, C.H. Loke, T. Kashiwagi, A. Akisawa, and B.B. Saha, *Experimental investigation of the silica gel–water adsorption isotherm characteristics.* Applied Thermal Engineering, 2001. **21**(16): p. 1631-1642.

285. Thu, K., A. Chakraborty, B.B. Saha, and K.C. Ng, *Thermo-physical properties of silica gel for adsorption desalination cycle.* Applied Thermal Engineering, 2013. **50**(2): p. 1596-1602.

286. Mohammed, R.H., O. Mesalhy, M.L. Elsayed, S. Hou, M. Su, and L.C. Chow, *Physical properties and adsorption kinetics of silica-gel/water for adsorption chillers.* Applied Thermal Engineering, 2018. **137**: p. 368-376.

287. Knaebel, K.S., *Chemical Engineering*. Vol. 102. 1995.

288. Ruthven, D.M., *Principles of adsorption and adsorption processes*. 1984, New York (USA): John Wiley and Sons, Inc.

289. Kotoh, K., M. Enoeda, T. Matsui, and M. Nishikawa, *A Multilayer Model for Adsorption of Water on Activated Alumina in Relation to Adsorption Potential.* Journal of Chemical Engineering of Japan, 1993. **26**(4): p. 355-360.

290. Sircar, S., M.B. Rao, and T.C. Golden, *Chapter 2.12 Drying of gases and liquids by activated alumina*, in *Studies in Surface Science and Catalysis*, A. Dąbrowski and V.A. Tertykh, Editors. 1996, Elsevier. p. 629-646.

291. Serbezov, A., *Adsorption Equilibrium of Water Vapor on F-200 Activated Alumina.* Journal of Chemical & Engineering Data, 2003. **48**(2): p. 421-425.

292. Srivastava, N.C. and I.W. Eames, *A review of adsorbents and adsorbates in solid–vapour adsorption heat pump systems.* Applied Thermal Engineering, 1998. **18**(9): p. 707-714.

293. Wang, L.W., R.Z. Wang, and R.G. Oliveira, *A review on adsorption working pairs for refrigeration.* Renewable and Sustainable Energy Reviews, 2009. **13**(3): p. 518-534.

294. Tatlier, M., G. Munz, and S.K. Henninger, *Relation of water adsorption capacities of zeolites with their structural properties.* Microporous and Mesoporous Materials, 2018. **264**: p. 70-75.

295. Liu, Q., N.C.O. Cheung, A.E. Garcia-Bennett, and N. Hedin, *Aluminophosphates for CO2 Separation.* ChemSusChem, 2011. **4**(1): p. 91-97.

296.   Chiyoda, O. and M.E. Davis, *Adsorption studies with gmelinite zeolites containing mono-, di- and tri-valent cations.* Microporous and Mesoporous Materials, 2000. **38**(2): p. 143-149.

3 MATERIALS AND METHODS:

DESCRIPTION AND CHARACTERIZATION

3.1 Adsorbents

MOFs show modular structure, which makes them ideal candidates in water sorption-based applications, as exposed in Chapter 2. This chapter covers the chemistry of the selected MOFs for water vapor adsorption. An overview of their synthesis, building blocks, characterization, structures, porosity, and some of their main applications will be presented in the next pages.

Aluminum fumarate, CAU-10, and MIL-160(Al) belong to the family of aluminum-based metal-organic frameworks (Al-MOFs). The Al-MOFs have been investigated and applied in different fields, such as sensing, catalysis, gas storage, gas purification, desalination, and water harvesting [1-6]. Due to their characteristics, such as high hydrothermal stability, low-cost, and non-toxic nature they are eligible adsorbents for water vapor capture [7-9].

MIL-100(Fe) is a nanoporous iron-based MOF, considered a promising water adsorbent due to its high hydrothermal stability, even after being exposed for weeks to boiling water or after forty adsorption/desorption water cycles [8, 10-14]. The high porosity and large specific surface areas presented by MIL-100(Fe) leads to its high water adsorption capacity [15]. Several studies used MIL-100(Fe) as water adsorbent for energy-efficient dehumidification and adsorptive heat transformation applications [12, 13, 16].

MIL-125(Ti)_NH$_2$ is a titanium-based MOF with potential applications in gas storage, gas separation, sensing, and photocatalysis [17-20]. MIL-125(Ti)_NH$_2$ is also a promising adsorbent for direct water capture from air, due to its high water adsorption capacity, high water stability, and thermal stability [18, 21, 22]. As proved in previous studies, performed by different authors, on powder samples [17, 23], MIL-125(Ti)_NH$_2$ is characterized by the "S" shaped water adsorption equilibrium isotherm. Indeed, the sharp increase in water adsorption at P/P$_o$ = 0.2 makes it a promising material for water capture, even in locations with low relative humidity.

3.1.1 Aluminum Fumarate (Al-Fum)

Al-Fum granules (Figure 3.1) used in experiments were produced and supplied by the Korea Research Institute of Chemical Technology (KRICT). Al-Fum presents a crystal structure of infinite Al-OH-Al chains connected by fumarate acid (organic linker), creating 1-D diamond-shaped pores, with a size of 5.7 × 6.0 Å^2 (Figure 3.2) [24-26]. Leung and her co-workers

improved the synthesis process, changing the hazardous chemical solvent dimethylformamide (DMF) by water [9, 27]. Another improvement in the synthesis method was the substitution of nitrate or chloride salts by aluminum sulfate, thus eliminating the safety hazard caused by nitrates and preventing possible future corrosion problems due to chloride salts [9].
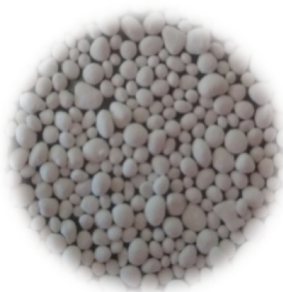
Figure 3.1. Al-Fum granules supplied by KRICT.
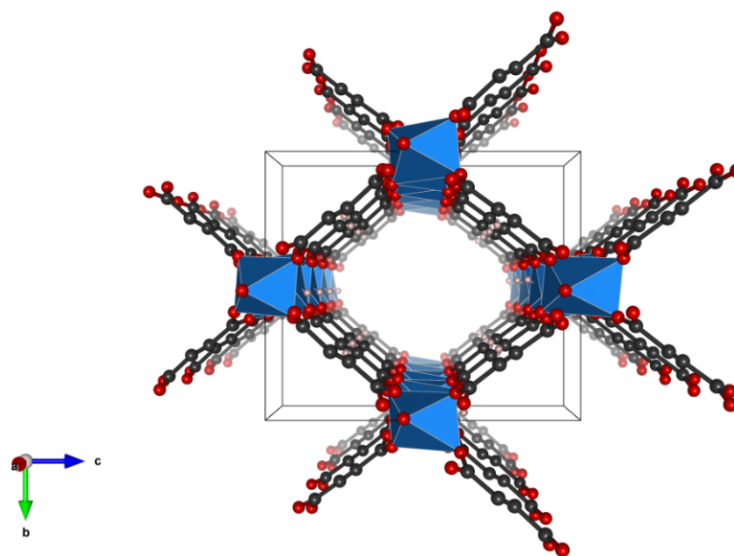
Figure 3.2. Crystal structure of Al-Fum. The oxygen atoms are shown in red, aluminum octahedra in blue, carbon in gray, and hydrogen atoms were omitted [25].

3.1.2 CAU-10

Likewise, Al-Fum, CAU-10 (CAU stands for Christian-Albrechts-University) granules were synthesized and prepared at KRICT (Figure 3.3). The material is built from inorganic aluminum chains octahedral linked via the carboxylate groups of 2,4-benzenedicarboxylate (BDC) ligand (Figure 3.4b) [28]. The octahedral AlO_6 (Figure 3.4a) is enclosed by four ligands and two

hydroxyl groups, with the hydroxyl ions providing bridge with Al centers, thus creating helical chains [29]. The helical chains present square shape channels with a side length of circa 5.6 Å (Figure 3.4c) [29].

Figure 3.3. CAU-10 granules as supplied by KRICT.
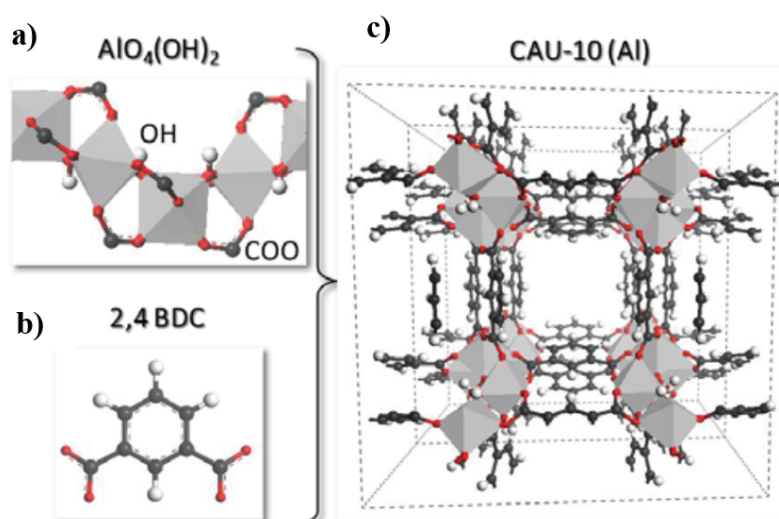
Figure 3.4. Schematic illustration of a) octahedral AlO_6; b) organic ligand 2,4-benzenedicarboxylate; c) crystal structure of CAU-10. Al polyhedra, carbon, oxygen, and hydrogen atoms correspond to light gray, gray, red, and white colors, respectively (adapted from [29]).

3.1.3 MIL-160(Al)

MIL-160(Al) granulates (MIL stands for Material Institute of Lavoisier) were provided by KRICT (Figure 3.5). The adsorbent is isostructural to CAU-10 [30]. This material is built up from inorganic aluminum helical chains which are connected by 2,5-furandicarboxylate groups

(Figure 3.6) [8, 28]. As in CAU-10, the helical chains are formed by the bridge between hydroxyl ions with the Al centers. The 3D framework presents square shape channels with a pore size of 4 to 6 Å (Figure 3.6) [2]. The material was synthesized in KRICT at large-scale, and the preparation was performed following the procedure described by Permyakova *et al.* [31].

Figure 3.5. MIL-160(Al) granulates as provided by KRICT.
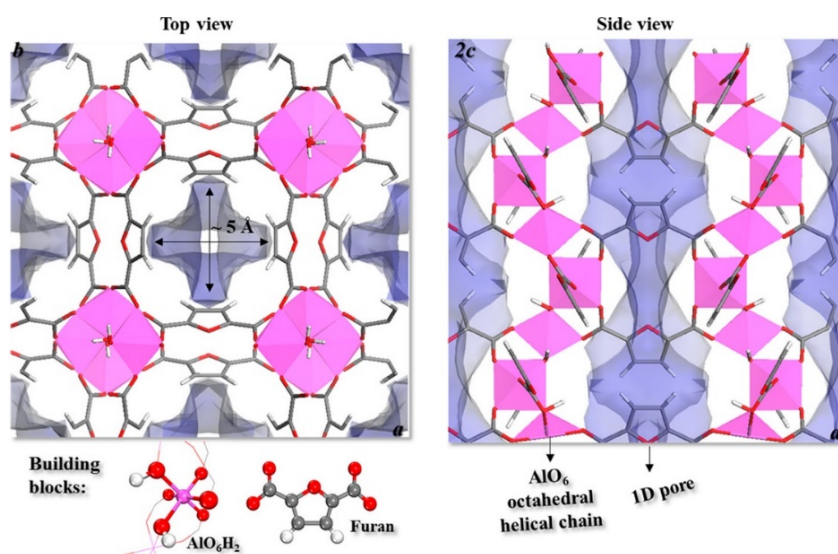
Figure 3.6. Crystal structure of MIL-160(Al) with a blue area representing available pore volume, and aluminum, oxygen, carbon, and hydrogen atoms are represented by pink, red, gray, and white colors, respectively [2].

3.1.4 MIL-100(Fe)

MIL-100(Fe) was also synthesized at KRICT (Figure 3.7) [11, 32] and prepared according to the procedure reported by Ribeiro *et al.* study [33]. The material has a three-dimensional

crystal structure which is composed of octahedral iron trimers (Figure 3.7a) connected through 1, 3, 5 – benzenetricarboxylate linkers (BTC) [34]. This framework provides two types of mesoporous cavities of 25 and 29 Å diameter (Figure 3.7c), which are accessible through micropores windows of 5.5 (pentagonal) and 8.6 Å (hexagonal) (Figure 3.7d) [11, 34, 35].

Figure 3.7. MIL-100(Fe) granules as provided by KRICT.
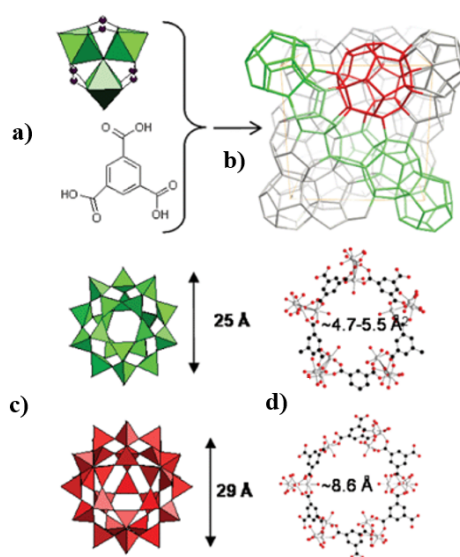
Figure 3.8. The general structure of MIL-100(Fe): a) octahedral iron trimers; b) MIL-100(Fe) cell; c) mesoporous cavities; and d) windows cages. Carbon, oxygen, and iron atoms are represented by black, red, and gray colors, respectively [34].

3.1.5 MIL-125(Ti)_NH$_2$

MIL-125(Ti)_NH$_2$ granules (Figure 3.9) were synthesized at KRICT, according to the procedure reported by Moreira *et al.* [36]. MIL-125(Ti)_NH$_2$ is isostructural to MIL-125(Ti),

and its structure is based on cyclic octamers of a corner- or edge-sharing titanium octahedral connected to 12 other octamers through the 2-amino-benzene-1,4-dicarboxylate linkers (Figure 3.10) [17]. The quasi-cubic tetragonal structure provides octahedral (~12.55 Å) and tetrahedral cages (~6.13 Å) [37]. Its narrow triangular windows are in the range of 5–7 Å [21, 37]. The free amino groups and titanium oxo-clusters are hydrophilic active sites, improving the adsorption of water molecules in the MOF [38]. MIL-125(Ti)_NH$_2$ granules were prepared by the wet granulation method described in the work by Regufe *et al.* [39].

Figure 3.9. MIL-125(Ti)_NH$_2$ granules as provided by KRICT.
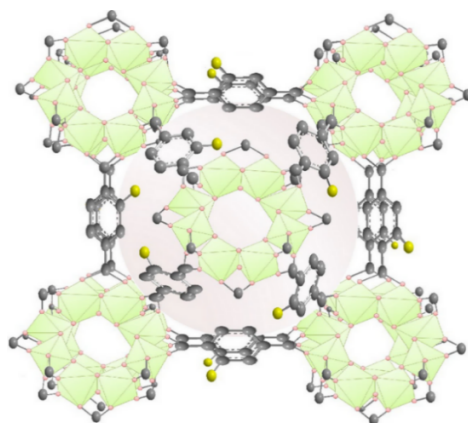
Figure 3.10. Crystal structure of MIL-125(Ti)_NH$_2$ (adapted from [40]). The color code is as follows: carbon – gray; oxygen – red; amina functional group (NH$_2$) – yellow; titanium (Ti) – green.

3.2 Gases

Oxygen (purity higher than 99.995%), nitrogen (purity higher than 99.995%), and carbon dioxide (purity higher than 99.998%) were used in the experiments. In the dynamic adsorption

experiments, MOFs were regenerated and activated by purging with helium (He) (purity higher than 99.999%). All gases were supplied by L'Air Liquide and were used without any pre-treatment.

3.3 Characterization of adsorbent materials

Material characterization is the first stage to predict the adsorption properties of porous materials. Surface and textural characterization of porous materials were obtained by using several methods, while thermal stability and composition were evaluated by thermogravimetric analysis (TGA).

3.3.1 Thermogravimetric analysis

TGA is a destructive technique where the weight variation of the material is monitored as a function of time or temperature in a given controlled atmosphere [41, 42]. The TGA curve represents a useful tool to obtain information regarding physical transitions and chemical reactions [43]. These phenomena result from a physical and chemical breakdown or formation of bonds along with the increase in the temperature [43].

The equipment Netzsch STA 409 PC Luxx (Figure 3.11) was used to perform TGA of the five selected adsorbents. Each analysis was carried out between 323 K and 1173 K at a heating rate of 10 K·min^{-1}. N$_2$ was used as carrying and protective gas with a flow rate of 50 mL·min^{-1}. Firstly, the system was calibrated, and then the crushed adsorbent was placed inside the crucible/sample holder (4), and the temperature was monitored by the thermostatic control (2).
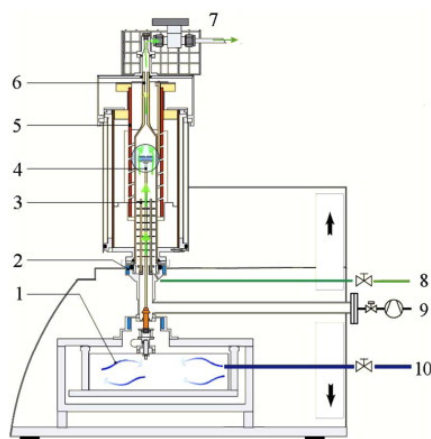
Figure 3.11. Scheme of the NETZSCH STA 409 PC Luxx® simultaneous thermal analyzer [44] (1: balance system, 2: thermostatic control, 3: radiation shield, 4: sample carrier, 5: heating element, 6: protective tube, 7: gas outlet, 8: purge gas inlet, 9: evacuating system, 10: protective gas inlet).

3.3.2 Characterization techniques

Helium picnometry is a technique used to determine the exact sample skeleton density of a given sample. In this work, it is of most importance for buoyancy correction, and consequent absolute adsorbed amount determination. Helium is the selected gas because it exhibits nearly ideal gas behavior; it is inert (does not adsorb), and presents a small atomic size. The measurements were realized at room temperature in an Isosorp Rubotherm® magnetic suspension microbalance (Figure 3.14).

Nitrogen adsorption at 77 K is the most widely used method to determine the specific surface area and pore size distribution of materials [45]. This technique is widely used to characterize the mesopores and micropores of porous materials [46, 47]. At low relative pressure, and after micropores are filled, the formation of monolayer takes place [46]. Multilayers start to form after complete creation of monolayer (relative pressure ~ 0.1), where the first adsorbed molecules act as active sites for the adsorption of the molecules of the following layer [46-49]. Brunauer–Emmett–Teller (BET) method followed the same assumptions of the Langmuir theory (Chapter 4) [48]. The N_2 adsorption equilibrium isotherms were measured in Micromeritics ASAP 2020 (V4.02) equipment at Departamento de Química Inorgánica of Malaga University (UMA). Prior to the determination of BET surface area, micropores size distribution, and micropores volume, the adsorbent samples were de-gasified at 423 K for 12 h under vacuum.

Carbon dioxide adsorption at 273 K is another useful technique to characterize porous solids in terms of the micropore surface area, micropore volume, and micropore size distribution [45]. Due to the higher adsorption temperature, comparatively with N_2 at 77 K, CO_2 molecules present higher kinetic energy allowing their access into the narrow pores [45]. CO_2 adsorption equilibrium isotherms were measured at Departamento de Química Inorgánica of UMA in a Micromeritics ASAP 2020 (V4.02) equipment at 273 K. The CO_2 adsorption measurements were done after degassing the sample at 423 K for 12 h under vacuum.

Mercury (Hg) intrusion porosimetry is a useful tool for porous material characterization. Pore size distribution, porosity, apparent particle density are some physical characteristics provided by this technique [50]. The method is reliable to minimum pore radius in a range of 50-100 Å and is more adequate for materials presenting larger pores (1000-10,000 Å) [49]. The gas present inside the sample is evacuated, and the mercury (a non-wetting liquid) is intruded into pores of the material at controlled pressure [51]. The pore size is inversely proportional to the pressure necessary to intrude the mercury into the pores, and the relationship is described through the Washburn equation (assuming cylindrical pores, with a circular opening in the cross-section) [52]

$$D = \frac{-4\gamma cos\theta}{P} \qquad\qquad (3.1)$$

where D is the diameter, P is the applied pressure, γ corresponds to surface tension, and θ is the contact angle.

Hg porosimetry analyses were performed to an aliquot of a fresh sample at Laboratório de Ensaios, Desgaste e Materiais (IPN - LED&MAT) on Micromeritics AutoPore IV 9500 (V1.07) equipment (MIL-125(Ti)_NH_2 sample) or at Departamento de Química Inorgánica of Malaga University (samples Al-Fum, CAU-10, MIL-160(Al) and MIL-100(Fe)), after degassing the sample at 423 K for 12 h under vacuum.

Scanning electron microscopy (SEM) is a versatile method for material and chemical composition characterization [53]. A high-energy (5–100 keV) and narrow electron beam scans pass across the sample under vacuum [54]. The interaction with the surface results in signs, which provide the formation of images [53, 54]. The most common signs are the backscattered electrons, secondary electrons (1–20 eV), and X-rays (Figure 3.12) [53, 54]. Each type of sign is related to a material region where it was detected and provide chemical and morphology

material information. Characteristic X-rays provide information related to material chemistry, whereas secondary electrons are useful, especially for topographic contrast, and backscattered electrons provide compositional and topographic information [53].
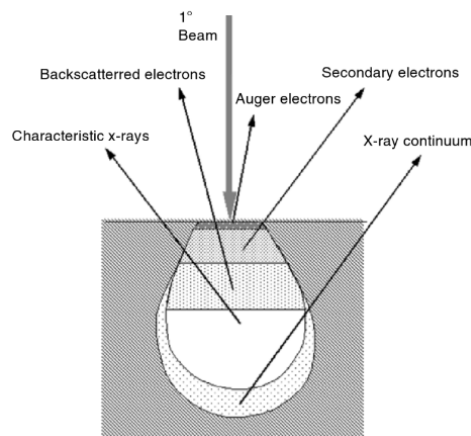
Figure 3.12. Electron beam interaction with a sample - types of signals generated [53].

Energy-dispersive X-ray analysis (EDX or EDS) is a technique coupled to SEM, Scanning Transmission Electron Microscopes (STEM), or Transmission Electron Microscopy (TEM) able to provide information about the elemental composition of the sample [55]. The electron beam on the surface and the penetration into the material result in characteristic X-ray emissions of excited specimens present or near to the sample surface [55, 56].

SEM/EDS analyses were carried out in Centro de Materiais da Universidade do Porto (UP-CEMUP) on FEI Quanta 400FEG ESEM/EDAX Genesis X4M instrument.

Mechanical strength is an important parameter to evaluate the mechanical properties of porous materials and subsequent applicability. Materials with low mechanical strength are not reliable to be used in harsher conditions [57]. Porosity, particle size and shape, and surface are some factors that affect the strength of particles [58, 59].

Particle crushing strength/hardness measurements were performed at Delft Solids Solutions B.V. with a Dr. Schleuniger type 5Y tablet hardness test that measures in a range of $1-400$ N.

X-ray diffraction is a non-destructive technique which identifies the crystallinity degree or amorphization [60, 61]. XRD is a powerful tool in polymorphs or quasi-isochemical compounds due to be impossible to use chemical characterization techniques in these materials

[62]. Crystallinity, structure imperfections, crystallite size, orientation, and strain, are some information possible to be determined by the XRD technique [55, 63, 64]. A monochromatic beam of X-rays (wavelength between 0.5 and 2 Å) is directed to the material resulting in diffracted X-rays (Figure 3.13) [55, 64]. X-rays diffraction pattern is described by Bragg's Law

$$n\lambda = 2d \times sin\theta \qquad (3.2)$$

where λ is the wavelength of the incident X-rays, d is the lattice spacing, n is the order of reflection, and θ is the angle of incidence.
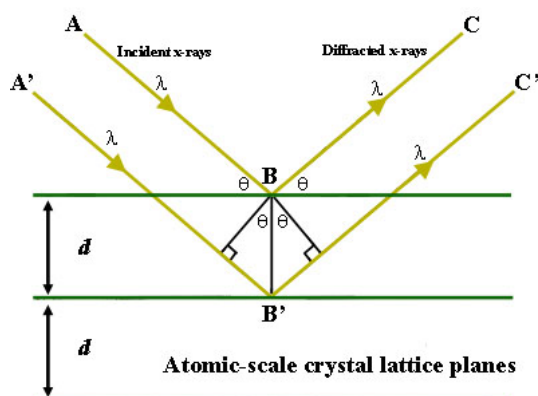
Figure 3.13. Diagram of X-rays diffraction and Bragg's law [65].

XRD patterns were performed at Laboratório Central de Análises (UA-LCA) by Empyrean equipment at Departamento de Química.

3.4 Adsorption equilibrium isotherms

The adsorption equilibrium isotherms of pure gases were performed in two different IsoSORP Rubotherm® magnetic suspension microbalances (MSB), both with a precision of 0.01 mg, and both operating in batch mode. The heating and cooling system is the main difference between them. In the MSB_1 (Figure 3.14a) it is used a jacket with fluid circulating through it to control the temperature, while in the MSB_2 (Figure 3.14b), the operating temperature is controlled by a cold gas cooling jacket (173 to 303 K) or an electrical heater (303 to 673 K).

E – Exhaust
P_1 to P_6 – Pressure transducers
RH – Relative humidity sensor
T – Thermostatic bath
TC – Thermocouple
V_1 to V_{11} – Valves
VP – Vacuum pump

1 – Electromagnet
2 – Permanent magnet
3 – Sensor core
4 – Sensor coils
5 – Measuring load coupling
6 – Basket
7 – Measuring cell
8 – Sinker
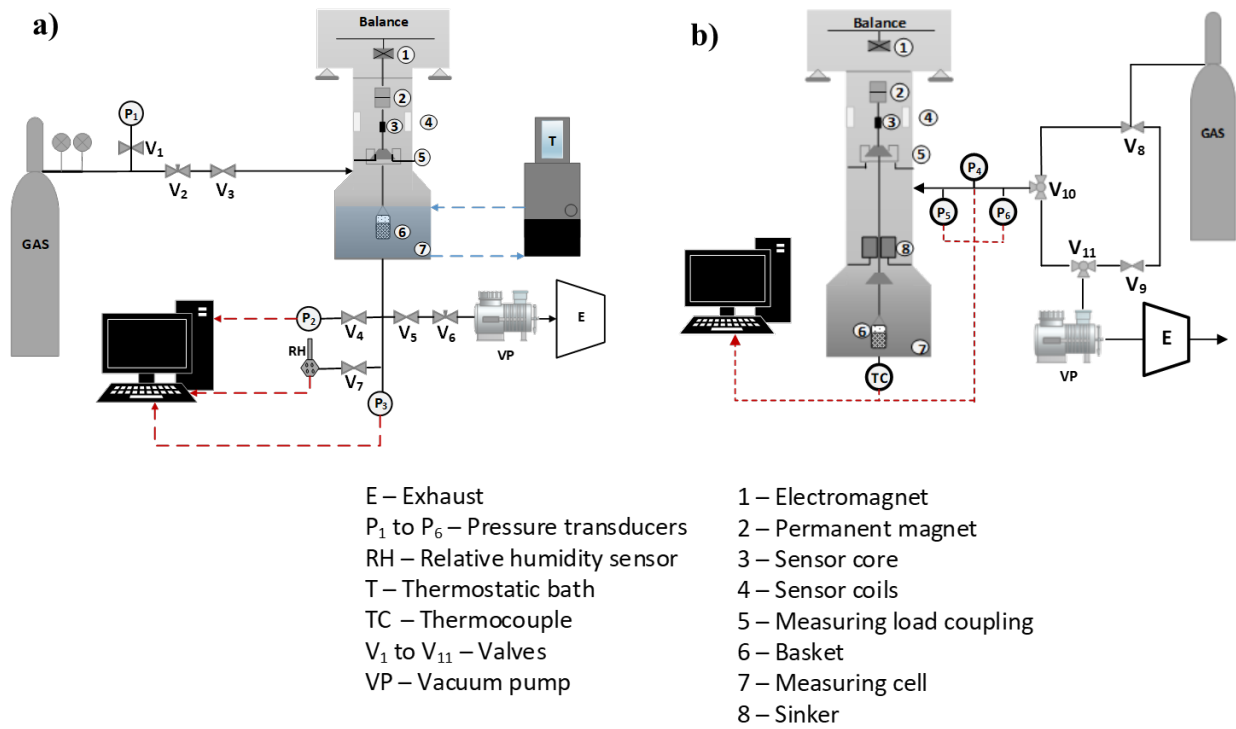
Figure 3.14. Schematic representation of the experimental setups for adsorption measurements (adapted from [66, 67]).

3.4.1 General description

The MSB$_1$ (Figure 3.14a) presents two different measuring positions enabled by two different vertical positions of the suspension magnet. The zero point position corresponds to the first position where the balance is tared and calibrated, using the value obtained for all subsequent measurements. In the second position, the electromagnet is energized, and the basket containing the sample is lifted and weighed.

The gas pressure inside the measuring cell is assessed employing two pressure transducers – P_2 and P_3 (General Electric, USA), with a range of 0 - 100 mbar, and 0 - 10 bar, respectively. While P_1 (General Electric, USA) operates between 0 - 350 mbar, and it assesses the pressure of the gas in the transfer line. The relative humidity and temperature are measured by a thermohygrometer (Testo, Germany) and a K-type thermocouple, respectively. Thermostatic bath (Huber K6, Germany) is connected to the jacketed cell of the microbalance, and temperature is controlled by fluid circulation inside it. The system is coupled to a vacuum pump (Alcatel Vacuum Technology, France), that allows regeneration of the sample, as well as

measuring adsorption equilibrium in the desorption branch. The data acquisition is carried out by LabVIEW software (Laboratory Virtual Instrument Engineering Workbench).

Unlike the MSB_1, MSB_2 (Figure 3.14b) has three different measuring positions. In the additional third position, an inert sinker is lifted along with the basket and the total masses are weighed. This procedure allows us to determine the density of the fluid phase in the adsorption chamber. The pressure is monitored by three pressures transducers located at the inlet of the balance, operating between 0 to 10 bar (P_6 – General Electric, USA), 0 to 200 bar (P_5 – General Electric, USA), and 0 to 100 mbar (P_4 – General Electric, USA) to measure low pressures. A thermocouple controls the temperature inside the balance. The vacuum pump (Edwards RV3, UK) has the same functionality as the vacuum pump in the MSB_1 set-up. A Rubotherm® software performs data acquisition.

3.4.2 Experimental procedure

For adsorption equilibrium measurements, first, the basket, metal hook and glass wool were weighted. The adsorbent and pre-weighted glass wool were placed in the basket. Then the basket was placed on the balance, suspended by an inert metal hook.

Prior to the adsorption measurements, each MOF sample was activated in situ at 423 K for 12 h under vacuum. Two helium pycnometry measurements were performed to the system, one with and other without adsorbent. Therefore, the determination of the exact dry mass of the sample and volume for the buoyancy correction was possible. The buoyancy force is the main inaccuracy in the gravimetric method, particularly significant for high pressures [68]. It is an upward force exerted by the bulk fluid in all suspension components of the balance lifted by the electromagnet but also affects the adsorbent and the adsorbate [68-70]. The absolute amount of gas adsorbed was calculated by the following equation [66],

$$q = \frac{\Delta m + \rho_G(V_S + V_C)}{m_S M_w} \frac{\rho_L}{\rho_L - \rho_G} \tag{3.3}$$

with Δm corresponding to the difference between the mass recorded by the MSB and the initial mass of the basket containing the activated sample and the glass wool; ρ_G is the density of the adsorbate gas at the measuring conditions (T, P); ρ_L is the density of the adsorbed phase, assuming that it is equal to the density of the liquid; V_S and V_c is the adsorbent volume and the

volume of the inert part (permanent magnet, basket, metal hook, and glass wool), respectively; m_S is the adsorbent mass, and M_w is the adsorbate molecular weight.

Gas was fed into the balance, contacting it with the adsorbent sample, aiming to achieve experimental points of adsorption equilibrium at different pressures. The equilibrium was reached when there was no variation in the pressure and mass with time ($<1x10^{-4}$ mg·s^{-1}). This procedure was repeated until reaching the highest desired pressure. Subsequently, the desorption branch of each adsorption equilibrium isotherm was obtained by depressurizing the balance's cell.

Water vapor adsorption equilibrium isotherms were conducted at different temperatures (283, 303, 323, and 343 K). The H$_2$O vapor was generated in a home-built vapor generator at room temperature and fed into the balance after degassing. Oxygen, nitrogen, and carbon dioxide adsorption equilibrium isotherms were performed at 283, 303 and 323 K, using high-purity gases as described above.

3.5 Dynamic experiments

3.5.1 General description

Adsorption breakthrough experiments were conducted on a bench-scale fixed-bed unit. Figure 3.15 illustrates the schematic representation of the experimental setup. The column pressure control was performed by a manual back pressure regulator (BPR, Swagelok Co., USA), and the column pressure was measured by a pressure transducer (PT, Swagelok Co., USA) placed at the exit of the column. Mass flow controllers (MFC$_1$ and MFC$_2$, Alicat Scientific Inc., USA) allowed controlling the inlet gas flow rates, while the total outlet gas flowrate was monitored by a mass flow meter (FM$_1$, Alicat Scientific, Inc., USA). The assessment of the relative humidity and temperature at the entrance and exit of the column was achieved by two Hygrotest 650 devices (HS$_1$ and HS$_2$, Testo AG, Germany). The temperature was also measured by one K-type thermocouple located in the middle of the column (T, Omega, USA). A Compact Digital Temperature Controller (TC, E5-CC, OMRON, Japan), connected to a heating rope (HR, Omega, UK), carried out the control of the column temperature. A home built bubbler (Neves & Neves Metalomecânica, Lda., Portugal) was employed to generate humidity transported by the entrance gas flow. The CO$_2$ concentration at the column outlet stream was measured by an

infra-red gas analyzer (Gas Data Ltd., UK). The unit is controlled by a LabVIEW based interface.
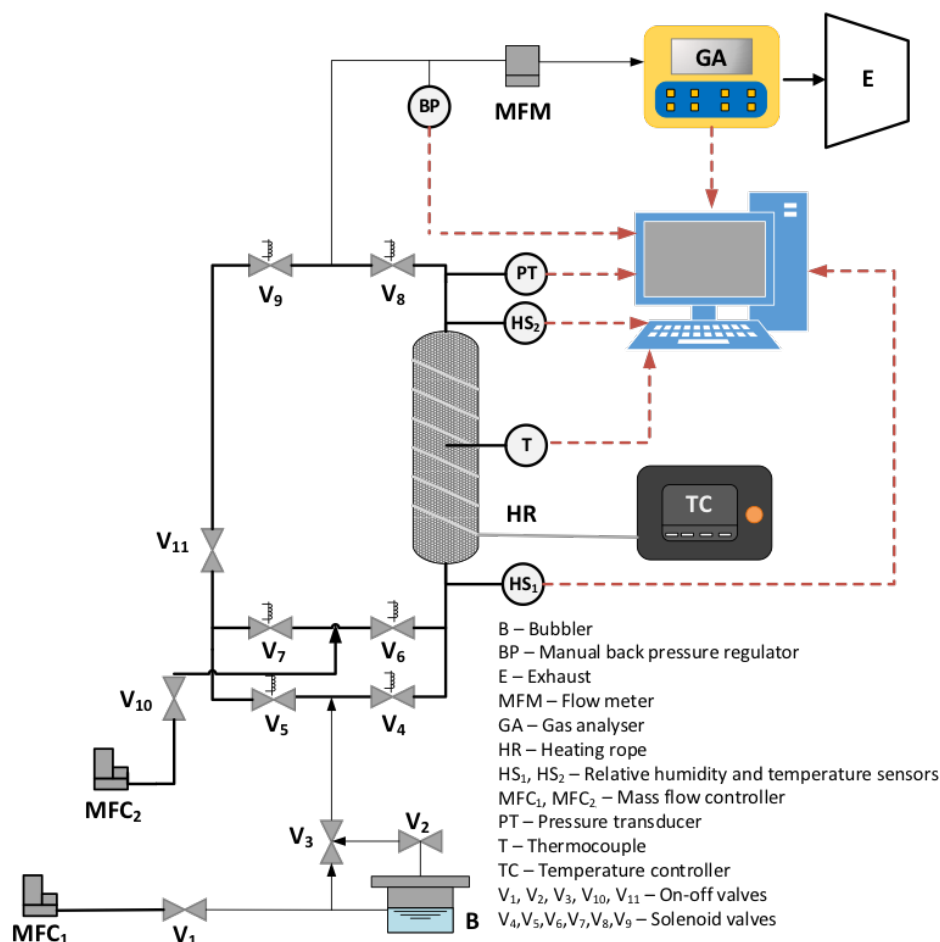
Figure 3.15. Scheme of the breakthrough experimental module in fixed bed column.
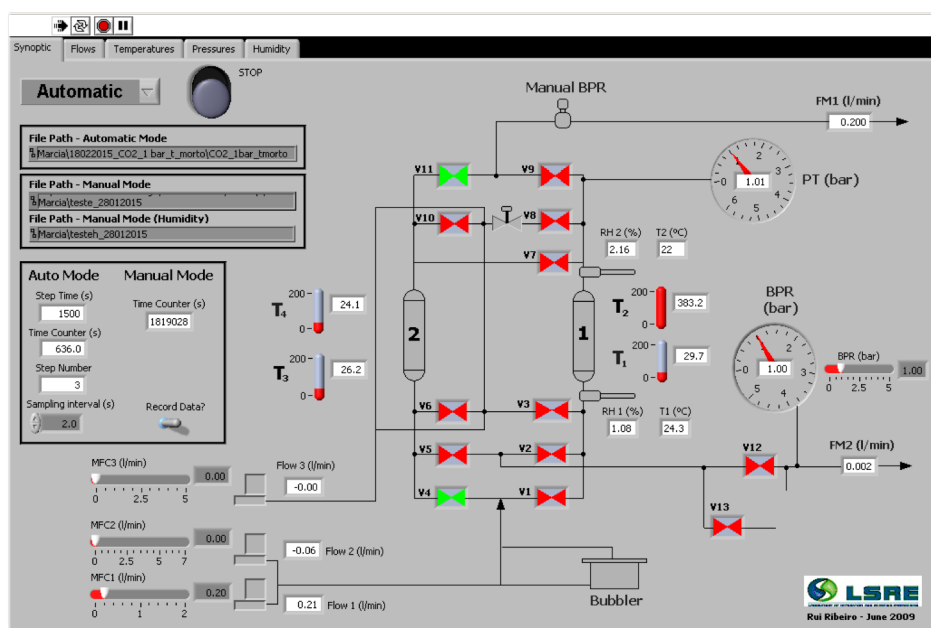
Figure 3.16. LabVIEW interface of the ESA unit control and data acquisition.

Different stainless-steel columns were packed with MOF's granules and both ends were capped with glass wool. Before the adsorption breakthrough experiments, the adsorbent was activated by heating up to 423 K under helium flow for 12 h.

3.5.2 Experimental procedure

The initial state of the column was fully regenerated and 0.2 SLPM of He flowing through it. The feed gas was obtained from the mixture of two individual gas streams, in which mass flow controllers controlled the flow rates. One gas stream consists of pure helium flow (0.1 SLPM) and the other stream consists of helium flow that passed previously through the bubbler, *i.e.*, saturated with water vapor (0.1 SLPM). The feed was switched to dry helium (0.2 SLPM) for desorption of the adsorbed water. The composition of the exit flow was analyzed during the adsorption and desorption by the gas analyzer (GA - Figure 3.15). This experimental protocol was repeated for CO_2 and N_2 saturated with water vapor.

A CO_2 breakthrough curve after adsorbent pre-saturation with water was also performed, *i.e.*, the adsorption bed is pre-saturated with a helium feed (0.2 SLPM) containing 50% RH, then pure helium gas stream (0.1 SLPM) was switched to a pure CO_2 stream (0.1 SLPM), maintaining constant the other helium stream saturated with water vapor (0.1 SLPM) passing through the water bubbler. This lead to a feed composition of 50% of CO_2 in helium, containing 50% of RH. Desorption followed the protocol mentioned previously.

3.6 Diffuse Reflectance Infrared Fourier Transform (DRIFT) spectra measurements

Diffuse Reflectance Infrared Fourier Transform (DRIFT) spectra were collected using a Nicolet 510-P FTIR spectrometer (Thermo Fisher Scientific, USA) equipped with a DiffusIR™ diffuse reflection accessory (PIKE Technologies, USA) and a chamber (DiffusIR environmental chamber, HTV, ambient to 500 °C, PIKE Technologies, USA). The temperature of the chamber was controlled using PIKE TempPRO software. Spectra were collected after 256 scans with a resolution of 4 cm^{-1} in the spectral range of 4000−400 cm^{-1}. The recorded absorbance values were transformed into the Kubelka-Munk units by OMNIC™ software. Figure 3.17 presents a scheme of the DRIFTS set-up. Additionally, Fourier transform infrared (FTIR) spectrum (4000–600 cm^{-1}) of MIL-160(Al) was acquired in a JASCO FT/IR-6800

spectrometer (JASCO Analytical Instruments, USA) equipped with a MIRacle™ Single Reflection ATR (attenuated total reflectance ZnSe crystal plate) accessory (PIKE Technologies, USA). The analyses were performed using 256 scans with a resolution of 4 cm^{-1}.

Prior to the collection of the DRIFT and FTIR spectra, adsorbent granules were grounded into a fine powder and pressed into the sample holder. The samples were analysed without any dilution. In a typical experiment, the sample was placed inside the chamber, which was then sealed and continuously purged with helium. Each sample was activated under He flow at 423 K for 3 h. Then, the sample was cooled to 298 K and a He flow saturated with water was passed over it. Infrared spectra were recorded periodically. The spectrum of pure He at ambient temperature (~ 298 K) was used as background. After that, MOF regeneration was performed by promoting water desorption at a controlled temperature ramp. In this case, the temperature inside the infrared chamber was increased at a rate of 10 K·min^{-1} to a determined value and a spectrum was measured after stabilizing the system for 15 min at each temperature plateau, when there is no change in the band intensities, implying that equilibrium has been reached.

In the He, CO_2 and He/CO_2 mixture experiments, a similar procedure of the experiments with saturated helium was adopted. He, CO_2 and He/CO_2 mixture saturated with water at ambient temperature were used as the background spectrum, respectively.
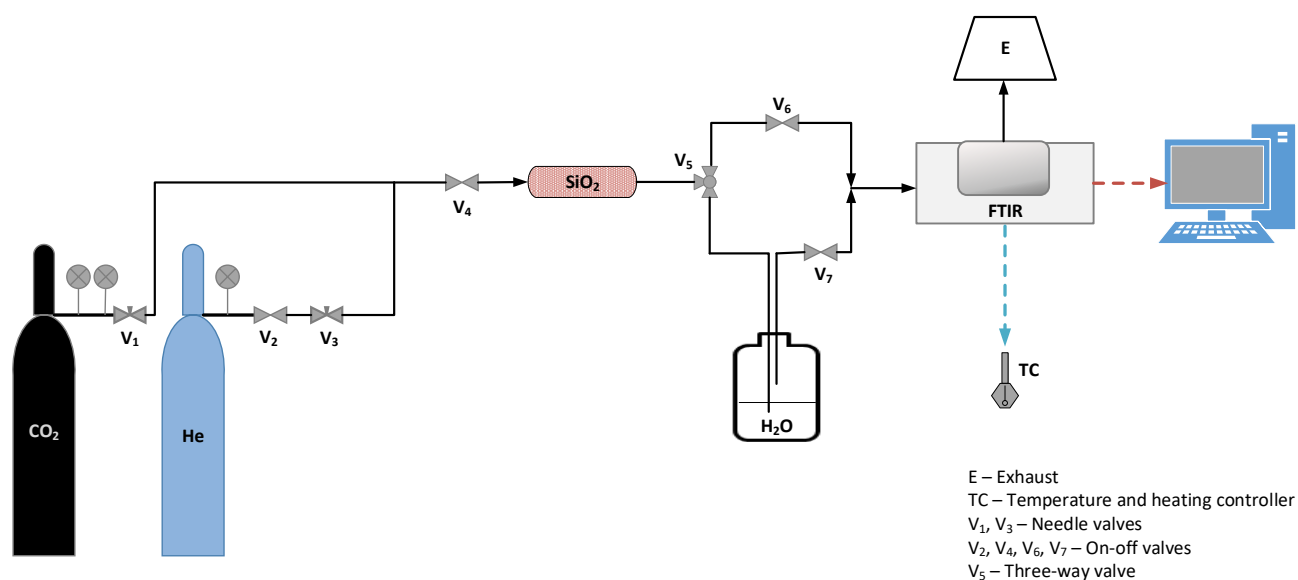
Figure 3.17. Schematic diagram of DRIFT measurements.

3.7 Adsorption bed regeneration with solar energy

The study of regeneration efficiency with solar energy was performed in a xenon test chamber (SOLARBOX 1500e, CO.FO.ME.GRA., Italy) (Figure 3.18). Different operating conditions for solar regeneration were tested. Regeneration of the adsorbent is necessary to strip the adsorbed water vapor, for its recovery. An efficient way of regenerating the adsorbent is by heating it using a gas stream or through a heat transfer surface (thermal method). The thermal regeneration of adsorbents usually is an energy-intensive process. Solar air heating systems have been recently proposed as a useful alternative for adsorbent regeneration, as mentioned before (Chapter 2) [71]. In arid regions with low humidity, there is an excellent availability of sunlight (>7 $kWh \cdot m^{-2} \cdot day^{-1}$, which are equivalent to 7 hours of 1 sun per day) [4]. The main advantage of the solar air heating system is that the necessary energy for the endothermic desorption process is provided by an inexhaustible natural resource (sun), which will lead to a significant reduction in energy costs. This process is similar to thermo-chemical heat storage systems, which utilize reversible exothermic/endothermic processes to store heat. In this case, the heat (promoted by solar irradiation) is used to enable the endothermic process (the desorption step [72]).

Static approache was studied, preceded by sample activation and column pressurization steps. In the experiments, both valves were closed. The temperature inside the column was recorded by K-type thermocouple along with the rise of irradiance (range between 250 to 950 $W \cdot m^2$). Sensor (S) measures the temperature inside the chamber. Equilibrium was attained when a constant temperature was recorded.
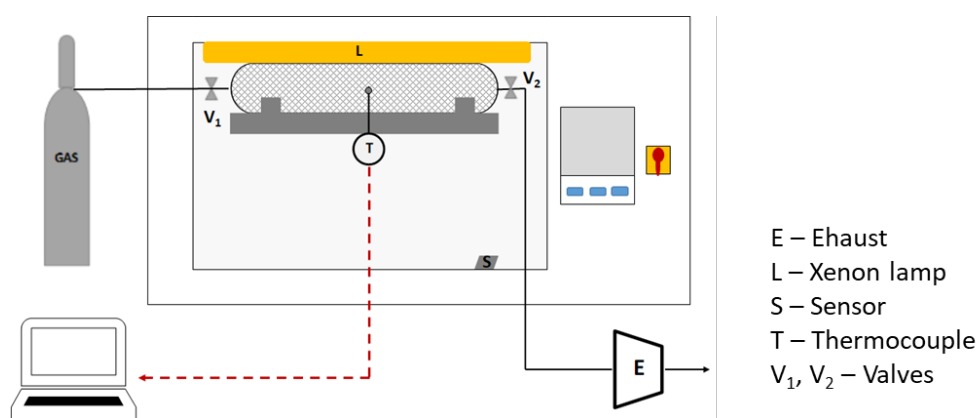
Figure 3.18. Schematic illustration of solar simulator.

References

1.   Weiss, A., N. Reimer, N. Stock, M. Tiemann, and T. Wagner, *Surface-modified CAU-10 MOF materials as humidity sensors: impedance spectroscopic study on water uptake.* Physical Chemistry Chemical Physics, 2015. **17**(33): p. 21634-21642.

2.   Borges, D.D., P. Normand, A. Permiakova, R. Babarao, N. Heymans, D.S. Galvao, C. Serre, G. De Weireld, and G. Maurin, *Gas Adsorption and Separation by the Al-Based Metal–Organic Framework MIL-160.* The Journal of Physical Chemistry C, 2017. **121**(48): p. 26822-26832.

3.   Elsayed, E., R. Al-Dadah, S. Mahmoud, P.A. Anderson, A. Elsayed, and P.G. Youssef, *CPO-27(Ni), aluminium fumarate and MIL-101(Cr) MOF materials for adsorption water desalination.* Desalination, 2017. **406**: p. 25-36.

4.   Kim, H., S. Yang, S.R. Rao, S. Narayanan, E.A. Kapustin, H. Furukawa, A.S. Umans, O.M. Yaghi, and E.N. Wang, *Water harvesting from air with metal-organic frameworks powered by natural sunlight.* Science, 2017. **356**(6336): p. 430-434.

5.   Hanikel, N., M.S. Prévot, F. Fathieh, E.A. Kapustin, H. Lyu, H. Wang, N.J. Diercks, T.G. Glover, and O.M. Yaghi, *Rapid Cycling and Exceptional Yield in a Metal-Organic Framework Water Harvester.* ACS Central Science, 2019.

6.   Elsayed, E., R. Al-Dadah, S. Mahmoud, A. Elsayed, and P.A. Anderson, *Aluminium fumarate and CPO-27(Ni) MOFs: Characterization and thermodynamic analysis for adsorption heat pump applications.* Applied Thermal Engineering, 2016. **99**: p. 802-812.

7.   Tannert, N., C. Jansen, S. Nießing, and C. Janiak, *Robust synthesis routes and porosity of the Al-based metal–organic frameworks Al-fumarate, CAU-10-H and MIL-160.* Dalton Transactions, 2019. **48**(9): p. 2967-2976.

8.   Cadiau, A., J.S. Lee, D. Damasceno Borges, P. Fabry, T. Devic, M.T. Wharmby, C. Martineau, D. Foucher, F. Taulelle, C.H. Jun, Y.K. Hwang, N. Stock, M.F. De Lange, F. Kapteijn, J. Gascon, G. Maurin, J.S. Chang, and C. Serre, *Design of hydrophilic metal*

organic framework water adsorbents for heat reallocation. Adv Mater, 2015. **27**(32): p. 4775-80.

9.   Gaab, M., N. Trukhan, S. Maurer, R. Gummaraju, and U. Müller, *The progression of Al-based metal-organic frameworks – From academic research to industrial production and applications.* Microporous and Mesoporous Materials, 2012. **157**: p. 131-136.

10.   Canioni, R., C. Roch-Marchal, F. Sécheresse, P. Horcajada, C. Serre, M. Hardi-Dan, G. Férey, J.-M. Grenèche, F. Lefebvre, J.-S. Chang, Y.-K. Hwang, O. Lebedev, S. Turner, and G. Van Tendeloo, *Stable polyoxometalate insertion within the mesoporous metal organic framework MIL-100(Fe).* Journal of Materials Chemistry, 2011. **21**(4): p. 1226-1233.

11.   Seo, Y.-K., J.W. Yoon, J.S. Lee, U.H. Lee, Y.K. Hwang, C.-H. Jun, P. Horcajada, C. Serre, and J.-S. Chang, *Large scale fluorine-free synthesis of hierarchically porous iron(III) trimesate MIL-100(Fe) with a zeolite MTN topology.* Microporous and Mesoporous Materials, 2012. **157**: p. 137-145.

12.   Jeremias, F., A. Khutia, S.K. Henninger, and C. Janiak, *MIL-100(Al, Fe) as water adsorbents for heat transformation purposes-a promising application.* Journal of Materials Chemistry, 2012. **22**(20): p. 10148-10151.

13.   Seo, Y.-K., J.W. Yoon, J.S. Lee, Y.K. Hwang, C.-H. Jun, J.-S. Chang, S. Wuttke, P. Bazin, A. Vimont, M. Daturi, S. Bourrelly, P.L. Llewellyn, P. Horcajada, C. Serre, and G. Férey, *Energy-Efficient Dehumidification over Hierachically Porous Metal–Organic Frameworks as Advanced Water Adsorbents.* Advanced Materials, 2012. **24**(6): p. 806-810.

14.   Küsgens, P., M. Rose, I. Senkovska, H. Fröde, A. Henschel, S. Siegle, and S. Kaskel, *Characterization of metal-organic frameworks by water adsorption.* Microporous and Mesoporous Materials, 2009. **120**(3): p. 325-330.

15. Feng, X., M. Qin, S. Cui, and C. Rode, *Metal-organic framework MIL-100(Fe) as a novel moisture buffer material for energy-efficient indoor humidity control.* Building and Environment, 2018. **145**: p. 234-242.

16. Cui, S., M. Qin, A. Marandi, V. Steggles, S. Wang, X. Feng, F. Nouar, and C. Serre, *Metal-Organic Frameworks as advanced moisture sorbents for energy-efficient high temperature cooling.* Scientific Reports, 2018. **8**(1): p. 15284.

17. Kim, S.-N., J. Kim, H.-Y. Kim, H.-Y. Cho, and W.-S. Ahn, *Adsorption/catalytic properties of MIL-125 and NH2-MIL-125.* Catalysis Today, 2013. **204**: p. 85-93.

18. Sohail, M., Y.N. Yun, E. Lee, S.K. Kim, K. Cho, J.N. Kim, T.W. Kim, J.H. Moon, and H. Kim, *Synthesis of Highly Crystalline NH2-MIL-125 (Ti) with S-Shaped Water Isotherms for Adsorption Heat Transformation.* Crystal Growth & Design, 2017. **17**(3): p. 1208-1213.

19. Sohail, M., H. Kim, and T.W. Kim, *Enhanced photocatalytic performance of a Ti-based metal-organic framework for hydrogen production: Hybridization with ZnCr-LDH nanosheets.* Scientific Reports, 2019. **9**(1): p. 7584.

20. Zhang, Y., Y. Chen, Y. Zhang, H. Cong, B. Fu, S. Wen, and S. Ruan, *A novel humidity sensor based on NH2-MIL-125(Ti) metal organic framework with high responsiveness.* Journal of Nanoparticle Research, 2013. **15**(10): p. 2014.

21. Vaesen, S., V. Guillerm, Q. Yang, A.D. Wiersum, B. Marszalek, B. Gil, A. Vimont, M. Daturi, T. Devic, P.L. Llewellyn, C. Serre, G. Maurin, and G. De Weireld, *A robust amino-functionalized titanium(iv) based MOF for improved separation of acid gases.* Chemical Communications, 2013. **49**(86): p. 10082-10084.

22. Wen, G. and Z.G. Guo, *Facile modification of NH2-MIL-125(Ti) to enhance water stability for efficient adsorptive removal of crystal violet from aqueous solution.* Colloids and Surfaces a-Physicochemical and Engineering Aspects, 2018. **541**: p. 58-67.

23.   Gordeeva, L.G., M.V. Solovyeva, and Y.I. Aristov, *NH2-MIL-125 as a promising material for adsorptive heat transformation and storage.* Energy, 2016. **100**(Supplement C): p. 18-24.

24.   Bozbiyik, B., J. Lannoeye, D.E. De Vos, G.V. Baron, and J.F.M. Denayer, *Shape selective properties of the Al-fumarate metal–organic framework in the adsorption and separation of n-alkanes, iso-alkanes, cyclo-alkanes and aromatic hydrocarbons.* Physical Chemistry Chemical Physics, 2016. **18**(4): p. 3294-3301.

25.   Splith, T., *Selbstdiffusion von Wasser in Schüttungen nanoporöser Kristalle für die adsorptive Wärmetransformation* in *Fakultät für Physik und Geowissenschaften.* 2018, Universität Leipzig.

26.   Alvarez, E., N. Guillou, C. Martineau, B. Bueken, B. Van de Voorde, C. Le Guillouzer, P. Fabry, F. Nouar, F. Taulelle, D. de Vos, J.-S. Chang, K.H. Cho, N. Ramsahye, T. Devic, M. Daturi, G. Maurin, and C. Serre, *The Structure of the Aluminum Fumarate Metal–Organic Framework A520.* Angewandte Chemie International Edition, 2015. **54**(12): p. 3664-3668.

27.   Leung, E., U. Müler, N. Trukhan, H. Mattenheimer, G. Cox, and S. Blei, *Process for preparation porous metal-organic frameworks based on aluminum fumarate*, in *BASF SF*. 2012. p. 9.

28.   Weiss, A., N. Reimer, N. Stock, M. Tiemann, and T. Wagner, *Screening of mixed-linker CAU-10 MOF materials for humidity sensing by impedance spectroscopy.* Microporous and Mesoporous Materials, 2016. **220**: p. 39-43.

29.   Borges, D.D., M. Guillaume , and D.S. Galvão, *Design of Porous Metal-Organic Frameworks for Adsorption Driven Thermal Batteries.* MRS Advances, 2017. **2**(9): p. 519–524.

30.   Reinsch, H., M.A. van der Veen, B. Gil, B. Marszalek, T. Verbiest, D. de Vos, and N. Stock, *Structures, Sorption Characteristics, and Nonlinear Optical Properties of a New Series of Highly Stable Aluminum MOFs.* Chemistry of Materials, 2013. **25**(1): p. 17-26.

31.   Permyakova, A., O. Skrylnyk, E. Courbon, M. Affram, S. Wang, U.H. Lee, A.H. Valekar, F. Nouar, G. Mouchaham, T. Devic, G. De Weireld, J.-S. Chang, N. Steunou, M. Frère, and C. Serre, *Synthesis optimization, shaping and heat reallocation evaluation of the hydrophilic Metal Organic Framework MIL-160(Al).* ChemSusChem, 2017: p. n/a-n/a.

32.   Yoon, J.W., Y.-K. Seo, Y.K. Hwang, J.-S. Chang, H. Leclerc, S. Wuttke, P. Bazin, A. Vimont, M. Daturi, E. Bloch, P.L. Llewellyn, C. Serre, P. Horcajada, J.-M. Grenèche, A.E. Rodrigues, and G. Férey, *Controlled Reducibility of a Metal–Organic Framework with Coordinatively Unsaturated Sites for Preferential Gas Sorption.* Angewandte Chemie International Edition, 2010. **49**(34): p. 5949-5952.

33.   Ribeiro, A.M., M.C. Campo, G. Narin, J.C. Santos, A. Ferreira, J.-S. Chang, Y.K. Hwang, Y.-K. Seo, U.H. Lee, J.M. Loureiro, and A.E. Rodrigues, *Pressure swing adsorption process for the separation of nitrogen and propylene with a MOF adsorbent MIL-100(Fe).* Separation and Purification Technology, 2013. **110**: p. 101-111.

34.   Horcajada, P., S. Surblé, C. Serre, D.-Y. Hong, Y.-K. Seo, J.-S. Chang, J.-M. Grenèche, I. Margiolaki, and G. Férey, *Synthesis and catalytic properties of MIL-100(Fe), an iron(iii) carboxylate with large pores.* Chemical Communications, 2007(27): p. 2820-2822.

35.   Qadir, N.U., S.A.M. Said, R.B. Mansour, K. Mezghani, and A. Ul-Hamid, *Synthesis, characterization, and water adsorption properties of a novel multi-walled carbon nanotube/MIL-100(Fe) composite.* Dalton Transactions, 2016. **45**(39): p. 15621-15633.

36.   Moreira, M.A., J.C. Santos, A.F.P. Ferreira, J.M. Loureiro, F. Ragon, P. Horcajada, P.G. Yot, C. Serre, and A.E. Rodrigues, *Effect of ethylbenzene in p-xylene selectivity of the porous titanium amino terephthalate MIL-125(Ti)_NH2.* Microporous and Mesoporous Materials, 2012. **158**: p. 229-234.

37.   Hu, S., M. Liu, K. Li, Y. Zuo, A. Zhang, C. Song, G. Zhang, and X. Guo, *Solvothermal synthesis of NH2-MIL-125(Ti) from circular plate to octahedron.* CrystEngComm, 2014. **16**: p. 9645–9650

38. Zhang, Y., Y. Chen, Y. Zhang, H. Cong, B. Fu, S. Wen, and S. Ruan, *A novel humidity sensor based on NH2-MIL-125(Ti) metal organic framework with high responsiveness.* Journal of Nanoparticle Research, 2013. **15**(10): p. 1-6.

39. Regufe, M.J., J. Tamajon, A.M. Ribeiro, A. Ferreira, U.H. Lee, Y.K. Hwang, J.-S. Chang, C. Serre, J.M. Loureiro, and A.E. Rodrigues, *Syngas Purification by Porous Amino-Functionalized Titanium Terephthalate MIL-125.* Energy & Fuels, 2015. **29**(7): p. 4654-4664.

40. Oveisi, M., M.A. Asli, and N.M. Mahmoodi, *MIL-Ti metal-organic frameworks (MOFs) nanomaterials as superior adsorbents: Synthesis and ultrasound-aided dye adsorption from multicomponent wastewater systems.* Journal of Hazardous Materials, 2018. **347**: p. 123-140.

41. Groenewoud, W.M., *CHAPTER 2 - THERMOGRAVIMETRY*, in *Characterisation of Polymers by Thermal Analysis*, W.M. Groenewoud, Editor. 2001, Elsevier Science B.V.: Amsterdam. p. 61-76.

42. Wunderlich, B., *Thermal Analysis*, in *Encyclopedia of Materials: Science and Technology*, K.H.J. Buschow, R.W. Cahn, M.C. Flemings, B. Ilschner, E.J. Kramer, S. Mahajan, and P. Veyssière, Editors. 2001, Elsevier: Oxford. p. 9134-9141.

43. McMillan, J., W. Adney, J. Mielenz, and K. Klasson, *Twenty-Seventh Symposium on Biotechnology for Fuels and Chemicals*. 2006: Humana Press Inc.

44. Zhaosheng, Y., M. Xiaoqian, and L. Ao, *Thermogravimetric analysis of rice and wheat straw catalytic combustion in air- and oxygen-enriched atmospheres.* Energy Conversion and Management, 2009. **50**(3): p. 561-566.

45. Lozano-Castelló, D., D. Cazorla-Amorós, and A. Linares-Solano, *Usefulness of CO2 adsorption at 273 K for the characterization of porous carbons.* Carbon, 2004. **42**(7): p. 1233-1242.

46. Zelenka, T., *Adsorption and desorption of nitrogen at 77 K on micro- and meso-porous materials: Study of transport kinetics.* Microporous and Mesoporous Materials, 2016. **227**: p. 202-209.

47. Sing, K., *The use of nitrogen adsorption for the characterisation of porous materials.* Colloids and Surfaces A: Physicochemical and Engineering Aspects, 2001. **187-188**: p. 3-9.

48. Do, D.D., *Adsorption Analysis: Equilibria and Kinetics.* Adsorption Analysis: Equilibria and Kinetics. 1998, Imperial College Press.

49. Ruthven, D.M., *Principles of adsorption and adsorption processes.* 1984, New York (USA): John Wiley and Sons, Inc.

50. Giesche, H., *Mercury Porosimetry: A General (Practical) Overview.* Particle & Particle Systems Characterization, 2006. **23**(1): p. 9-19.

51. Thomas, W.J. and B. Crittenden, *2 - Adsorbents*, in *Adsorption Technology & Design*, W.J. Thomas and B. Crittenden, Editors. 1998, Butterworth-Heinemann: Oxford. p. 8-30.

52. Webb, P., *An Introduction To The Physical Characterization of Materials by Mercury Intrusion Porosimetry with Emphasis On Reduction And Presentation of Experimental Data* Pharm Online, 2001.

53. Zhou, W. and Z.L. Wang, *Scanning Microscopy for Nanotechnology. Techniques and Applications.* 2007, New York, United States: Springer. 536.

54. Ratner, B.D., *Chapter I.1.5 - Surface Properties and Surface Characterization of Biomaterials*, in *Biomaterials Science (Third Edition)*, B.D. Ratner, A.S. Hoffman, F.J. Schoen, and J.E. Lemons, Editors. 2013, Academic Press. p. 34-55.

55. Welker, R.W., *Developments in Surface Contamination and Cleaning.* Detection, Characterization, and Analysis of Contaminants, ed. R. Kohli and K.L. Mittal. Vol. 4. 2011: Elsevier.

56.   Neikov, O.D. and N.A. Yefimov, *Chapter 1 - Powder Characterization and Testing*, in *Handbook of Non-Ferrous Metal Powders (Second Edition)*, O.D. Neikov, S.S. Naboychenko, and N.A. Yefimov, Editors. 2019, Elsevier: Oxford. p. 3-62.

57.   Ishizaki, K., S. Komarneni, and M. Nanko, *Porous Materials: Process technology and applications*. Materials Technology Series. Vol. 4. Springer US. 240.

58.   Pitchumani, R., O. Zhupanska, G.M.H. Meesters, and B. Scarlett, *Measurement and characterization of particle strength using a new robotic compression tester.* Powder Technology, 2004. **143-144**: p. 56-64.

59.   Meesters, G. *How to quantify particle strength - Wear and Breakage.* [cited 2019 07 october]; Available from: https://www.solids-solutions.com/uploads/paginas/P&G%20%208%20-%20Particle%20strength.pdf.

60.   da Silva Júnior, W.F., J.G. de Oliveira Pinheiro, C.D.L.F.A. Moreira, F.J.J. de Souza, and Á.A.N. de Lima, *Chapter 15 - Alternative Technologies to Improve Solubility and Stability of Poorly Water-Soluble Drugs*, in *Multifunctional Systems for Combined Delivery, Biosensing and Diagnostics*, A.M. Grumezescu, Editor. 2017, Elsevier. p. 281-305.

61.   Ahmed, S., M.A. Sheraz, and I. Ahmad, *Chapter Three - Tolfenamic Acid*, in *Profiles of Drug Substances, Excipients and Related Methodology*, H.G. Brittain, Editor. 2018, Academic Press. p. 255-319.

62.   Artioli, G., *X-Ray Diffraction, Studies of Inorganic Compounds and Minerals*, in *Encyclopedia of Spectroscopy and Spectrometry (Third Edition)*, J.C. Lindon, G.E. Tranter, and D.W. Koppenaal, Editors. 2017, Academic Press: Oxford. p. 676-683.

63.   Louër, D., *Powder X-Ray Diffraction, Applications*, in *Encyclopedia of Spectroscopy and Spectrometry*, J.C. Lindon, Editor. 1999, Elsevier: Oxford. p. 1865-1875.

64.   Prelas, M.A., G. Popovici, and L.K. Bigelow, *Handbook of industrial diamonds and diamond films*. 1998, New York: Marcel Dekker.

65.   Henry, D., N. Eby, J. Goodge, and D. Mogk. *X-ray reflection in accordance with Bragg's Law.*   [cited   2019   7   october];   Available   from: https://serc.carleton.edu/research_education/geochemsheets/BraggsLaw.html.

66.   Moreira, M.A., A.M. Ribeiro, A.F.P. Ferreira, and A.E. Rodrigues, *Cryogenic pressure temperature swing adsorption process for natural gas upgrade.* Separation and Purification Technology, 2017. **173**: p. 339-356.

67.   Rubotherm, *Magnetic suspension balances.* Rubotherm.

68.   Nguyen, H.G.T., J.C. Horn, M. Thommes, R.D. van Zee, and L. Espinal, *Experimental aspects of buoyancy correction in measuring reliable high-pressure excess adsorption isotherms using the gravimetric method.* Measurement Science and Technology, 2017 **28**(12).

69.   Rouquerol, J., F. Rouquerol, P. Llewellyn, and R. Denoyel, *Surface excess amounts in high-pressure gas adsorption: Issues and benefits.* Colloids and Surfaces A: Physicochemical and Engineering Aspects, 2016. **496**: p. 3-12.

70.   Ratnakar, R.R. and B. Dindoruk, *Adsorption Isotherms and Permeability of Tight Shales Using Magnetic Suspension Balance Experiments*, in *SPE Annual Technical Conference and Exhibition*. 2018, Society of Petroleum Engineers: Dallas, Texas, USA. p. 23.

71.   Khuzhakulov, S.M., G.N. Uzakov, and A.B. Vardiyashvili, *Effectiveness of solar heating systems for the regeneration of adsorbents in recessed fruit and vegetable storages.* Applied Solar Energy, 2013. **49**(4): p. 257-260.

72.   Dicaire, D. and F.H. Tezel, *Use of adsorbents for thermal energy storage of solar or excess heat: improvement of energy density.* International Journal of Energy Research, 2013. **37**(9): p. 1059-1068.

4 MATHEMATICAL MODEL

4.1 Adsorption equilibrium models

Adsorption equilibrium isotherms were regressed against adsorption equilibrium isotherm models to correlate adsorbed amount data with meaningful thermodynamic models that can be introduced in the process models. Several equilibrium isotherm models used to model adsorption equilibrium (kinetic and/or thermodynamic) of gases are presented in the literature. They can be based on empirical or experimental data, and on thermodynamic and kinetic reasoning [1, 2]. Several equilibrium isotherm models can be used to fit experimental equilibrium data.

The Langmuir model, the Cooperative Multi-Molecular Sorption (CMMS) equations, the Dual Ising-Single Langmuir (DISL) model, and the Polanyi's potential theory, were the selected equilibrium isotherm models to fit experimental equilibrium data.

4.1.1 Langmuir model

The Langmuir model is a theoretical model for monolayer adsorption with a fixed number of identical adsorption sites on the adsorbent surface [2, 3]. This model reconciles the pressure of the gas with the amount of gas adsorbed [3]. The Langmuir model assumes that one site on the adsorbent surface can accommodate one adsorbate molecule, all adsorption sites on the surface are energetically identical and constant, and adsorbate molecules are adsorbed in localized surface sites and does not exist interaction between neighboring adsorbed molecules [2-4]. Langmuir model can be expressed as follows:

$$q = q_m \frac{KP}{1+KP} \tag{4.1}$$

where q is the adsorbed amount on the adsorbent, q_m is the saturation adsorption capacity, P is the pressure, and K is the adsorption equilibrium constant.

The van't Hoff law expresses the temperature dependence of the Langmuir adsorption equilibrium constant (K):

$$K = K_\infty e^{\left(\frac{-\Delta H}{R_g T}\right)} \tag{4.2}$$

with K_∞ corresponding to a constant containing the entropy term at infinite temperature, $-\Delta H$ is the heat of adsorption, R_g is the ideal gas constant (8.314 J·mol⁻¹·K⁻¹), and T is the absolute temperature of the system.

4.1.2 CMMS model

The CMMS model accounts for both water physisorption (Langmuir) and the interaction between adsorbed water and other water molecules that leads to the formation of water clusters (Ising) [5, 6]. Indeed, its mathematical expression results from the combination of each independent model to represent the two sites of water adsorption [5, 7, 8].

$$q = q_{sat\,I}\frac{K_o\,P}{(K_o\,P + w_I^2)} + q_{sat\,L}\frac{K_L\,P}{(1 + K_L\,P)} \tag{4.3}$$

where

$$w_I = \frac{1}{2}\left(1 - K_I\,P + \sqrt{(1 - K_I\,P)^2 + 4K_o\,P}\right) \tag{4.4}$$

and

$$K_I = K_{\infty,I}\,e^{\left(\frac{-\Delta H_I}{R_g T}\right)} \tag{4.5}$$

$$K_o = K_{\infty,o}\,e^{\left(\frac{-\Delta H_0}{R_g T}\right)} \tag{4.6}$$

$$K_L = K_{\infty,L}\,e^{\left(\frac{-\Delta H_L}{R_g T}\right)} \tag{4.7}$$

where q is the total adsorbed amount, $q_{sat\,I}$ is the specific saturation adsorption capacity in Ising isotherm, $q_{sat\,L}$ is the specific saturation adsorption capacity in Langmuir isotherm, and $K_{\infty,o}$, $K_{\infty,L}$, $K_{\infty,I}$ are the equilibrium constants of Langmuir-Ising isotherm, and their temperature dependence is given by the van't Hoff law.

4.1.3 DISL model

The DISL model results from the junction of the independent Langmuir model with two sites equally well represented by the Ising model and is an extension of the CMMS model (Equation

4.3). The water cluster formation (Ising) occurs in the two different cavities of MIL-100(Fe), as presented in Chapter 3 (Figure 3.8). The model is described by equation 4.8:

$$q = q_{sat\,L}\frac{K_L\,P}{(1+K_L\,P)} + \sum_{i=A,B} q_{sat\,I,i}\frac{K_{o,i}\,P}{(K_{o,i}\,P+w_{I,i}^2)} \tag{4.8}$$

where A and B correspond to each one of the MIL-100(Fe) cages.

4.1.4 Polanyi´s potential theory

Polanyi's potential theory suggests the presence of a surface force field, leading to equipotential surfaces defining the specific volume of gas adsorbed [2, 9-11]. The adsorption potential (ε) is independent of temperature, resulting in an adsorption characteristic curve [10, 11].

Adsorption potential is defined in terms of one mole of perfect gas as [9, 12, 13]:

$$\varepsilon = \int_P^{Po} v\,dP = R_g T \ln\left(\frac{P_o}{P}\right) \tag{4.9}$$

where P_0 is the saturation vapor pressure and v is the volume.

4.2 Isosteric heats of adsorption

The isosteric heat of adsorption ($Q_{iso} = -\Delta H_{iso}$) corresponds to the released energy in adsorption [2, 13, 14]. Isosteric heat of adsorption at zero loading is a measure of the binding energy of the most energetically favorable binding site on the adsorbent surface. The isosteric heat of adsorption is determined by applying the Clausius-Clapeyron equation:

$$Q_{iso} = -\Delta H_{iso} = R_g T^2 \left(\frac{\partial \ln P}{\partial T}\right)_q \tag{4.10}$$

Neglecting the temperature dependence of the isosteric heat of adsorption, integration of the above gives,

$$\ln P = -\frac{-\Delta H}{R}\frac{1}{T} + A \tag{4.11}$$

where A is the integration constant.

4.3 Fixed-bed adsorption model

A phenomenological model was developed to describe the dynamic adsorption behavior in the adsorber, packed with the shaped adsorbent. The fixed-bed presents three phases (Figure 4.1):

i.   the gas phase, energy exchange with column wall and gas phase, and mass exchange with solid phase;

ii.   the solid phase, the phase where occurs adsorption and diffusion;

iii.   the column wall, energy may be transferred to (or from) the surroundings.
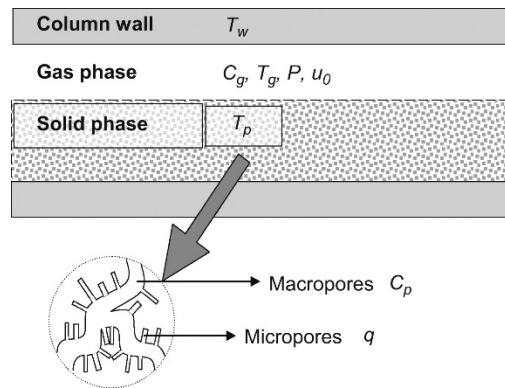
Figure 4.1. Adsorption bed schema: column wall, gas phase, and solid phase (macropores and micropores) [15].

The model includes mass, energy, and momentum balances. The main assumptions taken in consideration were: (i) ideal gas behavior for the fluid phase; (ii) no radial gradients (mass, heat, velocity); (iii) the film model was considered to describe external mass and heat transfer; (iv) the bi-disperse nature of the adsorbent was taken into consideration, and the internal mass transfer resistances were described by bi-linear driving force (Bi-LDF), with diffusion in macropores and micropores; (v) the temperature is homogeneous inside each particle (the heat transfer in solid particles is higher than in the gas phase); (vi) the Ergun equation is valid locally, and (vii) constant porosity. The model was validated against the bench-scale breakthrough experimental results. The model was solved in gPROMS® (PSE, UK) with the axial domain discretized using the second-order orthogonal collocation on 200 finite elements as the numerical method.

4.3.1 Mass, Energy and Momentum balances

The **material balance** in the gas phase for each component is defined as,

$$\frac{\partial}{\partial z}\left(\varepsilon D_{ax} C_{g,T} \frac{\partial y_i}{\partial z}\right) - \frac{\partial}{\partial z}\left(u_0 C_{g,i}\right) - \varepsilon \frac{\partial C_{g,i}}{\partial t} - (1-\varepsilon) a_p k_f \left(C_{g,i} - \overline{C_{p,i}}\right) = 0 \tag{4.12}$$

where z is the axial position inside adsorption bed, ε is the bed porosity, D_{ax} is the mass axial dispersion coefficient, $C_{g,T}$ and $C_{g,i}$ correspond to the total and component i gas phase concentration, respectively, y_i is the molar fraction of component i, u_0 is the superficial gas velocity, t is the time, a_p is the particle external specific area, k_f is the film mass transfer coefficient, and $\overline{C_{p,i}}$ is the average of the particle concentration of component i in the macropores.

The mass transfer in particle macropores is described by the Linear Drive Force (LDF) in the following mass balance,

$$\frac{\partial \overline{C_{p,i}}}{\partial t} = \frac{\Omega_p D_{p,i} Bi_i}{R_p^2 (1 + Bi_i)} \left(C_{g,i} - \overline{C_{p,i}}\right) - \frac{\rho_p}{\varepsilon_p} \frac{\partial \overline{q_i}}{\partial t} \tag{4.13}$$

while micropore mass transfer is expressed as,

$$\frac{\partial \overline{q_i}}{\partial t} = \frac{\Omega_c D_{c,i}}{r_c^2} \left(q_i^* - \overline{q_i}\right) \tag{4.14}$$

where Ω_p and Ω_c are the LDF factor for macropores and micropores, respectively, $D_{p,i}$ and $D_{c,i}$ are respectively the macropore and micropore diffusivity coefficient, Bi_i is the mass transfer Biot number, R_p is the particle radius, ρ_p is the particle density, ε_p is the particle porosity, $\overline{q_i}$ is the average adsorbed phase concentration of component i, r_c is the crystal radius, and q_i^* is the adsorbed concentration of component i in equilibrium with $\overline{C_{p,i}}$.

The **momentum balance** is described by Ergun's Equation, considering only the pressure drop and velocity change, as defined by the following equation,

$$-\frac{\partial P}{\partial z} = 150 \frac{\mu (1-\varepsilon)^2}{\varepsilon^3 d_p^2} u_0 + 1.75 \frac{(1-\varepsilon)\rho_g}{\varepsilon^3 d_p} |u_0| u_0 \tag{4.15}$$

where μ is the bulk gas mixture viscosity, d_p is the particle diameter, and ρ_g is the gas density.

The **energy balance** in the gas phase is defined as,

$$\frac{\partial}{\partial z}\left(\lambda \frac{\partial T_g}{\partial z}\right) - u_0 C_{g,T} C_p \frac{\partial T_g}{\partial z} + \varepsilon R_g T_g \frac{\partial C_{g,T}}{\partial t} - (1-\varepsilon)a_p h_f\left(T_g - T_p\right) - \frac{4h_w}{d_{wi}}\left(T_g - T_w\right) -$$

$$\varepsilon C_{g,T} \tilde{C}_v \frac{\partial T_g}{\partial t} = 0 \tag{4.16}$$

where T_g, T_p, and T_w are respectively the gas, the particle, and the wall temperature, λ is the heat axial dispersion coefficient, C_p is the gas mixture molar specific heat at constant pressure, $\tilde{C}_v$ is the molar heat capacities of the gas at constant volume, R_g is the ideal gas constant, h_f is the film heat transfer coefficient between the gas and particle, while h_w correspond to the film heat transfer coefficient between the gas and the wall, and d_{wi} is the wall internal diameter.

In the solid phase, no temperature gradient inside the particle is considered, and the following equation gives the energy balance,

$$(1-\varepsilon)\left[\varepsilon_p \sum_{i=1}^n \overline{C_{p,i}}\, C_{v,i} + \rho_p \sum_{i=1}^n \overline{q_i} C_{v,ads,i} + \rho_p \hat{C}_{ps}\right]\frac{\partial T_p}{\partial t} = (1-\varepsilon)\varepsilon_p R_g T_p \frac{\partial \overline{C_{p,T}}}{\partial t} +$$

$$\rho_b \left[\sum_{i=1}^n \left(-\Delta H_{iso,i}\right)\frac{\partial \overline{q_i}}{\partial t}\right] + (1-\varepsilon)a_p h_f\left(T_g - T_p\right) \tag{4.17}$$

with $C_{v,i}$ corresponding to the molar specific heat at constant volume of the component i, while $C_{v,ads,i}$ is the molar specific heat at constant volume of the component i in the adsorbed phase, $\hat{C}_{ps}$ is the adsorbent specific heat per mass unit at constant pressure, $\overline{C_{p,T}}$ is the average total concentration, and ρ_b is the bulk density of the bed.

The energy balance equation to the bed wall is described as,

$$\rho_w \hat{C}_{p,w} \frac{\partial T_w}{\partial t} = \alpha_w h_w\left(T_g - T_w\right) - \alpha_{w\ell} U(T_w - T_\infty) \tag{4.18}$$

where ρ_w is the column wall density, $\hat{C}_{p,w}$ is the column wall specific heat per mass unit at constant pressure, U is the overall heat transfer coefficient, T_∞ is the ambient temperature, and α_w is the ratio of the internal surface area to the column wall volume, while $\alpha_{w\ell}$ is the ratio of the logarithmic mean surface to the column wall volume.

4.3.2 Transport parameters and physical bed properties

The transport parameter values and physical bed properties required in the mathematical model can be determined through the following expressions.

α_w and $\alpha_{w\ell}$ are defined as

$$\alpha_w = \frac{D_w}{e(D_w+e)} \tag{4.19}$$

and

$$\alpha_{w\ell} = \frac{1}{(D_w+e)\ln\left(\frac{D_w+e}{D_w}\right)} \tag{4.20}$$

where D_w is the bed diameter, and e is the thickness of the shell.

The **pore diffusivity** $(D_{p,i})$ can be determined by the following equation,

$$\frac{1}{D_{p,i}} = \tau_p\left(\frac{1}{D_{m,i}} + \frac{1}{D_{k,i}}\right) \tag{4.21}$$

where τ_p is the pore tortuosity, $D_{m,i}$ is the molecular bulk diffusion coefficient of component i within the gas mixture, and $D_{k,i}$ is the Knudsen diffusivity of component i.

The molecular diffusivity for the mixture is given by,

$$D_{m,i} = \frac{1-y_i}{\sum_{\substack{j=1 \\ j\neq i}}^{n}\frac{y_j}{D_{m,ij}}} \tag{4.22}$$

where y_j is the molar fraction of the component j and $D_{m,ij}$ is the binary molecular diffusivity, that can be estimated from:

$$D_{m,ij} = 0.01881\frac{T^{1.5}\left(\frac{1}{M_i}+\frac{1}{M_j}\right)^{0.5}}{P\sigma_{ij}^2\Omega_{\mathrm{D}}} \tag{4.23}$$

where Mi and M_j are the molecular weights of components i and j, respectively. The characteristic Lennard-Jones length for ij interaction (σ_{ij}) can be calculated from the individual Lennard-Jones parameters by a simple mixing rule,

$$\sigma_{ij} = \frac{\sigma_i + \sigma_j}{2} \tag{4.24}$$

and the collision integral for diffusion (Ω_D) can be calculated from the following empirical relation [16]

$$\Omega_D = 1.06036 T^{*-0.1561} + 0.193 e^{-0.47635 T^*} + 1.03587 e^{-1.52996 T^*} + 1.76474 e^{-3.89411 T^*} \tag{4.25}$$

with

$$T^* = \frac{kT}{\epsilon_{ij}} \tag{4.26}$$

where k is Boltzmann's constant and

$$\epsilon_{ij} = \sqrt{\epsilon_i \epsilon_j} \tag{4.27}$$

with ϵ_i and ϵ_j are the Lennard-Jones characteristic energy of components i and j, respectively.

For estimating Knudsen diffusivity of component i ($D_{k,i}$), the following equation can be used,

$$D_{k,i} = 9.7 \cdot 10^{-9} R_p \sqrt{\frac{T}{M_i}} \tag{4.28}$$

Wakao and Funazkri [17] proposed the following correlation to calculate the **mass axial dispersion coefficient** (D_{ax}) in the limiting case of a porous bed with a rectangular isotherm:

$$\frac{\varepsilon D_{ax}}{D_m} = 20 + 0.5 Sc Re \tag{4.29}$$

where D_m is the molecular diffusivity, Sc and Re correspond respectively to the Schmidt and Reynolds numbers and can be given by the following equations:

$$Sc = \frac{\mu}{\rho_g D_m} \tag{4.30}$$

$$Re = \frac{\rho_g u_o D_h}{\mu} \tag{4.31}$$

where D_h is the hydraulic diameter, which is defined as,

$$D_h = \frac{6V_p}{S_p} \tag{4.32}$$

where V_p is the particle volume, and S_p is the particle's external surface area.

The viscosity of the gas mixture can be calculated from the method of Wilke [18],

$$\mu = \sum_{i=1}^{n} \frac{y_i \mu_i}{\sum_{j=1}^{n} y_i \phi_{ij}} \tag{4.33}$$

where Wilke's ϕ_{ij} coefficients are given by

$$\phi_{ij} = \frac{\left[1+\left(\frac{\eta_i}{\eta_j}\right)^{1/2}\left(\frac{M_j}{M_i}\right)^{1/4}\right]^2}{\left[8\left(1+\frac{M_i}{M_j}\right)\right]^{1/2}} \tag{4.34}$$

and the viscosity of individual components (μ_i) is a function of temperature and can be calculated from the method of Chung [19]

$$\mu_i = 4.0785 \cdot 10^{-6} \frac{F_c(M_i T)^{1/2}}{V_{c,i}^{2/3} \Omega_v} \tag{4.35}$$

where $V_{c,i}$ is the critical volume of component i, Ω_v is the collision integral for viscosity, and factor F_c has been empirically given by,

$$F_c = 1 - 0.2756 w_i + 0.059035 \mu_{r,i}^4 + \zeta \tag{4.36}$$

where ζ is a special correction parameter for highly polar substances, (in the present case it can be considered $\zeta = 0$); ω_i is the acentric factor of the component i, and μ_r is a dimensionless dipole moment given as,

$$\mu_{r,i} = 131.3 \frac{\mu_i}{(V_{c,i} T_{c,i})^{1/2}} \tag{4.37}$$

where $\mu_{r,i}$ is the dipole moment of component i in debyes, and $T_{c,i}$ is the critical temperature of component i. The collision integral for viscosity can be estimated by the empirical equation proposed Neufeld *et al.* [16],

$$\Omega_v = 1.16145(T^*)^{-0.14874} + 0.52487e^{-0.77320T^*} + 2.16178e^{-2.43787T^*} \tag{4.38}$$

valid for $0.3 \leq T^* \leq 100$ with $\qquad\qquad T^* = 1.2593T_r \tag{4.39}$

and $\qquad\qquad\qquad\qquad\qquad T_r = \dfrac{T}{T_c} \tag{4.40}$

The previously presented correlation for axial dispersion coefficient (equation 4.29) is valid for $3 < \text{Re} < 10000$, while the following correlation proposed by Edwards *et al.* [20] was applied to calculate the axial dispersion for $0.008 < \text{Re} < 50$:

$$\frac{\varepsilon D_{ax}}{D_m} = 0.73\varepsilon + 0.5\frac{ScRe}{1+13\times0.5\left(\frac{\varepsilon}{ScRe}\right)} \tag{4.41}$$

The **diffusional time constant for the crystals** (K_c) is defined as,

$$K_c = 15\frac{D_c}{r_c{}^2} \tag{4.42}$$

where D_c is the intracrystalline diffusion coefficient. The LDF approximation at the crystal level is only valid if,

$$\frac{D_{c,i}t}{r_c{}^2} > 0.1 \tag{4.43}$$

with $D_{c,i}$ is the diffusivity of component i, and has exponential dependence of temperature,

$$D_{c,i} = D_{c,i}^0 exp\left(\frac{-E_{a,i}}{R_gT}\right) \tag{4.44}$$

where $D_{c,i}^0$ is the limiting diffusivity at infinite temperatures, $E_{a,i}$ is the activation energy of component i, and the following equations can compute them,

$$D_{c,i}^0 = 1.633 \cdot 10^{-10}\sqrt{\frac{E_{a,i}}{M_i}} \tag{4.45}$$

$$E_{a,i} = 0.45\left(-\Delta H_{iso,i}\right) \tag{4.46}$$

The **film heat transfer coefficient between the gas and particle** (h_f) is given by,

$$\frac{h_{f,i}D_h}{k_{g,i}} = 2.0 + 1.1Re^{0.6}Pr^{1/3} \tag{4.47}$$

where k_g is the gas thermal conductivity and Pr is the Prandtl number, which are defined as,

$$Pr = \frac{\hat{C}_p \mu}{k_g} \tag{4.48}$$

$$k_g = \sum_{i=1}^{n} \frac{y_i k_{g,i}}{\sum_{j=1}^{n} y_i \phi_{ij}} \tag{4.49}$$

with $k_{g,i}$ defined as,

$$k_{g,i} = \frac{\mu_i}{M_i} 1000 \left(C_{p,i} + \frac{5}{4} R_g \right) \tag{4.50}$$

where $\hat{C}_p$ corresponds to the gas mixture molar specific heat at constant pressure and $C_{p,i}$ is the molar specific heat at constant pressure of component i.

The **film heat transfer coefficient between the gas and column wall** (h_w) can be estimated by the Wasch and Froment correlation [21],

$$\frac{h_w d_{wi}}{k_g} = 140 + 0.013396 \frac{d_{wi}^2}{d_p k_g} Re \tag{4.51}$$

The **film mass transfer coefficient of component i** ($k_{f,i}$) is obtained by,

$$k_{f,i} = \frac{Sh D_{m.i}}{2R_p} \tag{4.52}$$

where S_h is the Sherwood number and is calculated by,

$$Sh = 2.0 + 1.1Sc^{1/3}Re^{0.6} \tag{4.53}$$

The **heat axial dispersion coefficient** (λ) can be given by,

$$\frac{\lambda}{k_g} = 7 + 0.5PrRe \tag{4.54}$$

The **Biot number** (Bi_i) of component i is defined as,

$$Bi_i = \frac{R_p k_{f,i}}{5 \varepsilon_p D_{p,i}} \tag{4.55}$$

The **overall heat transfer coefficient** (U) can be determined by,

$$\frac{1}{U} = \frac{1}{h_w} + \frac{e d_{wi}}{\lambda_w d_{ln}} + \frac{d_{wi}}{d_{we} h_{ex}} \tag{4.56}$$

where λ_w is the wall conductivity, d_{we} is the external diameter of the column, h_{ex} is the external convective heat transfer coefficient, and d_{ln} is obtained by the following expression,

$$d_{ln} = \frac{d_{we} - d_{wi}}{ln\left(\frac{d_{we}}{d_{wi}}\right)} \tag{4.57}$$

Churchill and Chu correlation can be used to estimate the external convective heat transfer coefficient (h_{ex}) [22],

$$\frac{h_{ex} L}{k_{g,ex}} = 0.68 + \frac{0.67 Ra^{1/4}}{\left[1 + \left(\frac{0.492}{Pr}\right)^{9/16}\right]^{4/9}} \tag{4.58}$$

where $k_{g,ex}$ is the thermal conductivity of the external gas, L is the column length, and Ra is the Rayleigh number which is defined by,

$$Ra = GrPr \tag{4.59}$$

with Gr corresponding to the Grashof number and defined as
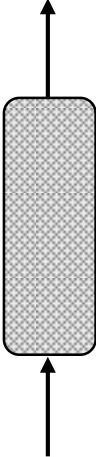
$$Gr = \frac{g\beta((T_w - T_\infty)L^3}{\nu_k^2} \tag{4.60}$$

where g is the acceleration of gravity (9.8 m·s^{-2}), β is the thermal expansion coefficient, ν_k is the kinematic viscosity of the external gas, and T_∞ is the external temperature.

4.3.3 Initial and boundary conditions

The initial and boundary conditions allow solving the partial differential equation (PDE) system. The orthogonal collocation on finite elements as the numerical method was used to solve the PDE system. The initial and boundary conditions employed in the mathematical model simulation steps are present in Table 4.1. For the fixed-bed experiments, a column filled with helium (inert gas) at operating temperature and pressure (initial conditions) was considered. Another assumption employed in the simulation was the fact that the pressure is measured at the end of the column.

Table 4.1. Initial and boundary conditions of mathematical model simulation.

Initial Conditions		
He	$y_{inert} = 1$ $C_{g,i} = 0 \text{ for } i \neq \text{inert}$ $C_{g,inert} = C_{g,T}$ $T_g = T_P = T_W = T_{inlet}$	
Boundary Conditions		
z = L z = 0	**Outlet**	$\dfrac{\partial C_{g,i}}{\partial z} = 0$ $\dfrac{\partial T_g}{\partial z} = 0$ $P = P_{outlet}$
	Inlet	$u_{o\ inlet}\,C_{inlet\,,i} = u_o C_{g,i} - \varepsilon D_{ax}\dfrac{\partial C_{g,i}}{\partial z}$ $u_{o\ inlet}\,C_{inlet\,,T} = u_o C_{g,T}$ $u_{o\ inlet}\,C_{inlet\,,T} C_p T_{inlet} = u_o C_{g,T} C_p T_g - \lambda\dfrac{\partial T_g}{\partial z}$

Notation

a_p	particle external specific area	[m²·kg⁻¹]
A	integration constant	[-]
Bi	mass transfer Biot number	[-]
$C_{g,i}$	gas phase concentration of component i	[mol·m⁻³]
$C_{g,T}$	total gas phase concentration	[mol·m⁻³]
C_p	gas mixture molar specific heat at constant pressure	[J·mol⁻¹·K⁻¹]
$C_{p,i}$	molar specific heat at constant pressure of component i	[J·mol⁻¹·K⁻¹]
$\overline{C_{p,i}}$	average of the particle concentration of component i in the macropores	[mol·m⁻³]
$\hat{C}_{ps}$	adsorbent specific heat per mass unit at constant pressure	[J·kg⁻¹·K⁻¹]
$\overline{C_{p,T}}$	average total concentration	[mol·m⁻³]
$\hat{C}_p$	gas mixture molar specific heat at constant pressure	[J·mol⁻¹·K⁻¹]
$\hat{C}_{p,w}$	column wall specific heat per mass unit at constant pressure	[J·kg⁻¹·K⁻¹]
$\tilde{C}_v$	molar heat capacities of the gas at constant volume	[J·mol⁻¹·K⁻¹]
$C_{v,ads,i}$	molar specific heat at constant volume of the component i in the adsorbed phase	[J·mol⁻¹·K⁻¹]
$C_{v,i}$	molar specific heat at constant volume of the component i	[J·mol⁻¹·K⁻¹]
d_p	particle diameter	[m]
d_{we}	external diameter of the column	[m]
d_{wi}	wall internal diameter	[m]
D_{ax}	mass axial dispersion coefficient	[m²·s⁻¹]
$D_{c,i}$	micropore diffusivity coefficient	[m²·s⁻¹]
$D_{c,i}^0$	limiting diffusivity at infinite temperatures	[m²·s⁻¹]
D_h	hydraulic diameter	[m]
$D_{k,i}$	Knudsen diffusivity of component i	[m²·s⁻¹]
D_m	molecular diffusivity	[m²·s⁻¹]
$D_{m,i}$	molecular bulk diffusion coefficient of component i	[m²·s⁻¹]
$D_{m,ij}$	binary molecular diffusivity	[m²·s⁻¹]
$D_{p,i}$	macropore diffusivity coefficient	[m²·s⁻¹]

D_w	bed diameter	[m]
e	thickness of the shell	[m]
$E_{a,i}$	activation energy of component i	[J·mol^{-1}]
F_c	correction factor of dilute gas viscosity	[-]
g	acceleration of gravity	[m·s^{-2}]
Gr	Grashof number	[-]
h_{ex}	external convective heat transfer coefficient	[W·m^{-2}·K^{-1}]
h_f	film heat transfer coefficient between the gas and particle	[W·m^{-2}·K^{-1}]
h_w	film heat transfer coefficient between the gas and the wall	[W·m^{-2}·K^{-1}]
k	Boltzmann's constant	[J·K^{-1}]
k_f	film mass transfer coefficient	[m·s^{-1}]
$k_{f,i}$	film mass transfer coefficient of component i	[m·s^{-1}]
k_g	gas thermal conductivity	[W·m^{-2}·K^{-1}]
$k_{g,ex}$	thermal conductivity of the external gas	[W·m^{-2}·K^{-1}]
K	adsorption equilibrium constant	[-]
K_c	diffusional time constant for the crystals	[s^{-1}]
K_∞	adsorption equilibrium constant at infinite temperature	[-]
$K_{\infty,o}, K_{\infty,L}, K_{\infty,I}$	equilibrium constants of Langmuir-Ising isotherm	[-]
L	column length	[m]
Mi	molecular weight of components i	[kg·mol^{-1}]
M_j	molecular weight of component j	[kg·mol^{-1}]
P	pressure	[Pa]
P_0	saturation vapor pressure	[Pa]
Pr	Prandtl number	[-]
q	total adsorbed amount	[mol·kg^{-1}]
$\overline{q_i}$	average adsorbed phase concentration of component i	[mol·kg^{-1}]
$\overline{q_i}$	adsorbed concentration of component i in equilibrium with $\overline{C_{p,i}}$	[mol·kg^{-1}]
q_m	saturation adsorption capacity	[mol·kg^{-1}]
$q_{sat\,I}$	specific saturation adsorption capacity in Ising isotherm	[mol·kg^{-1}]
$q_{sat\,L}$	specific saturation adsorption capacity in Langmuir isotherm	[mol·kg^{-1}]
Q_{iso}	isosteric heat of adsorption	[J·mol^{-1}]
r_c	crystal radius	[m]

R_g	ideal gas constant	[J·mol^{-1}·K^{-1}]
R_p	particle radius	[m]
Ra	Rayleigh number	[-]
Re	Reynolds number	[-]
S_h	Sherwood number	[-]
S_p	particle's external surface area	[m^2]
Sc	Schmidt number	[-]
t	time	[s]
T	temperature	[K]
$T_{c,i}$	critical temperature of component i	[K]
T_g	gas temperature	[K]
T_p	particle temperature	[K]
T_w	wall temperature	[K]
T_∞	external temperature	[K]
u_0	superficial gas velocity	[m·s^{-1}]
U	overall heat transfer coefficient	[W·m^{-2}·K^{-1}]
$V_{c,i}$	critical volume of component i	[m^3]
V_p	particle volume	[m^3]
ω_i	acentric factor of the component i	[-]
y_i	molar fraction of component i	[-]
y_j	molar fraction of the component j	[-]
z	axial position inside adsorption bed	[m]

Greek letters

α_w	ratio of the internal surface area to the column wall volume	[m^{-1}]
$\alpha_{w\ell}$	ratio of the logarithmic mean surface to the column wall volume	[m^{-1}]
β	thermal expansion coefficient	[K^{-1}]
$-\Delta H$	heat of adsorption	[J·mol^{-1}]
$-\Delta H_{iso}$	isosteric heat of adsorption	[J·mol^{-1}]
ε	bed porosity	[-]
ε_p	particle porosity	[-]
$\mathcal{E}$	adsorption potential	[J·mol^{-1}]
ϵ_i	Lennard-Jones characteristic energy of component i	[J]
ϵ_j	Lennard-Jones characteristic energy of component j	[J]
ζ	correction parameter for highly polar substances	[-]
λ	heat axial dispersion coefficient	[W·m^{-2}·K^{-1}]
λ_w	wall conductivity	[W·m^{-1}·K^{-1}]
μ	bulk gas mixture viscosity	[Pa·s^{-1}]
μ_i	viscosity of component i	[Pa·s^{-1}]
μ_r	reduced dipole moment	[-]
$\mu_{r,i}$	dipole moment of component i	[D]
v	volume	[m^3]
v_k	kinematic viscosity of the external gas	[m^2·s^{-1}]
ρ_b	bulk density	[kg·m^{-3}]
ρ_g	gas density	[kg·m^{-3}]
ρ_p	particle density	[kg·m^{-3}]
ρ_w	column wall density	[kg·m^{-3}]
σ_i	individual Lennard-Jones parameter of component i	[Å]
σ_j	individual Lennard-Jones parameter of component j	[Å]
σ_{ij}	characteristic Lennard-Jones length for ij interaction	[Å]
τ_p	pore tortuosity	[-]
ϕ_{ij}	Wilke's coefficients	[-]
Ω_c	LDF factor for macropores	[-]

Ω_D	collision integral for diffusion	[-]
Ω_p	LDF factor for micropores	[-]
Ω_v	collision integral for viscosity	[-]

Abbreviations

CMMS	Cooperative Multi-Molecular Sorption
DISL	Dual Ising-Single Langmuir
LDF	Linear Drive Force
PDE	Partial Differential Equation

References

1.   Yang, R.T., *Gas Separation by Adsorption Processes*. 1987: Butterworth-Heinemann. 632.

2.   Do, D.D., *Adsorption Analysis: Equilibria and Kinetics*. 1998, Imperial College Press.

3.   Abdullah, M.A., L. Chiang, and M. Nadeem, *Comparative evaluation of adsorption kinetics and isotherms of a natural product removal by Amberlite polymeric adsorbents.* Chemical Engineering Journal, 2009. **146**(3): p. 370-376.

4.   Limousin, G., J.P. Gaudet, L. Charlet, S. Szenknect, V. Barthès, and M. Krimissa, *Sorption isotherms: A review on physical bases, modeling and measurement.* Applied Geochemistry, 2007. **22**(2): p. 249-275.

5.   Coelho, J.A., A.M. Ribeiro, A.F.P. Ferreira, S.M.P. Lucena, A.E. Rodrigues, and D.C.S. De Azevedo, *Stability of an Al-Fumarate MOF and Its Potential for CO2 Capture from Wet Stream.* Industrial and Engineering Chemistry Research, 2016. **55**(7): p. 2134-2143.

6.   Rutherford, S.W., *Probing the Mechanism of Water Adsorption in Carbon Micropores with Multitemperature Isotherms and Water Preadsorption Experiments.* Langmuir, 2006. **22**(24): p. 9967-9975.

7.   Rutherford, S.W., *Modeling water adsorption in carbon micropores: study of water in carbon molecular sieves.* Langmuir, 2006. **22**(2): p. 702-708.

8.   Furmaniak, S., A.P. Terzyk, G.S. Szymański, P.A. Gauden, M. Motak, P. Kowalczyk, and R. G., *Thermodynamics of the CMMS approach and carbon surface chemistry in SO2 adsorption.* Langmuir, 2006. **22**(16): p. 6887-6892.

9.   Ruthven, D.M., *Principles of adsorption & adsorption processes*. 1984: John Wiley & Sons, Inc.

10.   Suzuki, M., *Adsorption engineering*. Chemical engineering monographs. Vol. 25. 1990: Elsevier.

11. Yang, K. and B. Xing, *Adsorption of Organic Compounds by Carbon Nanomaterials in Aqueous Phase: Polanyi Theory and Its Application.* Chemical Reviews, 2010. **110**(10): p. 5989-6008.

12. Thomas, W.J. and B. Crittenden, *3 - Fundamentals of adsorption equilibria*, in *Adsorption Technology & Design*. 1998, Butterworth-Heinemann: Oxford. p. 31-65.

13. Ribeiro, R.P.P.L., *Electric Swing Adsorption for Gas Separation and Purification*, in *Department of Chemical Engineering*. 2013, Faculty of Engineering of University of Porto.

14. Sircar, S., R. Mohr, C. Ristic, and M.B. Rao, *Isosteric Heat of Adsorption: Theory and Experiment.* The Journal of Physical Chemistry B, 1999. **103**(31): p. 6539-6546.

15. Ribeiro, A.M., C.A. Grande, F.V.S. Lopes, J.M. Loureiro, and A.E. Rodrigues, *A parametric study of layered bed PSA for hydrogen purification.* Chemical Engineering Science, 2008. **63**(21): p. 5258-5273.

16. Neufeld, P.D., A.R. Janzen, and R.A. Aziz, *Empirical Equations to Calculate 16 of the Transport Collision Integrals Ω(l, s)* for the Lennard-Jones (12–6) Potential.* The Journal of Chemical Physics, 1972. **57**(3): p. 1100-1102.

17. Wakao, N. and T. Funazkri, *Effect of fluid dispersion coefficients on particle-to-fluid mass transfer coefficients in packed beds: Correlation of sherwood numbers.* Chemical Engineering Science, 1978. **33**(10): p. 1375-1384.

18. Wilke, C.R., *A Viscosity Equation for Gas Mixtures.* The Journal of Chemical Physics, 1950. **18**(4): p. 517-519.

19. Chung, T.H., M. Ajlan, L.L. Lee, and K.E. Starling, *Generalized multiparameter correlation for nonpolar and polar fluid transport properties.* Industrial & Engineering Chemistry Research, 1988. **27**(4): p. 671-679.

20. Edwards, M.F. and J.F. Richardson, *Gas dispersion in packed beds.* Chemical Engineering Science, 1968. **23**(2): p. 109-123.

21.   de Wasch, A.P. and G.F. Froment, *Heat transfer in packed beds.* Chemical Engineering Science, 1972. **27**(3): p. 567-576.

22.   Churchill, S.W. and H.H.S. Chu, *Correlating equations for laminar and turbulent free convection from a horizontal cylinder.* International Journal of Heat and Mass Transfer, 1975. **18**(9): p. 1049-1053.

5 ADSORBENTS CHARACTERIZATION AND ADSORPTION EQUILIBRIUM

5.1 Adsorbents characterization

Thermogravimetric analyses, textural, morphologic and crystallographic characterization were performed by different techniques, as previously described in Chapter 3. The key results, regarding the Al-Fum, CAU-10, MIL-160(Al), MIL-100(Fe), and MIL-125(Ti)_NH$_2$ samples, and drawn conclusions are outlined in this chapter.

5.1.1 Thermogravimetric analyses

Thermogravimetric analyses on dry MOFs (He), after their regeneration, and saturated with water (He+H$_2$O) were performed (Figure 5.1) through a Netzsch STA 409 PC Luxx set-up.

The dry Al-Fum TG curve shows one distinct mass loss event between 700 and 800 K, while for the saturated sample, two mass loss stages occurred. Namely, the desorption of water molecules at 325 K to 400 K, representing about 20% of weight loss, and starting of the material degradation at 800 K. Thermal stability is in agreement with Mani *et al.* [1] and Karmakar *et al.* [2] studies, who reported, for this MOF, thermal stability until around 700 K. MIL-160(Al) TGA profile exhibits two different mass loss stages, namely a first stage from 300 K to 400 K, and the second one localized on the range of 650 K to 800 K. The first step can be attributed to water desorption with a weight loss of 22.5 % in the saturated material. The second stage is ascribed to the MOF framework combustion. For temperature above 800 K, the framework is degraded, thus producing an alumina residue (Al$_2$O$_3$) that represents about 50 % of the initial dry mass, as also observed on Al-Fum TG. The ratio is in accordance with the stoichiometric ratio between the inorganic and organic building blocks. The thermal stability of this material is in good agreement with the thermal stability reported in the literature for MIL-160(Al) materials [3-8]. CAU-10 presents similar mass loss steps to the ones observed for MIL-160(Al), the first step also between 300 K to 400 K; however, the second stage is localized at a higher temperature in the range of 800 to 930 K, with the formation of Al$_2$O$_3$. In the range of 675 K to 725 K, a small mass loss of about 2.4% and 1.7% for dry and saturated CAU-10, respectively, was observed. The Al$_2$O$_3$ residue formed is about half of the initial dry mass, in line with the previous referred Al-based MOFs. The TG curve obtained for MIL-100(Fe) agrees with the results published by Simon and co-workers [9] exhibiting three mass loss stages. The first stage is attributed to the desorption of water molecules (32.8% for saturated material), while the following steps are related to degradation of the MOF structure, by the organic ligand

decomposition, followed by the reduction of the iron oxide (Fe_2O_3) [10]. The TG curve of MIL-125(Ti)_NH_2 for the dry sample presents mainly mass loss in one step, about 640 K, which represents the thermal stability of the material. This step corresponds to the degradation of the framework and consequent TiO_2 formation. The TG of the saturated sample, besides the mass loss due to its thermal decay, as previously said at 640 K has a first step at about 390 K. This first step can be associated with the water desorption, representing about 20% of its original wet mass, in agreement with the literature reported data [11]. To conclude, excepting to MIL-100(Fe), all the selected samples are thermally stable at least up to 650 - 700 K.

e)
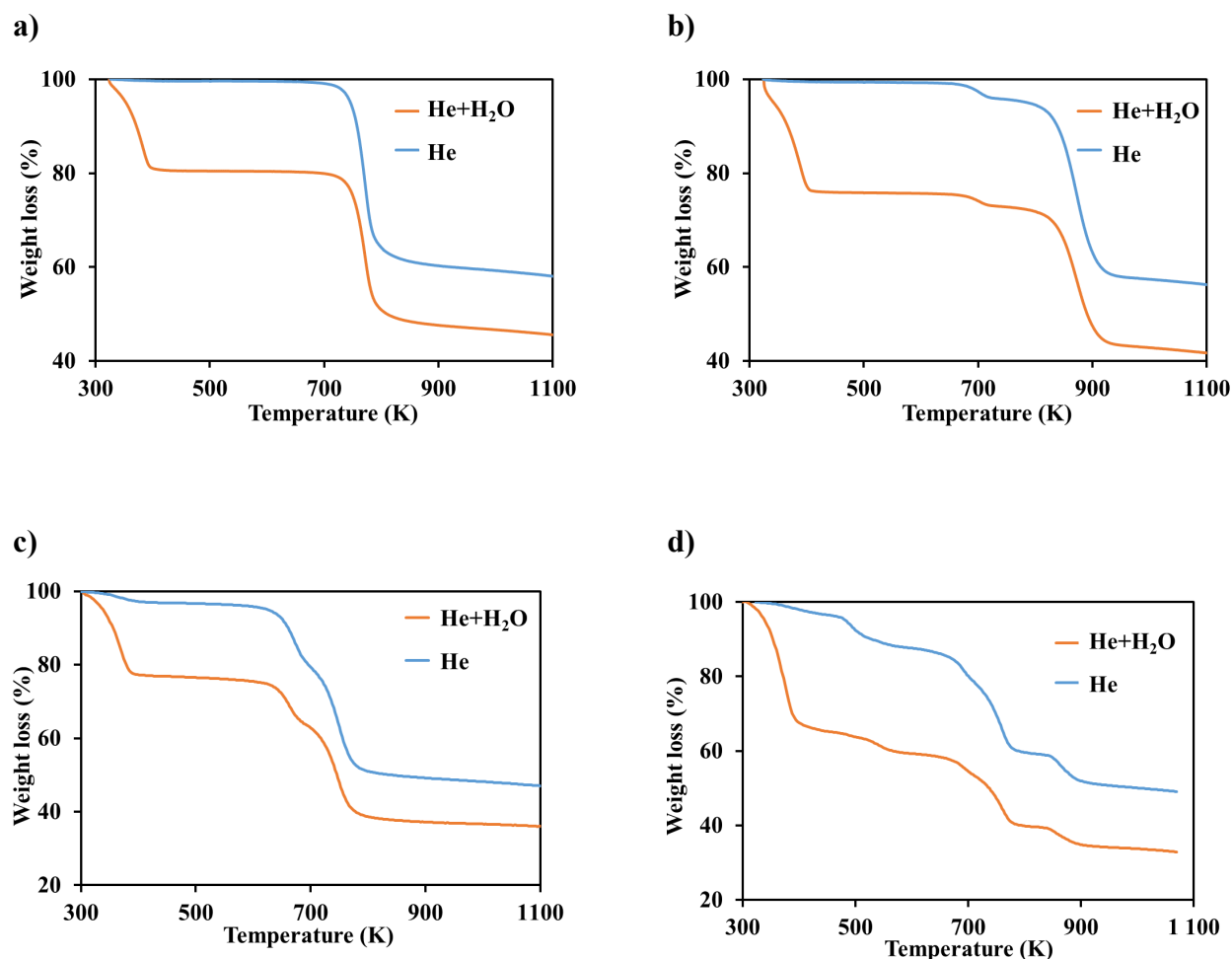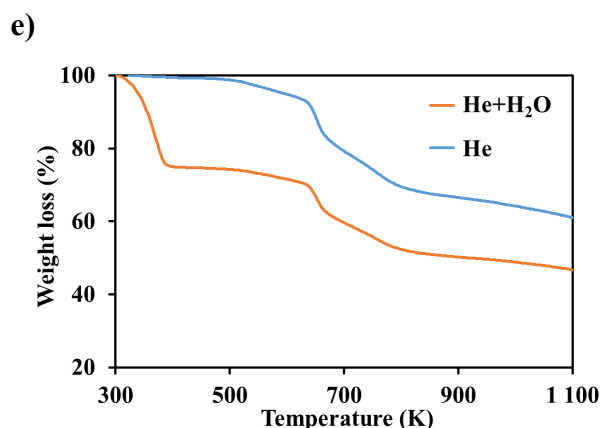
Figure 5.1. TGA curves of (a) Al-Fum, (b) CAU-10, (c) MIL-160(Al), (d) MIL-100(Fe), and (e) MIL-125(Ti)_NH$_2$ after regeneration (He) and after material saturation (He + H$_2$O).

5.1.2 Textural, morphologic and crystallographic characterization

Textural, morphologic and crystallographic characterization was performed according to the procedures reported in Chapter 3. He pycnometry, N$_2$ adsorption-desorption at 77 K, CO$_2$ adsorption at 273 K, SEM/EDS analysis, Hg intrusion porosimetry, XRD analysis, and mechanical resistance tests were carried out on all samples.

The **N$_2$ physisorption equilibrium isotherms at 77 K** are shown in Figure 5.2a–e). Characterization by N$_2$ adsorption at 77 K allowed to determine the surface area and micropore volume for each material, and the obtained values are reported in Table 5.1. As can be seen, MIL-160(Al) is characterized by a Type I shape behavior (Figure 5.2c), according to the IUPAC classification, corresponding to the characteristic isotherm shape obtained in microporous materials (pore diameter < 2 nm). The N$_2$ adsorption-desorption equilibrium isotherm obtained is consistent with the study performed by Permyakova and co-workers in MIL-160(Al) granules [6]. Both MIL-160(Al) granulated samples, reported in this work and by Permyakova *et al.* [6], present a higher N$_2$ adsorbed amount when compared to MIL-160(Al) pellets, reported by Gökpinar *et al.* [8], but lower compared with MIL-160(Al) powder [5, 6], as expected.

As reported in the literature, the combination of Type I and Type IV isotherm of MIL-100(Fe) (Figure 5.2d) presents two uptakes (P/P$_o$ ~ 0.04 and 0.12) due to its two cage typologies (microporous: 5.5 – 8.6 Å; mesoporous: 25 – 29 Å) [12, 13]. The shape of N$_2$ adsorption equilibrium isotherm is in good agreement with the literature, for shaped material, presenting

values below the reported ones for powder, as expected [12, 14-17]. Nevertheless, the isotherm shape is similar to one reported by Valekar *et al.* in MIL-100(Fe) granules, although its adsorption loadings are slightly higher [17]. However, N_2 adsorbed amount is more similar to the values obtained on MIL-100(Fe) pellets of the same study [17].

The pores networks of the other three materials are also composed of micropores and mesopores. The adsorption equilibrium isotherms feature a Type I shape with a high N_2 adsorbed amount at low relative pressures, proving the presence and accessibility of micropores in those materials. The hysteresis loops are of type H2, a fingerprint of the existence of mesoporous and/or macroporous structures [18]. Al-Fum (Figure 5.2a) N_2 adsorption equilibrium isotherm presents a similar shape to other isotherms reported in the literature, for relative pressures below 0.8 [8, 18, 19]. However, for high relative pressures ($P/P_o > 0.8$) the N_2 loading values do not present the abrupt increase, which is characteristic of Al-Fum [3, 19]. Besides the adsorption equilibrium isotherm shape, the N_2 adsorbed amount itself also shows comparable values with those reported on Al-Fum powder [8, 18] and Al-Fum granules [19, 20], except the values reported on the study by Gökpinar *et al.* [8], for a granular sample, which are lower. Regarding CAU-10 material (Figure 5.2b), the isotherm curve is in good agreement with the literature [21]. MIL-125(Ti)_NH_2 (Figure 5.2e) presented an N_2 adsorption equilibrium isotherm similar to other already present on the open literature [22-27]. Yet, the N_2 adsorbed amount is lower than the reported ones, for MIL-125(Ti)_NH_2 pellets and granules [24, 26].

a)

b)

c)

d)

e)
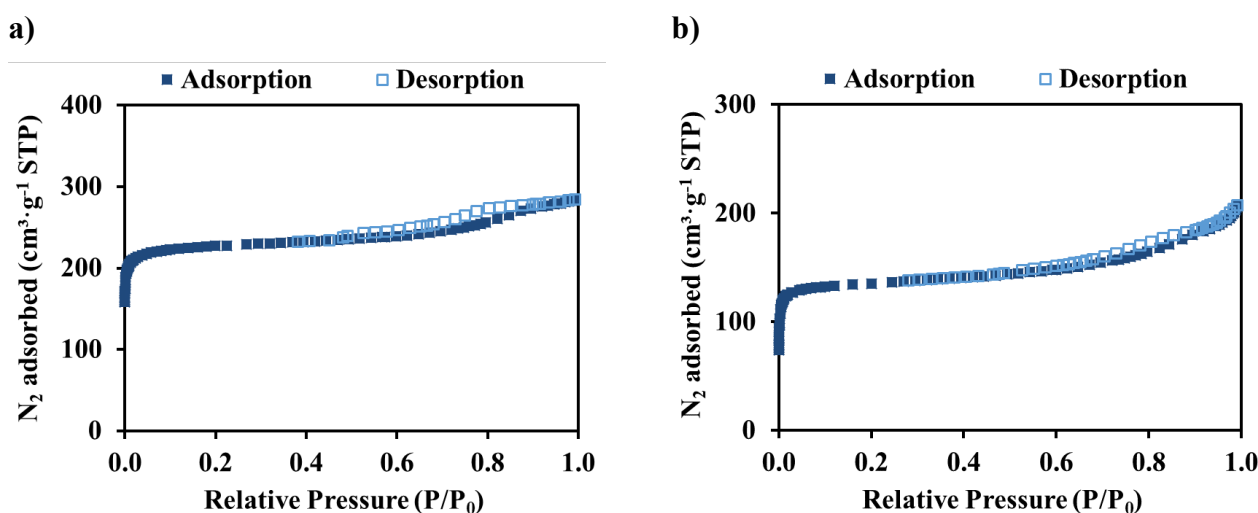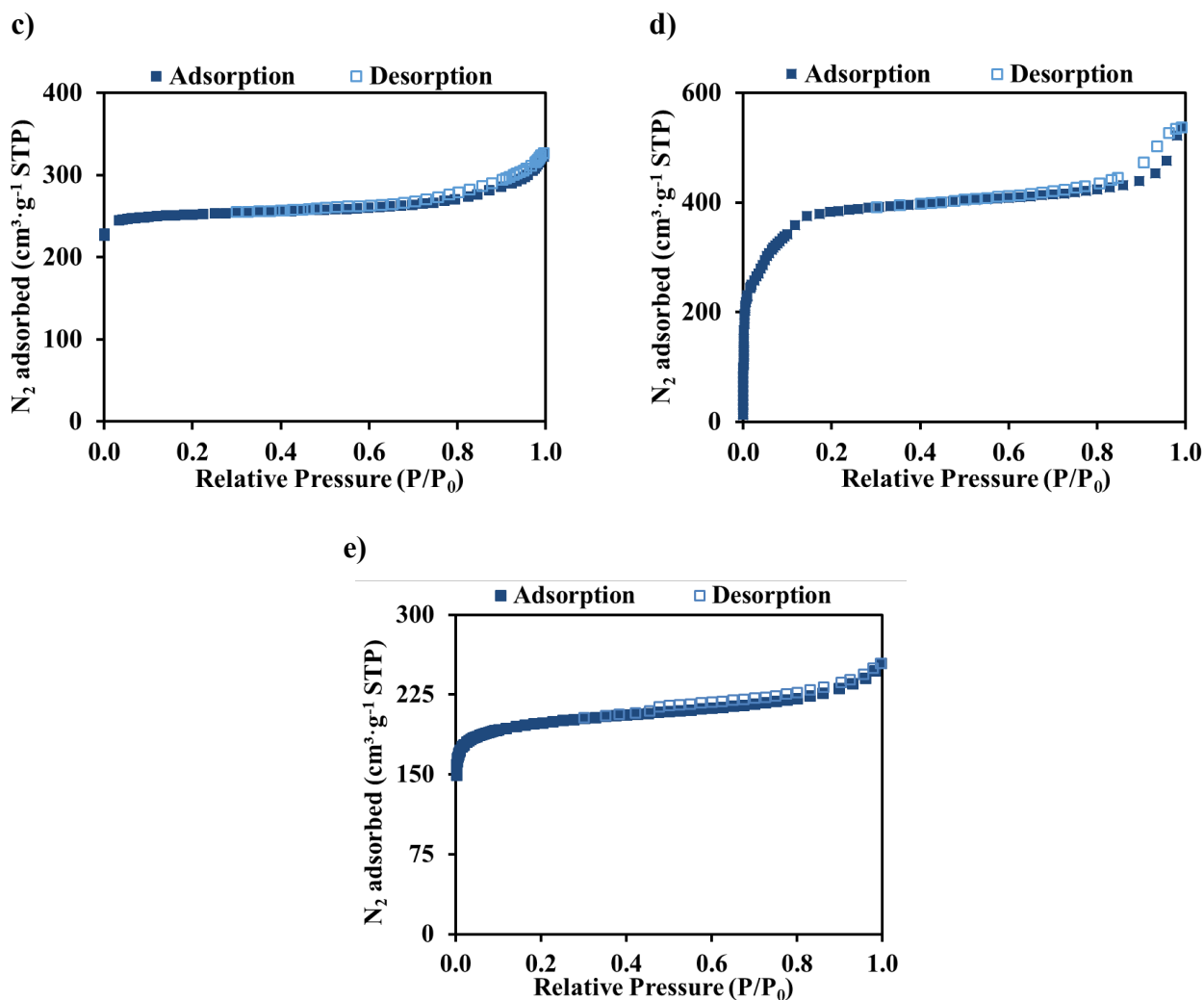
Figure 5.2. N_2 adsorption-desorption equilibrium isotherms at 77 K for (a) Al-Fum, (b) CAU-10, (c) MIL-160(Al), (d) MIL-100(Fe), and (e) MIL-125(Ti)_NH_2.

Figure 5.3 presents the **CO_2 adsorption equilibrium isotherms at 273 K** of the five MOF samples obtained after activation under vacuum at 423 K for 12 h, as mentioned in Chapter 3. Unlike N_2 at 77 K, CO_2 adsorption at 273 K does not present diffusion limitations on the narrow micropores (< 0.7 nm) due to its higher kinetic energy (high adsorption temperature) [28].
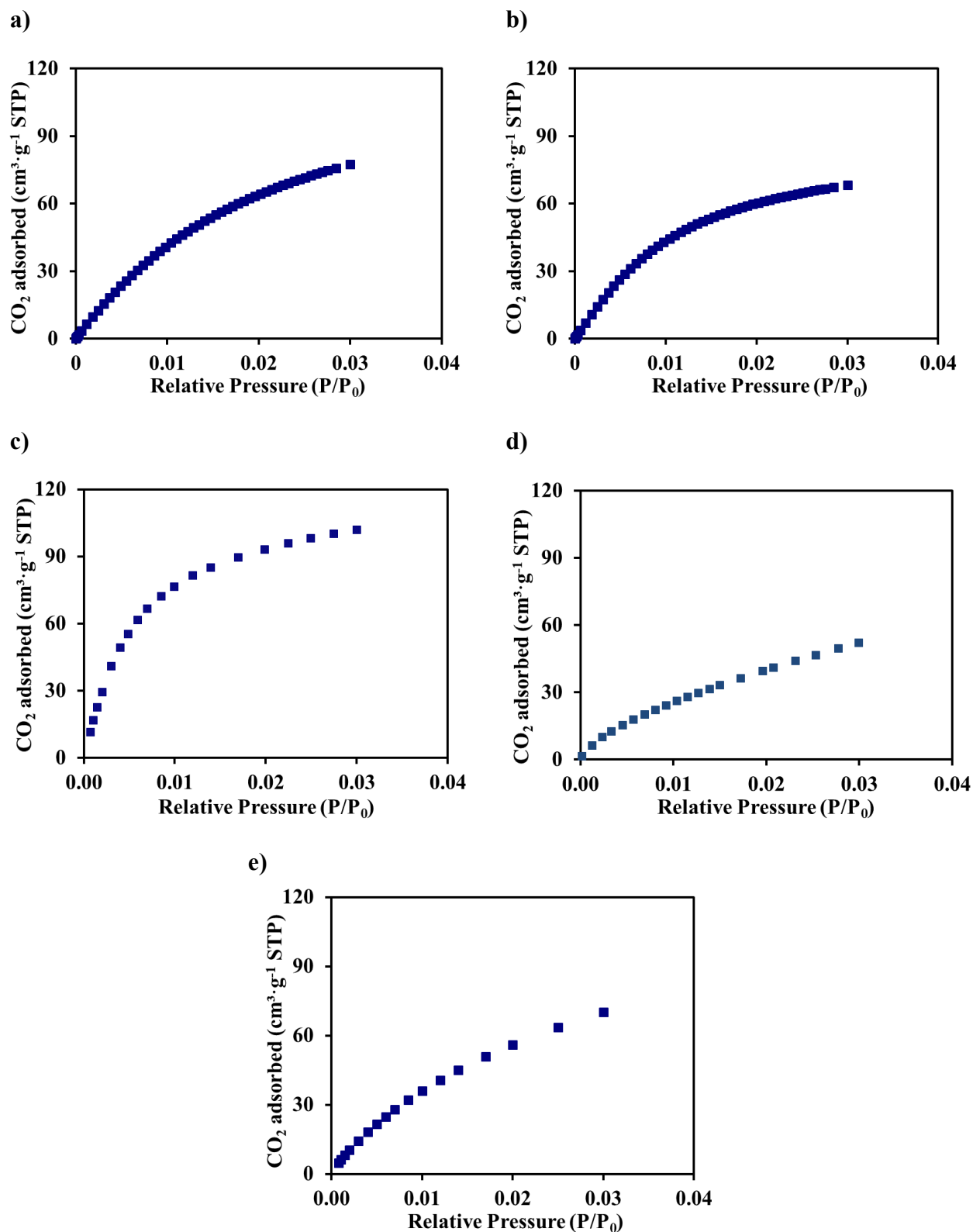
Figure 5.3. Adsorption equilibrium isotherms of CO_2 at 273 K on (a) Al-Fum, (b) CAU-10, (c) MIL-160(Al), (d) MIL-100(Fe), and (e) MIL-125(Ti)_NH_2.

All the materials show Type I shape CO_2 adsorption equilibrium isotherms, according to the IUPAC classification, a characteristic behavior of microporous materials. The presence of narrow pores in the materials is clear, but an apparent adsorption plateau is not evident at low tested pressures, particularly in Al-Fum, MIL-125(Ti)_NH$_2$, and MIL-100(Fe). At low pressures, MIL-160(Al) presents the highest affinity with CO_2, followed by CAU-10, Al-Fum, MIL-125(Ti)_NH$_2$, and MIL-100(Fe).

Hg intrusion porosimetry (MIP) analysis: the macroporosity was characterized by the intrusion of Hg into the macropores by increasing the intrusion cell pressure (Chapter 3). The results are displayed in Figure 5.4 in the form of log differential pore volume versus diameter ($DV/D\log d$) since is the most appropriate representation of pore size distribution (PSD) by MIP [29]. All the materials present a developed macroporosity, due to the presence of interparticle voids generated during the shaping of the material [8, 17]. The obtained average (macro)pore diameters for the five samples are summarized in Table 5.1.

a)

b)

c)

d)

e)
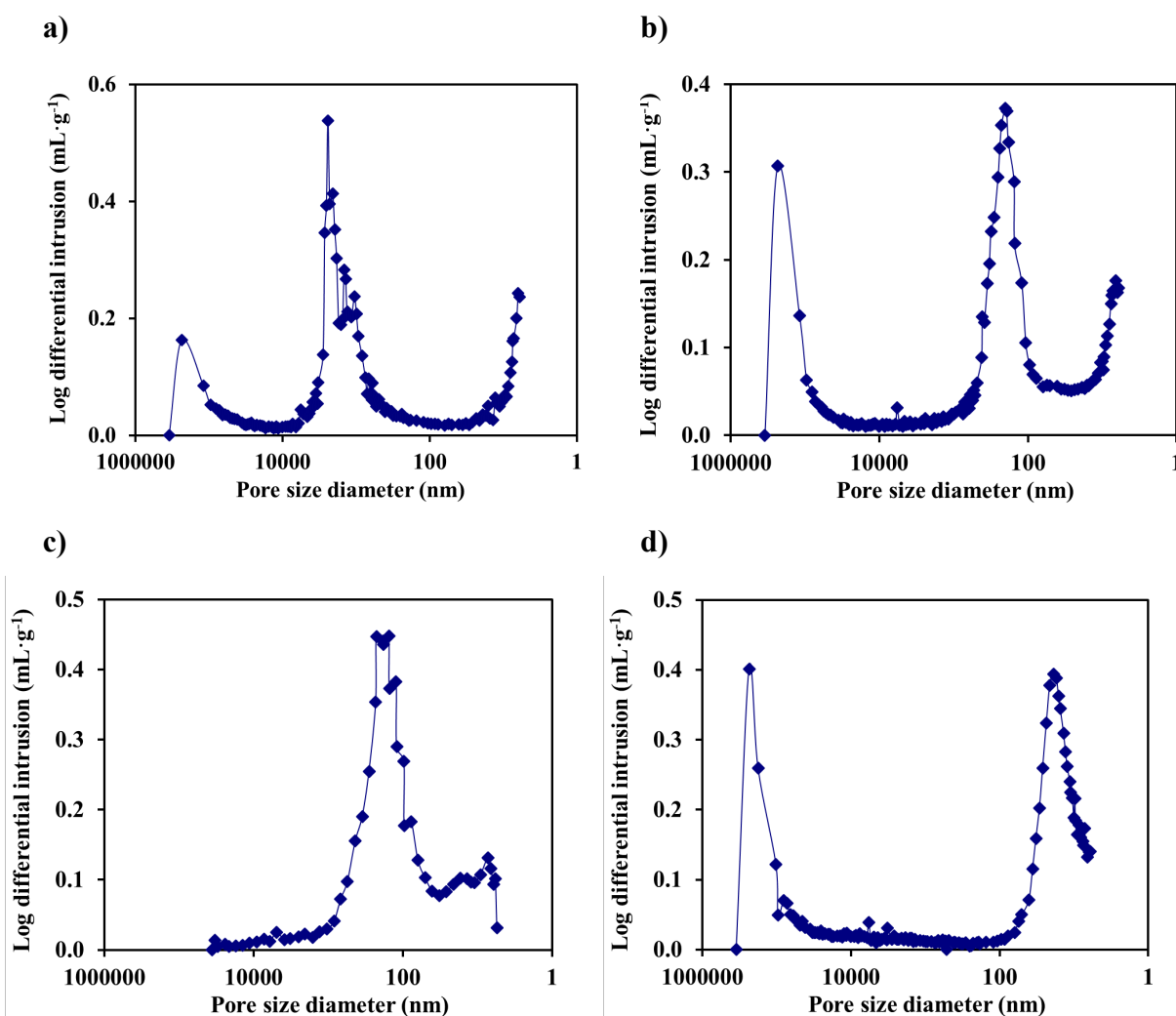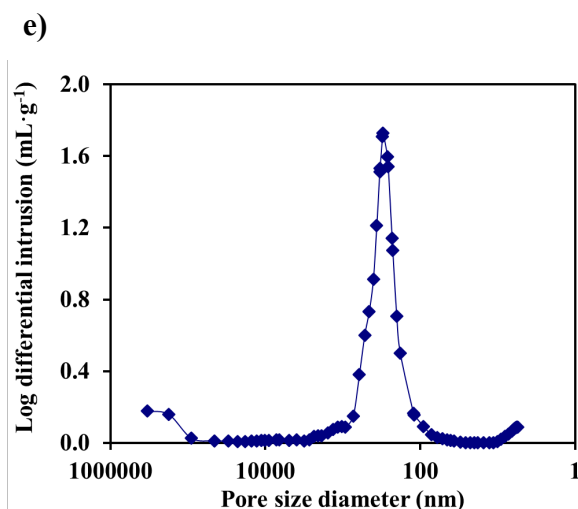
Figure 5.4. Pore size distribution by Hg intrusion on (a) Al-Fum, (b) CAU-10, (c) MIL-160(Al), (d) MIL-100(Fe), and (e) MIL-125(Ti)_NH$_2$.

Indeed, the main results of the samples's textural properties obtained by complementary characterization techniques are presented in Table 5.1. Langmuir, Dubinin-Radushkevich (DR), and BET were the three models used to estimate the surface area. Additionally, N$_2$ adsorption equilibrium isotherms allowed to evaluate the micropores volume (t-plot micropore area) and the total pore volume. Micropore volumes were also obtained by employing the DR (limiting micropore volume) method to the CO$_2$ adsorption equilibrium data. Particle porosity, average (macro)pore diameter, particle apparent density, and apparent skeletal density were obtained through the Hg porosimetry, while He pycnometry was used for assessing the solid density.

Table 5.1. Summary of textural characterization of Al-Fum, CAU-10, MIL-160(Al), MIL-100(Fe), and MIL-125(Ti)_NH_2.

Properties	Al-Fum	CAU-10	MIL-160(Al)	MIL-100(Fe)	MIL-125(Ti)_NH$_2$
Surface area ($m^2 \cdot g^{-1}$)	1005 [a] / 747 [b]	603 [a] / 730 [b]	1108 [a] / 1019 [b]	1904 [a] / 491 [b]	662 [c] / 733 [b]
Micropore volume ($cm^3 \cdot g^{-1}$)	0.299 ± 0.008 [d] / 0.32 [e]	0.292 ± 0.006 [d] / 0.18 [e]	0.409 ± 0.023 [d] / 0.37 [e]	0.197 ± 0.006 [d] / 0.56 [e]	0.294 ± 0.006 [d] / 0.29 [e]
Total pore volume ($cm^3 \cdot g^{-1}$)	0.43	0.29	0.50	0.83	0.39
Particle apparent density ($g \cdot mL^{-1}$) [f]	0.839 (P=0.0036 MPa)	0.865 (P=0.0036 MPa)	0.817 (P=0.0345 MPa)	0.692 (P=0.0036 MPa)	0.586 (P=0.0037 MPa)
Apparent solid density ($g \cdot mL^{-1}$) [g]	1.182	1.299	1.224	0.963	1.089
Solid (skeleton) density ($g \cdot mL^{-1}$) [h]	1.618	1.476	1.354	1.515	1.296
Particle porosity (%)	29.0	33.4	33.1	28.2	46.2
Average pore diameter (nm)	58.0	53.3	45.5	29.1	175.1

a) Surface area determined by the Langmuir method; b) Equivalent surface area determined by the DR model; c) Surface area determined by the BET method; d) Limiting micropore volume determined; e) t-plot micropore area; f) ρ_{ap} = mass/pellet volume; g) $\rho_{s,Hg}$ = mass/(pellet volume - (macro + meso) pore volume); h) $\rho_{sk, He}$ = mass/solid volume = mass/(pellet volume - (macro + meso + micro) pore volume)).

SEM and EDS analysis: samples morphology was analyzed by **SEM** micrography (Table 5.2), while **EDS** (Figure 5.5) provided information about the MOFs chemical composition (Chapter 3). The SEM images are not very clear due to the sample surface charging, leading to surface instability of the material. For this reason, it was not also possible to perform EDS analysis on MIL-160(Al). The SEM images reveal that all materials present crystals with irregular size and shape. CAU-10 granules are predominantly of about 1 mm and show powdery surface. The CAU-10 faceted crystals present size between 1.5 and 3.8 µm. The particle size of MIL-160(Al) granules is about 3 mm, with crystal size of about 0.7 µm. MIL-100(Fe) presents particles with a coarse surface and length of about 1 mm, and most of the crystals have an average dimension of 0.4 µm. MIL-125(Ti)_NH_2 exhibits crystals with irregular shapes and different sizes, ranging from 90 nm to 2 µm. Al-Fum porous surface is composed of irregular agglomerates with different sizes.

Table 5.2. Scanning electron micrographs on the granulate, granulated surface, and on the interior of granulate of Al-Fum, CAU-10, MIL-160(Al), MIL-100(Fe), and MIL-125(Ti)_NH$_2$.
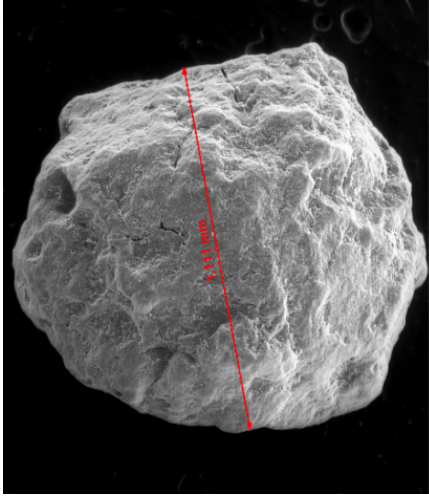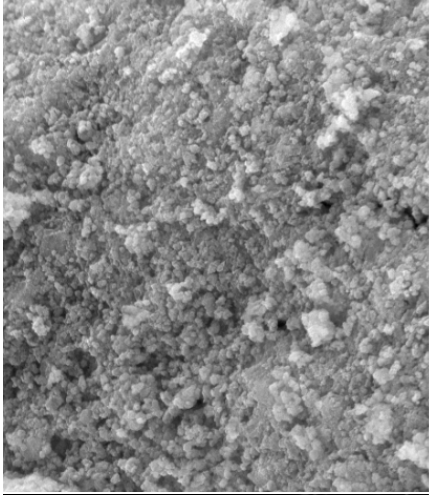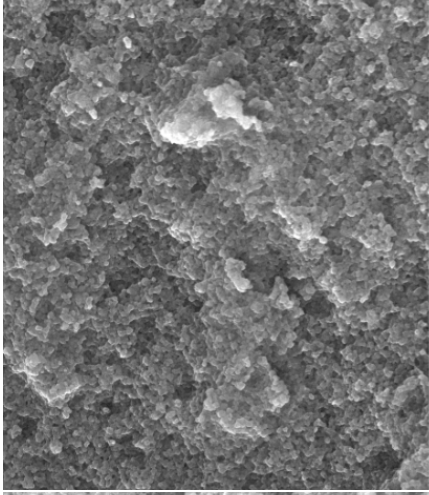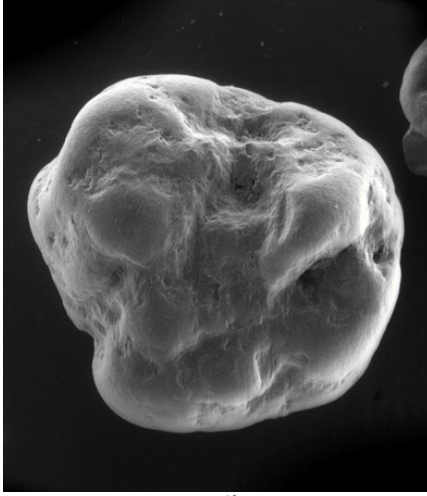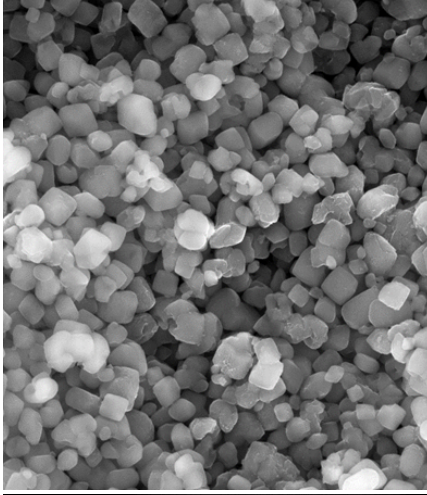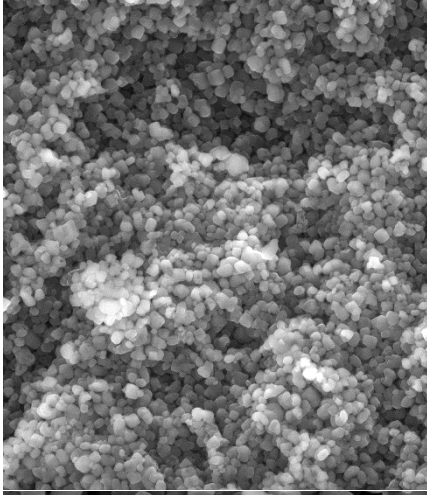
Table 5.2. Scanning electron micrographs on the granulate, granulated surface, and on the interior of granulate of Al-Fum, CAU-10, MIL-160(Al), MIL-100(Fe), and MIL-125(Ti)_NH$_2$.

The Al-Fum, CAU-10, and MIL-100(Fe) EDS spectra (Figure 5.5a-c) present the elements expected except the gold (Au) and palladium (Pd), which can be related to the coating of the material, and the silicon (Si) probably used as the binder, in the form of silica, during the granules shaping. MIL-125(Ti)_NH$_2$ spectrum confirms the presence of carbon, nitrogen, oxygen, and titanium atoms (Figure 5.5d), which is in agreement with the expected adsorbent composition.
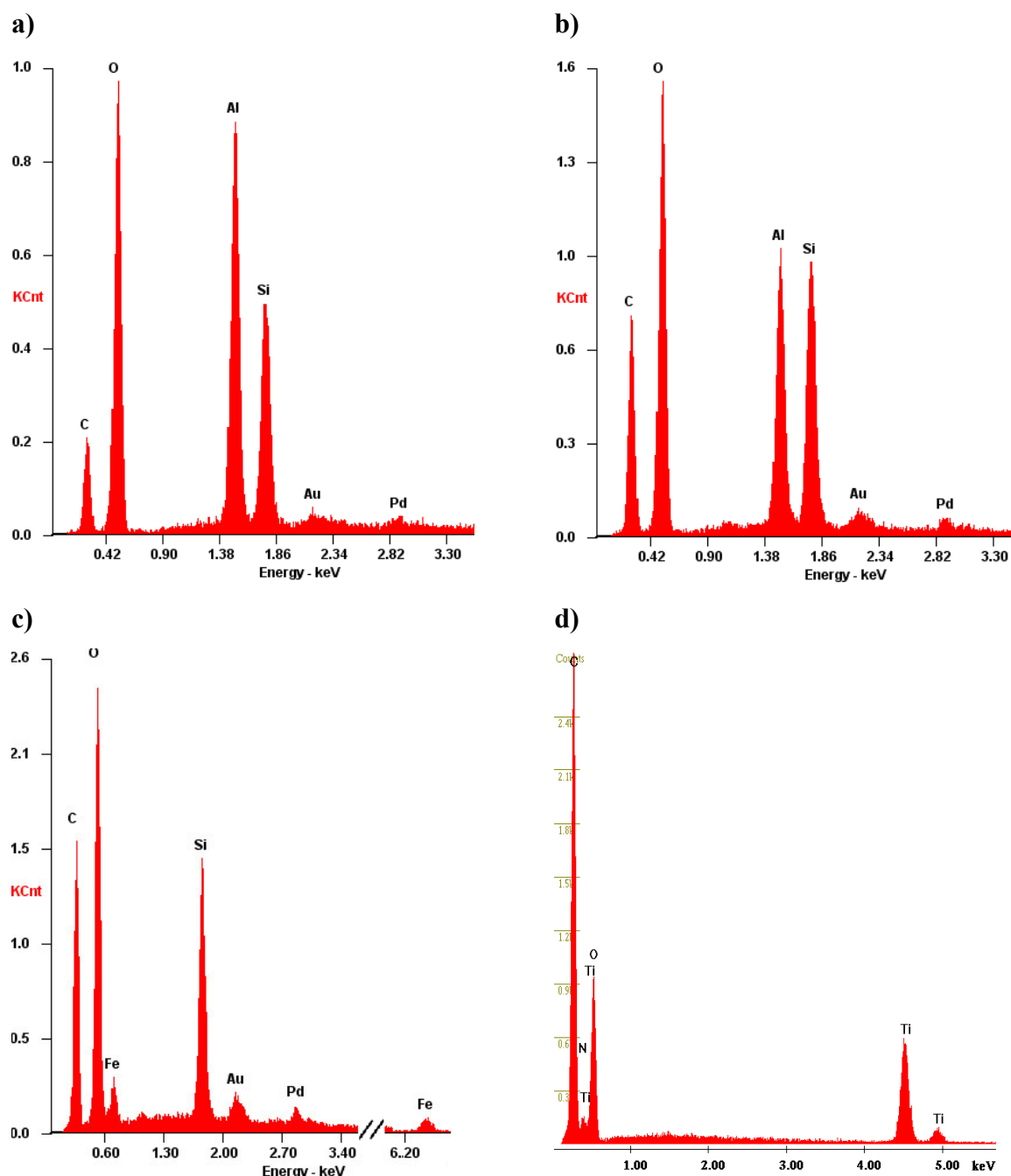
Figure 5.5. EDS spectrum of (a) Al-Fum, (b) CAU-10, (c) MIL-100(Fe), and (d) MIL-125(Ti)_NH$_2$.

The measurements of **single particle crushing strength** were performed for all MOF samples. The maximum compressive strength was evaluated for each granule (Figure 5.6), placed on its most stable position. For MIL-125(Ti)_NH$_2$, only 21 of the 61 analyzed particles were considered in the statistical evaluation due to the low crushing strength values. Table 5.3 summarizes data of crushing strength tests on each material, namely the number of particles tested, strength average, the standard deviation (STD), and the maximum and minimum strength values.

MIL-100(Fe) presents the highest mechanical resistance in opposition to CAU-10 where all particles presented a maximum crushing force of 1 N, which corresponds to the minimum value of the detection limit. Additionally, for Al-Fum, only five particles present a mechanical strength higher than 1 N.

a)

b)

c)

d)

e)
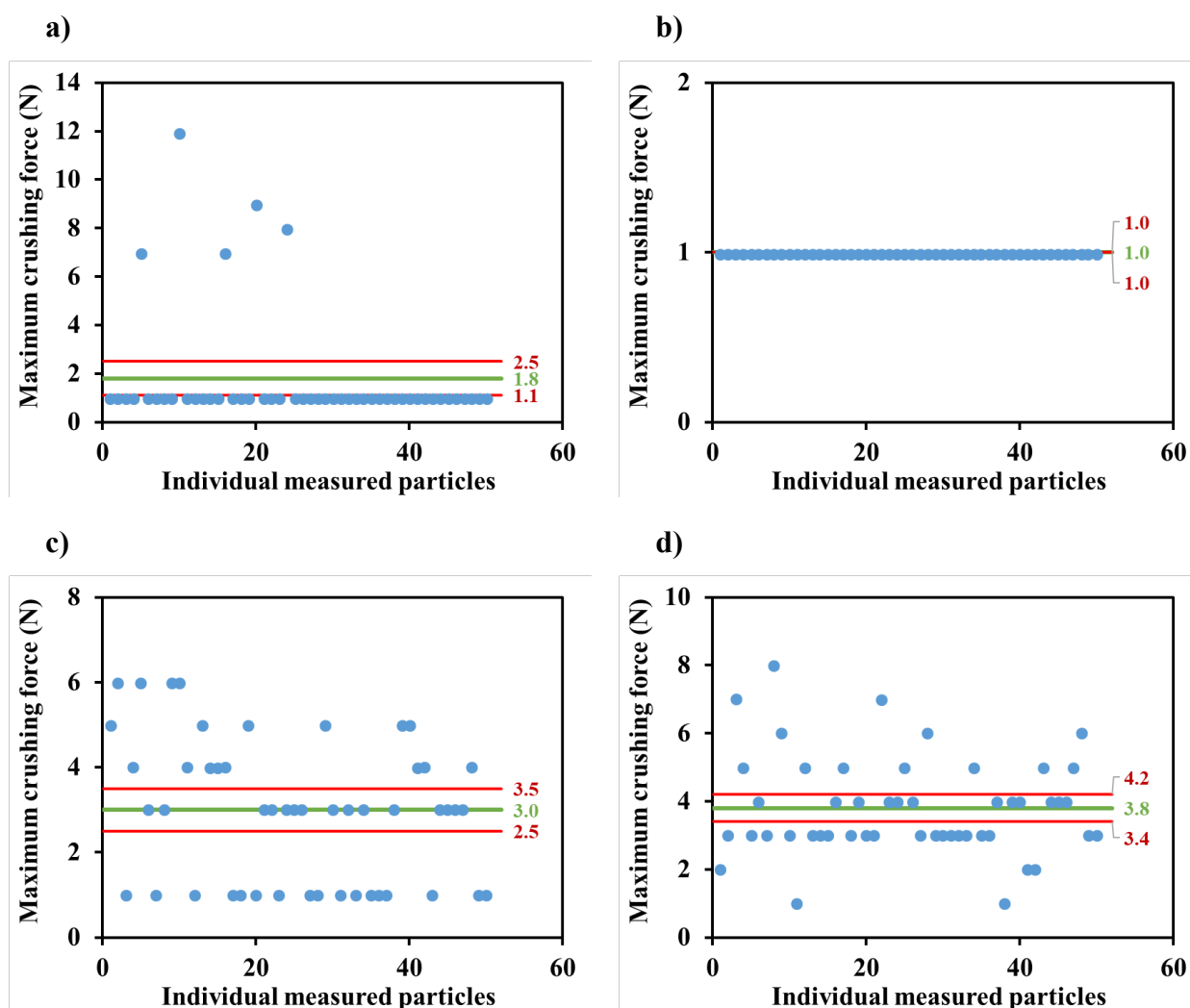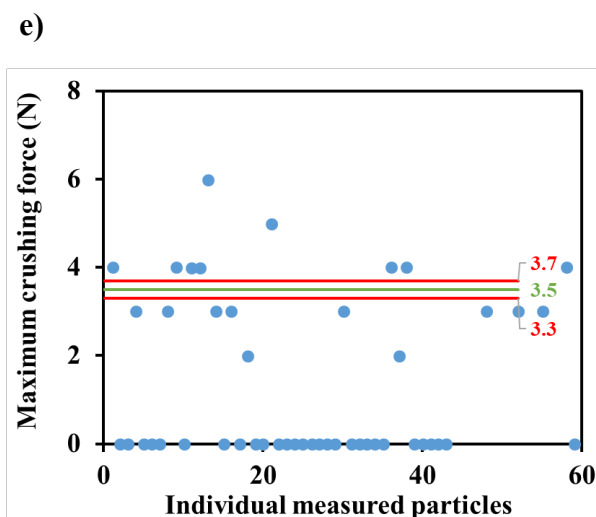
Figure 5.6. Maximum radial crushing strength of individual measured particles in the (a) Al-Fum, (b) CAU-10, (c) MIL-160(Al), (d) MIL-100(Fe), and (e) MIL-125(Ti)_NH₂. (—) represents the average, and (—) corresponds to a 95 % confidence interval of the average.

Table 5.3. Crushing strength of the five MOF samples.

Parameters (N)	Al-Fum	CAU-10	MIL-160(Al)	MIL-100(Fe)	MIL-125(Ti)_NH₂
Nº of particles	50	50	33	48	21
Crushing strength average	1.8	1.0	3.0	3.8	3.5
STD	2.4	0.0	1.7	1.4	0.9
Minimum value	1	1	1	1	< 2
Maximum value	12	1	6	8	6

Figure 5.7 illustrates the **XRD pattern** of each MOF sample. The XRD patterns revealed pronounced diffraction peaks (crystal phase) without a significant presence of broad peaks (amorphous phase), thus proving the crystallinity of all samples. All the materials displayed peaks at low angles ($2\theta < 20°$). MIL-100(Fe) and MIL-125(Ti)_NH₂ display peaks with the lowest relative intensities. The formation of nanocrystals on Al-Fum is probably responsible for the presence of small broad Bragg reflection peaks, as occurred in other reported studies [18, 30]. CAU-10 presents high crystallinity with high relative intensities of the reflections up to 30° (2θ). Some similarity between XRD patterns of MIL-160(Al) and CAU-10 is observed; however, MIL-160(Al) pattern presented smaller relative intensities of the diffraction Bragg peaks. This similarity was expected since both materials are isostructural, as previously

mentioned in Chapter 3. The MIL-100(Fe) diffraction pattern is in accordance with the pattern reported in the literature for this structure [9, 31-33]. MIL-125(Ti)_NH_2 shows similarity with XRD patterns described in the literature, particularly for low angles ($10° < 2θ < 20°$) [22, 34].
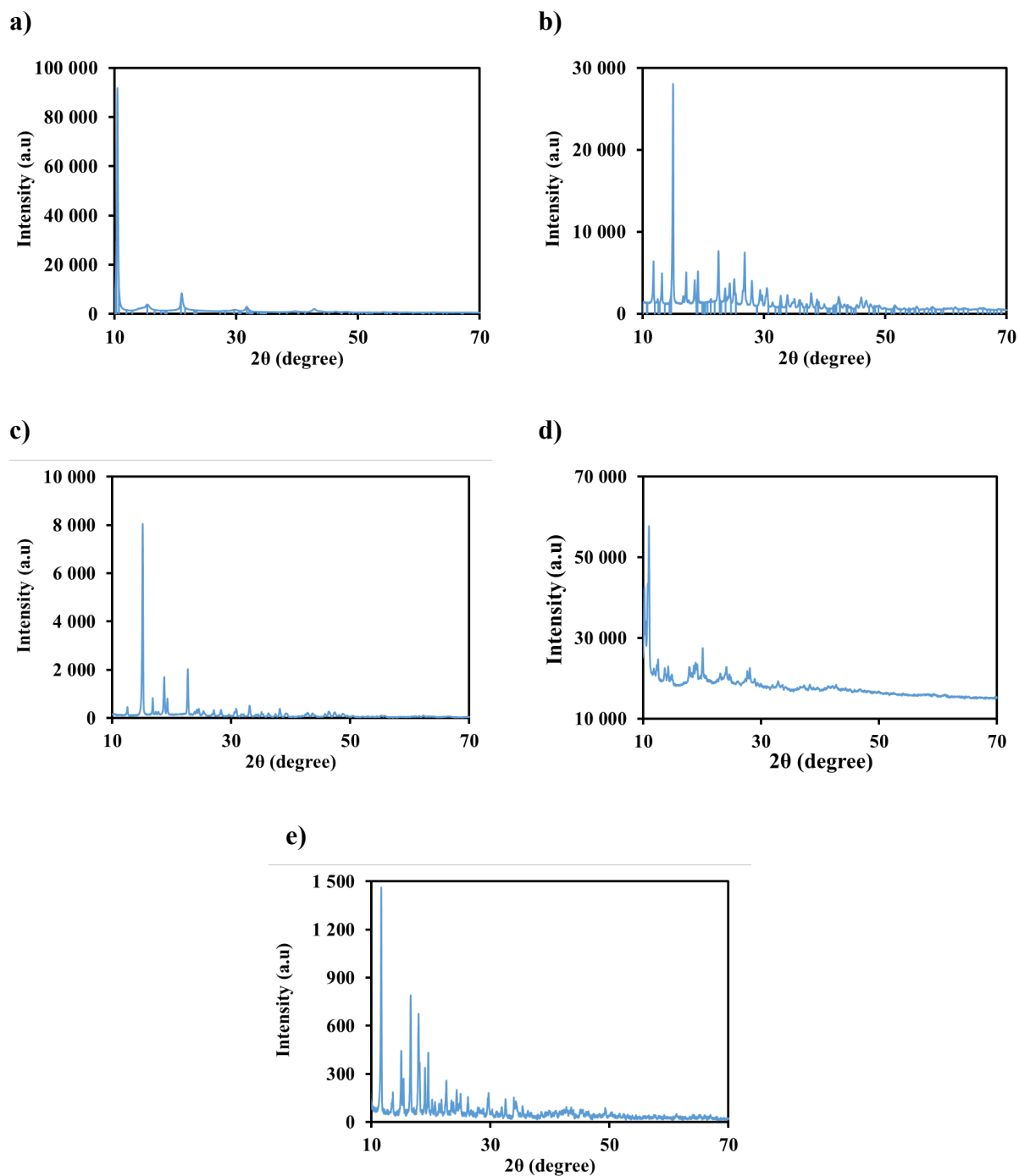
Figure 5.7. XRD pattern of shaped (a) Al-Fum, (b) CAU-10, (c) MIL-160(Al), (d) MIL-100(Fe), and (e) MIL-125(Ti)_NH_2.

5.2 Adsorption equilibrium data

Adsorption equilibrium data of CO_2, N_2, and O_2 were assessed on MIL-160(Al), MIL-100(Fe), and MIL-125(Ti)_NH_2, at 283 K, 303 K, and 323 K, in the MSB_1 (Figure 3.14a). The CO_2 and N_2 adsorption equilibrium isotherms on MIL-125(Ti)_NH_2 at 303 K, 323 K, and 343 K were previously reported by Regufe *et al.* [35]. The adsorption equilibrium isotherms of these air components allowed to evaluate their affinity towards the material and predict the possible competition on co-adsorption with water molecules. The Langmuir model was regressed against the experimental adsorption equilibrium data of CO_2, N_2, and O_2. On CAU-10 and Al-Fum, these gases were not measured due to the results obtained in the previously mentioned materials, which led to conclude on the inexistence of competition between the air gases and vapor water.

Water adsorption equilibrium isotherms were performed in all materials in the temperature range of 283 K to 343 K. On MIL-125(Ti)_NH_2 and MIL-100(Fe), measurements were performed in the MSB_1 (Figure 3.14a) at 283 K, 303 K, and 323 K, while on MIL-160(Al), CAU-10, and Al-Fum the measurements were performed in the temperature range of 303 K to 343 K, in the MSB_2 (Figure 3.14b). The use of two different microbalances for the same type of measurements was due to technical problems in the initially selected MSB_1, thus leading to a tuning of the temperature of the measurements on MIL-160(Al), CAU-10, and Al-Fum. Water adsorption equilibrium data were fitted using the CMMS model, the DISL model, and Polanyi's theory model. The Polanyi's theory is a predictive model of H_2O vapor adsorption equilibrium isotherms at different temperatures, which relates the amount adsorbed with the equilibrium adsorption potential providing a characteristic adsorption curve independent of temperature [36-39]. The characteristic curve is dependent on the adsorbent and adsorbate structure and only can be applied when water adsorption does not affect the MOF's structure [40, 41].

5.2.1 Al-Fum

H_2O vapor adsorption equilibrium isotherms were determined at 303 K, 313 K, 323 K, and 343 K between 0 and 34 mbar (Figure 5.8). The adsorption equilibrium isotherms obtained experimentally were fitted by the CMMS model (Chapter 4, eq. 4.3). Two different sets of fitting parameters were obtained for the adsorption equilibrium isotherms (Fitting 1 and Fitting 2), and they are summarized in Table 5.4. The water vapor adsorption equilibrium isotherms

present a Type IV shape following the IUPAC classification, and are similar to previous results reported in the literature [42-46]. At low-pressure region ($P/P_o < 0.25$ and $P/P_o < 0.28$ at 303 and 313 K, respectively), the material presents a hydrophobic behavior. The water vapor uptake reaches the saturation plateau at 303 K for a relative pressure of 38.5 % (13.5 mol·kg^{-1}). When comparing results for the same temperature, in the Han *et al.* [47] and Gökpinar *et al.* [45] studies, the adsorbed amount values are comparatively higher (the water vapour adsorbed was 15.8 and 14.3 mol·kg^{-1}, respectively at relative pressure of about 0.30). The same discrepancies in the amount of water vapor adsorbed occurred at 313 K and 323 K, presenting lower values compared to those reported in the Han *et al.* [47], Gökpinar *et al.* [45], and Lenzen *et al.* [46] studies.

Figure 5.8. Water vapor adsorption-desorption equilibrium isotherms on Al-Fum at 303 K, 313 K, 323 K, and 343 K as a function of (a) relative pressure and (b) absolute pressure (filled symbols: adsorption, open symbols: desorption), and CMMS fitting lines (a, b – Fitting 1; c, d – Fitting 2) (Chapter 4, eq. 4.3).

Table 5.4. Fitting parameters of CMMS model for water adsorption equilibrium isotherms on Al-Fum.

CMMS parameter	Value	
	Fitting 1	Fittting 2
q_{satL} (mol·kg^{-1})	1.95	13.8
q_{satI} (mol·kg^{-1})	12.1	10.9
$K_{\infty, I}$ (bar^{-1})	2.45×10^{-8}	1.60×10^{-8}
$K_{\infty,o}$ (bar^{-1})	1.54×10^{-7}	5.05×10^{-9}
$K_{\infty,L}$ (bar^{-1})	3.92×10^{-9}	8.45×10^{-7}
$-\Delta H_I$ (kJ·mol^{-1})	55.4	56.2
$-\Delta H_o$ (kJ·mol^{-1})	32.0	43.0
$-\Delta H_L$ (kJ·mol^{-1})	59.6	40.8

Figure 5.9 plots the adsorbed amount against the equilibrium adsorption potential at 303 K, 313 K, 323 K, and 343 K, yielding a single characteristic curve as predicted by the Polanyi's theory.

Figure 5.9. Polanyi's characteristic curve of water on Al-Fum at 303 K, 313 K, 323 K, and 343 K (filled symbols: adsorption, open symbols: desorption).

The isosteric heat of adsorption of water on Al-Fum was determined by the Clausius-Clapeyron equation (Chapter 4, eq. 4.10), applied to experimental data of the four temperatures

(303 K, 313 K, 323 K, and 343 K). The computed isosteric heat of adsorption values are in the range of 50.6 to 60.6 kJ·mol^{-1}. The values obtained are similar to isosteric heat range values reported in previous studies performed by Han *et al.* (45.3 to 51.6 kJ·mol^{-1}) [47], Teo *et al.* (36.7 to 52.5 kJ·mol^{-1}) [43], and Gökpinar *et al.* (46.6 to 55.8 kJ·mol^{-1}) [45].
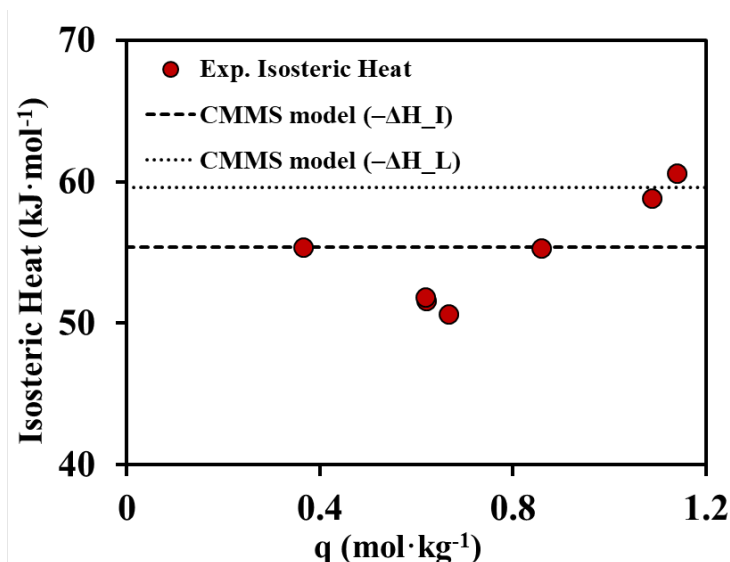
Figure 5.10. Isosteric heat of adsorption as a function of H_2O adsorption loading on Al-Fum.

5.2.2 CAU-10

H_2O vapor adsorption equilibrium isotherms were determined at four different temperatures (303 K, 313 K, 323 K, 343 K) in the pressure range of 0 to 32 mbar. Adsorption equilibrium isotherms were fitted by the CMMS model (Chapter 4, eq. 4.3), and the parameters are shown in Table 5.5. Figure 5.11 shows the adsorption equilibrium isotherms on CAU-10, revealing a characteristic Type IV shape, by the IUPAC classification. No hysteresis is observed in the desorption-branch isotherms. The shape of the obtained adsorption equilibrium isotherms is similar to the shape of the adsorption equilibrium isotherms already reported in the literature; yet, the steep rise observed usually is not so sharp [44, 48, 49]. Nonetheless, in the study performed by Cadiau and his co-workers, the same sudden increase was observed [4]. This sharp rise in the adsorption equilibrium isotherms occurs at a relative pressure of 0.18 (7.5 mbar), 0.21 (16 mbar), 0.24 (29 mbar), and 0.32 for 303 K, 313 K, 323 K, and 343 K, respectively. Indeed, until the steep rise, the material presents a hydrophobic behavior. The increase on the water uptake at 303 K starts at $P/P_o = 18$ %, reaching the saturation plateau at a relative pressure of 20 % P/P_o with 13.5 mol·kg^{-1}, while in López-Cervantes *et al.* study [48],

the step occurred in the relative pressure range of 0.20 to 0.40 (16.0 mol·kg^{-1}). However, Cadiau and co-workers reported a sharp rise in the range of 0.15 to 0.18 (15.7 mol·kg^{-1}) [4].
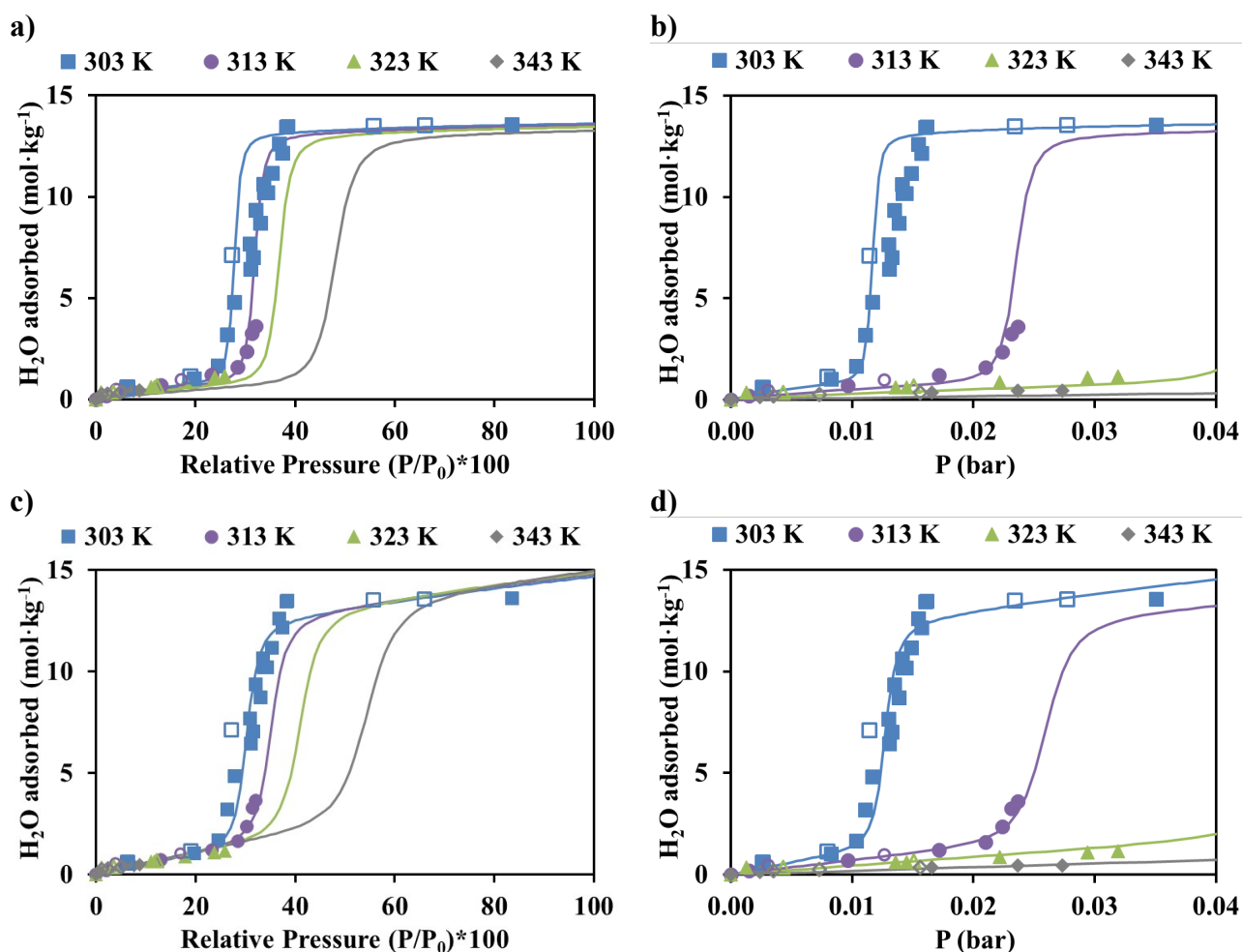
a)   b)
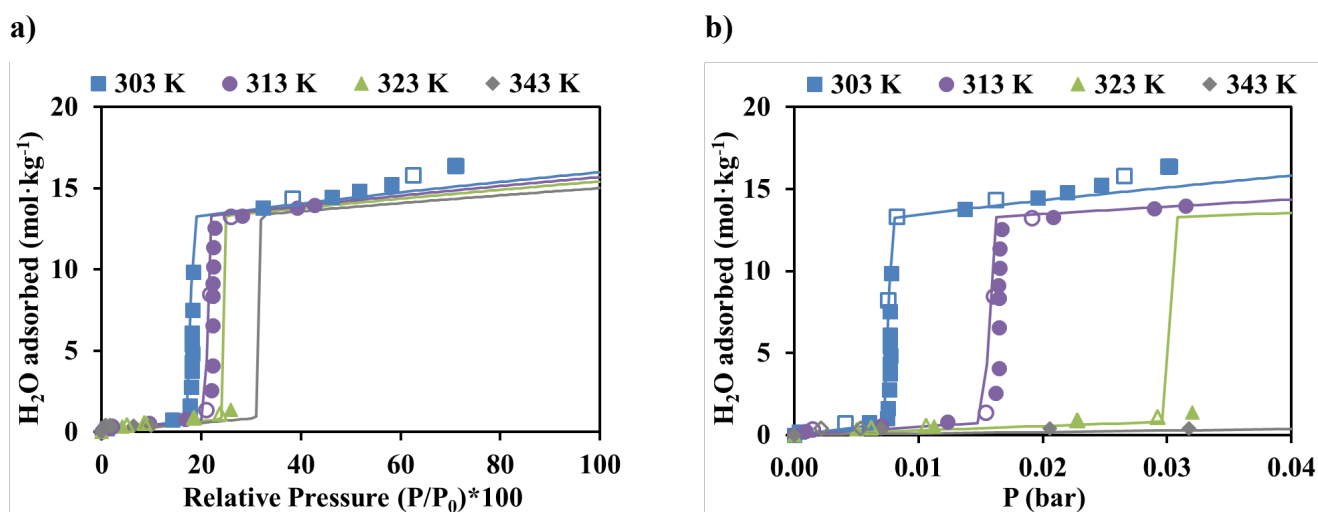
Figure 5.11. Water vapor adsorption-desorption equilibrium isotherms on CAU-10 at 303 K, 313 K, 323 K, and 343 K as function of (a) relative pressure and (b) absolute pressure (filled symbols: adsorption, open symbols: desorption), and CMMS fitting lines (Chapter 4, eq. 4.3).

Table 5.5. Fitting parameters of CMMS model for water adsorption isotherms on CAU-10.

CMMS parameter	Value
q_{satL} (mol·kg^{-1})	20.2
q_{satI} (mol·kg^{-1})	12.5
$K_{\infty,I}$ (bar^{-1})	2.99×10^{-8}
$K_{\infty,o}$ (bar^{-1})	8.50×10^{-9}
$K_{\infty,L}$ (bar^{-1})	5.25×10^{-9}
$-\Delta H_I$ (kJ·mol^{-1})	56.0
$-\Delta H_o$ (kJ·mol^{-1})	24.0
$-\Delta H_L$ (kJ·mol^{-1})	52.1

Figure 5.12 shows the Polanyi's characteristic curves of CAU-10 at different temperatures, which collapse into a single curve, as can be observed.
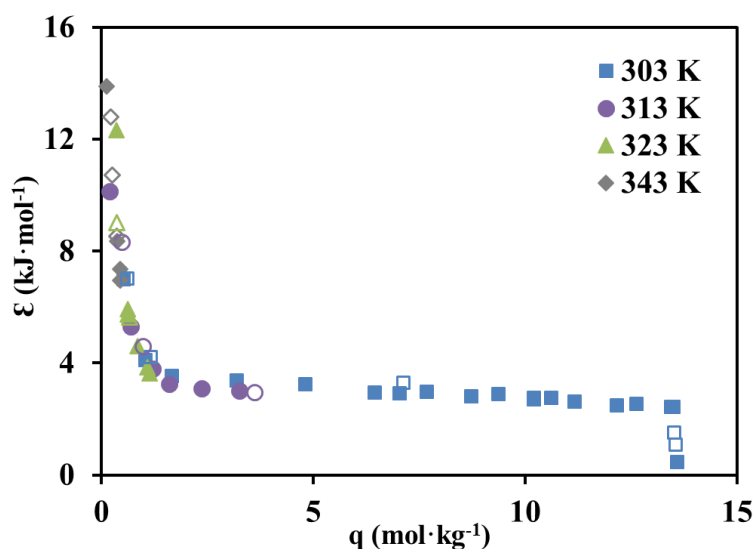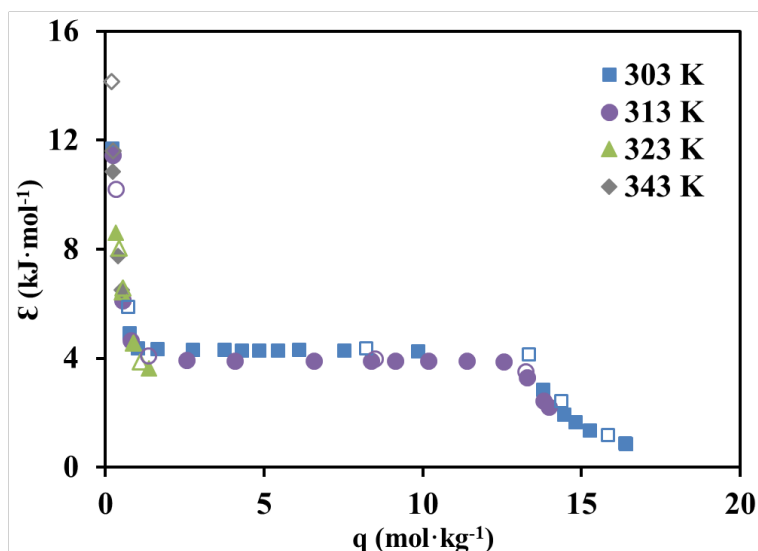
Figure 5.12. Polanyi's characteristic curve of water on CAU-10 at 303 K, 313 K, 323 K and 343 K (filled symbols: adsorption, open symbols: desorption).

Figure 5.13 shows the isosteric heat of adsorption as a function of loading, obtained by applying the Clausius-Clapeyron equation (Chapter 4, eq. 4.10) to the experimental data. An increase of the isosteric heats of adsorption values with the loading is visible. The isosteric heat values tend to values above the enthalpic parameters obtained when regressing the CMMS model against the experimental data reported in Table 5.5. The obtained isosteric heat of adsorption values are in accordance with the values reported in the literature by Cadiau *et al.* (~ 50.0 kJ·mol⁻¹) [4], determined by Clausius-Clapeyron equation. In the study performed by Teo and Chakraborty the estimated enthalpic parameter was 54.6 kJ·mol⁻¹ [44].
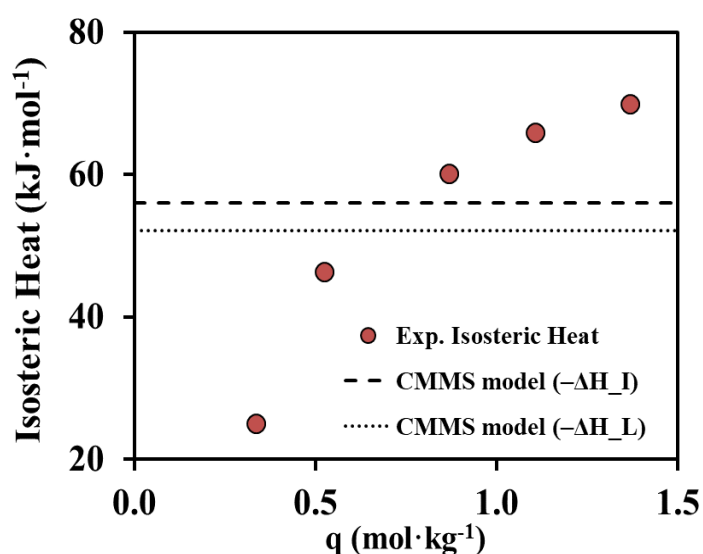
Figure 5.13. Isosteric heat as a function of H_2O loading on CAU-10.

5.2.3 MIL-160(Al)

O₂, N₂, and CO₂ adsorption equilibrium data were assessed at 283 K, 303 K, and 323 K on MIL-160(Al) (Figure 5.14). These adsorption equilibrium data were fitted with the Langmuir model (Chapter 4, eq. 4.1). The parameter estimation was carried out by minimizing the sum of the square of the differences between the predicted and experimental values, using the Excel Solver. Table 5.6 presents the Langmuir model parameters for each adsorbate. In all adsorption equilibrium isotherms, no hysteresis was observed. O_2 and N_2 adsorption equilibrium isotherms exhibit an almost linear shape and similar adsorbed amount. CO_2 adsorption equilibrium isotherms present a Type I shape according to IUPAC classification, which agrees with adsorption on microporous adsorbents [50]. A similar pattern was also previously presented for CO_2 adsorption on Al-MOF [20]. The adsorbed amount increases following the sequence $N_2 < O_2 < CO_2$, which agrees with previous results reported for CO_2 and N_2 on MIL-160(Al) [50]. Adsorption equilibrium data on O_2 on MIL-160(Al) are not available in the literature. CO_2 adsorption equilibrium isotherm at 303 K is in agreement with the results previously reported in the literature for shaped MIL-160(Al) [50]. In Borges *et al.* study, at 1.49 bar and 303 K, the CO_2 amount adsorbed was 4.06 mol·kg⁻¹, which is in excellent agreement with the one reported in our study (CO_2 amount adsorbed of 3.96 mol·kg⁻¹ at 1.49 bar and 303 K) [50]. MIL-160(Al) can adsorb about 20 % more CO_2 than aluminum fumarate MOF at 303 K, and 30 % at 323 K [20]. Regarding N_2 adsorption equilibrium isotherms, the same linear shape is presented in the study performed by Borges and co-workers and identical adsorbed amounts of N_2 at the same conditions (at 2.9 bar, the N_2 adsorbed amount was 0.53 mol·kg⁻¹) [50].

c)
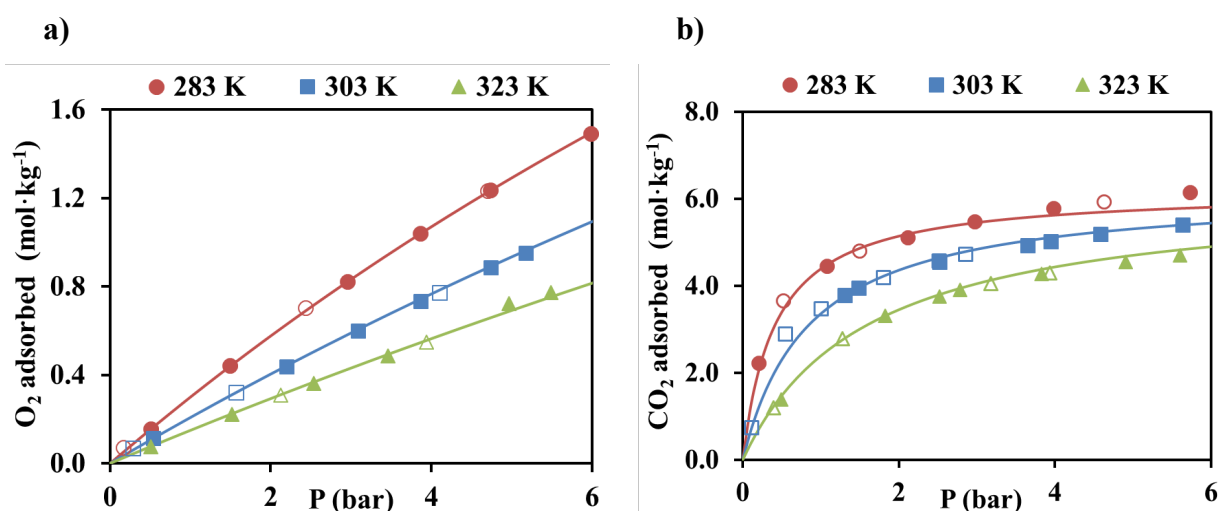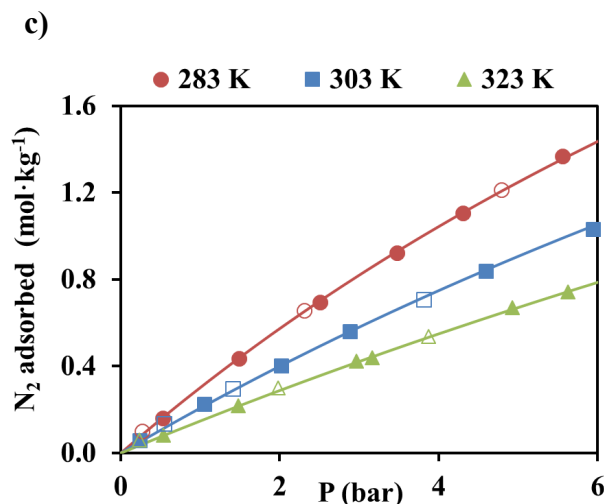
Figure 5.14. Adsorption–desorption equilibrium isotherms of (a) O_2, (b) CO_2, and (c) N_2 on MIL-160(Al) at 283 K, 303 K and 323 K (filled symbols: adsorption, open symbols: desorption). The lines represent the Langmuir model fittings.

Table 5.6. Langmuir model parameters for CO_2, N_2, and O_2 on MIL-160(Al).

Gas	q_m (mol·kg^{-1})	$K_\infty \times 10^5$ (bar^{-1})	$-\Delta H$ (kJ·mol^{-1})
CO_2	6.21	4.53	25.6
N_2	5.77	0.14	14.1
O_2	7.43	0.13	13.6

The isosteric heats of adsorption were calculated by the Clausius-Claperyon equation. These values were compared with the enthalpic parameter of the Langmuir model (Figure 5.15). With the increase of loading, the computed isosteric heats of adsorption seem to converge to the values obtained by regressing the experimental data to the Langmuir model (Table 5.6). The constant values obtained for N_2 and O_2 indicate that the energetic homogeneity assumed by the Langmuir model is valid for these two compounds. While the slight decrease of the isosteric heat of adsorption with loading observed for CO_2, indicates at least two different sites, or the presence of repulsive forces between neighboring adsorbed CO_2 molecules. Nevertheless, the Langmuir model describes the adsorption equilibrium for this adsorbate at the studied conditions (see Figure 5.14). Additionally, CO_2 and N_2 isosteric heats of adsorption in this work are slightly lower than those reported in Borges *et al.* study (33.0 and 16.7 kJ·mol^{-1}, respectively), but closer to CO_2 isosteric heat of adsorption presented in Brandt *et al.* study (29.8 kJ·mol^{-1} at 4 mol·kg^{-1}) [50, 51].
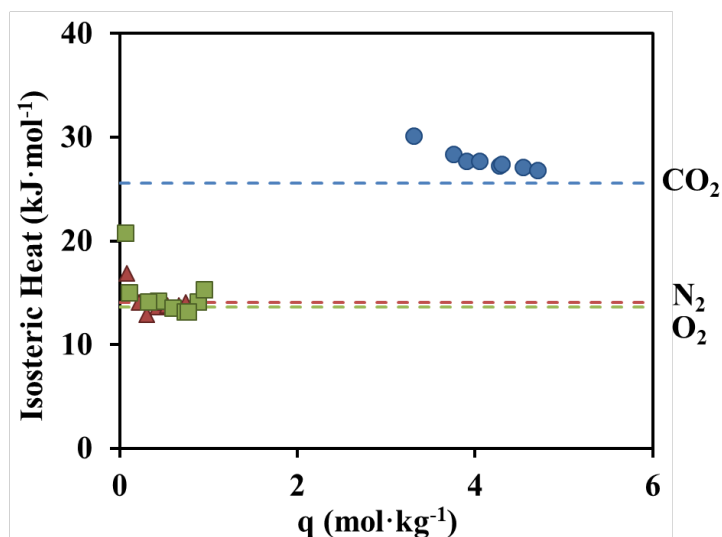
Figure 5.15. Isosteric adsorption heats as a function of adsorbent loading for N_2 (triangles), CO_2 (circles), and O_2 (squares) on MIL-160(Al). The dashed lines correspond to the heat of adsorption obtained by the Langmuir model.

H_2O vapor adsorption equilibrium isotherms at 303, 323, and 343 K were measured in the range of pressures between 0 – 32 mbar (Figure 5.16b). The adsorption equilibrium data were fitted by the CMMS model (Chapter 4, eq. 4.3), and the obtained parameters are presented in Table 5.7. CMMS model was capable of describing the H_2O vapor adsorption behavior on MIL-160(Al). Adsorption equilibrium isotherms exhibit an S shape (Type V isotherm, according to IUPAC classification) (see Figure 5.16a), confirming the hydrophilic nature of the adsorbent [4, 6, 20, 38, 52]. As stated in the Cadiau *et al.* study, the hydrophilic nature of MIL-160(Al) is due to the interaction of water molecules and the hydroxyl groups which are present in the pores [4]. The isotherms shape is in agreement with the ones already reported in the open literature [4, 5, 7, 19, 53, 54], but in the Wahiduzzaman *et al.* study, at 303 K for lower relative pressures (P/P_o < 0.16), the amount adsorbed values are comparatively lower to the ones reported in this study (*e.g.*, P/P_o = 0.089 presents 1.5 mol·kg^{-1} of H_2O adsorbed amount) [5]. Yet, for higher relative pressures (P/P_o > 0.16), the values are higher (about 17%) than those reported in this study [5]. By comparing further the obtained values for the H_2O vapor adsorbed amount with others in the literature, one can see that they are slightly lower than the ones reported in the Wang *et al.* study [54], for relative pressures between 0.15 and 0.80; however, for relative pressures below and above this range, they are very similar. In Cadiau *et al.* and Hastürk *et al.* studies, the reported adsorbed amount values agree with the ones presented in Figure 5.16 [4, 19].
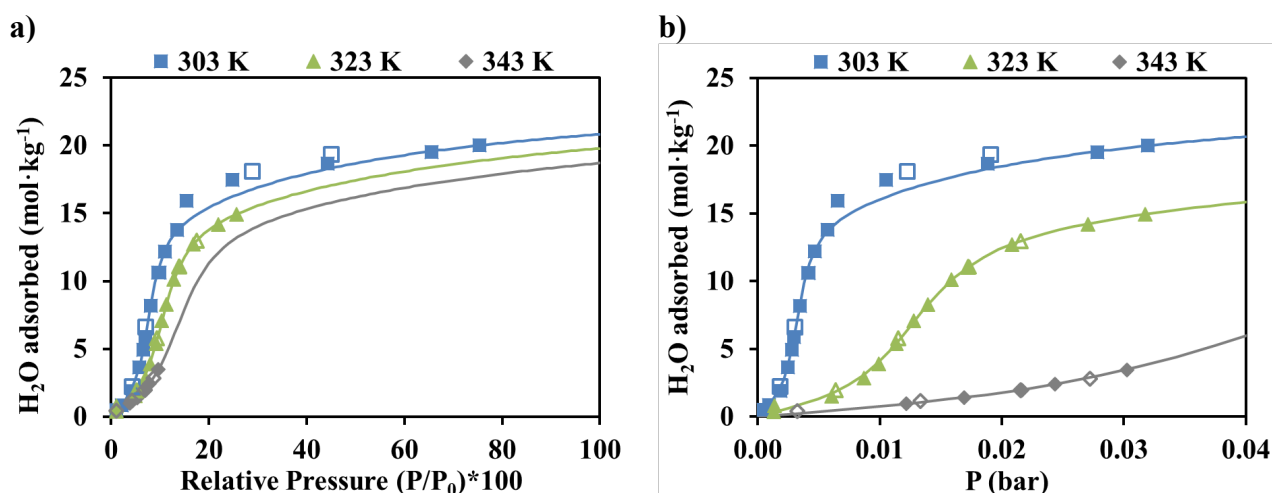
Figure 5.16. Water vapor adsorption-desorption equilibrium isotherms on MIL-160(Al) at 303 K, 323 K, and 343 K as a function of (a) relative pressure and (b) absolute pressure (filled symbols: adsorption, open symbols: desorption), and CMMS fitting lines (Chapter 4, eq. 4.3).

Table 5.7. Fitting parameters of CMMS model for water adsorption equilibrium on MIL-160(Al).

CMMS parameter	Value
q_{satL} (mol·kg^{-1})	13.2
q_{satI} (mol·kg^{-1})	11.3
$K_{\infty,I}$ (bar^{-1})	5.24×10^{-8}
$K_{\infty,o}$ (bar^{-1})	2.81×10^{-7}
$K_{\infty,L}$ (bar^{-1})	7.08×10^{-9}
$-\Delta H_I$ (kJ·mol^{-1})	56.6
$-\Delta H_o$ (kJ·mol^{-1})	43.9
$-\Delta H_L$ (kJ·mol^{-1})	57.6

Polanyi's characteristic curve for MIL-160(Al) is presented in Figure 5.17; however, a small deviation is visible at the temperature of 303 K. This deviation increases mainly for loadings above 14 mol·kg^{-1}. Similar characteristic curve was reported by Gordeeva *et al.* [55], presenting a small divergence compared to this study in the inflection point between 16 to 20 mol·kg^{-1}.
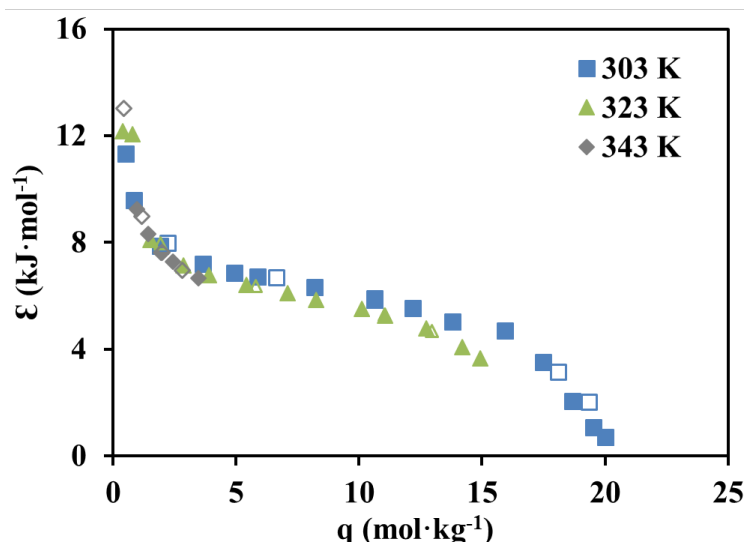
Figure 5.17. Polanyi's characteristic curve of water on MIL-160(Al) at 303 K, 323 K and 343 K (filled symbols: adsorption, open symbols: desorption).

The isosteric heat of adsorption was determined, based on the experimental equilibrium data at three temperatures, by the Clausius-Clapeyron equation (Chapter 4, eq. 4.10) (Figure 5.18). The isosteric heat values obtained are between 50.7 and 53.7 kJ·mol^{-1}, close to the value attained by the CMMS model for the enthalpic Langmuir site parameter $- -\Delta H_L$. Additionally, they are also in good agreement with those reported in the literature by Cadiau *et al.* (54 kJ·mol^{-1}) [4], Cui *et al.* (50 kJ·mol^{-1}) [53], Gökpinar *et al.* (52.1 kJ·mol^{-1}) [8], and Permyakova *et al.* (56.4 kJ·mol^{-1}) [6].
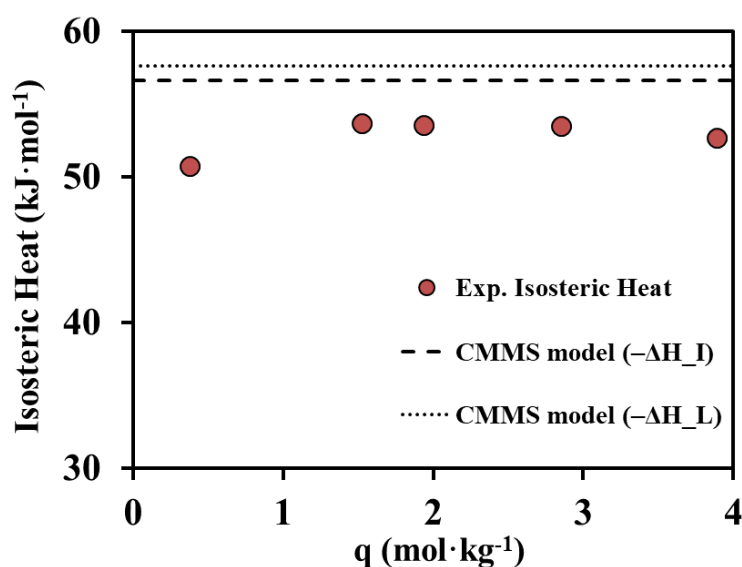
Figure 5.18. Isosteric heat as a function of H$_2$O loading on MIL-160(Al).

5.2.4 MIL-100(Fe)

O_2, CO_2, and N_2 adsorption equilibrium isotherms at 283 K, 303 K, and 323 K were well described with the Langmuir model (Figure 5.19). The obtained adsorption equilibrium model parameters are given in Table 5.8. All isotherms were seemly fitted, although in N_2 adsorption equilibrium isotherm at 323 K is visible a small deviation. This same adsorption equilibrium isotherm is the only one that presents hysteresis, yet it is not significant. Indeed, adsorption equilibrium isotherms with almost a linear shape were observed for O_2 and N_2, while CO_2 shows a typical monotonic isotherm (Type I), according to IUPAC classification [56]. CO_2 is the gas that presents higher affinity towards MIL-100(Fe) followed by O_2 and N_2. N_2 adsorption equilibrium isotherms shape follows the reported literature [31, 57-60]. Moreover, the N_2 loading is similar to the one reported in Kim *et al.* study [31], in granules, at 283 K, but at high pressures starts to deviate. Namely, at 5 bar, it was obtained 0.59 mol·kg^{-1}, while Kim *et al.* [31] reports about 0.70 mol·kg^{-1}. At 323 K, the N_2 adsorbed amount agrees with the values recorded by Ribeiro *et al.* [60] for similar granulated material. The O_2 adsorption equilibrium isotherms obtained are in agreement with previous isotherms reported in the literature for MIL-100(Fe) [58], as well as the CO_2 adsorption equilibrium isotherm's shape [61-64].

a)

b)

c)
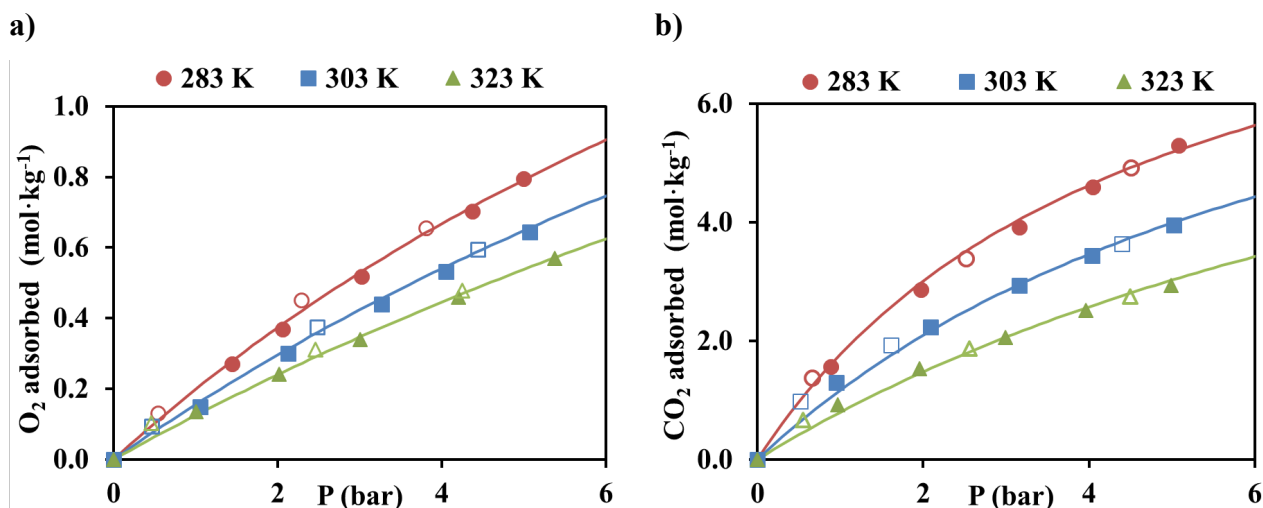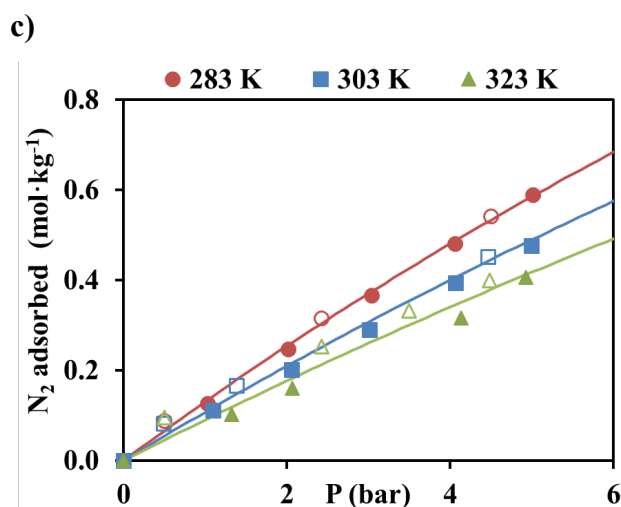
Figure 5.19. Adsorption–desorption equilibrium isotherms of (a) O_2, (b) CO_2, and (c) N_2 on MIL-100(Fe) at 283 K, 303 K, and 323 K (filled symbols: adsorption, open symbols: desorption). The lines represent the Langmuir model fittings.

Table 5.8. Langmuir model parameters for CO_2, N_2, and O_2 on MIL-100(Fe).

Gas	q_m (mol·kg^{-1})	$K_\infty \times 10^3$ (bar^{-1})	$-\Delta H$ (kJ·mol^{-1})
CO_2	9.97	0.14	17.3
N_2	4.44	1.4	7.22
O_2	3.13	1.3	9.31

The isosteric heats of adsorption as a function of the adsorbate loading (CO_2, O_2, and N_2) are presented in Figure 5.20. As expected, N_2 and O_2 have similar isosteric heats of adsorption, and they tend to the value obtained by regressing the Langmuir model against the adsorption equilibrium experimental data. Additionally, similar behavior was observed for the CO_2's isosteric heat of adsorption. The isosteric heats of adsorption computed for the CO_2 are lower than those reported in the study performed by Mei *et al.* (30 – 26 kJ·mol^{-1} at 0.25 and 1.8 mol·kg^{-1}, respectively) [62]. Nonetheless, in a study by Mutyala *et al.* [63], the reported isosteric heats of adsorption are lower, *e.g.,* 8.9 kJ·mol^{-1} for 1.1 mol$_{CO2}$·kg^{-1}. The isosteric heat of adsorption values for O_2 are similar to Gallis *et al.* study [58], reporting values in the range of 8.5 to 6.2 kJ·mol^{-1} for O_2 loadings between 0.01 and 0.11 mol$_{O2}$·kg^{-1}. Additionally, the N_2 isosteric heats of adsorption values, also presented in the above mentioned study, are between

11.5 and 9.1 kJ·mol^{-1} for loadings up to 0.11 mol·kg^{-1}. These values are slightly higher than in this study [58]. Kim *et al.* [31] obtained N$_2$ heat of adsorption in the range of 20.6 and 18.5 kJ·mol^{-1}, for adsorption coverages between 0.06 and 0.76 mol$_{N2}$·kg^{-1}.
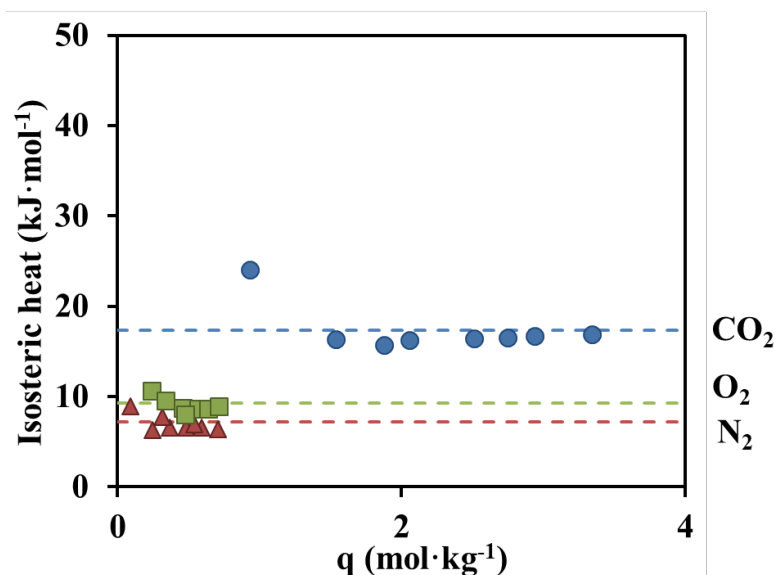
Figure 5.20. Isosteric heats of adsorption as a function of loading for N$_2$ (triangles), CO$_2$ (circles), and O$_2$ (squares) on MIL-100(Fe). The dashed lines correspond to the adsorption heat obtained by the Langmuir model.

H$_2$O vapor adsorption equilibrium isotherms measured at three temperatures are shown in Figure 5.21. The DISL model (Chapter 4, eq. 4.8) provided a satisfactory fitting of experimental data. Table 5.9 presents the parameters obtained by the regression of the model against the experimental data. At 283 K and 303 K, isotherms present three distinct steps. The first step occurs at low relative pressures (P/P$_o$ < 0.21) possibly corresponding to the adsorption on the open metal sites. The following step (0.21 < P/P$_o$ < 0.30) corresponds to the filling of the smaller mesopores/cages (25 Å) followed by the last step (0.36 < P/P$_o$ < 0.40) which occurs due to the filling in the larger pores/cages (29 Å). The water adsorption equilibrium isotherms follow the shape reported in the literature [15, 65-68] and classified as Type VI according to the IUPAC classification. At 303 K, Mileo *et al.* [15] reported higher values of the amount adsorbed, and the saturation plateaus occurred for higher relative pressures (at relative pressures of 0.4 and 0.56). Water adsorption equilibrium isotherm at 323 K followed the same trend, presenting H$_2$O adsorbed amounts lower than those reported in the Küsgens *et al.* study [65]. At relative pressure of 0.16, the amount adsorbed in Küsgens *et al.* study [65] was 6.55 mol·kg^{-1} against 3.73 mol·kg^{-1} in the present study.
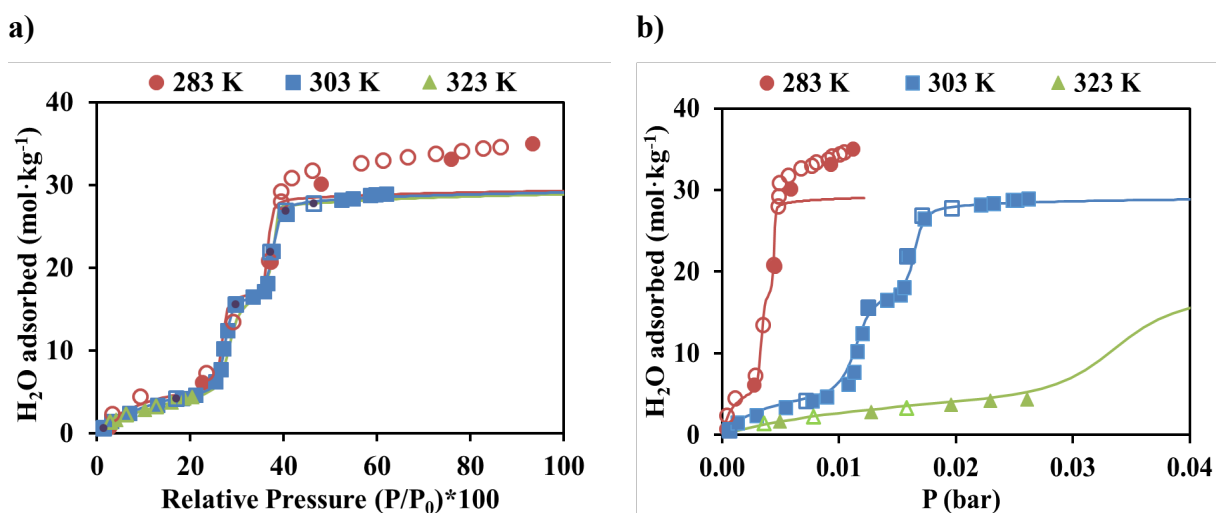
Figure 5.21. Water vapor adsorption-desorption equilibrium isotherms on MIL-100(Fe) at 283 K, 303 K, and 323 K as a function of (a) relative pressure and (b) absolute pressure (filled symbols: adsorption, open symbols: desorption), and DISL model (lines) (Chapter 4, eq. 4.8).

Table 5.9 DISL model parameters for water adsorption on MIL-100(Fe).

DISL parameter	Value
q_{satL} (mol·kg^{-1})	6.84
$q_{satI,1}$ (mol·kg^{-1})	12.3
$q_{satI,2}$ (mol·kg^{-1})	10.4
$K_{\infty,I,1}$ (bar^{-1})	2.35×10^{-6}
$K_{\infty,I,2}$ (bar^{-1})	5.17×10^{-7}
$K_{\infty,o,1}$ (bar^{-1})	1.04×10^{-5}
$K_{\infty,o,2}$ (bar^{-1})	2.34×10^{-2}
$K_{\infty,L}$ (bar^{-1})	1.15×10^{-7}
$-\Delta H_{I,1}$ (kJ·mol^{-1})	43.9
$-\Delta H_{I,2}$ (kJ·mol^{-1})	46.8
$-\Delta H_{o,1}$ (kJ·mol^{-1})	20.5
$-\Delta H_{o,2}$ (kJ·mol^{-1})	1.33
$-\Delta H_{L}$ (kJ·mol^{-1})	54.0

The Polanyi characteristic curves of water vapor on MIL-100(Fe) are shown in Figure 5.22. As predicted by the Polanyi potential theory, the characteristic curves at different temperatures fell onto a single one, although from 28 mol·kg^{-1} a small deviation is presented. The characteristic curve shape is similar to the one reported in the Gordeeva *et al.* [55] study, which used data assessed by Jeremias and co-workers, in a MIL-100(Fe) powder sample [69]. Comparatively with MIL-100(Fe) in powder form, the inflection points occurred at lower water adsorbed amounts.
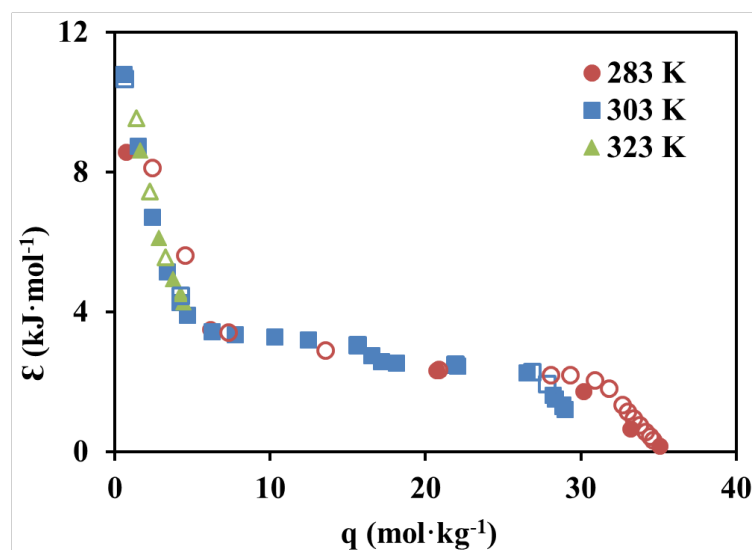
Figure 5.22. Polanyi's characteristic curve of water on MIL-100(Fe) at 283 K, 303 K, and 323 K (filled symbols: adsorption, open symbols: desorption).

Isosteric heats of adsorption of water vapor on MIL-100(Fe) obtained through the Clausius-Clapeyron equation are plotted in Figure 5.23. The isosteric heats of adsorption tend to increase with the H$_2$O loadings, almost reaching the $-\Delta H$ Langmuir parameter value at the water uptake of 4.40 mol·kg^{-1}. These values are in accordance with the average heat of adsorption of 48.83 kJ·mol^{-1} determined by Küsgens *et al.* [65]. The isosteric heat values obtained in the Jeremias *et al.* [69] study are in between 49.1 and 88.4 kJ·mol^{-1} for H$_2$O loadings between 3.05 and 23.6 mol·kg^{-1}. However, the heat of adsorption obtained in the same study by calorimetry was of 44.4 kJ·mol^{-1}, which agrees well with the value reported in this study.
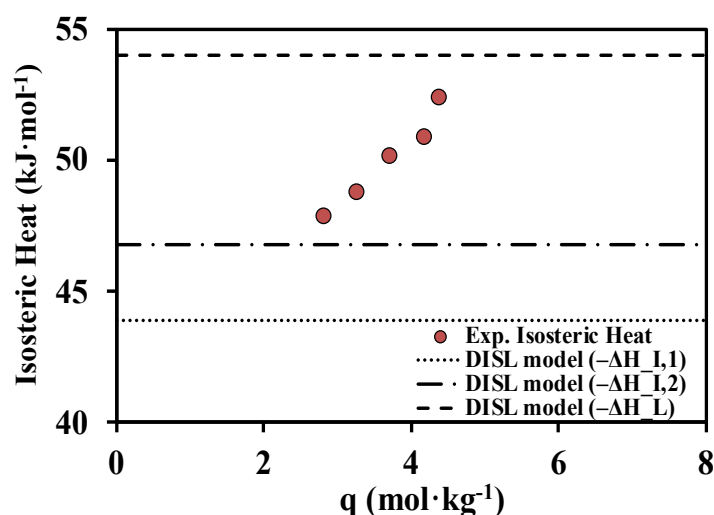
Figure 5.23. Isosteric heat as a function of H_2O loading on MIL-100(Fe).

5.2.5 MIL-125(Ti)_NH$_2$

Adsorption equilibrium isotherms for CO$_2$ and N$_2$ (283 K) **and O$_2$** (283 K, 303 K, and 323 K), on MIL-125(Ti)_NH$_2$, are represented in Figure 5.24. The Langmuir model was regressed against the experimental adsorption equilibrium data, and the model parameters are included in Table 5.10.

The O_2 and N_2 adsorption equilibrium isotherms present an almost linear shape while the CO_2 adsorption equilibrium isotherms are of Type I according to the IUPAC classification [56]. The amount adsorbed of O_2 and N_2 on MIL-125(Ti)_NH$_2$ are comparable, as already observed for MIL-100(Fe) and MIL-160(Al) materials, probably due to their similar molecular properties, such as kinetic diameters (3.46 Å and 3.64 Å for O_2 and N_2, respectively) and polarizability (1.58×10^{-30} m^3 and 1.74×10^{-30} m^3 for O_2 and N_2, respectively), controlling their affinity towards the adsorbent [70-72]. It should be noted that there is no data available in the literature on O_2 adsorption on MIL-125(Ti)_NH$_2$. Regarding the N_2 adsorbed amount, Kim *et al.* [22] reported the same linear behavior at 298 K. At 0.98 bar and 298 K, the N_2 amount adsorbed was 0.24 mol·kg^{-1}. This amount is in excellent agreement with the one reported in this study for the shaped material. The CO_2 and N_2 isotherms for this material at 303 K, 323 K, and 343 K were previously reported by Regufe *et al.* [35]. The CO_2 and N_2 isotherms at 303 K and 323 K reported in that study are shown together with those obtained in the present study at 283 K (Figure 5.24b and c, respectively). The amounts of CO_2 adsorbed at 273 K, and 288 K presented by Kim *et al.* [22] were slightly higher than those in the present study, possibly due

to the powder form of the material used in the study. Also, Wiersum *et al.* reported a higher amount of CO_2 adsorbed at 303 K [73].

a)

b)

c)
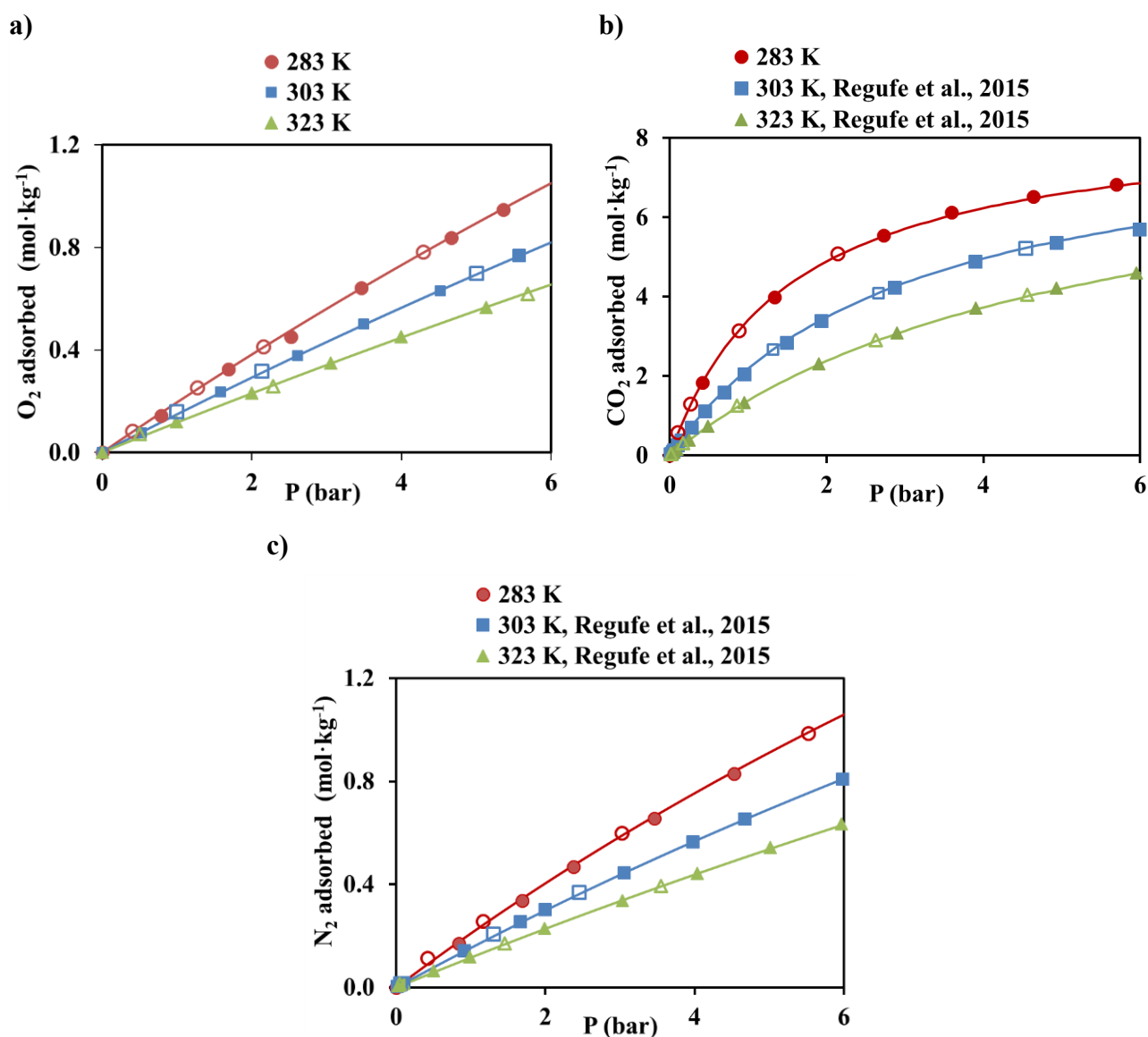
Figure 5.24. Adsorption–desorption equilibrium isotherms of (a) O_2, (b) CO_2, and (c) N_2 on MIL-125(Ti)_NH_2 at 283 K, 303 K [35] and 323 K [35] (filled symbols: adsorption, open symbols: desorption). The lines represent the Langmuir model fittings.

Table 5.10. Langmuir adsorption isotherm fitting parameters for CO_2, N_2, and O_2 on MIL-125(Ti)_NH$_2$.

Gas	q_m (mol·kg^{-1})	$K_\infty \times 10^5$ (bar^{-1})	$-\Delta H$ (kJ·mol^{-1})
CO_2	8.60	3.05	23.5
N_2	5.56	29.3	11.5
O_2	8.36	34.7	10.0

Figure 5.25 presents the isosteric heats of adsorption for N_2, CO_2 and O_2 as a function of the adsorbate loadings. The CO_2 values are close to those reported by Regufe *et al.* [35] and by Vaesen *et al.* [27], 21.9 and 29.8 kJ·mol^{-1}, determined by the Clausius-Clapeyron equation application and microcalorimetry, respectively. Rada *et al.* [11] obtained CO_2 isosteric heat of adsorption values ranging from 24.5 to 26.1 kJ·mol^{-1}. Kim *et al.* [22] reported an isosteric heat of adsorption value of 31.5 kJ·mol^{-1} at the CO_2 loading of 2.35 mol·kg^{-1}, while Brandt and co-workers [51] obtained 27.3 kJ·mol^{-1} for 2.03 mol·kg^{-1}. Wiersum *et al.* [73] assessed the heat of adsorption by microcalorimetry, obtaining 29.2 kJ·mol^{-1} for 2.27 mol·kg^{-1}. In meanwhile, for N_2 the isosteric heat of adsorption is almost constant, while for O_2 slightly increases with the loading. The isosteric adsorption heat for N_2 determined in the present study is similar to that reported by Regufe *et al.* [35] as 11.7 kJ·mol^{-1}.
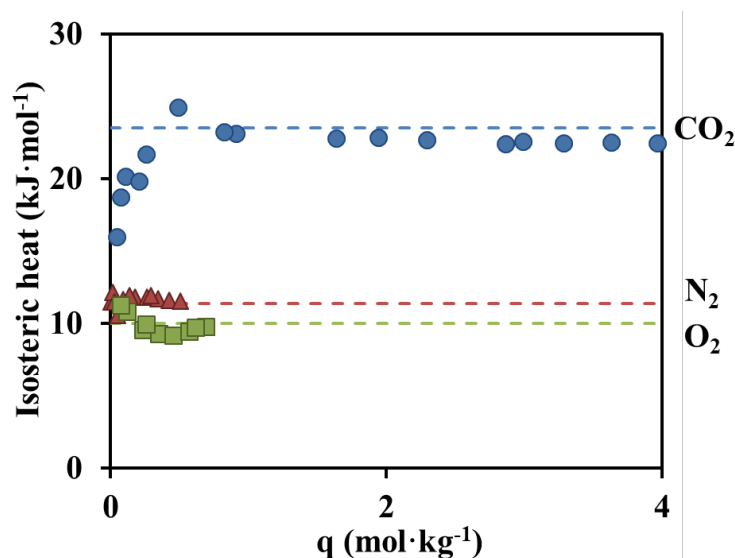
Figure 5.25. Isosteric adsorption heats as a function of adsorbent loading for N_2 (triangles), CO_2 (circles) and O_2 (squares) on MIL-125(Ti)_NH$_2$. The dashed lines correspond to the isosteric adsorption heat obtained by the Langmuir model.

The **H$_2$O vapor adsorption equilibrium isotherms** measured at 293, 305, and 323 K in the range of 0–20 mbar are shown in Figure 5.26. No hysteresis loop was observed in the measured isotherms, and this is in good agreement with the results reported by Logan *et al.* and Canivet *et al.*, in the same material, but in powder form [74, 75]. This fact might be due to a favorable combination of the three parameters that control the shape of water adsorption equilibrium isotherms: pore size, morphology, and surface chemistry [75]. The isotherms are Type IV according to IUPAC classification, though it is difficult to confirm this without higher resolution at low partial pressures [76, 77]. At low relative pressures (P/P$_o$< 0.2), the adsorbent does not adsorb or adsorbs only a small amount of water. The increase in the adsorbed amount with the pressure can be due to the formation of water clusters, followed by the formation of a monolayer covering the surface at medium P/P$_o$ [78]. Such an adsorbent can be classified as a hydrophobic or weakly hydrophilic material [78]. This pattern of water adsorption is in agreement with the trend reported in studies performed by Jeremias *et al.* [25], Kim *et al.* [22], Logan *et al.* [74], and Canivet *et al.* [75]. The measured water vapor uptake at a relative pressure of 0.83 is 20.2 mol·kg^{-1}. This amount of water adsorbed is in agreement with that given in the literature. Canivet *et al.* [75] and Jeremias *et al.* [25] reported the amounts of water adsorbed at P/P$_o$=0.8 and 298 K as 20.6 mol·kg^{-1} and 20.7 mol·kg^{-1}, respectively, for the adsorbent in the powder form. In another study, Kim *et al.* [22] presented a value of 36.5 mol·kg^{-1} at P/P$_o$ = 0.96.

The water vapor adsorption equilibrium data can be described well by the CMMS model (Chapter 4, eq. 4.3). The model parameters (Table 5.11) were obtained by minimizing the sum of the square of the differences between the predicted and experimentally measured adsorbed amounts using the Excel Solver.

a)

b)
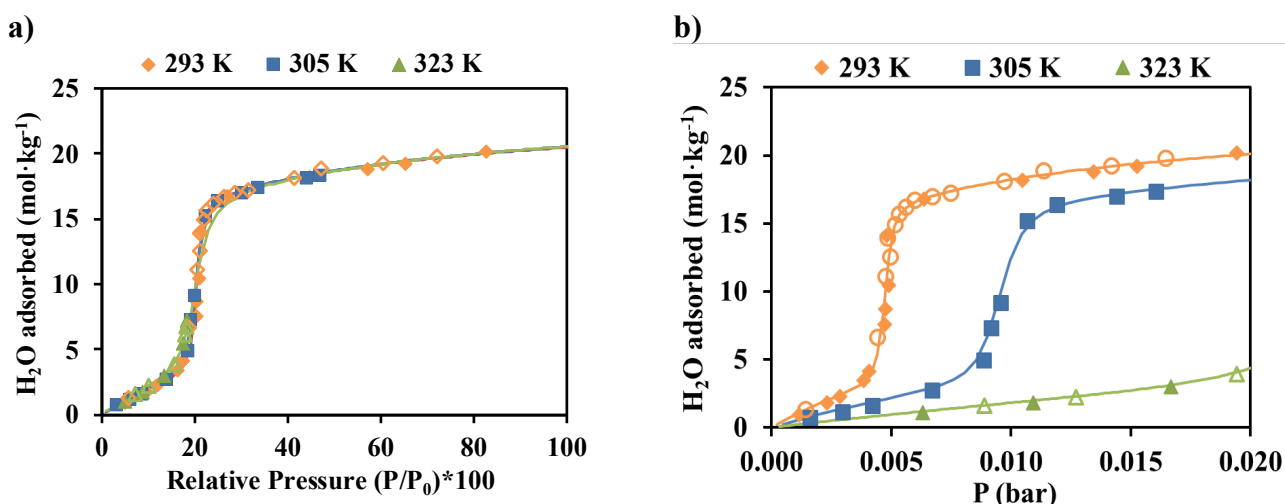
Figure 5.26. Water vapor adsorption-desorption equilibrium isotherms on MIL-125(Ti)_NH$_2$ at 293 K, 305 K, and 323 K as a function of (a) relative pressure and (b) absolute pressure (filled symbols: adsorption, open symbols: desorption), and CMMS model (lines) (Chapter 4, eq. 4.3).

Table 5.11. Fitting parameters of CMMS model for water adsorption isotherms.

CMMS parameter	Value
q_{satL} (mol·kg^{-1})	11.0
q_{satI} (mol·kg^{-1})	13.0
$K_{\infty,I}$ (bar^{-1})	3.81×10^{-6}
$K_{\infty,o}$ (bar^{-1})	0.299
$K_{\infty,L}$ (bar^{-1})	2.14×10^{-6}
$-\Delta H_I$ (kJ·mol^{-1})	43.4
$-\Delta H_o$ (kJ·mol^{-1})	0.0
$-\Delta H_L$ (kJ·mol^{-1})	42.9

The physisorption of water in the selected adsorbent is corroborated by the fact that the adsorbed amount decreases with temperature (Figure 5.26b). Moreover, when the isotherms are represented as a function of relative pressure (P/P$_o$) the three isotherms collapse in one (Figure 5.26a), independent of temperature. Indeed, the same Polanyi's characteristic curve for MIL-125(Ti)_NH$_2$ was obtained at the three different temperatures (Figure 5.27).
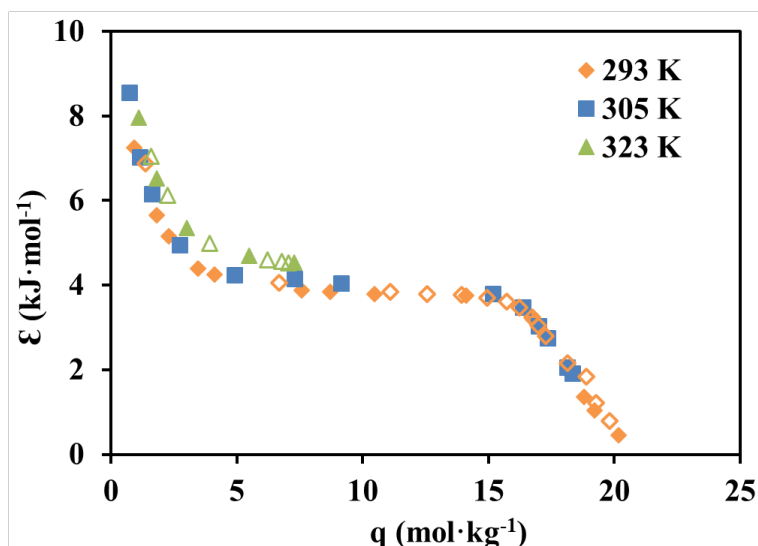
Figure 5.27. Polanyi's characteristic curve of water on MIL-125(Ti)_NH_2 at 293 K, 305 K, and 323 K (filled symbols: adsorption, open symbols: desorption).

As already mentioned, Polanyi's theory is a predictive model to estimate the adsorption capacity independently of temperature [35, 79]. Even though at a temperature of 323 K, a small deviation is observed, the characteristic curve of water on MIL-125(Ti)_NH_2 is evident. Gordeeva *et al.* [55] study reported a similar characteristic curve for MIL-125(Ti)_NH_2 in powder form but diverging in the inflection point at 21.1 mol·kg^{-1} against to the reported in this study at 15.2 mol·kg^{-1}. A similar shape of the characteristic curve of water was recorded in CMS (carbon molecular sieve) 3K, although the adsorption loadings are lower [80]. The isosteric heat of adsorption was calculated by employing the Clausius-Clapeyron equation for different loadings at the three temperatures. It can be seen in Figure 5.28 that the isosteric heat of water adsorption lies in the range of 39.1 to 41.6 kJ·mol^{-1}. These values are in agreement with those obtained by the CMMS fitting. However, Gordeeva *et al.* [81] presented a slightly higher value for the isosteric heat of adsorption (between 49.7 and 54.9 kJ·mol^{-1}). Nonetheless, the values determined in this study are in accordance with those reported for water adsorption on other MOFs [38, 65, 75, 82].
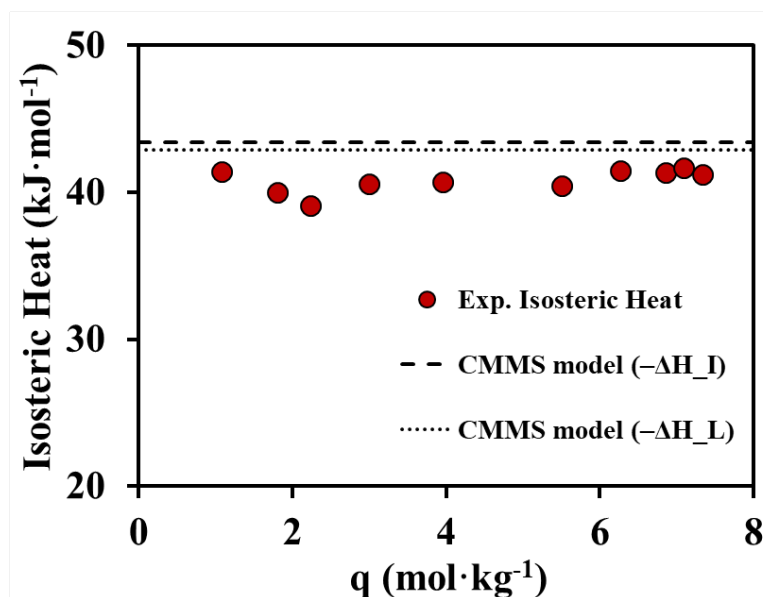
Figure 5.28. Isosteric heat as a function of H_2O loading on MIL-125(Ti)_NH_2.

5.3   Summary

Figure 5.29 presents a comparative summary of the textural characterization performed on the five MOF samples. Figure 5.29a) shows typical microporous Type I isotherms for all MOFs except for MIL-100(Fe). The MIL-100(Fe) isotherm shape (Type I and IV) indicates the presence of micro and mesoporous cages. Low hysteresis loops were detected and can be related to the presence of meso or macropores in the shaped material. N_2 adsorption uptake is significantly higher in MIL-100(Fe), consistent with the higher pore volume (Table 5.1). The affinity order is as follows MIL-100(Fe) > MIL-160(Al) > Al-Fum > MIL-125(Ti)_NH_2 > CAU-10. The opposite occurs with CO_2 adsorption at 273 K, demonstrating the mesoporous nature of MIL-100(Fe). MIL-160(Al) possesses the highest CO_2 adsorption uptake, exhibiting the CO_2 maximum capacity of 101.9 $cm^3 \cdot g^{-1}$ at 1 bar. All the adsorption isotherms of CO_2 show Type I shape, typical of microporous and narrow mesoporous adsorbents.

The MOFs samples are thermally stable at least up to 650 K, excepting the MIL-100(Fe). CAU-10 is the MOF which remains stable until higher temperature (~ 900 K).
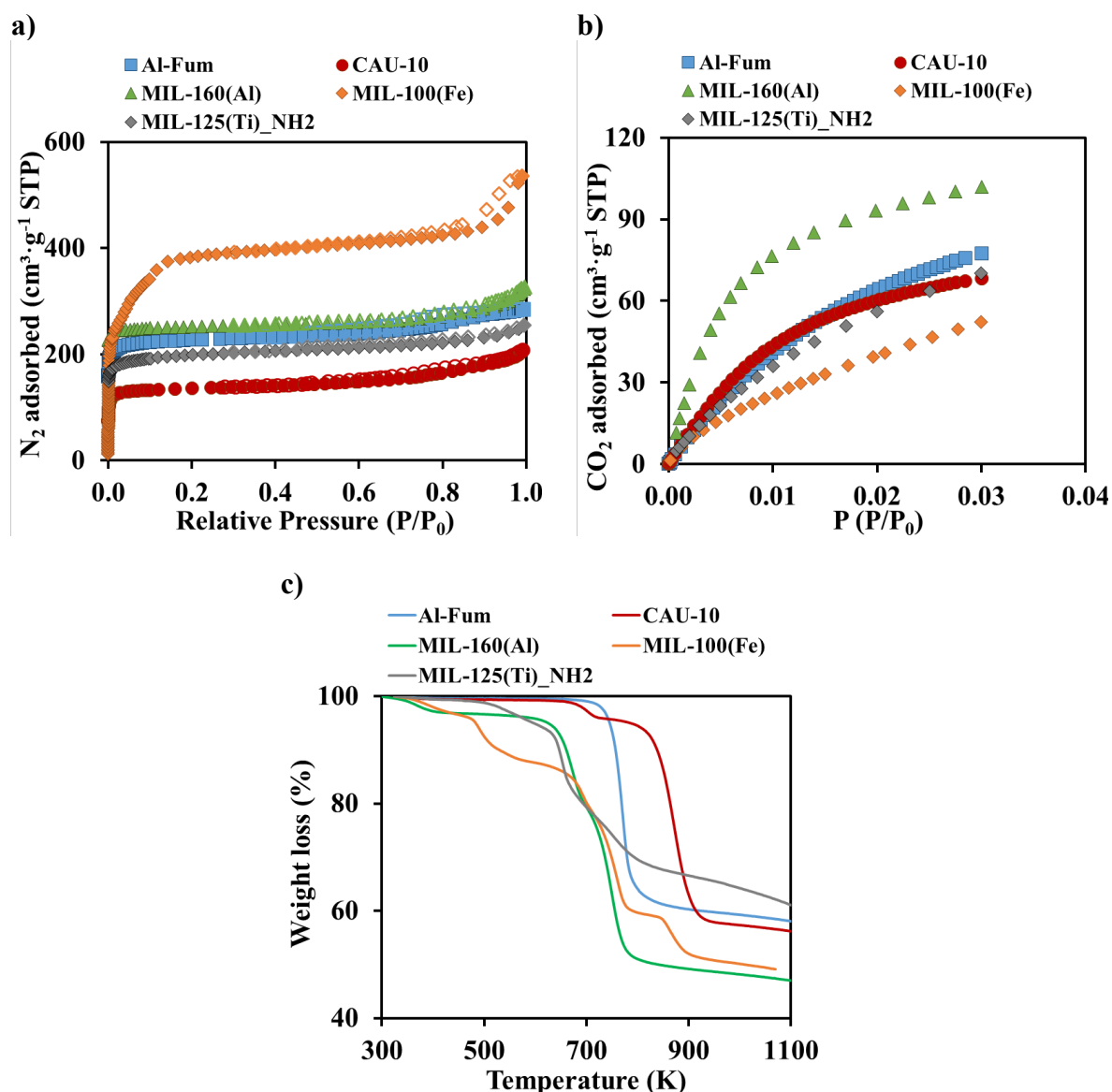
Figure 5.29. Characterization of (a) N_2 adsorption-desorption at 77 K, (b) CO_2 adsorption at 273 K, and (c) TGA curves, on Al-Fum, CAU-10, MIL-160(Al), MIL-100(Fe), and MIL-125(Ti)_NH_2.

The comparison of the H_2O vapor adsorption equilibrium isotherms at 303 K of the selected promising adsorbents is reported in Figure 5.30a) and Figure 5.30b). All the MOF samples presented S-shaped adsorption equilibrium isotherms. Al-Fum, CAU-10, and MIL-125(Ti)_NH_2 presented Type IV shape, while MIL-160(Al) and MIL-100(Fe) shown Type V and Type VI shape, respectively. All MOF samples, except Al-Fum, are suitable for water capture in arid regions ($P/P_o < 0.3$) because presented steep step at low relative pressures. MIL-160(Al) is suitable for regions with relative humidity as low as 10 %, while CAU-10 and MIL-125(Ti)_NH_2 are proper for water harvesting in regions with about 20 % RH. Al-Fum displays

a sharp uptake for relative pressures between 25 % and 38.5 %. Globally, MIL-100(Fe) presented the highest water uptake for RH superior to 0.37, due to capillary condensations in its two different cavities (25 and 29 Å). As previously mentioned, MIL-100(Fe) exhibited two steep steps at $0.21 < P/P_o < 0.30$ and $0.36 < P/P_o < 0.40$. This characteristic provides MIL-100(Fe) to be adaptable to arid but will achieve its highest potential in more humid regions.

The water adsorption on the five MOFs proved to obey the Polanyi potential theory, and each one is well described by a characteristic single curve (Figure 5.30c). Characteristic curves have identical shapes presenting double inflection, which could be related to a bi-modal energy distribution, as observed for water adsorption on activated carbon [83]. MIL-100(Fe) is the adsorbent with a higher affinity to water molecules, adsorbing at high Polanyi adsorption potential.

The experimental isosteric heats of adsorption were determined as a function of the adsorbed amount by the Clausius-Clapeyron equation (Figure 5.30d). Globally, the water isosteric heats on five metal-organic frameworks were in good agreement to the values reported in the literature. Al-Fum showed the highest values, and MIL-125(Ti)_NH₂ provided the lowest values. MIL-160(Al) and MIL-125(Ti)_NH₂ show a decreasing tendency due to the weakening of adsorption affinity after the complete filling of the smaller pores. On the remaining MOFs, an unclear trend is observed, not allowing an evident conclusion about interactions between water molecules and MOFs structure.
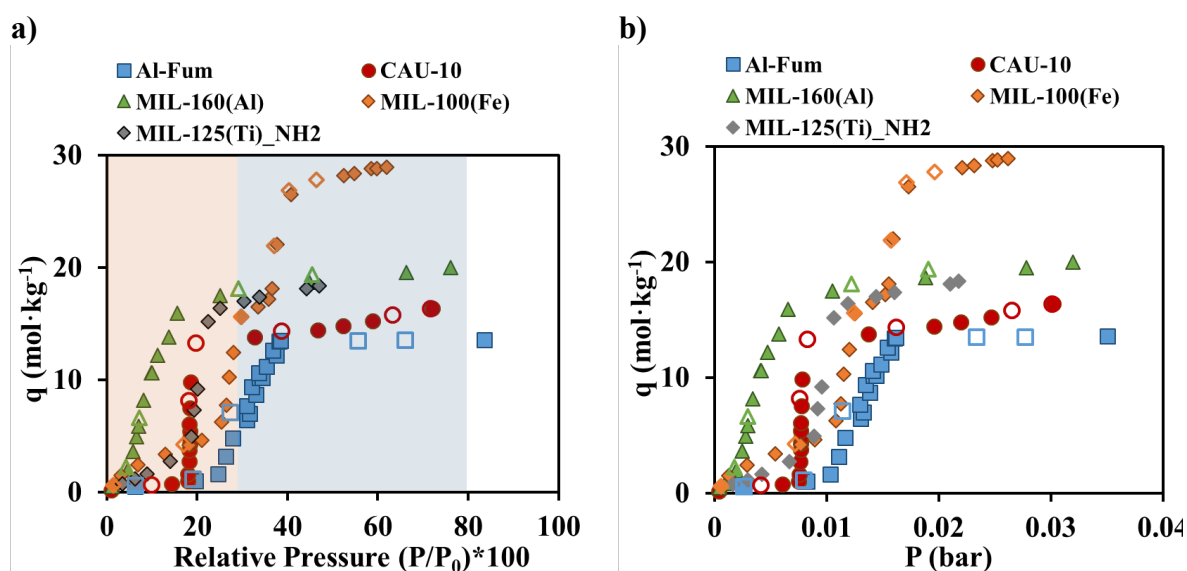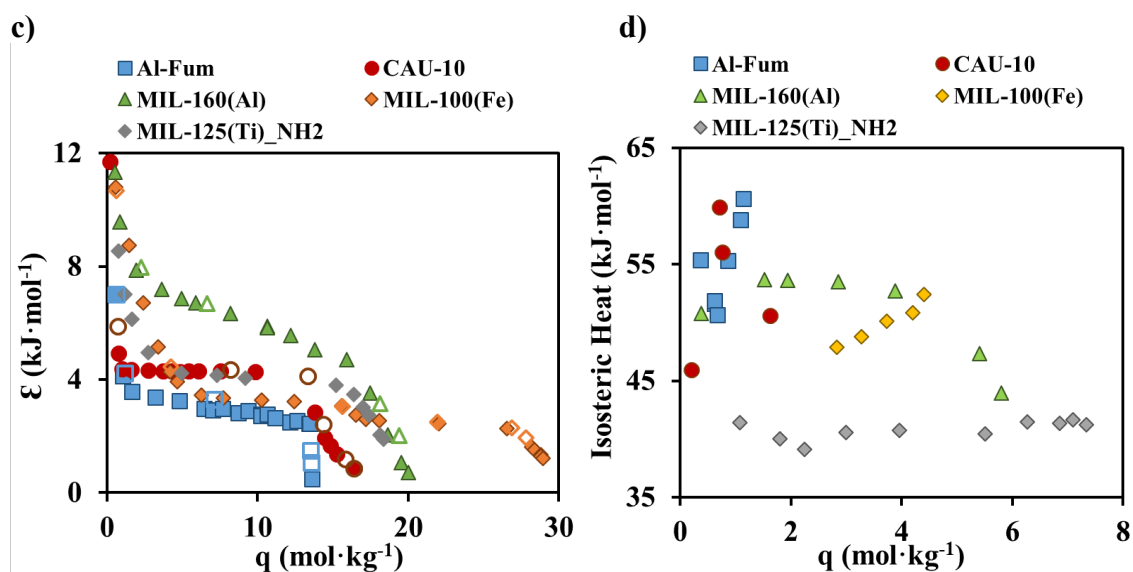
Figure 5.30. Water vapor adsorption-desorption equilibrium isotherms at 303 K as a function of (a) relative pressure and (b) absolute pressure; (c) water adsorption characteristic curves; and isosteric heats of adsorption on Al-Fum, CAU-10, MIL-160(Al), MIL-100(Fe), and MIL-125(Ti)_NH_2. (Arid region – % RH < 30, Humid region – 30 < % RH < 80, Fog region – % RH < 80; according to Tu *et al.* study [84]).

References

1. Mani, M.R., R. Chellaswamy, Y.N. Marathe, and V.K. Pillai, *Enhanced nucleation of polypropylene by metal–organic frameworks (MOFs) based on aluminium dicarboxylates: influence of structural features.* RSC Advances, 2016. **6**(3): p. 1907-1912.

2. Karmakar, S., J. Dechnik, C. Janiak, and S. De, *Aluminium fumarate metal-organic framework: A super adsorbent for fluoride from water.* Journal of Hazardous Materials, 2016. **303**: p. 10-20.

3. Tannert, N., C. Jansen, S. Nießing, and C. Janiak, *Robust synthesis routes and porosity of the Al-based metal–organic frameworks Al-fumarate, CAU-10-H and MIL-160.* Dalton Transactions, 2019. **48**(9): p. 2967-2976.

4. Cadiau, A., J.S. Lee, D. Damasceno Borges, P. Fabry, T. Devic, M.T. Wharmby, C. Martineau, D. Foucher, F. Taulelle, C.H. Jun, Y.K. Hwang, N. Stock, M.F. De Lange, F. Kapteijn, J. Gascon, G. Maurin, J.S. Chang, and C. Serre, *Design of hydrophilic metal organic framework water adsorbents for heat reallocation.* Adv Mater, 2015. **27**(32): p. 4775-80.

5. Wahiduzzaman, M., D. Lenzen, G. Maurin, N. Stock, and M.T. Wharmby, *Rietveld Refinement of MIL-160 and Its Structural Flexibility Upon H2O and N2 Adsorption.* European Journal of Inorganic Chemistry, 2018. **2018**(32): p. 3626-3632.

6. Permyakova, A., O. Skrylnyk, E. Courbon, M. Affram, S. Wang, U.-H. Lee, A.H. Valekar, F. Nouar, G. Mouchaham, T. Devic, G. De Weireld, J.-S. Chang, N. Steunou, M. Frère, and C. Serre, *Synthesis Optimization, Shaping, and Heat Reallocation Evaluation of the Hydrophilic Metal–Organic Framework MIL-160(Al).* ChemSusChem, 2017. **10**(7): p. 1419-1426.

7. Schlüsener, C., M. Xhinovci, S.-J. Ernst, A. Schmitz, N. Tannert, and C. Janiak, *Solid-Solution Mixed-Linker Synthesis of Isoreticular Al-Based MOFs for an Easy Hydrophilicity Tuning in Water-Sorption Heat Transformations.* Chemistry of Materials, 2019. **31**(11): p. 4051-4062.

8. Gökpinar, S., S.-J. Ernst, E. Hastürk, M. Möllers, I. El Aita, R. Wiedey, N. Tannert, S. Nießing, S. Abdpour, A. Schmitz, J. Quodbach, G. Füldner, S.K. Henninger, and C. Janiak, *Air-Con Metal–Organic Frameworks in Binder Composites for Water Adsorption Heat Transformation Systems.* Industrial & Engineering Chemistry Research, 2019.

9. Simon, M.A., E. Anggraeni, F.E. Soetaredjo, S.P. Santoso, W. Irawaty, T.C. Thanh, S.B. Hartono, M. Yuliana, and S. Ismadji, *Hydrothermal Synthesize of HF-Free MIL-100(Fe) for Isoniazid-Drug Delivery.* Scientific Reports, 2019. **9**(1): p. 16907.

10. Tang, J. and J. Wang, *Fe-based metal organic framework/graphene oxide composite as an efficient catalyst for Fenton-like degradation of methyl orange.* RSC Advances, 2017. **7**(80): p. 50829-50837.

11. Rada, Z.H., *Adsorption of gases (CO2, CH4) using novel porous materials (MOFs)*, in *Department of Chemical Engineering.* 2016, Curtin University.

12. Horcajada, P., S. Surblé, C. Serre, D.-Y. Hong, Y.-K. Seo, J.-S. Chang, J.-M. Grenèche, I. Margiolaki, and G. Férey, *Synthesis and catalytic properties of MIL-100(Fe), an iron(iii) carboxylate with large pores.* Chemical Communications, 2007(27): p. 2820-2822.

13. Nehra, M., N. Dilbaghi, N.K. Singhal, A.A. Hassan, K.-H. Kim, and S. Kumar, *Metal organic frameworks MIL-100(Fe) as an efficient adsorptive material for phosphate management.* Environmental Research, 2019. **169**: p. 229-236.

14. Yuan, B., X. Wang, X. Zhou, J. Xiao, and Z. Li, *Novel room-temperature synthesis of MIL-100(Fe) and its excellent adsorption performances for separation of light hydrocarbons.* Chemical Engineering Journal, 2019. **355**: p. 679-686.

15. Mileo, P.G.M., K. Ho Cho, J. Park, S. Devautour-Vinot, J.-S. Chang, and G. Maurin, *Unraveling the Water Adsorption Mechanism in the Mesoporous MIL-100(Fe) Metal–Organic Framework.* The Journal of Physical Chemistry C, 2019. **123**(37): p. 23014-23025.

16.   Shi, J., S. Hei, H. Liu, Y. Fu, F. Zhang, Y. Zhong, and W. Zhu, *Synthesis of MIL-100(Fe) at Low Temperature and Atmospheric Pressure.* Journal of Chemistry, 2013. **2013**: p. 4.

17.   Valekar, A.H., K.-H. Cho, U.H. Lee, J.S. Lee, J.W. Yoon, Y.K. Hwang, S.G. Lee, S.J. Cho, and J.-S. Chang, *Shaping of porous metal–organic framework granules using mesoporous ρ-alumina as a binder.* RSC Advances, 2017. **7**(88): p. 55767-55777.

18.   Zhou, L., X. Zhang, and Y. Chen, *Facile synthesis of Al-fumarate metal–organic framework nano-flakes and their highly selective adsorption of volatile organic compounds.* Materials Letters, 2017. **197**: p. 224-227.

19.   Hastürk, E., S.-P. Höfert, B. Topalli, C. Schlüsener, and C. Janiak, *Shaping of MOFs via freeze-casting method with hydrophilic polymers and their effect on textural properties.* Microporous and Mesoporous Materials, 2019: p. 109907.

20.   Coelho, J.A., A.M. Ribeiro, A.F.P. Ferreira, S.M.P. Lucena, A.E. Rodrigues, and D.C.S.d. Azevedo, *Stability of an Al-Fumarate MOF and Its Potential for CO2 Capture from Wet Stream.* Industrial & Engineering Chemistry Research, 2016. **55**(7): p. 2134-2143.

21.   Reinsch, H., S. Waitschat, and N. Stock, *Mixed-linker MOFs with CAU-10 structure: synthesis and gas sorption characteristics.* Dalton Transactions, 2013. **42**(14): p. 4840-4847.

22.   Kim, S.-N., J. Kim, H.-Y. Kim, H.-Y. Cho, and W.-S. Ahn, *Adsorption/catalytic properties of MIL-125 and NH2-MIL-125.* Catalysis Today, 2013. **204**: p. 85-93.

23.   Isaka, Y., Y. Kondo, Y. Kawase, Y. Kuwahara, K. Mori, and H. Yamashita, *Photocatalytic production of hydrogen peroxide through selective two-electron reduction of dioxygen utilizing amine-functionalized MIL-125 deposited with nickel oxide nanoparticles.* Chemical Communications, 2018. **54**(67): p. 9270-9273.

24.   Sohail, M., Y.N. Yun, E. Lee, S.K. Kim, K. Cho, J.N. Kim, T.W. Kim, J.H. Moon, and H. Kim, *Synthesis of Highly Crystalline NH2-MIL-125 (Ti) with S-Shaped Water*

Isotherms for Adsorption Heat Transformation. Crystal Growth & Design, 2017. **17**(3): p. 1208-1213.

25. Jeremias, F., V. Lozan, S.K. Henninger, and C. Janiak, *Programming MOFs for water sorption: amino-functionalized MIL-125 and UiO-66 for heat transformation and heat storage applications.* Dalton Transactions, 2013. **42**(45): p. 15967-15973.

26. Moreira, M.A., M.P.S. Santos, C.G. Silva, J.M. Loureiro, J.-S. Chang, C. Serre, A.F.P. Ferreira, and A.E. Rodrigues, *Adsorption equilibrium of xylene isomers and ethylbenzene on MIL-125(Ti)_NH2: the temperature influence on the para-selectivity.* Adsorption, 2018. **24**(8): p. 715-724.

27. Vaesen, S., V. Guillerm, Q. Yang, A.D. Wiersum, B. Marszalek, B. Gil, A. Vimont, M. Daturi, T. Devic, P.L. Llewellyn, C. Serre, G. Maurin, and G. De Weireld, *A robust amino-functionalized titanium(iv) based MOF for improved separation of acid gases.* Chemical Communications, 2013. **49**(86): p. 10082-10084.

28. Lozano-Castelló, D., D. Cazorla-Amorós, and A. Linares-Solano, *Usefulness of CO2 adsorption at 273 K for the characterization of porous carbons.* Carbon, 2004. **42**(7): p. 1233-1242.

29. Liu, K. and M. Ostadhassan, *The impact of pore size distribution data presentation format on pore structure interpretation of shales.* Advances in Geo-Energy Research, 2019. **3**(2): p. 187-197.

30. Alvarez, E., N. Guillou, C. Martineau, B. Bueken, B. Van de Voorde, C. Le Guillouzer, P. Fabry, F. Nouar, F. Taulelle, D. de Vos, J.-S. Chang, K.H. Cho, N. Ramsahye, T. Devic, M. Daturi, G. Maurin, and C. Serre, *The Structure of the Aluminum Fumarate Metal–Organic Framework A520.* Angewandte Chemie International Edition, 2015. **54**(12): p. 3664-3668.

31. Kim, P.-J., Y.-W. You, H. Park, J.-S. Chang, Y.-S. Bae, C.-H. Lee, and J.-K. Suh, *Separation of SF6 from SF6/N2 mixture using metal–organic framework MIL-100(Fe) granule.* Chemical Engineering Journal, 2015. **262**: p. 683-690.

32. Seo, Y.-K., J.W. Yoon, J.S. Lee, U.H. Lee, Y.K. Hwang, C.-H. Jun, P. Horcajada, C. Serre, and J.-S. Chang, *Large scale fluorine-free synthesis of hierarchically porous iron(III) trimesate MIL-100(Fe) with a zeolite MTN topology.* Microporous and Mesoporous Materials, 2012. **157**: p. 137-145.

33. Zhang, F., J. Shi, Y. Jin, Y. Fu, Y. Zhong, and W. Zhu, *Facile synthesis of MIL-100(Fe) under HF-free conditions and its application in the acetalization of aldehydes with diols.* Chemical Engineering Journal, 2015. **259**: p. 183-190.

34. Sun, D., L. Ye, and Z. Li, *Visible-light-assisted aerobic photocatalytic oxidation of amines to imines over NH2-MIL-125(Ti).* Applied Catalysis B: Environmental, 2015. **164**: p. 428-432.

35. Regufe, M.J., J. Tamajon, A.M. Ribeiro, A. Ferreira, U.H. Lee, Y.K. Hwang, J.-S. Chang, C. Serre, J.M. Loureiro, and A.E. Rodrigues, *Syngas Purification by Porous Amino-Functionalized Titanium Terephthalate MIL-125.* Energy & Fuels, 2015. **29**(7): p. 4654-4664.

36. Bałys, M., J. Szczurowski, L.A. Czepirski, and M. Kochel, *Adsorption Potential Theory for Description of n-Butane Adsorption on Activated Carbon.* 2017, 2017. **71**(2).

37. Xu, Z., W. Zhang, B. Pan, C. Hong, L. Lv, Q. Zhang, B. Pan, and Q. Zhang, *Application of the Polanyi potential theory to phthalates adsorption from aqueous solution with hyper-cross-linked polymer resins.* Journal of Colloid and Interface Science, 2008. **319**(2): p. 392-397.

38. Ruthven, D.M., *Principles of Adsorption and Adsorption Processes.* 1984, New York: John Wiley and Sons.

39. Meurant, G., A. Dabrowski, and J.M. Lemm, *Applications in Industry.* Vol. 120A. 1998: 17th December 1998. 1064.

40. Long, C., A. Li, H. Wu, F. Liu, and Q. Zhang, *Polanyi-based models for the adsorption of naphthalene from aqueous solutions onto nonpolar polymeric adsorbents.* Journal of Colloid and Interface Science, 2008. **319**(1): p. 12-18.

41.   Meyers, R.A., *Encyclopedia of Environmental Analysis and Remediation*. Vol. 8. 1998: John Wiley and Sons Ltd.

42.   Coelho, J.A., *Avaliação da estabilidade e adsorção de CO2 em estruturas metalorgânicas*, in *Chemical Engineering*. 2016, Universidade Federal do Ceará.

43.   Teo, H.W.B., A. Chakraborty, Y. Kitagawa, and S. Kayal, *Experimental study of isotherms and kinetics for adsorption of water on Aluminium Fumarate.* International Journal of Heat and Mass Transfer, 2017. **114**: p. 621-627.

44.   Teo, H.W.B. and A. Chakraborty, *Aluminium Based Zeolites and MOFs for Adsorption Cooling.* Transactions of the Japan Society of Refrigerating and Air Conditioning Engineers, 2018. **advpub**.

45.   Gökpinar, S., S.-J. Ernst, E. Hastürk, M. Möllers, I. El Aita, R. Wiedey, N. Tannert, S. Nießing, S. Abdpour, A. Schmitz, J. Quodbach, G. Füldner, S.K. Henninger, and C. Janiak, *Air-Con Metal–Organic Frameworks in Binder Composites for Water Adsorption Heat Transformation Systems.* Industrial & Engineering Chemistry Research, 2019. **58**(47): p. 21493-21503.

46.   Lenzen, D., J. Zhao, S.-J. Ernst, M. Wahiduzzaman, A. Ken Inge, D. Fröhlich, H. Xu, H.-J. Bart, C. Janiak, S. Henninger, G. Maurin, X. Zou, and N. Stock, *A metal–organic framework for efficient water-based ultra-low-temperature-driven cooling.* Nature Communications, 2019. **10**(1): p. 3025.

47.   Han, B. and A. Chakraborty, *Water adsorption studies on synthesized alkali-ions doped Al-fumarate MOFs and Al-fumarate + zeolite composites for higher water uptakes and faster kinetics.* Microporous and Mesoporous Materials, 2019. **288**: p. 109590.

48.   López-Cervantes, V.B., E. Sánchez-González, T. Jurado-Vázquez, A. Tejeda-Cruz, E. González-Zamora, and I.A. Ibarra, *CO2 adsorption under humid conditions: Self-regulated water content in CAU-10.* Polyhedron, 2018. **155**: p. 163-169.

49. Teo, H.W.B. and A. Chakraborty, *Water Adsorption on Various Metal Organic Framework.* IOP Conference Series: Materials Science and Engineering, 2017. **272**: p. 012019.

50. Borges, D.D., P. Normand, A. Permiakova, R. Babarao, N. Heymans, D.S. Galvao, C. Serre, G. De Weireld, and G. Maurin, *Gas Adsorption and Separation by the Al-Based Metal–Organic Framework MIL-160.* The Journal of Physical Chemistry C, 2017. **121**(48): p. 26822-26832.

51. Brandt, P., A. Nuhnen, M. Lange, J. Möllmer, O. Weingart, and C. Janiak, *Metal–Organic Frameworks with Potential Application for SO2 Separation and Flue Gas Desulfurization.* ACS Applied Materials & Interfaces, 2019. **11**(19): p. 17350-17358.

52. Leclerc, M. and R. Gauvin, *Functional materials for energy, sustainable development and biomedical sciences.* 2014.

53. Cui, S., A. Marandi, G. Lebourleux, M. Thimon, M. Bourdon, C. Chen, M.I. Severino, V. Steggles, F. Nouar, and C. Serre, *Heat properties of a hydrophilic carboxylate-based MOF for water adsorption applications.* Applied Thermal Engineering, 2019. **161**: p. 114135.

54. Wang, S., J.S. Lee, M. Wahiduzzaman, J. Park, M. Muschi, C. Martineau-Corcos, A. Tissot, K.H. Cho, J. Marrot, W. Shepard, G. Maurin, J.-S. Chang, and C. Serre, *A robust large-pore zirconium carboxylate metal–organic framework for energy-efficient water-sorption-driven refrigeration.* Nature Energy, 2018. **3**(11): p. 985-993.

55. Gordeeva, L.G., M.V. Solovyeva, A. Sapienza, and Y.I. Aristov, *Potable water extraction from the atmosphere: Potential of MOFs.* Renewable Energy, 2020. **148**: p. 72-80.

56. Thommes, M., K. Kaneko, V. Neimark Alexander, P. Olivier James, F. Rodriguez-Reinoso, J. Rouquerol, and S.W. Sing Kenneth, *Physisorption of gases, with special reference to the evaluation of surface area and pore size distribution (IUPAC Technical Report)*, in *Pure and Applied Chemistry*. 2015. p. 1051.

57.   Li, Y.-X., Y.-N. Ji, M.-M. Jin, S.-C. Qi, S.-S. Li, D.-M. Xue, M.B. Yue, X.-Q. Liu, and L.-B. Sun, *Controlled Construction of Cu(I) Sites within Confined Spaces via Host–Guest Redox: Highly Efficient Adsorbents for Selective CO Adsorption.* ACS Applied Materials & Interfaces, 2018. **10**(46): p. 40044-40053.

58.   Gallis, D.F.S., K.W. Chapman, M.A. Rodriguez, J.A. Greathouse, M.V. Parkes, and T.M. Nenoff, *Selective O2 Sorption at Ambient Temperatures via Node Distortions in Sc-MIL-100.* Chemistry of Materials, 2016. **28**(10): p. 3327-3336.

59.   Peng, J., S. Xian, J. Xiao, Y. Huang, Q. Xia, H. Wang, and Z. Li, *A supported Cu(I)@MIL-100(Fe) adsorbent with high CO adsorption capacity and CO/N2 selectivity.* Chemical Engineering Journal, 2015. **270**: p. 282-289.

60.   Ribeiro, A.M., M.C. Campo, G. Narin, J.C. Santos, A. Ferreira, J.-S. Chang, Y.K. Hwang, Y.-K. Seo, U.H. Lee, J.M. Loureiro, and A.E. Rodrigues, *Pressure swing adsorption process for the separation of nitrogen and propylene with a MOF adsorbent MIL-100(Fe).* Separation and Purification Technology, 2013. **110**: p. 101-111.

61.   Vo, T.K., Y.-S. Bae, B.-J. Chang, S.-Y. Moon, J.-H. Kim, and J. Kim, *Highly CO selective Cu(I)-doped MIL-100(Fe) adsorbent with high CO/CO2 selectivity due to π complexation: Effects of Cu(I) loading and activation temperature.* Microporous and Mesoporous Materials, 2019. **274**: p. 17-24.

62.   Mei, L., T. Jiang, X. Zhou, Y. Li, H. Wang, and Z. Li, *A novel DOBDC-functionalized MIL-100(Fe) and its enhanced CO2 capacity and selectivity.* Chemical Engineering Journal, 2017. **321**: p. 600-607.

63.   Mutyala, S., S.M. Yakout, S.S. Ibrahim, M. Jonnalagadda, and H. Mitta, *Enhancement of CO2 capture and separation of CO2/N2 using post-synthetic modified MIL-100(Fe).* New Journal of Chemistry, 2019. **43**(24): p. 9725-9731.

64.   Ben-Mansour, R., N.A.A. Qasem, and M.A. Habib, *Adsorption characterization and CO2 breakthrough of MWCNT/Mg-MOF-74 and MWCNT/MIL-100(Fe) composites.* International Journal of Energy and Environmental Engineering, 2018. **9**(2): p. 169-185.

65.   Küsgens, P., M. Rose, I. Senkovska, H. Fröde, A. Henschel, S. Siegle, and S. Kaskel, *Characterization of metal-organic frameworks by water adsorption.* Microporous and Mesoporous Materials, 2009. **120**(3): p. 325-330.

66.   Jeremias, F., A. Khutia, S.K. Henninger, and C. Janiak, *MIL-100(Al, Fe) as water adsorbents for heat transformation purposes-a promising application.* Journal of Materials Chemistry, 2012. **22**(20): p. 10148-10151.

67.   Kim, S.-I., T.-U. Yoon, M.-B. Kim, S.-J. Lee, Y.K. Hwang, J.-S. Chang, H.-J. Kim, H.-N. Lee, U.H. Lee, and Y.-S. Bae, *Metal–organic frameworks with high working capacities and cyclic hydrothermal stabilities for fresh water production.* Chemical Engineering Journal, 2016. **286**: p. 467-475.

68.   Zu, K., S. Cui, and M. Qin, *Performance comparison between metal-organic framework (MOFs) and conventional desiccants (silica gel, zeolite) for a novel high temperature cooling system.* IOP Conference Series: Materials Science and Engineering, 2019. **609**: p. 052013.

69.   Jeremias, F., A. Khutia, S.K. Henninger, and C. Janiak, *MIL-100(Al, Fe) as water adsorbents for heat transformation purposes - A promising application.* Journal of Materials Chemistry, 2012. **22**(20): p. 10148-10151.

70.   de Visser, S.P., *Polarizability-based equation of state: Application to CO, N2 and O2.* Chemical Physics Letters, 2011. **515**(1): p. 170-172.

71.   Pillai, R.S., S.A. Peter, and R.V. Jasra, *Adsorption of carbon dioxide, methane, nitrogen, oxygen and argon in NaETS-4.* Microporous and Mesoporous Materials, 2008. **113**(1): p. 268-276.

72.   Park, Y.-J., S.-J. Lee, J.-H. Moon, D.-K. Choi, and C.-H. Lee, *Adsorption Equilibria of O2, N2, and Ar on Carbon Molecular Sieve and Zeolites 10X, 13X, and LiX.* Journal of Chemical & Engineering Data, 2006. **51**(3): p. 1001-1008.

73. Wiersum, A.D., J.-S. Chang, C. Serre, and P.L. Llewellyn, *An Adsorbent Performance Indicator as a First Step Evaluation of Novel Sorbents for Gas Separations: Application to Metal–Organic Frameworks.* Langmuir, 2013. **29**(10): p. 3301-3309.

74. Logan, M.W., J.D. Adamson, D. Le, and F.J. Uribe-Romo, *Structural Stability of N-Alkyl-Functionalized Titanium Metal–Organic Frameworks in Aqueous and Humid Environments.* ACS Applied Materials & Interfaces, 2017. **9**(51): p. 44529-44533.

75. Canivet, J., J. Bonnefoy, C. Daniel, A. Legrand, B. Coasne, and D. Farrusseng, *Structure–property relationships of water adsorption in metal–organic frameworks.* New Journal of Chemistry, 2014. **38**(7): p. 3102-3111.

76. Basmadjian, D., *The Little Adsorption Book: A Practical Guide for Engineers and Scientists.* CRC Press 1996

77. Regufe, M.J., *Syngas purification using MIL-125(Ti)_NH2*, in *Chemical Engineering*. 2014, University of Porto.

78. Ng, E.-P. and S. Mintova, *Nanoporous materials with enhanced hydrophilicity and high water sorption capacity.* Microporous and Mesoporous Materials, 2008. **114**(1): p. 1-26.

79. Yang, K. and B. Xing, *Adsorption of Organic Compounds by Carbon Nanomaterials in Aqueous Phase: Polanyi Theory and Its Application.* Chemical Reviews, 2010. **110**(10): p. 5989-6008.

80. Ribeiro, R.P.P.L., *Electric Swing Adsorption for Gas Separation and Purification*, in *Department of Chemical Engineering*. 2013, Faculty of Engineering of University of Porto.

81. Gordeeva, L.G., M.V. Solovyeva, and Y.I. Aristov, *NH2-MIL-125 as a promising material for adsorptive heat transformation and storage.* Energy, 2016. **100**(Supplement C): p. 18-24.

82. Furukawa, H., F. Gándara, Y.-B. Zhang, J. Jiang, W.L. Queen, M.R. Hudson, and O.M. Yaghi, *Water Adsorption in Porous Metal–Organic Frameworks and Related Materials.* Journal of the American Chemical Society, 2014. **136**(11): p. 4369-4381.

83. Bradley, R.H. and B. Rand, *A comparison of the adsorption behaviour of nitrogen, alcohols and water towards active carbons.* Carbon, 1991. **29**(8): p. 1165-1172.

84. Tu, Y., R. Wang, Y. Zhang, and J. Wang, *Progress and Expectation of Atmospheric Water Harvesting.* Joule, 2018. **2**(8): p. 1452-1475.

6 WATER ADSORPTION DYNAMIC STUDIES WITH FIXED-BED EXPERIMENTS

6.1   Fixed-bed dynamic experiments

Dynamic adsorption experiments were conducted at 298 K and 1 bar, in a fixed-bed bench-scale unit, previously described in Chapter 3. Breakthrough experiments provided knowledge about water adsorption dynamic behavior and allowed the validation of the proposed mathematical model. Breakthrough experiments with N_2 and CO_2 were performed to study their influence on the co-adsorption with water, especially CO_2, since it is the one with the highest affinity towards the adsorbent from the three permanent gases (CO_2, N_2, and O_2). Different fixed-bed experiments were performed to obtain the breakthrough curves for single components and multi-components, namely:

Experiment 1 – **Single component breakthrough experiment (inert background)**. Firstly, the column is filled with He with a constant volumetric flow rate of 0.200 SLPM. In the adsorption step, the feed is a mixture of two individual gas streams. One gas stream consists of pure helium (0.100 SLPM), and the other stream consists of helium saturated with water vapor (0.100 SLPM). As a final step, the feed was switched back to dry helium (0.200 SLPM) for the desorption of the adsorbed water;

Experiment 2 – **Binary breakthrough experiment (CO_2 co-adsorption)**. The experimental protocol is the same as previously described, except that the water vapor is carried by a CO_2 stream, instead of He. The composition of the exit flow was analyzed during the adsorption and desorption by an Infra-Red gas detector;

Experiment 3 – **Binary breakthrough experiment (N_2 co-adsorption)**. The procedure of this experiment is similar to the one of **Experiment 2**, the water vapour is carried out by a N_2 stream. The desorption is achieved with a dry He stream as in **Experiment 1**;

Experiment 4 – **Pseudo ternary breakthrough experiment (N_2 background and CO_2 co-adsorption)**. The present experiment follows a similar procedure as **Experiment 2**, but the dry He stream is replaced by a dry N_2 stream;

Experiment 5 – **Binary breakthrough experiment (counter- and co-adsorption of CO_2)**. The adsorption bed is pre-saturated with water (0.200 SLPM of He containing 50% RH), then pure helium gas stream (0.100 SLPM) was switched to a pure CO_2 stream (0.100 SLPM), maintaining constant the RH, with a 0.100 SLPM of helium fully saturated with water vapor.

This led to a feed composition of 50% of CO_2 balanced with helium, and 50% of RH. Desorption was performed with dry He;

Experiment 6 – Single component breakthrough experiment (CO_2 adsorption in inert background). The column is initially conditioned with dry He (0.200 SLPM). The feed is then changed to a stream of 50 % of CO_2 balanced with He (0.200 SLPM). The desorption step is carried out with pure He. The outlet stream composition was analyzed and recorded with an Infra-Red gas detector;

All the experiments mentioned above were performed on MIL-125(Ti)_NH$_2$ and MIL-160(Al) adsorbents to evaluate the competition of CO_2 and N_2 with H_2O vapor. On the remaining MOFs, only **Experiment 1** was performed. All dead volumes of the system were assessed and taking into consideration to correct the dynamic response of the system.

Breakthrough curves obtained by the dynamic adsorption were compared to the prediction of the proposed mathematic model (Chapter 4). The main characteristics of the bed properties used in the breakthrough experiments and the transport parameters used on the modelling of these experiments, are presented in Table 6.1.

Table 6.1. Characteristics of the adsorption bed and transport parameter of MOFs.

		Al-Fum	CAU-10	MIL-160(Al)	MIL-100(Fe)	MIL-125(Ti)_NH$_2$
Bed properties	Bed length (cm)	8.5	8.4	8.4	12.0	8.7
	Bed diameter (cm)	2.1	2.1	2.1	2.1	2.1
	Mass of packed adsorbent (g)	14.4	14.6	12.0	19.7	9.4
	ε	0.42	0.42	0.49	0.32	0.47
Transport parameters	D_{ax} (m$^2 \cdot$s^{-1})	2.00×10^{-4}	2.60×10^{-4}	1.50×10^{-4}	1.10×10^{-4}	1.33×10^{-4}
	k_f (m$\cdot$s^{-1})	1.25×10^{-1}	4.69×10^{-2}	3.78×10^{-2}	1.25×10^{-1}	1.25×10^{-1}
	h_f (W$\cdot$m$^{-2} \cdot$K^{-1})	59.1	50.2	40.5	84.6	73.5
	h_w (W$\cdot$m$^{-2} \cdot$K^{-1})	181	181	182	181	60
	U (W$\cdot$m$^{-2} \cdot$K^{-1})	40	44	40	40	20

6.1.1 Al-Fum

Figure 6.1 shows water breakthrough where water vapor was carried with pure He (**Experiment 1 protocol**). The same stepped water vapor breakthrough curve was obtained as previously reported by Bozbiyik *et al.* [1] in water breakthrough curves on Al-Fum at 303 K for relative humidity of 39% and 75%. Two compressive fronts are observed, the first up to $P/P_o = 0.17$, followed by a second compressive front from $P/P_o = 0.20$ up to $P/P_o = 0.42$. A small dispersive front is observed between both ($P/P_o = 0.17 - P/P_o = 0.20$), due to the knee observed in the isotherm. The desorption step starts by presenting a dispersive front from $P/P_o = 0.43$ to 0.24 and then an abrupt compressive front to conclude the regeneration. The observed steps in the breakthrough curve are in agreement with the shape of water vapor adsorption equilibrium isotherm (Figure 5.8) which presented an inflexion point at about $P/P_o = 0.22$.

Figure 6.1. Water vapor adsorption-desorption breakthrough curve obtained on Al-Fum at 298 K (Points represent experimental data, full line corresponds to simulation results, and the vertical dashed line represents the beginning of the regeneration step).

The simulation results cannot predict well the RH level at which step happens, but the overall dynamic behaviour is predicted. Due to this mismatch between experimental and simulation results, further studies will be necessary before moving to the process simulation.

6.1.2 CAU-10

Water breakthrough curve on CAU-10, following the protocol described for **Experiment 1**, is present in Figure 6.2. The water vapor breakthrough curve corroborates the water vapor adsorption equilibrium isotherms (inflexion point at $P/P_o = 0.18$) presenting two consecutive shock waves. The same behaviour is observed for desorption, however between the two shock fronts is observed some dispersive mass front. Indeed, the dynamic response of the system followed the expected response taking into consideration the water vapor adsorption equilibrium isotherm trend at 303 K (Figure 5.11). Therefore, one can conclude that mass transfer limitations are not observed at these experimental conditions.
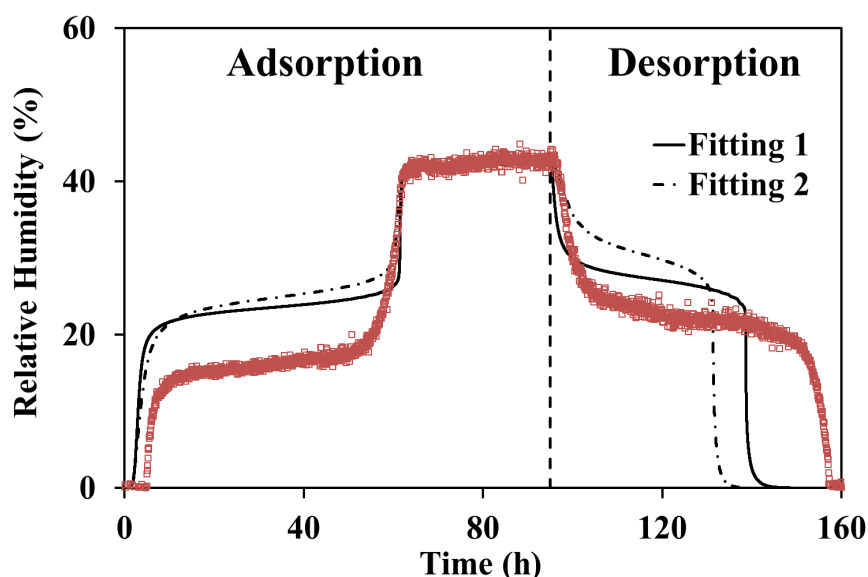

Figure 6.2. Water vapor adsorption-desorption breakthrough curve obtained on CAU-10 at 298 K (Points represent experimental data, full line corresponds to simulation results, and dashed line represents the beginning of the regeneration step).

The model prediction can predict fairly well the experimental results, there one can consider that the global model (fixed-bed model + adsorption equilibrium model) for this material was validated and can be used for process simulation on the next chapter.

6.1.3 MIL-160(Al)

The water vapor breakthrough curve on MIL-160(Al) is displayed in Figure 6.3 (**Experiment 1 protocol**). Firstly, a dispersive front up to $P/P_o = 0.05$ is presented, then a

compressive front ($0.05 < P/P_o < 0.55$) is visible concluding the adsorption step. Similar behavior was observed during the desorption step with a dispersive front from $P/P_o = 0.50$ to 0.14, and then a compressive front ($P/P_o = 0.14$ to 0). The observed behavior is in agreement with water vapor adsorption equilibrium isotherm at 303 K presented in Figure 5.16. The developed mathematical model can predict well the H_2O vapor breakthrough dynamic behavior on MIL-160(Al).
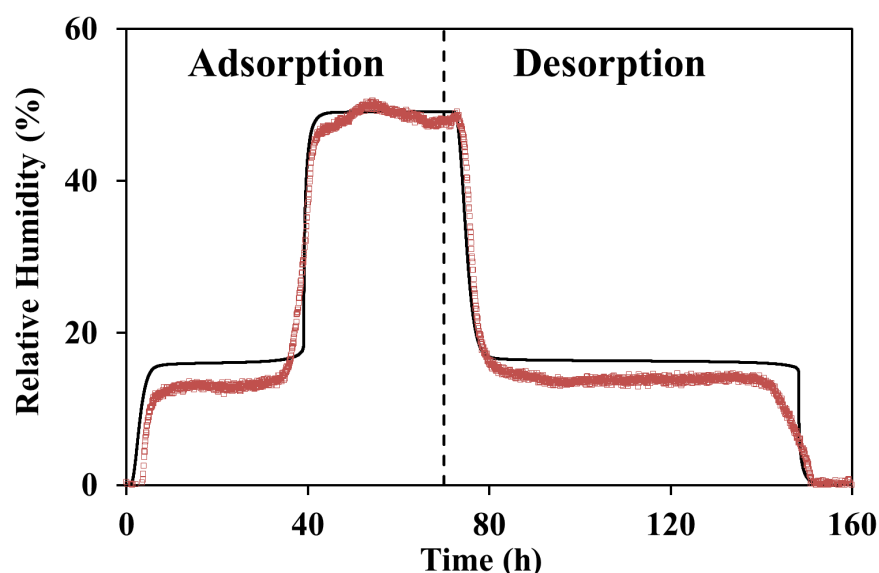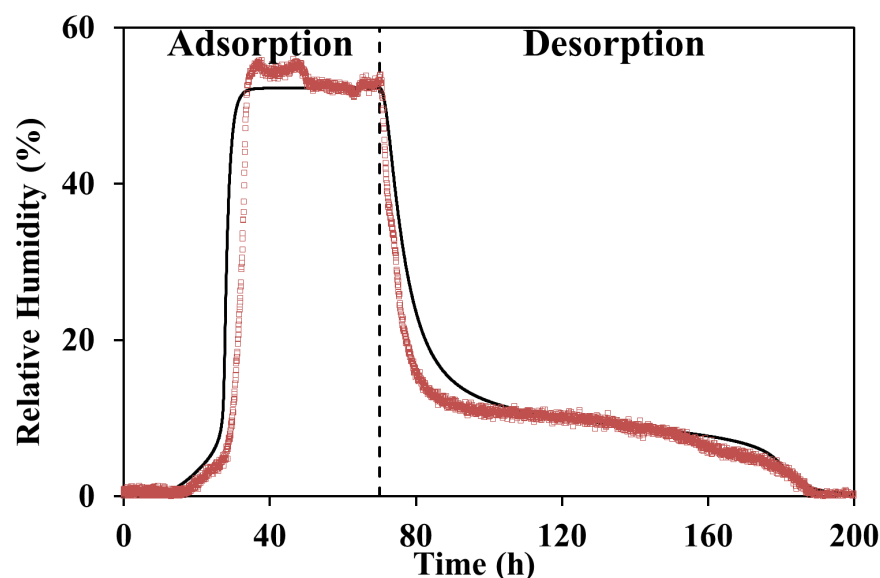

Figure 6.3. Water vapor adsorption-desorption breakthrough curve obtained on MIL-160(Al) at 298 K (Points represent experimental data, full line corresponds to simulation results, and dashed line represents the beginning of the regeneration step).

Figure 6.4 represents the H_2O vapor breakthrough history in co-adsorption with N_2 (**Experiment 3 protocol**). As already observed in Figure 6.3, H_2O vapor history in N_2 presents a dispersive front, due to the unfavourable shape of the isotherm at low coverage ($P/P_o < 0.06$), followed by a compressive front up to $P/P_o \sim 0.50$. During the desorption step, a dispersive front from $P/P_o = 0.52$ to 0.15 is presented and then compressive front is observed. The fixed bed proposed model proved to predict well the dynamic behavior of water adsorption in the presence of N_2. This fact leads to conclude that the presence of N_2 did not influence water adsorption on MIL-160(Al), since no competition term is taking in consideration in the adsorption equilibrium model. This might be due to the weak affinity of N_2 towards the adsorbent when compared to the water adsorption affinity at high RH.
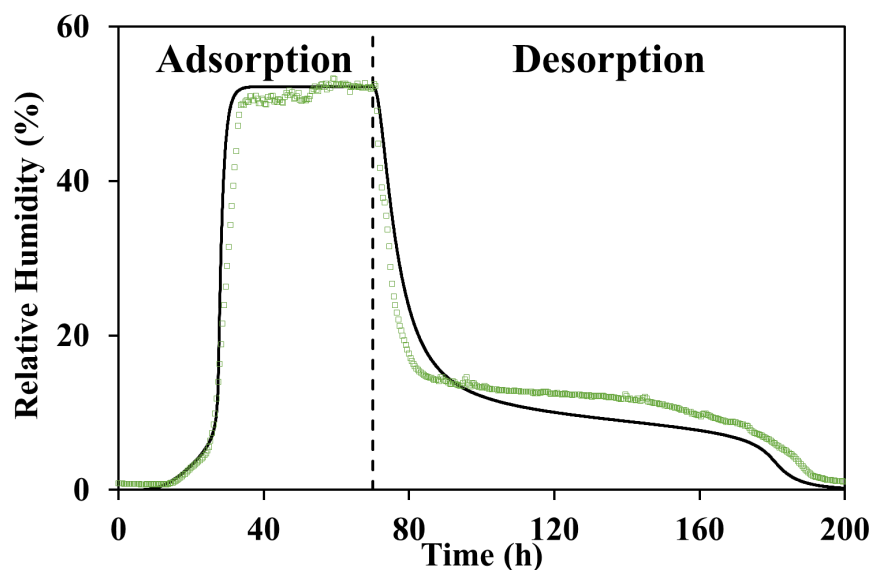
Figure 6.4. Breakthrough curve of a binary mixture of dry He with saturated N_2 (50% RH), on MIL-160(Al) at 298 K, in terms of relative humidity (Points represent experimental data, full line corresponds to simulation results, and the dashed line represents the beginning of the regeneration step).

The influence of CO_2 co-adsorption with water was studied. The water breakthrough curve, in the presence of 50% of CO_2 in He (**Experiment 2 protocol**) and in N_2 (**Experiment 4 protocol**), are presented in Figure 6.5a) and Figure 6.5b), respectively. Great similarity between both breakthrough curves is presented, leading to conclude the N_2 behaves as an inert gas. The observed behaviour for the two experiments is similar to the one described above. The fixed bed model presented does not consider any competition between water and CO_2 and proved to predict fairly the dynamic behavior of water in the adsorption step, failing more in the desorption step. The model underpredicts the water adsorbed amount to some degree, which can be an evidence of a synergetic behaviour during the co-adsorption of water and CO_2. However, the amount of CO_2 existing in the atmosphere is far lower than the 50% (*i.e.* 500 ppm). Therefore, one will not introduce any correction to the model, in order to predict this synergetic behavior.

a)

b)
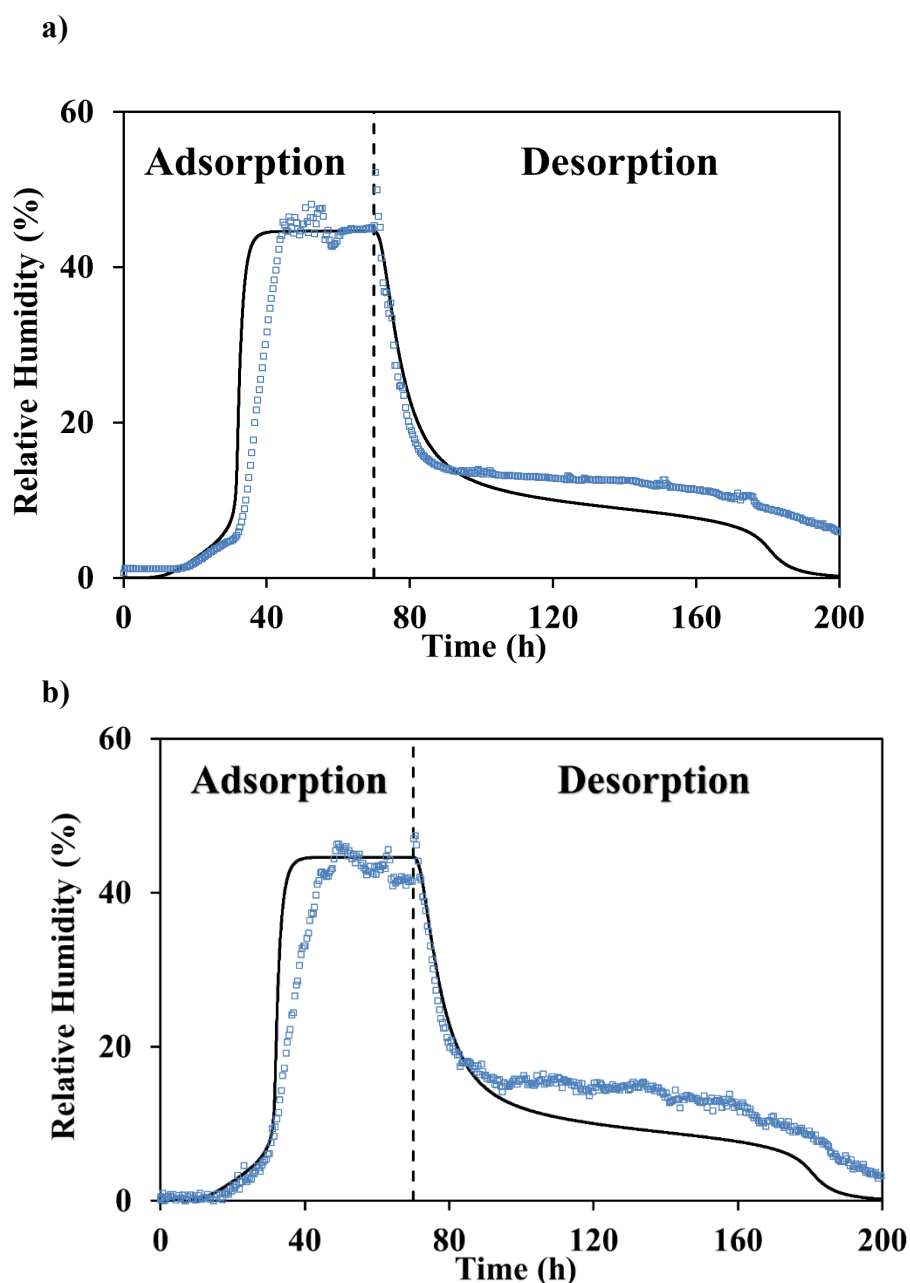
Figure 6.5. Water breakthrough curve of a binary mixture of (a) dry He with saturated CO_2 (45% RH), and (b) dry N_2 with saturated CO_2 (44% RH), on MIL-160(Al) at 298 K, in terms of relative humidity (Points represent experimental data, full line corresponds to simulation results, and the dashed line represents the beginning of the regeneration step).

6.1.4 MIL-100(Fe)

On MIL-100(Fe), **Experiment 1 protocol** was followed to perform a single component water adsorption breakthrough, the results are displayed in Figure 6.6. Firstly, a compressive front up to $P/P_o = 0.20$, then a dispersive front is observed up to $P/P_o = 0.22$, then are observed

two compressive fronts up to $P/P_o = 0.33$ and $P/P_o = 0.51$. The desorption step exhibits first a dispersive front between $P/P_o = 0.51$ and 0.38, followed by two compressive mass fronts. The water vapor breakthrough curve follows the water vapour adsorption equilibrium isotherm, which exhibits 3 adsorption steps (Figure 5.21). The model describes well the observed experimental results, leading to a validation of the full model.

Figure 6.6. Water vapor adsorption-desorption breakthrough curve obtained on MIL-100(Fe) at 298 K (Points represent experimental data, full line corresponds to simulation results, and dashed line represents the beginning of the regeneration step).

6.1.5 MIL-125(Ti)_NH$_2$

The adsorption breakthrough curve of water vapor presented a compressive front up to $P/P_o = 0.17$, followed by a small dispersive front between $P/P_o = 0.17$ and 0.21, and then a compressive front up to $P/P_o = 0.5$ (Figure 6.7). A similar pattern was also observed during the desorption with a dry flow of helium through the bed: dispersive from $P/P_o = 0.5$ to 0.23 and then compressive, as expected from the shape of the water adsorption isotherms (Figure 5.26).
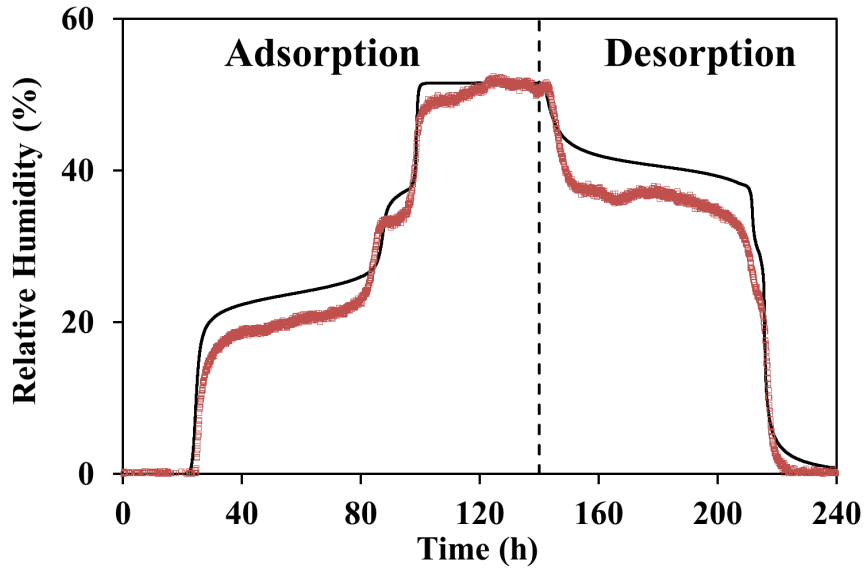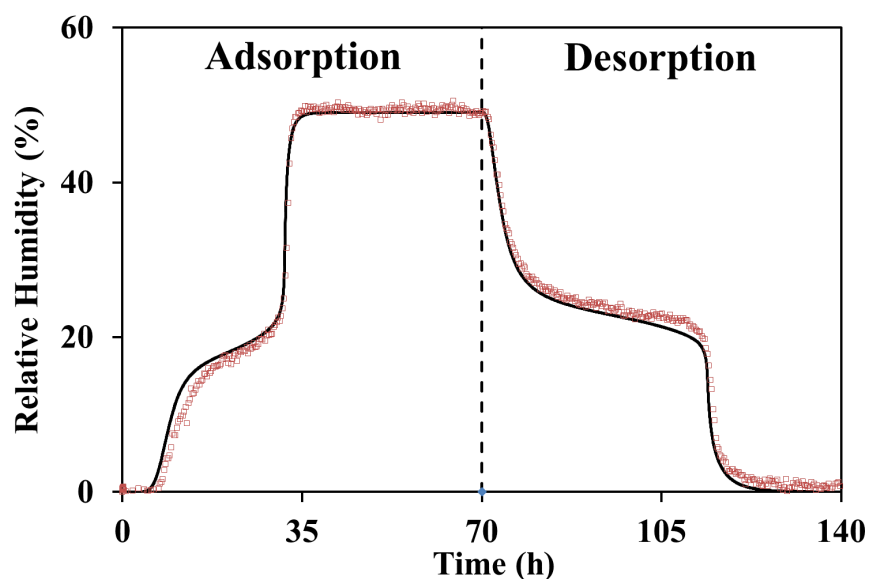
Figure 6.7. Water vapor adsorption-desorption breakthrough curve obtained on MIL-125(Ti)_NH$_2$ at 298 K (Points represent experimental data, full line corresponds to simulation results, and dashed line represents the beginning of the regeneration step).

The H$_2$O vapor breakthrough history in co-adsorption with N$_2$ (**Experiment 3 protocol**) is presented in Figure 6.8. It shows a compressive front up to P/P$_o$ = 0.20, a dispersive front between P/P$_o$ = 0.20 and 0.22, and then a compressive front up to P/P$_o$ ~ 0.42. In the desorption step, a dispersive front from P/P$_o$ = 0.43 to 0.22 is showed, followed by a compressive front. A great similarity between the simulation results and the experimental dynamic behaviour of water adsorption using N$_2$ as a carrier is observed, proving the weak affinity of N$_2$ towards the adsorbent, therefore not strong enough to compete with water adsorption on MIL-125(Ti)_NH$_2$.
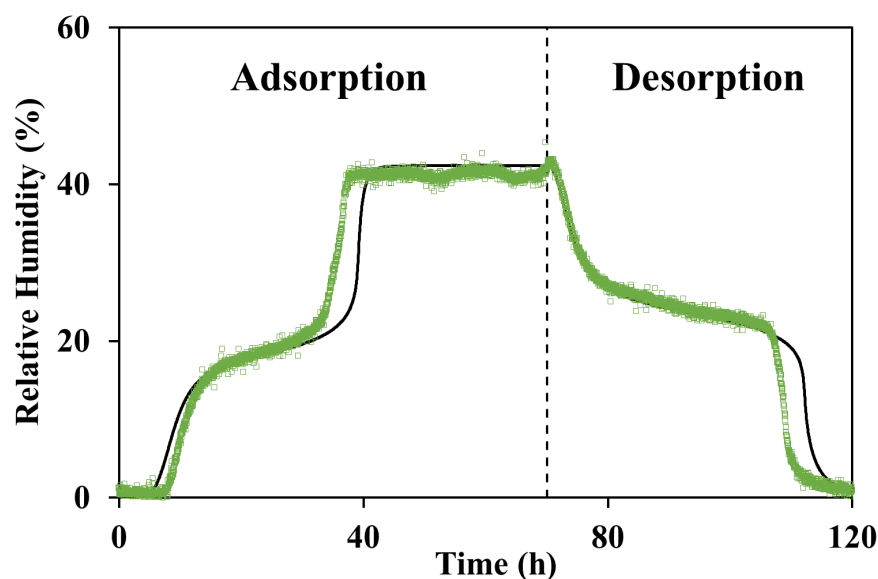
Figure 6.8. Breakthrough curve of a binary mixture of dry He with saturated N_2 (42% RH), on MIL-125(Ti)_NH_2 at 298 K, in terms of relative humidity (Points represent experimental data and the dashed line represents the beginning of the regeneration step).

The water vapor breakthrough curve on MIL-125(Ti)_NH_2 in co-adsorption with CO_2 are presented in Figure 6.9. The water breakthrough curve presented in Figure 6.9a) follows the protocol described for **Experiment 2** type. The observed behavior is similar to the water vapor experiment without CO_2 (Figure 6.7). Moreover, the same pattern is also observed for the water vapor breakthrough experiment using N_2 as balancing gas (**Experiment 4 protocol**).

a)

b)
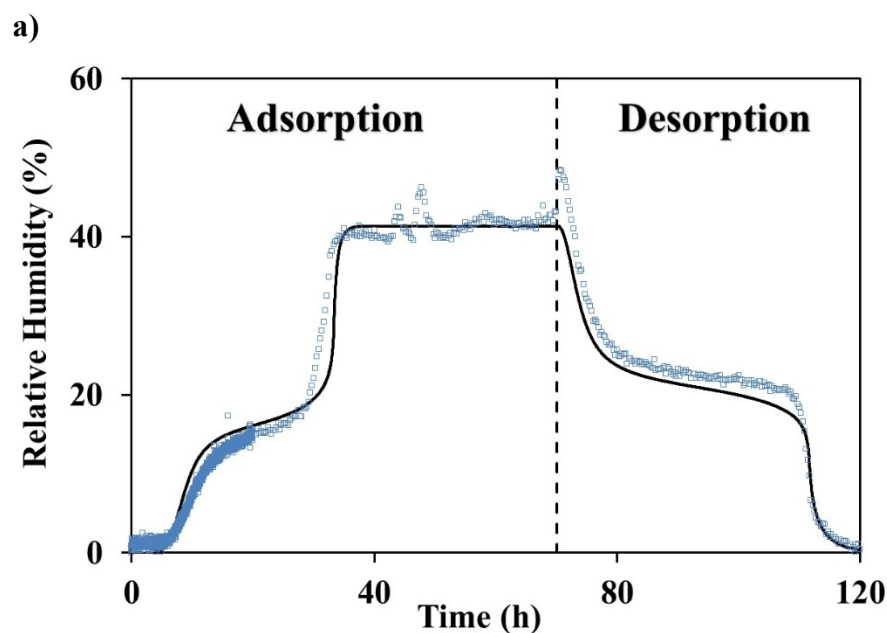
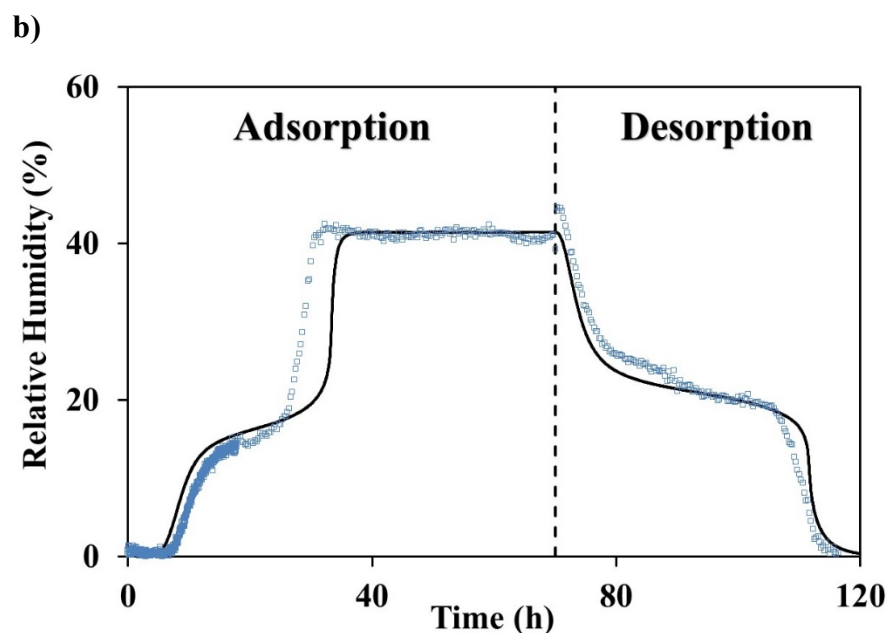Figure 6.9. Water breakthrough curve of a binary mixture of (a) dry He with saturated CO_2 (41% RH), and (b) dry N_2 with saturated CO_2 (41% RH), on MIL-125(Ti)_NH_2 at 298 K, in terms of relative humidity (Points represent experimental data and the dashed line represents the beginning of the regeneration step).

6.2 DRIFT Experiments

DRIFTS measurements were performed to evaluate water adsorption and desorption and the temperature effect in the regeneration of the material. CO_2 adsorption, and CO_2 and H_2O vapor co-adsorption were also studied by DRIFT to evaluate the impact of the adsorption competition between CO_2 and H_2O.

An attempt to evaluate the water adsorption kinetics was performed by integrating the DRIFT spectra in the water fingerprint region after subtracting the area corresponding to the spectrum of the dry (regenerated) MOFs.

6.2.1 MIL-160(Al)

The DRIFT spectrum of the fully activated MIL-160(Al) is presented in Figure 6.10. A broadband can be observed in the range 3000 - 3700 cm^{-1} (Figure 6.10a), which is attributed to the stretching vibration of hydroxyl groups of the aluminum oxide-hydroxide chains, also identified by Wahiduzzaman and co-workers [2], at 3617 and 3355 cm^{-1}. The weak band peaking at 3620 cm^{-1} corresponds to the stretching vibration of isolated hydroxyl groups. Due

to the high oscilations in the signal intensity in Figure 6.10b), a DRIFT-ATR spectrum was performed (Figure 6.11). The stretching vibration of the C=C bond in the furan ring and the wagging vibration of the –CH– group may be observed at 1585 and 1417 cm^{-1}, respectively. The bands corresponding to the asymmetric and symmetric stretching vibrations of the ester C–O–C groups and the =C–O–C= vibration of the furan rings are visible in the range between 1000 and 1300 cm^{-1}. Finally, the band at 782 cm^{-1} can be ascribed to the C–H out-of-plane bending vibrations of the furan ring [2], while the band peaking at 646 cm^{-1} is attributed to the stretching vibrations of the Al–O bond in the octahedral structure of AlO$_6$ [3].
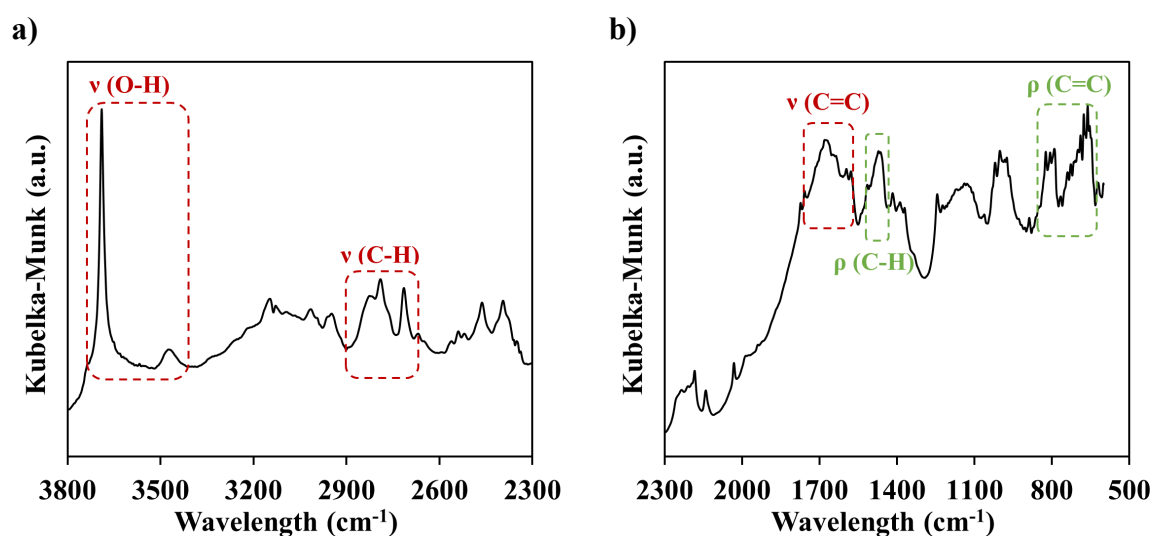

Figure 6.10. DRIFT spectrum of activated MIL-160(Al) in the region of (a) 3800–2300 cm^{-1} and (b) 2300–600 cm^{-1}.
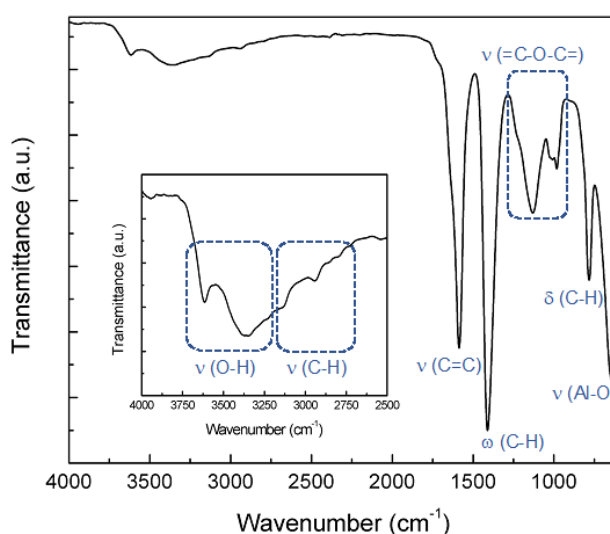
Figure 6.11. DRIFT-ATR spectrum of MIL-160(Al). Inset: Spectrum magnification of the 4000-2500 cm^{-1} zone.

The impact of temperature on MIL-160(Al) was evaluated by DRIFT spectra analyses (Figure 6.12). On non-activated MIL-160(Al), the DRIFT spectrum for each rise of temperature was collected. While the temperature increased, the IR absorption intensity, between 3800 cm^{-1} and 2300 cm^{-1}, decreased due to moisture and other air components desorption (Figure 6.12a). The spectra shown in Figure 6.12b) prove the thermal stability of MIL-160(Al), already assessed by TGA.
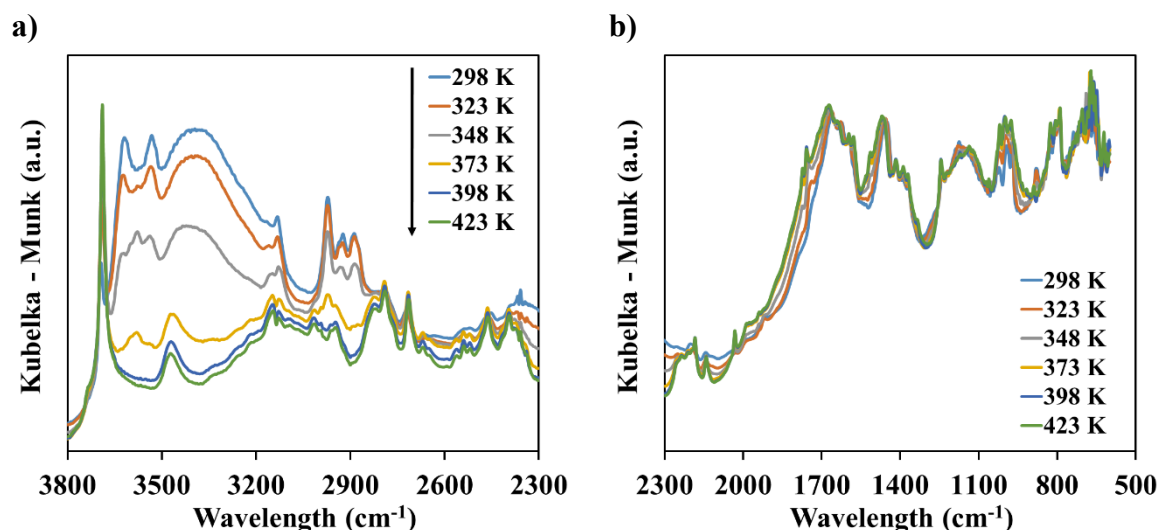
Figure 6.12. DRIFT spectrum of MIL-160(Al) during the regeneration step in the region of (a) 3800–2300 cm^{-1} and (b) 2300–600 cm^{-1}.

After MIL-160(Al) activation, the material was exposed to water vapor, and spectra were collected periodically until reaching the material saturation (Figure 6.13). Along with the water adsorption, a large band started to appear in the region of 3680 to 2850 cm^{-1} (Figure 6.13a). Between 1880 and 600 cm^{-1} no noteworthy changes were observed, concluding that the presence of water does not affect the material structure, which remains stable.

Figure 6.13. DRIFT spectrum of MIL-160(Al) during water adsorption in the region of (a) 3800–2300 cm^{-1} and (b) 2300–600 cm^{-1}.

Figure 6.14 illustrates the spectra collected during the co-adsorption of CO_2 and H_2O. In Figure 6.14a), a similar shape of the large band presented in Figure 6.13a) is visible. However, in the 2430–2230 cm^{-1} region, a continuous peak started to appear, probably due to the CO_2 adsorption. To further understand the origin of this peak, CO_2 adsorption experiments were performed.
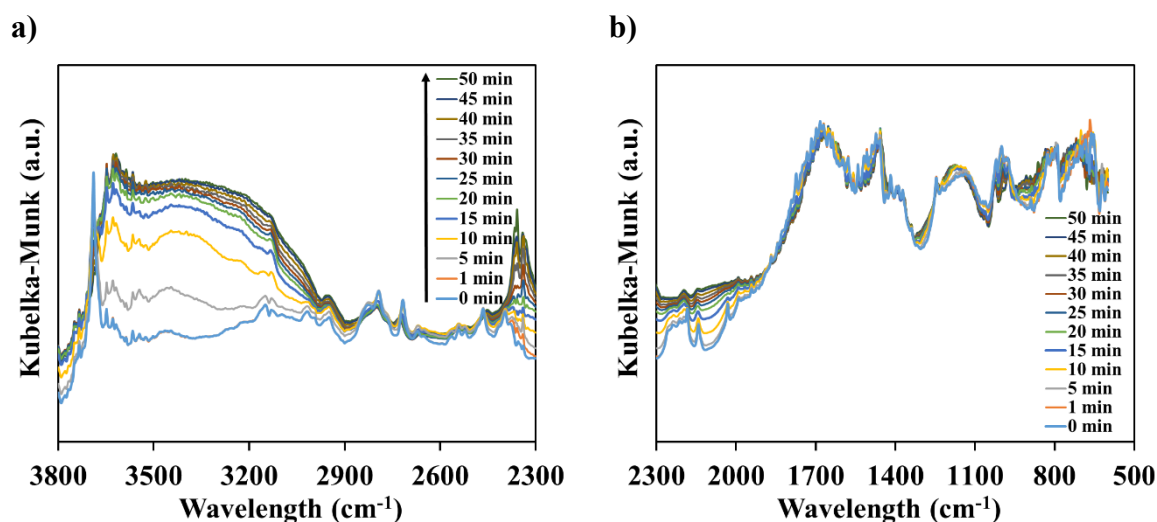
Figure 6.14. DRIFT spectrum of MIL-160(Al) during co-adsorption of water and CO_2 in the region of (a) 3800–2300 cm^{-1} and (b) 2300–600 cm^{-1}.

Figure 6.15 exhibits the spectra collect throughout the CO_2 adsorption. These spectra allowed to prove the broadband presented in Figure 6.13a) and Figure 6.14a) (3680–2850 cm^{-1})

is related to the water adsorption, and it is not present in Figure 6.15a), as expected. Besides, CO_2 is responsible for the continuous increase of the peak in the range of 2430–2230 cm^{-1}, as observed in Figure 6.14b) and Figure 6.15b).
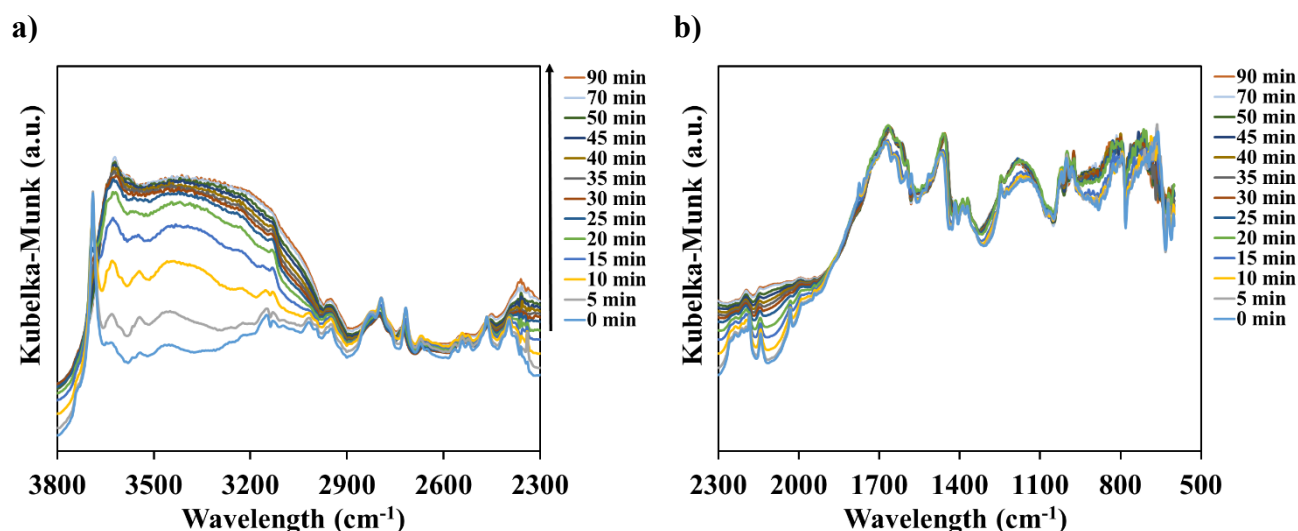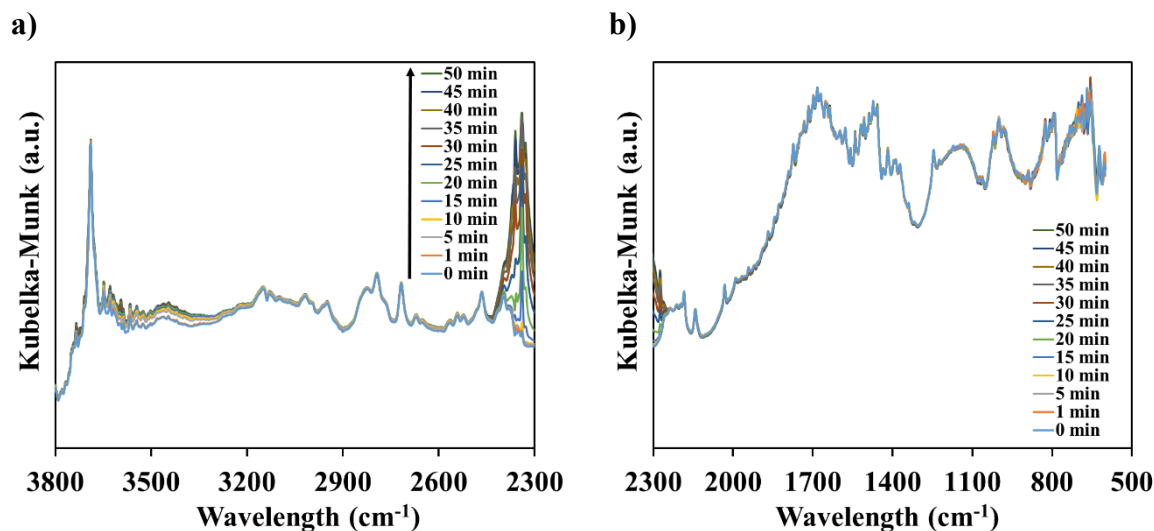

Figure 6.15. DRIFT spectrum of MIL-160(Al) during CO_2 adsorption in the region of (a) 3800–2300 cm^{-1} and (b) 2300–600 cm^{-1}.

The quantification of the water amount adsorbed in the MIL-160(Al) over time was determined (Figure 6.16) by the integration of the DRIFT spectra in the 3850–2400 cm^{-1} region (Figure 6.13a) after correction with the DRIFT spectrum area of the regenerated MIL-160(Al) (Figure 6.10a). The amount adsorbed increased linearly until 20 minutes of water exposure. A slower increase was observed along with the progress of water adsorption; a plateau was reached at c.a. 75 minutes of adsorption.
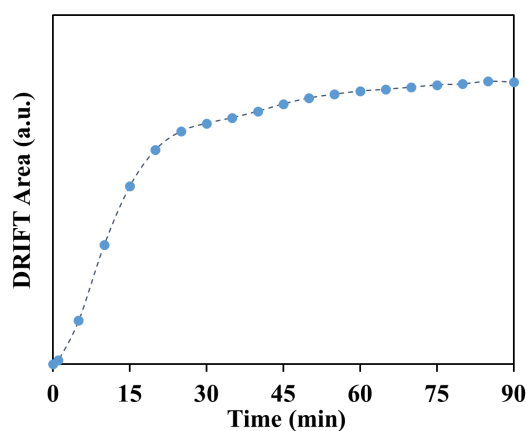
Figure 6.16. Variation of the area of the MIL-160(Al) DRIFT spectra with time during adsorption of H_2O (integration over 3850–2400 cm^{-1}).

6.2.2 MIL-100(Fe)

The DRIFT spectrum of activated MIL-100(Fe) is represented in Figure 6.17. In the 3700–2700 cm^{-1} region, bands assigned to the O-H group's asymmetric stretching vibration, were detected (Figure 6.17a). The OH group's stretching vibrational band was previously reported at 3418 cm^{-1} and 3675 cm^{-1} by Mutyala *et al.* [4] and by Valekar *et al.* [5], respectively. At 2360 and 2320 cm^{-1}, two peaks can be attributed to O=C=O stretching CO_2 mode. In Figure 6.17b), asymmetric stretching vibration of C=C bands is visible at 1650 cm^{-1}, while at 1350 cm^{-1} and 1250 cm^{-1}, two O-H bending vibrational peaks are assigned. Two asymmetric C-H bending vibrational peaks of benzene are presented at 1890 cm^{-1} and 870 cm^{-1}. In the range of 1250 to 1060 cm^{-1}, a broad IR band attributed to C-O stretching vibration is shown.
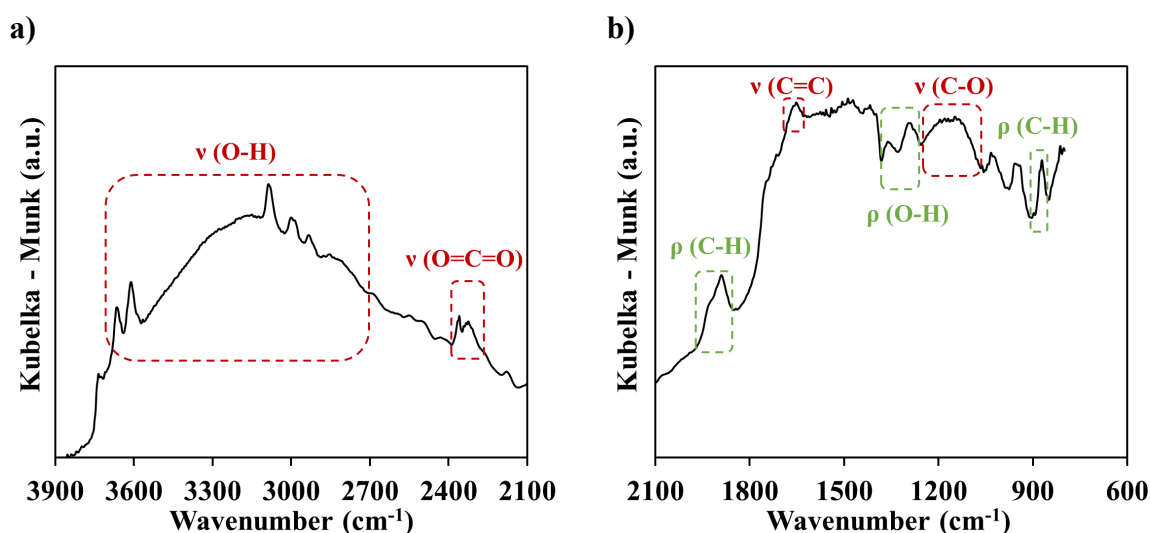
Figure 6.17. DRIFT spectrum of activated MIL-100(Fe) in the region of (a) 3900–2100 cm^{-1} and (b) 2100–600 cm^{-1}.

The continuous temperature increase led to a decrease of O-H asymmetric stretching band intensity due to the desorption of moisture from the material (Figure 6.18a), progressively appearing peaks of the dehydrated groups (at 3665 and 3610 cm^{-1}), such as in the sample reported by Seo *et al.* [6]. In the region of 1700–700 cm^{-1} (Figure 6.18b), the spectra maintained unchanged, demonstrating structural stability upon exposure to high temperatures, following the already observed TGA results.

a)

b)

Figure 6.18. DRIFT spectrum of MIL-100(Fe) during the regeneration step in the region of (a) 3900–2100 cm^{-1} and (b) 2100–800 cm^{-1}.

Figure 6.19 shows the spectra collected periodically during the water vapor adsorption. The band in the range of 3700 to 1700 cm^{-1} increased throughout the time, due to the exposure to water, as well as, for the band in the 1050–800 cm^{-1} region (Figure 6.19). As observed in Figure 6.18a), moisture minimizes the presence of dehydrated groups of MIL-100(Fe) structure. In Figure 6.19b), minimal intensities changes were observed between 1750 and 1050 cm^{-1}.

a)

b)

Figure 6.19. DRIFT spectrum of MIL-100(Fe) during water adsorption in the region of (a) 3900–2100 cm^{-1} and (b) 2100–800 cm^{-1}.

In Figure 6.20, spectra of the water and CO_2 co-adsorption experiments presented a similar behavior to the spectra of the single component water adsorption. The most significant difference occurred at the $2385–2285$ cm^{-1} region assigned to the CO_2 fingerprint.
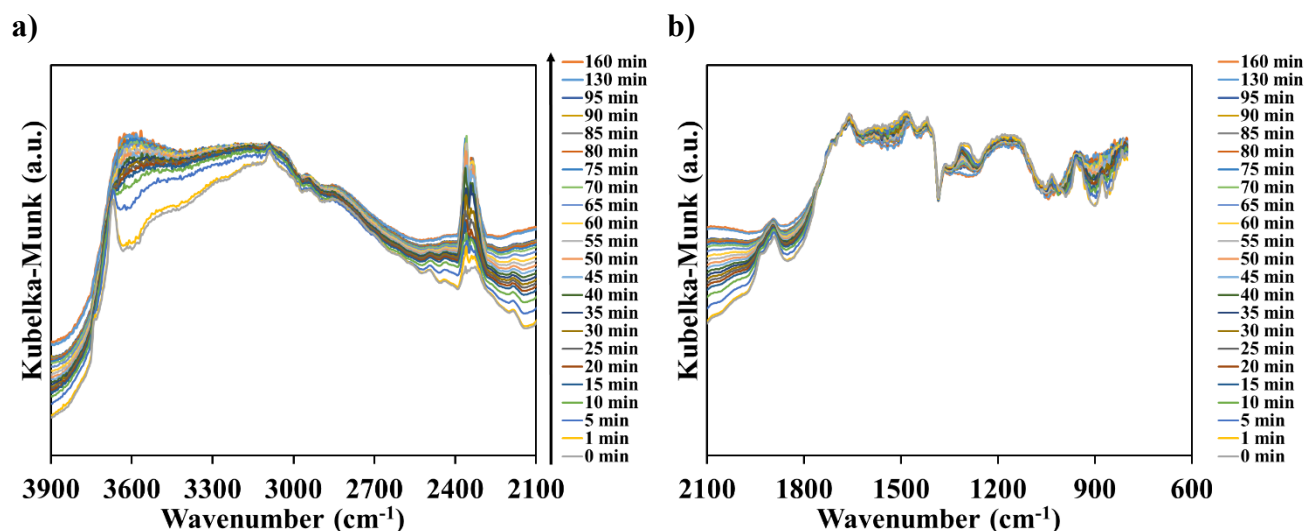
Figure 6.20. DRIFT spectrum of MIL-100(Fe) during co-adsorption of water and CO_2 in the region of (a) $3900–2100$ cm^{-1} and (b) $2100–800$ cm^{-1}.

CO_2 adsorption experiments corroborated the assignment of CO_2 adsorbed structure to the $2385–2285$ cm^{-1} region (Figure 6.21a). No other remarkable changes during the CO_2 adsorption were observed (Figure 6.21b).
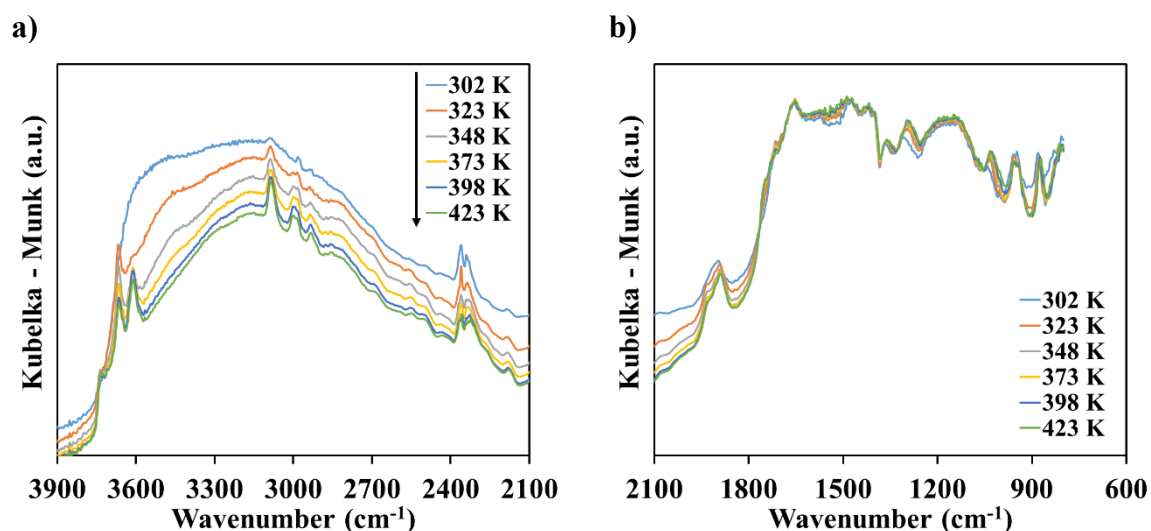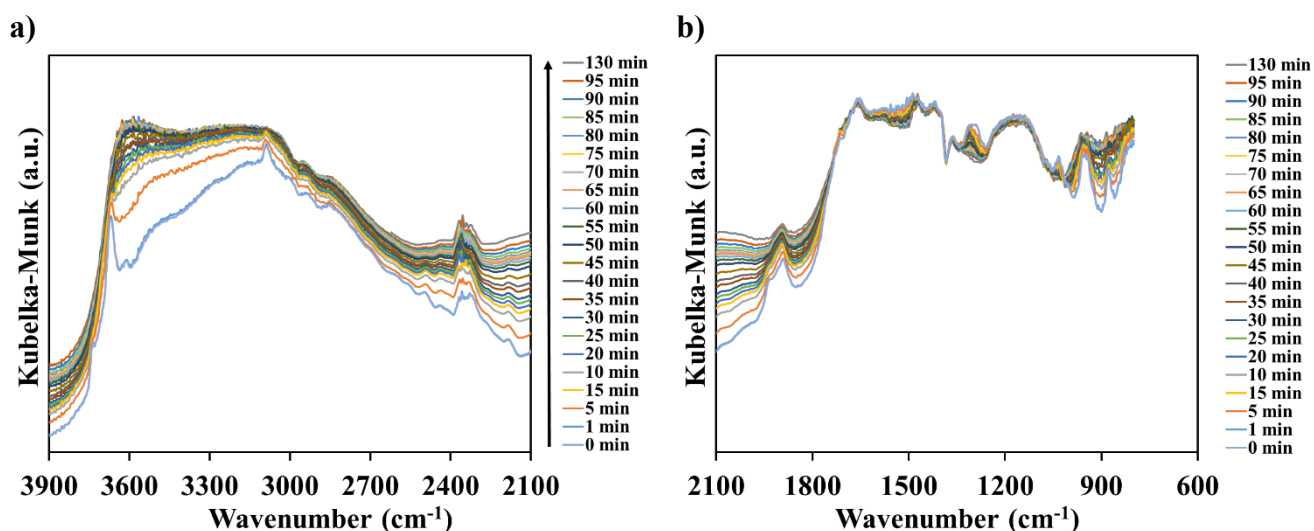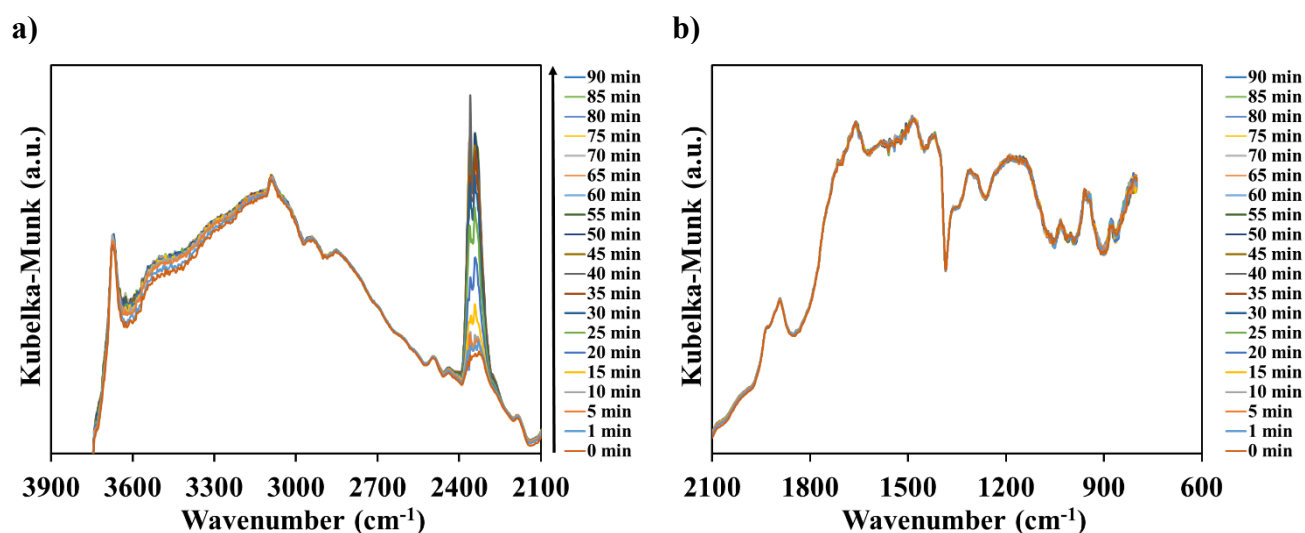

Figure 6.21. DRIFT spectrum of MIL-100(Fe) during CO_2 adsorption in the region of (a) $3900–2100$ cm^{-1} and (b) $2100–600$ cm^{-1}.

Figure 6.22 corresponds to the integration of MIL-100(Fe) DRIFT spectra area over the 4000-2400 cm^{-1} region for 130 minutes of the water adsorption experiments. A rapid increase in the water adsorption in the first 20 minutes was observed. However, the observed behavior is as it is expected for adsorption uptake experiments.
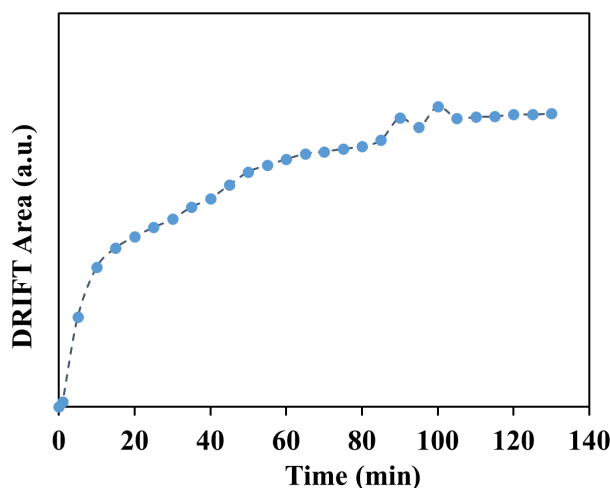
Figure 6.22. Variation of the area of the MIL-100(Fe) DRIFT spectra with time during adsorption of H$_2$O (integration over 4000–2400 cm^{-1}).

6.2.3 MIL-125(Ti)_NH$_2$

The DRIFT spectrum of dry MIL-125(Ti)_NH$_2$, displayed in Figure 6.23a), exhibits three typical vibrational bands in the 3800–3200 cm^{-1} region, peaking at 3500 cm^{-1}, 3380 cm^{-1}, and 3680 cm^{-1}. The first two bands are assigned to asymmetrical and symmetrical stretching vibrations of the amine groups, respectively, while the latter to the stretching vibrations of the isolated OH groups. The amino-stretching vibrations were previously detected at 3519.5 cm^{-1} and 3388.4 cm^{-1} by Nasalevich *et al.* [7] and 3686 cm^{-1}, 3430 cm^{-1}, and 2550 cm^{-1} by Vaesen *et al.* [8]. In the 1800–600 cm^{-1} fingerprint region of the spectrum (Figure 6.23b), the bands detected around 1600 and 1500 cm^{-1} are combination bands assigned to carbonyl asymmetric stretching vibrations. In contrast, those at about 1440 and 1400 cm^{-1} are attributed to carbonyl symmetric stretching vibrations. The band at 1630 cm^{-1} can be assigned to the N–H bending (scissoring) vibration. The C–N stretching vibrations of the linker's aromatic amines (2-aminoterephthalic acid) results in the bands at 1250 cm^{-1} and 1340 cm^{-1} [9]. Finally, the bands ascribed to Ti–O–Ti–O stretching vibrations appear in the region of 800-600 cm^{-1} [10].
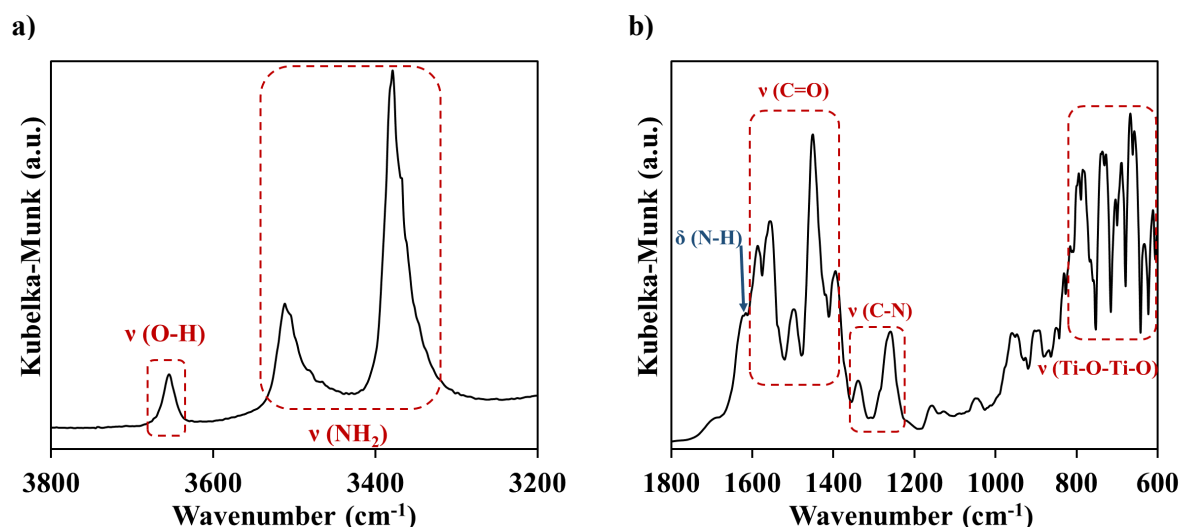
Figure 6.23. DRIFT spectrum of MIL-125(Ti)_NH$_2$ in the region of (a) 3800–3200 cm^{-1} and (b) 1800–600 cm^{-1}.

The regenerative effect of temperature is visible on the MIL-125(Ti)_NH$_2$ evolving spectra reported in Figure 6.24. The first spectrum, taken at room temperature (298 K), corresponds to a sample that was analyzed as received (Figure 6.24a). An increase in the signal intensity in the 3800-2400 cm^{-1} region was observed due to moisture present in the sample. As the temperature was increased up to 373 K, the signal's intensity decreased due to the water desorption. No significant changes were observed in the spectra above that temperature, implying a complete dehydration (regeneration) of the sample. During the heating, the vibrations of the structural units of the sample practically remained unchanged, indicating the high thermal stability of MIL-125(Ti)_NH$_2$ (Figure 6.24b).
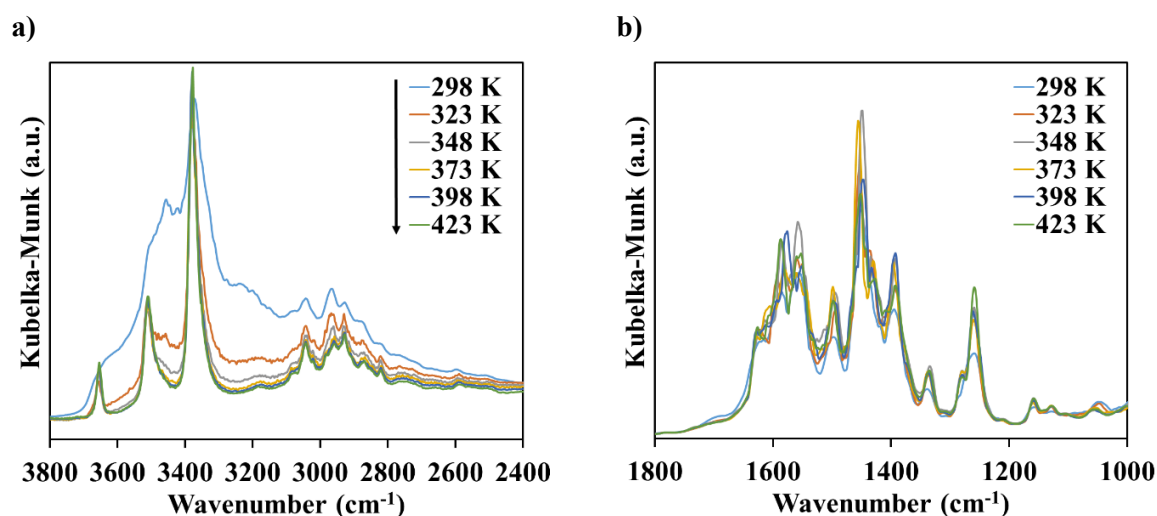
Figure 6.24. DRIFT spectrum of MIL-125(Ti)_NH$_2$ during regeneration step in the region of (a) 3800–2400 cm^{-1} and (b) 1800–1000 cm^{-1}.

From the spectra collected periodically during the water vapor adsorption experiments (Figure 6.25a), it can be seen that the intensities of the bands in the 3800–2400 cm^{-1} region continuously increased with the time of exposure to water vapor. The increase was fast, also indicating fast adsorption kinetics of water vapor adsorption in MIL-125(Ti)_NH$_2$. The unchanged intensities of the bands after the 35 min of exposure to water vapor indicate that the equilibrium has been reached. Intensities of the bands associated with the structural vibrations of the solid, in the region of 1800-1000 cm^{-1} (Figure 6.25b), have not been changed remarkably, indicating structural stability of the sample upon exposure to water vapor for at least 40 min. In this spectral region, a band at c.a. 1640 cm^{-1} which is assigned to the O–H bending vibrations, appeared just after 1 min of exposure to water vapor.
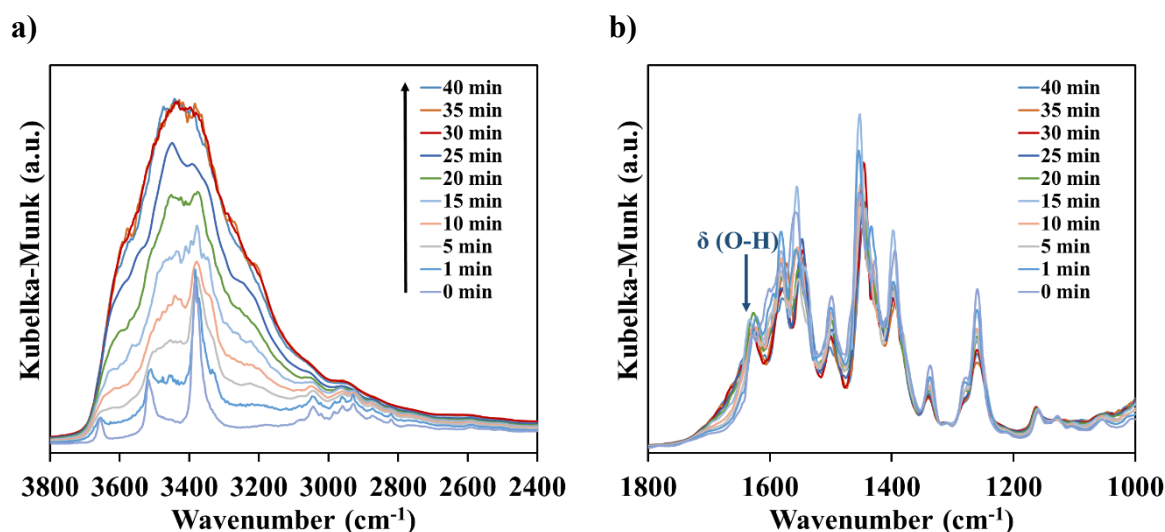
Figure 6.25. DRIFT spectrum of MIL-125(Ti)_NH$_2$ during water adsorption in the range of (a) 3800–2400 cm^{-1} and (b) 1800–1000 cm^{-1}.

After several cycles of adsorption/regeneration, the DRIFT spectra of the MIL-125(Ti)_NH$_2$ remained mostly unchanged (Figure 6.26), which indicates that the material did not suffer any major structural modification upon cyclic water adsorption. This conclusion is corroborated by the textural characterization performed to the sample used in the microbalance to access the adsorption equilibrium. The surface area and pore volume are in good agreement with the ones published for a fresh sample of the same shaped material and powder [9, 11].
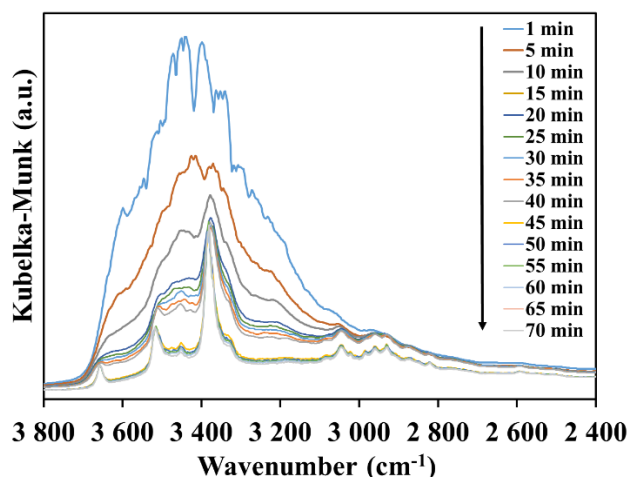
Figure 6.26. DRIFT spectra of MIL-125(Ti)_NH_2 regeneration at room temperature after water adsorption.

The spectra collected during the co-adsorption of CO_2 and H_2O on MIL-125(Ti)_NH_2 are depicted in Figure 6.27. In the 3800–2400 cm^{-1}, the continuous growth in intensity of the bands is observed due to the water adsorption (Figure 6.27a). In Figure 6.27b) appears two peaks, at 2360 and 2340 cm^{-1}, corresponding to the asymmetric stretching mode of CO_2 [12] adsorbed on MIL-125(Ti)_NH_2.

a)   b)
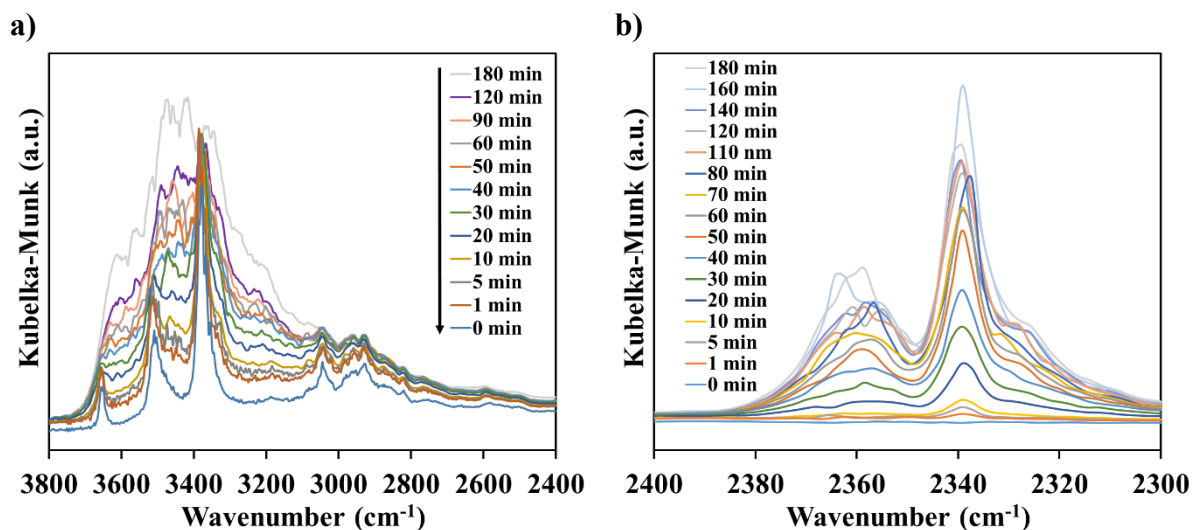
Figure 6.27. DRIFT spectrum collected during co-adsorption of H_2O and CO_2 in the region of (a) 3800–2400 cm^{-1} and (b) 2400–2300 cm^{-1}.

This same CO_2 asymmetric stretching mode is observed in the CO_2 adsorption on MIL-125(Ti)_NH_2 (Figure 6.28b). Figure 6.28a) is not visible any significant structure difference, maintaining almost constant the intensities of the peaks.

a)

b)
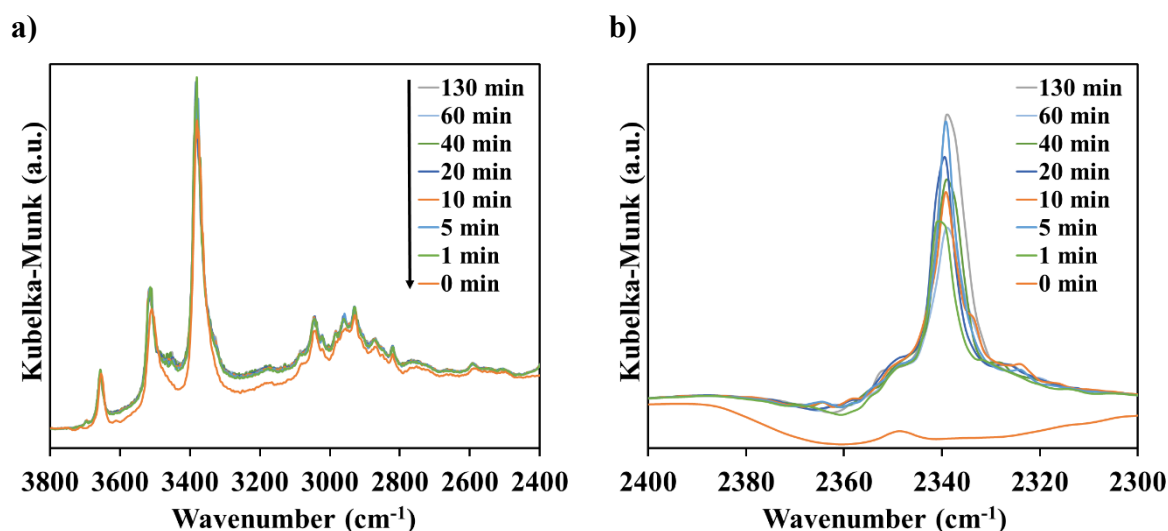
Figure 6.28. DRIFT spectrum collected during CO_2 adsorption in the region of (a) 3800–2400 cm^{-1} and (b) 2400–2300 cm^{-1}.

Figure 6.29 presents the integration of DRIFT spectra in the 3800-2400 cm^{-1} region of MIL-125(Ti)_NH$_2$. It is observed that the amount adsorbed increased linearly during the first 30 minutes of the exposure to water vapor. Then, the adsorption rate has slowed down until reaching a quasi-plateau at c.a. 80 minutes.
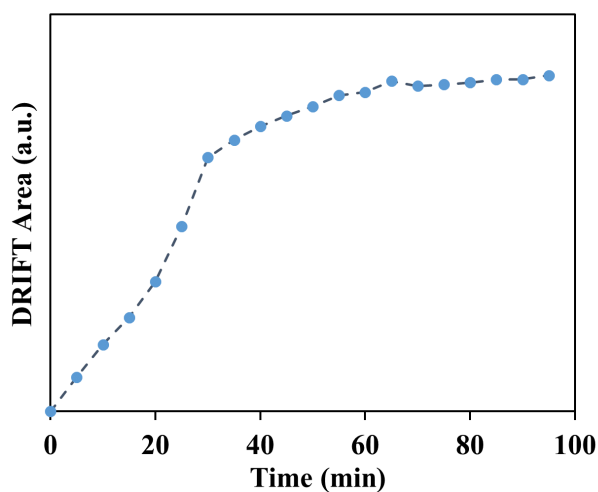
Figure 6.29. Variation of the area of the MIL-125(Ti)_NH$_2$ DRIFT spectra with time during adsorption of H_2O (integration over 3800-2400 cm^{-1}).

6.3 Summary

Water vapour breakthrough curves in inert helium followed the expected behavior based on the water vapor adsorption equilibrium isotherm for all MOFs. This indicates that under such experimental conditions the dynamic response of the system for the five MOFs is controlled by the adsorption equilibrium and not adsorption kinetics. Furthermore, the dynamic adsorption behavior of water adsorption in the fixed bed for the different MOFs is well predicted by the developed model, excepting on Al-Fum adsorbent. The similarity between water breakthrough curves in inert helium and with co-adsorption with other gases, namely N_2 and/or CO_2, allowed to conclude they do not influence on H_2O adsorption significantly. This is corroborated by the fact that the fixed bed model predicts the water vapour dynamic behaviour without taking into consideration the competition with these gases.

DRIFT analysis revealed that MIL-125(Ti)_NH$_2$, MIL-100(Fe), and MIL-160(Al) structures remained stable after several water adsorption/regeneration cycles. MOFs structures were exposed at different temperatures with no impact on spectra, proving so to be thermal stable. Furthermore, the uptake information taken from the DRIFT based experiments, evidence that water adsorption is a fast phenomenon in the evaluated MOFs.

References

1. Bozbiyik, B., T. Van Assche, J. Lannoeye, D.E. De Vos, G.V. Baron, and J.F.M. Denayer, *Stepped water isotherm and breakthrough curves on aluminium fumarate metal–organic framework: experimental and modelling study.* Adsorption, 2017. **23**(1): p. 185-192.

2. Wahiduzzaman, M., D. Lenzen, G. Maurin, N. Stock, and M.T. Wharmby, *Rietveld Refinement of MIL-160 and Its Structural Flexibility Upon H2O and N2 Adsorption.* European Journal of Inorganic Chemistry, 2018. **2018**(32): p. 3626-3632.

3. Tarte, P., *Infra-red spectra of inorganic aluminates and characteristic vibrational frequencies of AlO4 tetrahedra and AlO6 octahedra.* Spectrochimica Acta Part A: Molecular Spectroscopy, 1967. **23**(7): p. 2127-2143.

4. Mutyala, S., S.M. Yakout, S.S. Ibrahim, M. Jonnalagadda, and H. Mitta, *Enhancement of CO2 capture and separation of CO2/N2 using post-synthetic modified MIL-100(Fe).* New Journal of Chemistry, 2019. **43**(24): p. 9725-9731.

5. Valekar, A.H., K.-H. Cho, U.H. Lee, J.S. Lee, J.W. Yoon, Y.K. Hwang, S.G. Lee, S.J. Cho, and J.-S. Chang, *Shaping of porous metal–organic framework granules using mesoporous ρ-alumina as a binder.* RSC Advances, 2017. **7**(88): p. 55767-55777.

6. Seo, Y.-K., J.W. Yoon, J.S. Lee, Y.K. Hwang, C.-H. Jun, J.-S. Chang, S. Wuttke, P. Bazin, A. Vimont, M. Daturi, S. Bourrelly, P.L. Llewellyn, P. Horcajada, C. Serre, and G. Férey, *Energy-Efficient Dehumidification over Hierachically Porous Metal–Organic Frameworks as Advanced Water Adsorbents.* Advanced Materials, 2012. **24**(6): p. 806-810.

7. Nasalevich, M.A., M.G. Goesten, T.J. Savenije, F. Kapteijn, and J. Gascon, *Enhancing optical absorption of metal-organic frameworks for improved visible light photocatalysis.* Chemical Communications, 2013. **49**(90): p. 10575-10577.

8. Vaesen, S., V. Guillerm, Q. Yang, A.D. Wiersum, B. Marszalek, B. Gil, A. Vimont, M. Daturi, T. Devic, P.L. Llewellyn, C. Serre, G. Maurin, and G. De Weireld, *A robust*

amino-functionalized titanium(iv) based MOF for improved separation of acid gases. Chemical Communications, 2013. **49**(86): p. 10082-10084.

9. Moreira, M.A., M.P.S. Santos, C.G. Silva, J.M. Loureiro, J.-S. Chang, C. Serre, A.F.P. Ferreira, and A.E. Rodrigues, *Adsorption equilibrium of xylene isomers and ethylbenzene on MIL-125(Ti)_NH2: the temperature influence on the para-selectivity.* Adsorption, 2018. **24**(8): p. 715-724.

10. Hu, S., M. Liu, K. Li, Y. Zuo, A. Zhang, C. Song, G. Zhang, and X. Guo, *Solvothermal synthesis of NH2-MIL-125(Ti) from circular plate to octahedron.* CrystEngComm, 2014. **16**: p. 9645–9650

11. Canivet, J., J. Bonnefoy, C. Daniel, A. Legrand, B. Coasne, and D. Farrusseng, *Structure-property relationships of water adsorption in metal-organic frameworks.* New Journal of Chemistry, 2014. **38**(7): p. 3102-3111.

12. Ali, M.W., W.P. Zheng, S. Sohail, Q.M. Li, W.W. Zheng, and H.Y. Zhang, *A genetically enhanced sterile insect technique against the fruit fly, Bactrocera dorsalis (Hendel) by feeding adult double-stranded RNAs.* Scientific Reports, 2017. **7**.

7 PROCESS DEVELOPMENT AND OPTIMIZATION

7.1 Process Design

A process to produce water harvesting from thin air by adsorption and its posterior condensation from the regeneration outlet stream was designed. The original idea is the exposure to atmospheric moist air during the night (feed step) with water capture by the MOF through the adsorption process. Then, at the purge step, the solar irradiation is used to induce the water desorption on MOF, following the cooling to temperatures below the water dew point to yield water (condensation). The duration of the cycle process was assumed to be approximately 24 hours. The influence of feed flowrate, purge-flowrate, feed duration, purge duration, purge feed composition, purge temperature, purge pressure, and the purge outlet stream's cooling temperature was studied in the process performance. The purge temperature was chosen according to the regeneration experiments using solar irradiance (Appendix A). Based on the IPMA (Instituto Português do Mar e da Atmosfera) data, mainland Portugal presents annual solar insolation between 1800 and 3100 hours (1930-1960) [1]. Porto presents a yearly average availability of global solar irradiance equal to 1628 kWh·m^{-2}, considering the data from Porto meteorological station from 2002 to 2007 [2], leading to an average irradiance of 525 to 904 W·m^{-2}. Even if these irradiances were not possible to be achieved in the experiments presented in Figure A.6, the tested irradiances (250 and 350 W·m^{-2}) were the basis for defining purge temperatures. According to IPMA, the maximum and minimum monthly averages of relative humidity in Portugal, in the 1971-2000 period, corresponds to 85% (January and December) and 56% (August), respectively [3]. For the development of process design, a relative humidity of 50% was considered, corresponding to the relative humidity defined in the irradiance experiments (Appendix A).

The different designs were compared in terms of their productivity (l·day^{-1}). The knowledge gathered with the design of MIL-125(Ti)_NH$_2$ based process, was used in the design of the processes based on the other adsorbents, CAU-10, MIL-160(Al), and MIL-100(Fe). The study with Al-Fum was not performed due to the lack of the mathematical model validation against the experimental results, as explained in the previous chapter. On MIL-160(Al), the operating conditions of the proposed Temperature Swing Adsorption (TSA) cycles were further optimized using the Particle Swarm Optimization (PSO) model; for the remaining materials, the optimal operating conditions and cycle design was done by trial and error. The main transport parameters are presented in Table 7.1.

Table 7.1. Transport parameters used in the processes simulation.

		CAU-10	MIL-160(Al)	MIL-100(Fe)	MIL-125(Ti)_NH$_2$
Transport parameters	D_{ax} (m$^2 \cdot$s^{-1})	5.16×10^{-4}	1.33×10^{-4}	2.43×10^{-4}	5.00×10^{-3}
	k_f (m$\cdot$s^{-1})	2.60×10^{-2}	1.25×10^{-1}	1.25×10^{-1}	1.25×10^{-1}
	h_f (W$\cdot$m$^{-2} \cdot$K^{-1})	27.3	40.4	84.6	73.5
	h_w (W$\cdot$m$^{-2} \cdot$K^{-1})	3.81	202	181	100
	U (W$\cdot$m$^{-2} \cdot$K^{-1})	0	0	0	0

The feed was kept constant, and considered to be at 298 K and 1.01 bar on all designed adsorption processes. The feed composition of 76.9% of N$_2$, 21.7% of O$_2$, and 1.4% of H$_2$O (RH of 50%) was established for all processes too.

7.1.1 MIL-125(Ti)_NH$_2$

The adsorption cyclic process initially considered is composed of two co-current steps, feed and purge. In the process design, a column with a volume of 0.98 m^3 (length = 1.25 m, diameter = 1 m) packed with MOFs granules (345 kg) operating under adiabatic conditions was considered. Schematic representation of the TSA process is shown in Figure 7.1, while the operating and feed conditions are given in Table 7.2.

Figure 7.1. Schematic representation of the TSA process unit packed with MIL-125(Ti)_NH$_2$ during the (a) feed step and (b) purge step.

After preliminary studies, it was concluded that 60200 s for feed and 14400 s for purge were the "optimal" times to achieve saturation of the bed during the feed and efficient regeneration during the purge, in the TSA mode (Run 1 – 8, Table 7.2).

A Pressure-Temperature Swing Adsorption (PTSA) process was also developed considering the same operating feed conditions as in the TSA process (Figure 7.2a). Aiming to reduce the purge temperature (313 and 323 K), a purge pressure of 0.3 bar was studied, based on its impact on the process productivity. The "optimal" times for the PTSA operation mode were 61000 s (feed) and 26000 s (purge) (Run 9 – 10a, Table 7.2). Additionally, a buffer tank was coupled with the PTSA process (Figure 7.2b) (Run 10b, Table 7.2). Indeed, the "dry" air produced during the feed step, can be stored and used during the regeneration step.
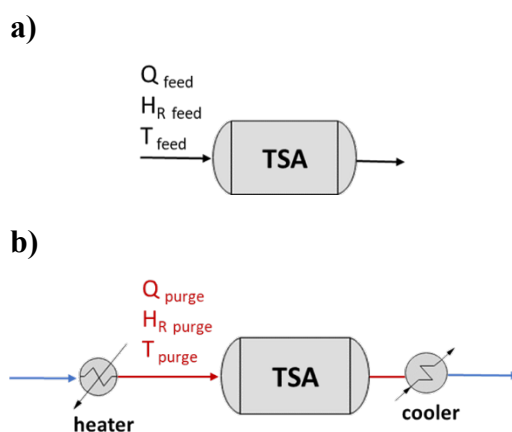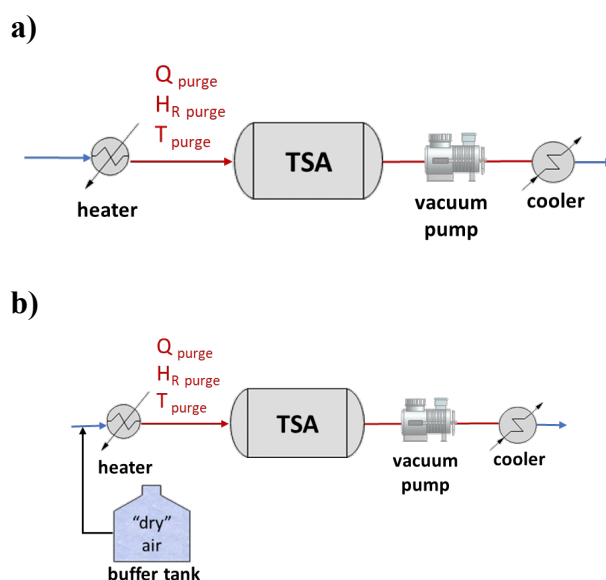

Figure 7.2. Schematic representation of the PTSA process unit packed with MIL-125(Ti)_NH$_2$ during the (a) purge step and (b) purge step with de-humified air.

Table 7.2. Harvested water productivity obtained by simulation for two AWVP cycles (TSA and PTSA).

Run	T_{purge} (K)	P_{purge} (bar)	$T_{condensation}$ (K)	Productivity		
				($l \cdot day^{-1}$)	($l \cdot day^{-1} \cdot ton^{-1}$)	($l \cdot day^{-1} \cdot m^{-3}$)
1	333	1.1	283	56.1	163	57.1
2	333	1.1	288	38.6	112	39.3
3	353	1.1	283	82.4	239	83.9
4	353	1.1	288	65.1	189	66.3
5	353	1.1	298	12.9	37	13.1
6	373	1.1	283	110.6	320	112.6
7	373	1.1	288	93.3	270	95.0
8	373	1.1	298	39.6	115	40.4
9	313	0.3	288	35.3	102	36.0
10a	323	0.3	288	52.8	153	53.8
10b	323	0.3	288	52.8	153	53.8

As expected, the highest productivity was obtained for the regeneration at the highest considered temperature (373 K) and condensation at the lowest evaluated temperature (283 K). The productivity of 320 $l \cdot day^{-1} \cdot ton^{-1}$ was obtained, which means we can produce about 320 $l \cdot day^{-1}$ with a unit of 2.84 m^3. With the goal of reducing the regeneration temperature, and decreasing refrigeration needed to condensate the water, a moderate vacuum (0.3 bar) was considered during the regeneration step (Runs 9, 10a, and 10b). Run 9 productivity is similar to the productivity of Run 2, yet it was achieved considering a regeneration temperature 20 K lower. Similar trend was observed for Run 10a and Run 1, regarding their performance, with a decrease of 10 K in the regeneration temperature. In Run 10b, it was considered the use of part of the de-humified air produced during the feed step to regenerate the column, but no significant impact was observed. Similar behavior was observed in the TSA process with de-humified air, the obtained results are not included within this chapter. Therefore, a buffer tank's addition to store the "dry" air to the AWVP unit is not required, keeping the unit simpler and with lower initial capital costs.

Figure 7.3 presents the history of gas temperature and RH at two different axial positions: 0.6 m and 1.25 m (outlet of the adsorber), at Cyclic Steady State (CSS), for Runs 3, 4, and 5. Figure 7.4 presents the internal profiles of RH (fluid-phase concentration) and adsorbed amount (adsorbed phase concentration), at two different cycle times: 5000 s (*i.e.*, 5000 s after the beginning of the feed step) and 65200 s (*i.e.*, 5000 s after the start of the purge step), at CSS, for Runs 3, 4, and 5. One can observe from both figures that the concentration shock wave only achieves the end of the column at the beginning of the regeneration step, *i.e.*, the feed step's duration is just enough to saturate the adsorber. The same is possible to be said about the regeneration step. Its duration is just long enough to achieve the desired working capacity (18.5 mol·kg^{-1}), yet it is too short, not allowing full regeneration of the bed during this step. Indeed, the efficiency of regeneration of the bed is guaranteed by the fact that the feed mass shock wave does not take over the regeneration mass shock wave during the feed step (at 5000 s of the feed step, they are 0.95 m apart – see Figure 7.4). The fact that one starts to feed the adsorber before full regeneration is achieved will allow some saving in heating costs of the purge stream and also increase the productivity.
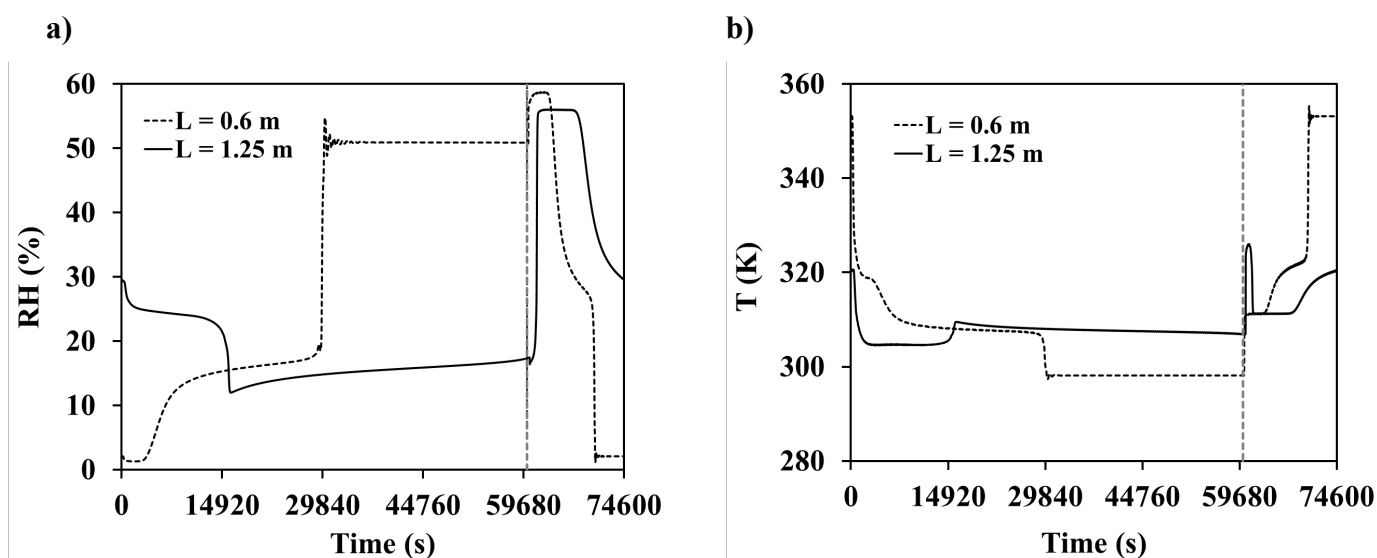
a)

b)

Figure 7.3. a) RH and b) gas temperature histories at two different axial positions: 0.6 m and 1.25 m, for Runs 3, 4 and 5.
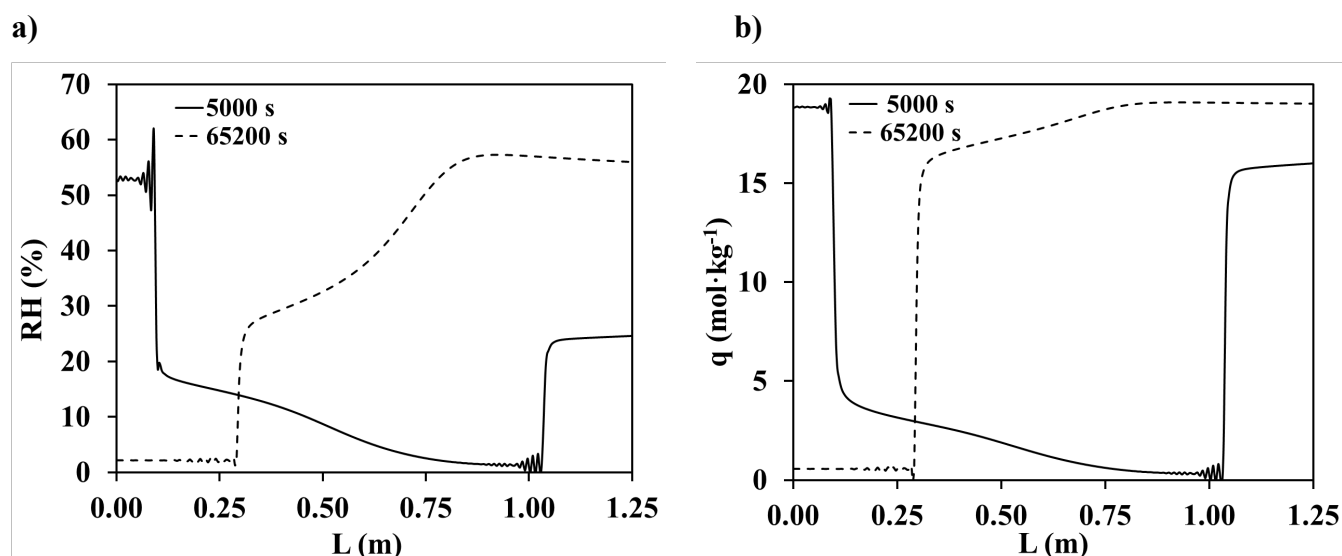
a)

b)

Figure 7.4. a) RH and b) adsorbed amount profiles at two different cycle times: 5000 s and 65200 s, for Runs 3, 4 and 5.

7.1.2 CAU-10

The TSA process (Figure 7.1), operating under adiabatic conditions, was the only considered design based on the MIL-125(Ti)_NH$_2$ process results. The column's dimensions were also maintained, allowing the packaging of 509 kg of CAU-10 adsorbent granules. Pressure and condensation temperature were considered to be 1.01 bar and 283 K, respectively. The feed and purge volumetric gas flow rates were kept equal as the previous material (0.30 m$^3 \cdot$s^{-1}). Different time steps (t$_{feed}$ and t$_{purge}$) were considered, and the results with the highest productivity are reported in Table 7.3. The total cycle duration obtained was, in general, higher than 24 hours. To reduce the cycle duration, the volume of the column was reduced to about a third of its initial column volume (0.98 m^3). The lower capacity of the column (volume = 0.35 m^3, length = 1.25 m, diameter = 0.6 m), which was packed only with 184 kg of CAU-10, allowed to obtain cycles with a total duration lower than 24 hours. As previously expected, the highest productivity was achieved for the regeneration at the highest considered temperature (373 K) on both bed dimensions. However, the productivity in terms of l·day^{-1} is similar (84.0 and 81.3 l·day^{-1} on the column volume of 0.98 and 0.35 m^3, respectively). When comparing in terms of mass or volume too, the TSA process with lower column volume presents the highest productivity (230 l·day^{-1}·m^{-3} and 443 l·day^{-1}·ton^{-1}) due to the need of shorter, maintaining the daily water harvesting capacity, with a third of mass/volume. Another advantage of the TSA process with

a lower column volume is the highest efficiency and reduced initial capital costs, needing lower cycle times and adsorbent mass.

Table 7.3. Harvested water productivity obtained in the TSA cycles for two different columns packed with CAU-10.

Column volume (m³)	T $_{purge}$ (K)	t_{feed} (s)	t_{purge} (s)	Productivity		
				($l \cdot day^{-1}$)	($l \cdot day^{-1} \cdot ton^{-1}$)	($l \cdot day^{-1} \cdot m^{-3}$)
	333	106000	58000	56.0	110	57.1
0.98	353	107000	32000	73.9	145	75.4
	373	106000	22000	84.0	165	85.7
	333	39000	21000	54.2	295	153
0.35	353	37000	12000	72.6	396	205
	373	38000	9000	81.3	443	230

The internal histories of RH and gas temperature at the middle position of the axial direction and the end of the column (0.6 and 1.25 m, respectively), at CSS, were computed for one of the most promising scenarios (productivity of 84.0 $l \cdot day^{-1}$ with a bed volume of 0.98 m³), and are presented in Figure 7.5. The internal profiles of RH and the adsorbed amount at CSS are shown in Figure 7.6 at 5000 s and 110000 s (*i.e.*, 5000 s after the beginning of regeneration step). The concentration shock wave reaches the end of the column at the beginning of the regeneration step, ensuring that the feed step duration is long enough to reach the saturation of the adsorbent, maximizing the use of its adsorption capacity. At 5000 s of the regeneration step, 1/5 of the packed bed is regenerated. The regeneration time cycle ends up before the complete regeneration of the packed bed. Indeed, as already observed for the case of MIL-125(Ti)_NH$_2$, the feed step starts before the full regeneration of the bed column leading to reduced costs inherent to regeneration energy and to increase the water harvesting capacity.

It must be highlighted that for the TSA process, considering a column volume of 0.35 m³, the histories and profiles followed the same trend as those shown for the case considering a column volume of 0.98 m³.
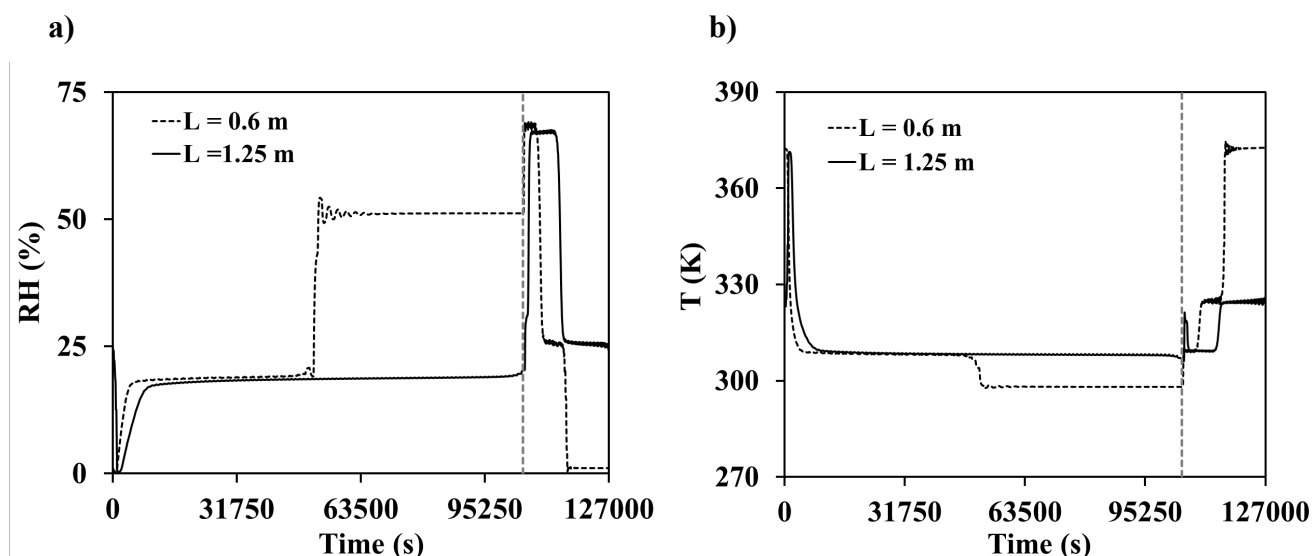
Figure 7.5. a) RH and b) gas temperature histories at two different axial positions: 0.6 m and 1.25 m, for the highest H_2O productivity on TSA column packed with CAU-10 (Vertical dashed line represents the beginning of the regeneration step).
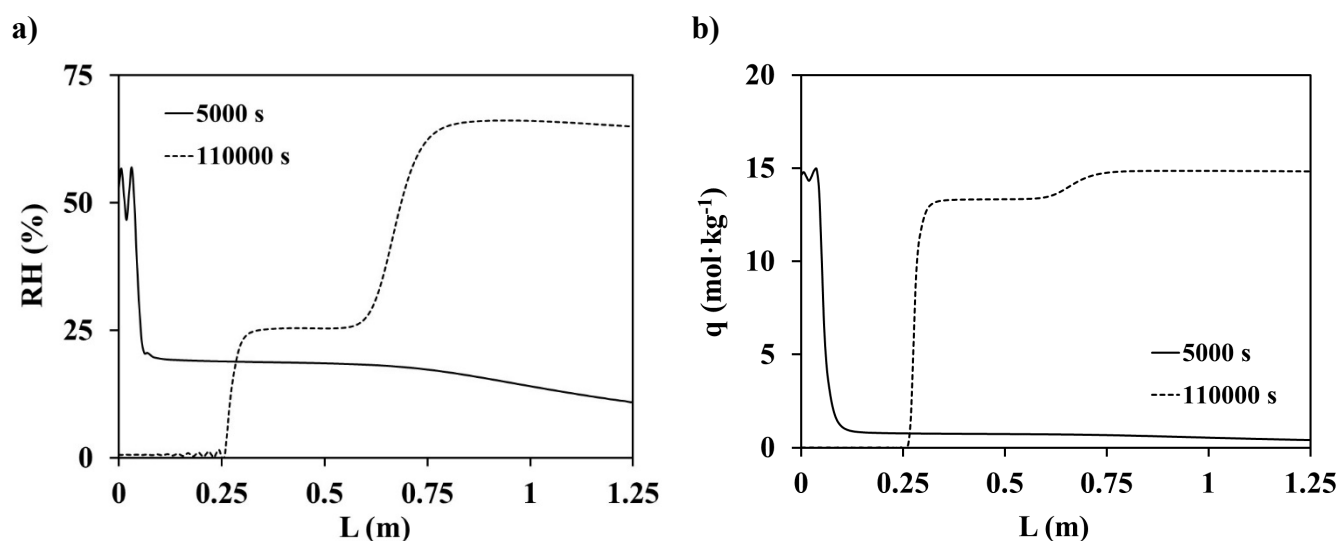
Figure 7.6. a) RH and b) adsorbed amount profiles at two different cycle times: 5000 s and 110000 s for the highest H_2O productivity on TSA column packed with CAU-10.

7.1.3 MIL-160(Al)

As in the study with CAU-10, the process considered to produce water harvesting using MIL-160(Al) as adsorbent corresponds to the TSA process presented in Figure **7.1**. Pressure and condensation temperature were maintained at 1.01 bar and 283 K, respectively, as well as, the column dimensions (length = 1.25 m, diameter = 1 m). Additionally, a column volume of

0.98 m^3 packed with 480 kg of MIL-160(Al) granules, operating under adiabatic conditions, was considered. The proposed TSA cycle operating conditions were optimized, and the steps duration (t$_\text{feed}$ and t$_\text{purge}$) were optimized to minimize a selected objective function.

The definition of the objective function in the optimization process is an essential factor. The optimization methodology followed an adapted PSO model developed by I. Nogueira, as a result of his doctoral thesis [4]. The PSO is a metaheuristic optimization algorithm developed by J. Kennedy (social psychologist) and R. Eberhart (electrical engineer) in 1995 [5-9]. This evolutionary computing method optimizes nonlinear functions and is inspired by social behavior and dynamic movements of natural swarms (bird flocks, schools of fish, and bees swarms) [5, 10]. The individual social behavior is influenced by its own experience and the accumulated experience of its swarm individuals [7, 11]. In the PSO algorithm, at each iteration, the particle/individual (i) tries to target its best position (personal best - $pbest$) and the best position of the particles of its group (global best - $gbest$), by adjusting its velocity [7, 11, 12]. The updated velocity and position of the individuals are given by [4, 7, 10-12]

$$v_i^{k+1} = v_i^K + c_1 \times r_1\left(pbest_i^k - s_i^k\right) + c_2 \times r_2\left(gbest_i^k - s_i^k\right) \tag{7.1}$$

$$s_i^{k+1} = s_i^k + v_i^{k+1} \tag{7.2}$$

with $i = 1, \dots, n$ in the n-dimensional space and $k = 0, \dots, k_{max}$; where v_i corresponds to the particle velocity, s_i is the particle position, c_1/c_2 are the search parameters (positive constants), r_1/r_2 are the random variables uniformly distributed between 0 and 1, and k and k_{max} is the number of iterations and the maximum number of iterations, respectively.

To maximize TSA water productivity (the quality parameter), was necessary the optimal definition of the unit operating variables, which in this case was simply the duration of each step. However, achieving a global optimum for those parameters is a difficult task; thus, the optimization problem was designed to get as close as possible to the global optimum. Therefore, it was proposed to apply an objective function with penalties, namely, a constant penalty was applied to a solution that violates the initially defined constraints. Hence, the objective function is defined as:

$$\min\,(J) = \sum_k^{nk} \left(\frac{1}{Pr_k}\right) \tag{7.3}$$

The assumptions defined were: time cycle process of approximately 24 hours; t_{feed} superior to t_{purge}; and optimized times in the range of 0 to 100000 s. The total number of particles and iterations selected was 25 and 50, respectively.

Considering a purge temperature of 353 K and equal feed and purge flow rates, four optimization runs were performed, one for each volumetric gas flow rate (0.10, 0.30, 0.40, and 0.50 $m^3 \cdot s^{-1}$) (Figure 7.7 and Table 7.4). The same procedure was repeated by fixating the volumetric gas flow rate at 0.30 $m^3 \cdot s^{-1}$ and considering different purge/regeneration temperatures (333, 353, 363, and 373 K (Figure 7.8 and Table 7.5).

Figure 7.7 shows the maximum productivity obtained by using each one of the flow rates. At the same time, Table 7.4 presents the optimal point found for the cycle steps duration (t_{feed} and t_{purge}) and the corresponding maximum productivity and standard deviation (std). One should note that each optimization run consists of three individual optimization trials, and the reported result for each run is the average of the three trials.

The maximum productivities vary between 22.3 $l \cdot day^{-1}$ (46.5 $l \cdot day^{-1} \cdot ton^{-1}$) and 147 $l \cdot day^{-1}$ (305 $l \cdot day^{-1} \cdot ton^{-1}$). As expected, total cycle duration decreases inversely with the flow rate.

Figure 7.7. Maximum water production by optimal unit performance parameters in terms of flow rate.

Table 7.4. Optimal unit point for different flow rates.

Q (m³·s⁻¹)	Productivity (l·day⁻¹)		t_{feed} (s)		t_{purge} (s)	
	value	std	value	std	value	std
0.10	22.3	4.6x10⁻²	60945	3000	26872	3500
0.30	89.3	1.3x10⁻³	56866	2600	24204	2100
0.40	118	1.0x10⁻⁵	43390	2.25	18486	2.85
0.50	147	1.0x10⁻⁵	35125	3.15	14994	2.75

Figure 7.8 represents the optimal unit productivity achieved after the optimization process for each purge temperature, while Table 7.5 presents more detailed the results of the optimal cycle. The productivity is directly proportional to the purge temperature, as predictable. The maximum productivity (111 l·day⁻¹) was obtained for the maximum purge temperature (373 K).
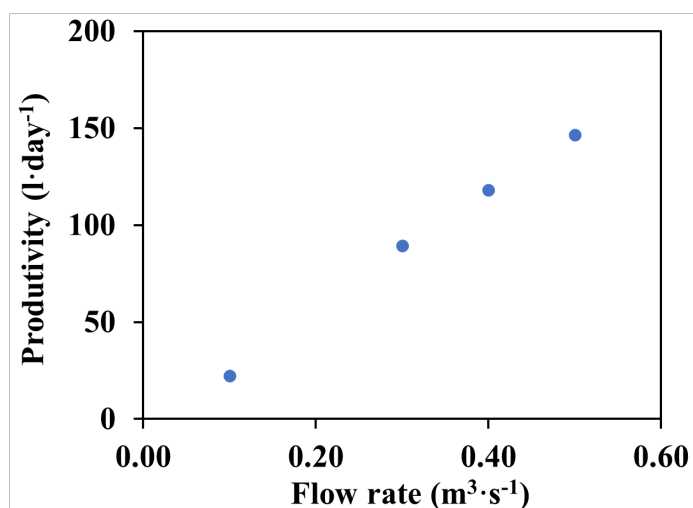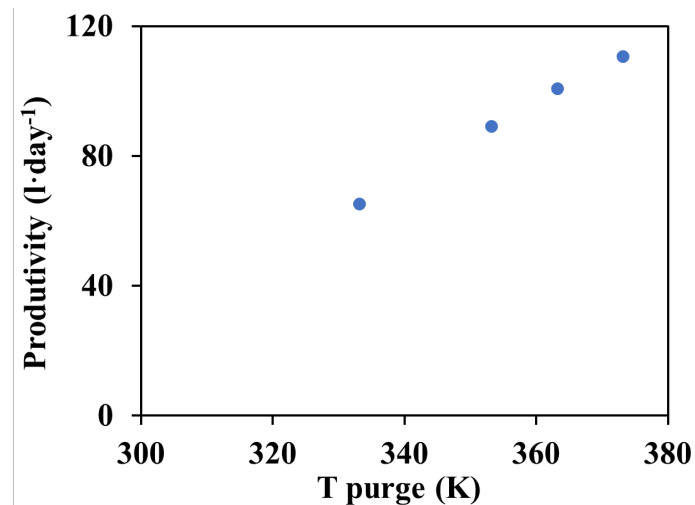

Figure 7.8. Maximum water production by optimal unit performance parameters in terms of regeneration temperature.

Table 7.5. Optimal unit point for different purge temperatures.

T_{purge} (K)	Productivity ($l \cdot day^{-1}$)		t_{feed} (s)		t_{purge} (s)	
	value	std	value	std	value	std
333	65.2	8.0×10^{-5}	53376	79.1	23787	73.9
353	89.3	1.3×10^{-3}	56866	2600	24204	2100
363	101	4.0×10^{-6}	57031	1.56	23317	0.55
373	111	2.0×10^{-6}	56705	4.00	21133	1.18

The most promising scenario was obtained for purge temperature equal to 353 K and a flow rate of 0.50 $m^3 \cdot s^{-1}$, with the highest H_2O productivity of 305 $l \cdot day^{-1} \cdot ton^{-1}$. The history of gas temperature and RH at two different axial positions: 0.6 m and 1.25 m (outlet of the adsorber), at CSS, are presented in Figure 7.9. At the beginning of the regeneration step (35125 s), the concentration shock wave has just achieved the column end, as can be observed in Figure 7.9a). Furthermore, the regeneration step ends up before the full regeneration of the bed. The full regeneration of the bed proceeds during the feed step. Indeed, the end of the bed is never fully regenerated, which can be easily understood since productivity is a time-based performance parameter. The time that it takes to regenerate the end part of the bed fully, might not be waged by the additional capacity gained.
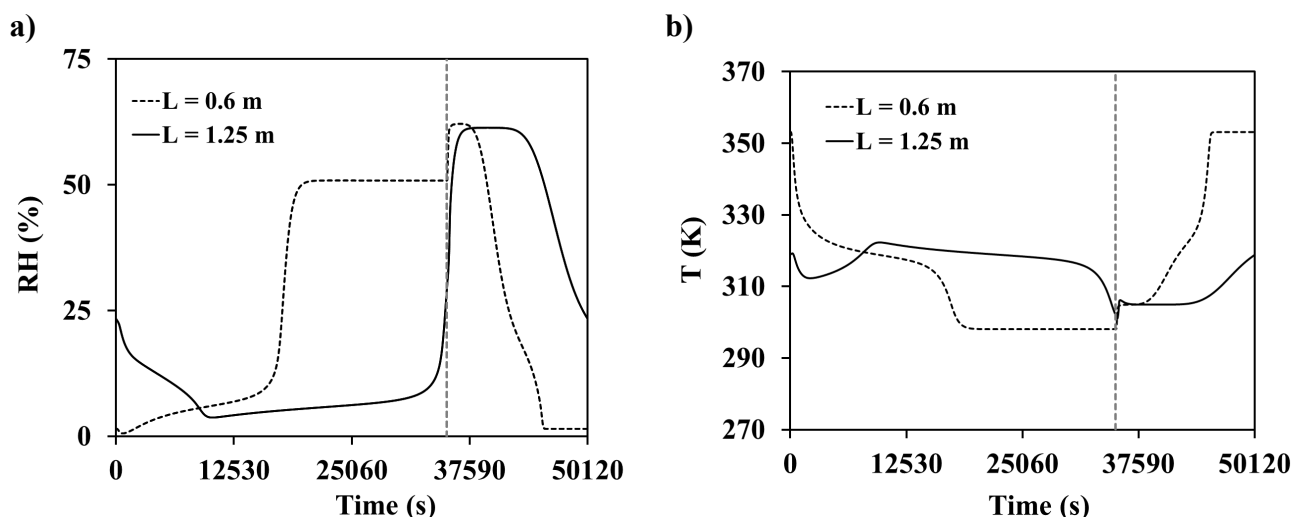

Figure 7.9. a) RH and b) gas temperature histories at two different axial positions: 0.6 m and 1.25 m, for the highest H_2O productivity on MIL-160(Al) (Vertical dashed line represents the beginning of the regeneration step).

The RH (fluid-phase concentration) and adsorbed amount (adsorbed phase concentration) profiles at two different cycle times (5000 s after the beginning of feed step and 5000 s after the start of the regeneration step – 40125 s), and at CSS, are presented in Figure 7.10. At the end of the desorption cycle, the column is not fully regenerated. Therefore, the adsorption step starts before full regeneration saving regeneration energy and improving productivity.
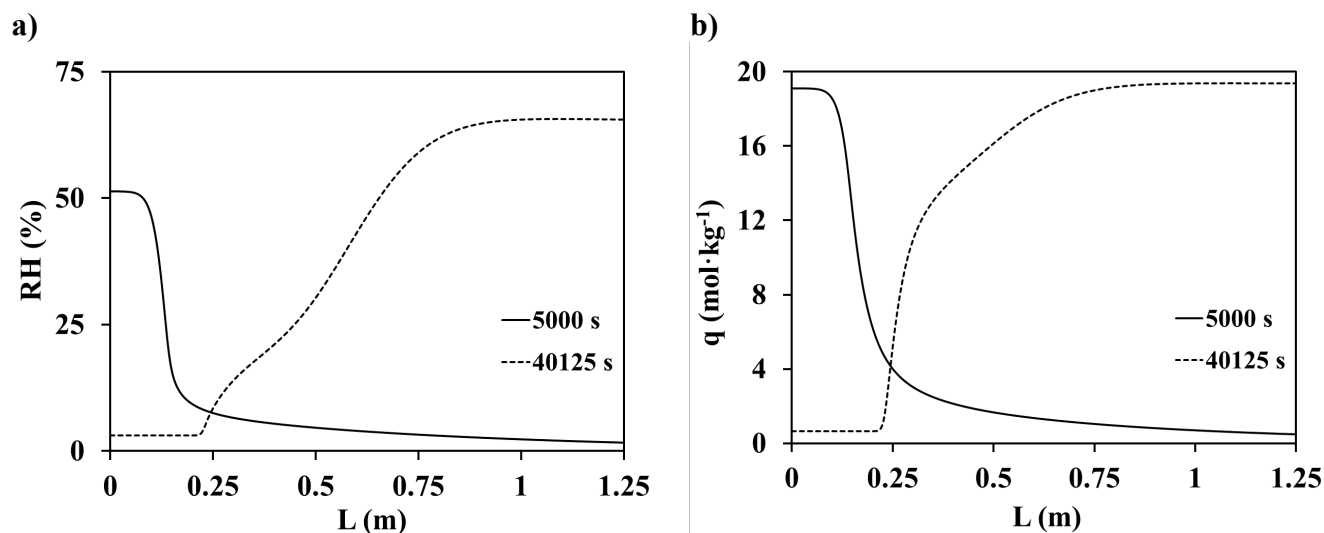

Figure 7.10. a) RH and b) adsorbed amount profiles at two different cycle times: 5000 s and 40125 s, for the highest H_2O on MIL-160(Al).

7.1.4 MIL-100(Fe)

The adsorption process study using MIL-100(Fe) as adsorbent followed the same procedure as the study with CAU-10, keeping the same operating conditions (pressure, condensation temperature, feed and purge volumetric gas flow rate) and dimensions of the column. The TSA column considered was packed with 407 kg of MIL-100(Fe) granules. As for CAU-10, different values of t_{feed} and t_{purge} were considered, and in Table 7.6 are presented the ones that achieved higher productivity. However, as happened in the CAU-10 study, the cycle times obtained exceeded 24 hours. To reduce the cycle times, the same strategy used in the CAU-10 was applied in the TSA process with MIL-100(Fe). The column with a volume of 0.35 m^3 (length = 1.25 m, diameter = 0.6 m) was packed with 147 kg of MIL-100(Fe), allowing a shorter cycle duration. The highest productivity was achieved for the highest regeneration temperature (373 K) on both two TSA designs (79.8 and 86.8 l·day^{-1} for column volumes of 0.98 and 0.35 m^3, respectively), as expected. The reduction of the TSA column volume beyond the reduction of cycle times allowed to achieve higher productivity (592 l·day^{-1}·ton^{-1}) than in the initial column

(196 l·day^{-1}·ton^{-1}) for the same feed and purge operating conditions due to the need of less adsorbent material. This adjustment in the TSA process promotes higher efficiency of the process and the reduction of the operating costs (*e.g.*, adsorbent cost).

Table 7.6. Harvested water productivity obtained in the TSA cycles for two different columns packed with MIL-100(Fe).

Column volume (m³)	T $_{purge}$ (K)	t_{feed} (s)	t_{purge} (s)	Productivity		
				(l·day^{-1})	(l·day^{-1}·ton^{-1})	(l·day^{-1}·m^{-3})
	333	153000	60000	61.0	150	62.2
0.98	353	158000	39000	72.7	179	74.2
	373	148000	29000	79.8	196	81.4
	333	53000	23000	63.7	434	182
0.35	353	51000	16000	79.2	540	226
	373	45000	11000	86.8	592	248

For one of the most promising scenarios (86.8 l·day^{-1}), at CSS, the internal histories of RH and gas temperature, at the middle and end column are presented in Figure 7.11. Additionally, the internal profiles of RH and the adsorbed amount, at CSS, are shown in Figure 7.12. On both figures it is possible to see that during the feed step, the shock wave achieves the end of the column only when the regeneration step is beginning. The duration of the feed and the regeneration step is enough to guarantee the saturation of the adsorbent and harvesting the maximum water capacity (about 30 mol·kg^{-1}). At 5000 s after the regeneration step, about 2/5 of the packed column is regenerated. The mass shock wave at the feed step does not overrides the shock wave developed during the regeneration. This fact also reduces the heating needs of the purge stream, and leads to an increase of the water harvesting.

a)

b)
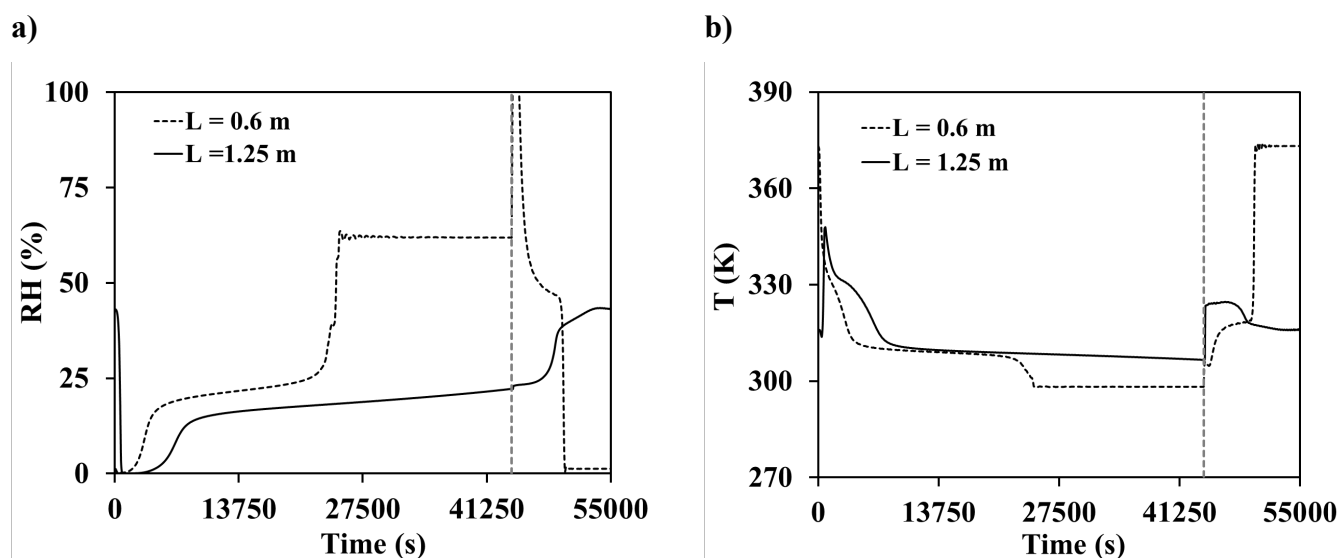
Figure 7.11. a) RH and b) gas temperature histories at two different axial positions: 0.6 m and 1.25 m, for the highest H_2O productivity on TSA column packed with MIL-100(Fe). (Vertical dashed line represents the beginning of the regeneration step).
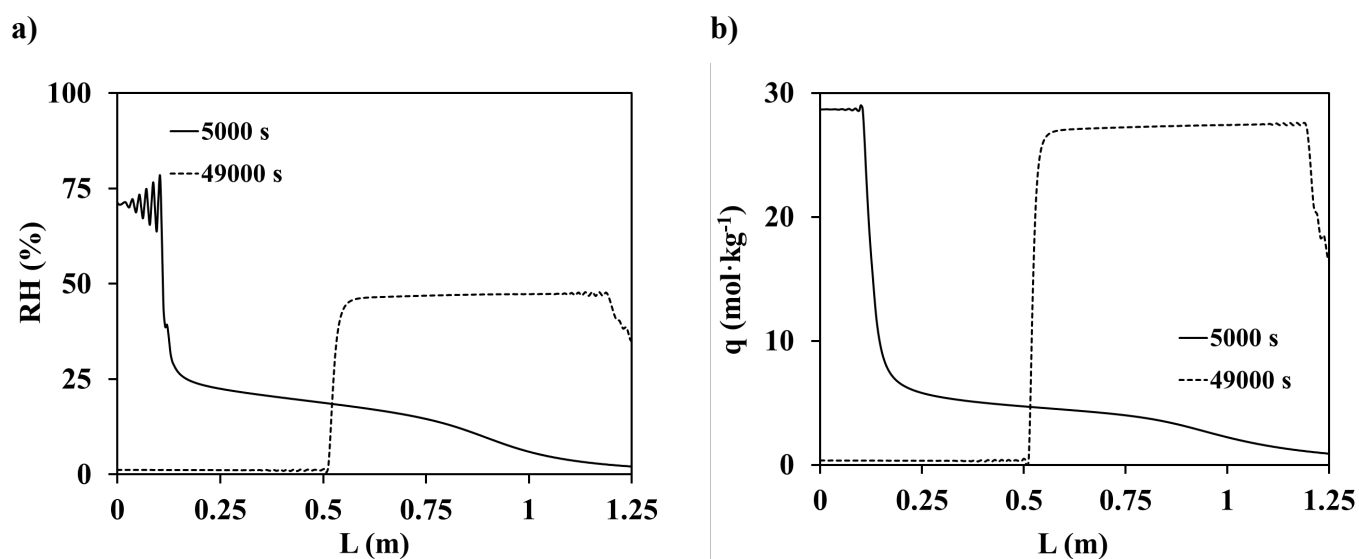
a)

b)

Figure 7.12. a) RH and b) adsorbed amount profiles at two different cycle times: 5000 s and 49000 s at the 0.35 m^3 TSA column volume, for the highest H_2O productivity achieved.

7.2 Summary

In this chapter, the development of different types of sorption based processes, for water harvesting, was presented. Initially, using MIL-125(Ti)_NH$_2$ as an adsorbent, three different designs were studied to achieve the highest productivity, such as TSA, PTSA, and PTSA coupled with a buffer tank. The TSA design process (purge and condensation temperature equal to 373 and 283 K, respectively; and flowrate of 0.30 m$^3 \cdot$s^{-1}) presented the highest productivity. A unit of 2.84 m^3 is capable of producing about 320 l$\cdot$day^{-1} of water. The same TSA design process was used in the design TSA processes with CAU-10, MIL-100(Fe), and MIL-160(Al). A metaeuristhic methodology for the optimization of cycle times was adopted in the process design with MIL-160(Al). Unlike the "manual optimization" of the steps times (t$_{feed}$ and t$_{purge}$) for the processes based on MIL-125(Ti)_NH$_2$, CAU-10, and MIL-100(Fe). Indeed, for MIL-160(Al) the cycle was optimized by employing a PSO algorithm. The TSA process with MIL-160(Al) was capable of producing at least 305 l$\cdot$day$^{-1}\cdot$ton^{-1} of water (purge temperature – 353 K, condensation temperature – 283 K, and flowrate – 0.50 m$^3 \cdot$s^{-1}). MIL-125(Ti)_NH$_2$ and ML-160(Al) proved to be promising materials for water harvesting achieving productivity of about 111 l$\cdot$day^{-1} for the same operating conditions (purge temperature – 373 K, condensation temperature – 283 K, and flowrate – 0.30 m$^3 \cdot$s^{-1}) but with different adsorbent mass (MIL-125(Ti)_NH$_2$ – 345 kg, and MIL-160(Al) – 480 kg). At the operating conditions mentioned before, 84.0 and 81.3 l$\cdot$day^{-1} was the water productivity achieved on CAU-10 for TSA column volume equal to 0.98 and 0.35 m^3, respectively, while the TSA process based on MIL-100(Fe) had a productivity of 79.8 and 86.8 l$\cdot$day^{-1}.

Notation

c_1/c_2	search parameters (cognitive and social)
$gbest$	global best position
i	individual/particle
J	objective function
k	number of iterations
L	column length
n_k	total number of instants of evaluation of the performance parameters
$pbest$	personal best position
P_{purge}	desorption pressure
P_r	productivity
q	total adsorbed amount
Q	volumetric gas flow
r_1/r_2	random variables
s_i	particle position
t_{feed}	adsorption time cycle
t_{purge}	desorption time cycle
T	temperature
$T_{condensation}$	condensation temperature
T_{purge}	purge temperature
v_i	particle velocity

Abbreviations

AWVP	Atmospheric Water Vapor Processing
CSS	Cyclic Steady State
IPMA	Instituto Português do Mar e da Atmosfera
MOF	Metal-Organic Framework
PSO	Particle Swarm Optimization
PTSA	Pressure-Temperature Swing Adsorption
RH	Relative humidity
std	standard deviation
TSA	Temperature Swing Adsorption

References

1.   Azevedo, A.J. and C. Marques, V. , *Atlas do Ambiente*. 1987: Secretaria de Estado do Ambiente e Recursos Naturais.

2.   Vieira, R., J. Neto, and Á. Silva, *Radiação Solar Global Anual Portugal Continental - Portugal Continental 2002–2007*. 2008: Instituto Português do Mar e da Atmosfera.

3.   Instituto Português do Mar e da Atmosfera (IPMA). *Portal do Clima*. [cited 2020; Available from: http://portaldoclima.pt/en/.

4.   Nogueira, I.B.d.R., *Optimization and Control of TMB, SMB and SMBR units*, in *Department of Chemical Engineering*. 2018, Faculty of Engineering of the Univerisity of Porto.

5.   Kennedy, J. and R. Eberhart. *Particle swarm optimization*. in *Proceedings of ICNN'95 - International Conference on Neural Networks*. 1995.

6.   Kennedy, J., R.C. Eberhart, and Y. Shi, *Swarm intelligence*. The Morgan Kaufmann Series in Artificial Intelligence, ed. D.B. Fogel. 2001.

7.   García-Gonzalo, E. and J.L. Fernández-Martínez, *A Brief Historical Review of Particle Swarm Optimization (PSO).* Journal of Bioinformatics and Intelligent Control, 2012. **1**(1): p. 3-16.

8.   Eberhart and S. Yuhui. *Particle swarm optimization: developments, applications and resources*. in *Proceedings of the 2001 Congress on Evolutionary Computation (IEEE Cat. No.01TH8546)*. 2001.

9.   Juneja, M. and S.K. Nagar. *Particle swarm optimization algorithm and its parameters: A review*. in *2016 International Conference on Control, Computing, Communication and Materials (ICCCCM)*. 2016.

10.   Banks, A., J. Vincent, and C. Anyakoha, *A review of particle swarm optimization. Part I: background and development.* Natural Computing, 2007. **6**(4): p. 467-484.

11.   Brandini, P.A.F., *Metaheurística Particle Swarm utilizada para Alocação Ótima de Bancos de Capacitores em Sistemas de Distribuição Radial*, in *Electrical engineering*. 2007, Universidade Estadual Paulista "Júlio de Mesquita Filho".

12.   Mei-Ping, S. and G. Guo-Chang. *Research on particle swarm optimization: a review*. in *Proceedings of 2004 International Conference on Machine Learning and Cybernetics (IEEE Cat. No.04EX826)*. 2004.

8 CONCLUSIONS AND FUTURE WORK

8.1 Conclusions

The main objective of this project was achieved by the design of different TSA processes for water harvesting from air. Indeed, the performance of the different MOFs to produce water was evaluated.

Initially, the textural, morphologic, and crystallographic characterization and thermogravimetric analyses of MOFs were performed. Excepting on MIL-100(Fe), all the MOFs presented Type I isotherms for N_2 adsorption at 77 K, typical of microporous adsorbents. Otherwise, MIL-100(Fe) showed Type I and IV isotherms, due to its micro and mesoporous cages. The N_2 adsorption results demonstrated a capacity order: MIL-100(Fe) > MIL-160(Al) > Al-Fum > MIL-125(Ti)_NH$_2$ > CAU-10, as expected, particularly for MIL-100(Fe) with the presence of higher pore volume. Adsorption properties were also evaluated by the single CO_2 adsorption equilibrium isotherms, at 273 K, demonstrating on all the materials a type I shape, characteristic of microporous, and narrow mesoporous adsorbents. CO_2 affinity presented the followed order of MIL-160(Al) > CAU-10 > Al-Fum > MIL-125(Ti)_NH$_2$ > MIL-100(Fe). Thermogravimetric analysis showed all the MOFs presented thermal stability at 650 K, excepting MIL-100(Fe).

Pure gas adsorption data of N_2, O_2, and CO_2, were performed at 283 K, 303 K, and 323 K, in the pressure range of 0 to 6 bar, on MIL-160(Al), MIL-100(Fe), and MIL-125(Ti)_NH$_2$. From the three gases, CO_2 is the one with the highest affinity towards the three adsorbents. On CAU-10 and Al-Fum, these gases were not measured due to the results obtained for the previously mentioned materials, weak or even no competition between these three gases and vapor water. For this same reason, DRIFTS analyses were also not performed in these two adsorbents. DRIFT analyses revealed that MIL-125(Ti)_NH$_2$, MIL-100(Fe), and MIL-160(Al) structures remained stable during the water vapor exposure.

Water vapor adsorption equilibrium isotherms on Al-Fum, CAU-10, and MIL-125(Ti)_NH$_2$ are of type IV according to IUPAC classification, and type V and type VI shape on the MIL-160(Al) and MIL-100(Fe), respectively. Except Al-Fum, all MOFs presented a sharp water uptake for low relative pressure (P/P$_o$ < 0.3) which makes them suitable for water harvesting in arid regions. MIL-160(Al) is the adsorbent more ideal in areas with very low relative humidity (10%). In comparison, CAU-10 and MIL-125(Ti)_NH$_2$ are appropriate for regions with about

20%, and Al-Fum is proper in areas with around 25 to 39% of relative humidity. Globally, MIL-100(Fe) is the adsorbent more versatile due to two different cavities in its structure. Its application can be flexible, since it adsorbs in two different moist regions, *i.e.*, in regions with relative humidity between 21 to 30%, and in the relative humidity range between 36 to 40%, achieves its highest capacity.

A characteristic curve for each MOF was described by applying Polanyi's theory model to the water vapor equilibrium isotherms. MIL-100(Fe) showed a higher Polanyi adsorption potential related to a higher affinity to water molecules. All curves presented double inflection, possibly associated with bi-modal energy distribution.

Water adsorption equilibrium isotherms were described by the Cooperative Multimolecular Sorption model on all the MOFs, except for MIL-100(Fe), for which was applied the Dual Ising-Single Langmuir model. On Al-Fum, two different sets of fitting parameters of the CMMS model (Fitting 1 and Fitting 2) were obtained. However, it was not possible to predict well fixed bed results on Al-Fum, with any of the sets, only the general tendencies were possible to predict. This fact restricts the possibility to develop the adsorptive process design based on Al-Fum. Yet, for the remaining four MOFs, the dynamic adsorption behavior of water in the fixed bed was well predicted by the developed model.

Furthermore, all the single water vapor adsorption breakthrough experiments corroborated the shape of the water vapor adsorption equilibrium isotherms. This fact demonstrates the dynamic behavior of water vapor is mainly controlled by the adsorption equilibrium, with no significant contribution of the adsorption kinetics. Water co-adsorption history proved that the presence of the other air components (CO_2, and/or N_2) does not affect water adsorption behavior.

Three different designs (TSA, PTSA, and PTSA coupled with a buffer tank) based on MIL-125(Ti)_NH_2 were studied, and the TSA design process presented the highest productivity. Then, the simple TSA design was considered for CAU-10, MIL-100(Fe), and MIL-160(Al). The TSA processes with MIL-125(Ti)_NH_2 (345 kg) and MIL-160(Al) (480 kg) were capable of producing 111 l·day^{-1} for the same operating conditions (purge temperature – 373 K, condensation temperature – 283 K, and flowrate – 0.30 m^3·s^{-1}). With CAU-10 and MIL-100(Fe), lower water productivity was achieved using the operating conditions mentioned before, corresponding to 84.0 and 79.8 l·day^{-1}, respectively.

The developed model is flexible and able to predict the process performance for different regions (*i.e.*, different relative humidity), adsorbents, and operating conditions (*e.g.*, purge and condensation temperature, pressure, and flowrate).

8.2 Future work

At the end of this research work, the development of the sorption process design using Al-Fum, as adsorbent stayed pendent. The repetition of the measurement of water vapor adsorption equilibrium isotherms, namely at 298 K, could help to achieve the most suitable set of fitting parameters to represent the water vapor dynamic behavior on Al-Fum.

The study of the relation between solar irradiance and temperature inside the column had some hindrance, namely not knowing the exact irradiance solar in the column surface, and that the equipment is not allowed to achieve temperatures higher than 373 K. This obstacle can be overcome by a pyranometer which can be used to measure the global solar irradiance on the local intended for assembly the water harvester device [1].

This research work could be the lead-off to the development of a proof-of-concept device of the sorption process and afterward to optimize the efficiency and productivity of the water harvester. For the adsorbent selection, should be considered the average relative humidity of the location and selected the MOF more suitable to the local in terms of relative humidity as presented in Chapter 5. Other promising adsorbents could be evaluated (*e.g.,* super moisture-adsorbent gel (SMAG) [2], and interpenetrating polymer network (IPN) [3]), or even the combination of MOFs with other materials (*e.g.,* metal coating [4], and hygroscopic salts [5]) to provide conductive heat transfer and/or improve adsorption properties. Also, the geometry of the water harvester and material can be optimized to promote the heat transfer leading to require low heating needs and condensation temperature closer to environment temperature (*e.g.,* modular beds and tubular solar still powered by a parabolic concentrator system) [6-8]

The water captured does not present harmful components in its composition due to the MOF's capacity of retaining only moisture into the pores [9-11]. However, the impact of air pollutants (*e.g.*, NO_x) in the MOFs adsorption performance and the development of strategies to avoid microbial proliferation on the device, studies are fundamental to warranty drinking water safety

[6, 7]. Afterward, if the purpose of the captured water is to drink, a mineralization process must be coupled to the water harvester.

References

1.   Lysko, M.D., *Measurement and models of solar irradiance*, in *Department of Physics*. 2006, Norwegian University of Science and Technology: Faculty of Natural Sciences and Technology.

2.   Zhao, F., X. Zhou, Y. Liu, Y. Shi, Y. Dai, and G. Yu, *Super Moisture-Absorbent Gels for All-Weather Atmospheric Water Harvesting.* Advanced Materials, 2019. **31**(10): p. 1806446.

3.   Matsumoto, K., N. Sakikawa, and T. Miyata, *Thermo-responsive gels that absorb moisture and ooze water.* Nature Communications, 2018. **9**(1): p. 2315.

4.   Jeremias, F., S.K. Henninger, and C. Janiak, *High performance metal–organic-framework coatings obtained via thermal gradient synthesis.* Chemical Communications, 2012. **48**(78): p. 9708-9710.

5.   Zhang, Y., L. Wu, X. Wang, J. Yu, and B. Ding, *Super hygroscopic nanofibrous membrane-based moisture pump for solar-driven indoor dehumidification.* Nature communications, 2020. **11**(1): p. 3302-3302.

6.   Hanikel, N., M.S. Prévot, and O.M. Yaghi, *MOF water harvesters.* Nature Nanotechnology, 2020. **15**(5): p. 348-355.

7.   LaPotin, A., H. Kim, S.R. Rao, and E.N. Wang, *Adsorption-Based Atmospheric Water Harvesting: Impact of Material and Component Properties on System-Level Performance.* Accounts of Chemical Research, 2019. **52**(6): p. 1588-1597.

8.   Elashmawy, M. and F. Alshammari, *Atmospheric water harvesting from low humid regions using tubular solar still powered by a parabolic concentrator system.* Journal of Cleaner Production, 2020. **256**: p. 120329.

9.   Xu, W. and O.M. Yaghi, *Metal–Organic Frameworks for Water Harvesting from Air, Anywhere, Anytime.* ACS Central Science, 2020. **6**(8): p. 1348-1354.

10.   Fathieh, F., M.J. Kalmutzki, E.A. Kapustin, P.J. Waller, J. Yang, and O.M. Yaghi, *Practical water production from desert air.* Science Advances, 2018. **4**(6): p. eaat3198.

11.   Liu, X., X. Wang, and F. Kapteijn, *Water and Metal–Organic Frameworks: From Interaction toward Utilization.* Chemical Reviews, 2020. **120**(16): p. 8303-8377.

APPENDIX A

   The irradiance, also known as flux density of radiant energy, is the radiant energy received per unit area [1, 2]. On a perpendicular plane with an average distance of 149.6 Gm between the Sun and Earth, the annual average solar radiation (solar constant) is about 1366 $W \cdot m^{-2}$ [2-6]. Daily average irradiance (insolation) in a yearly cycle at the top of the atmosphere obtained empirically is presented in Figure A.1. The insolation varies all over the spatial and temporal scale.
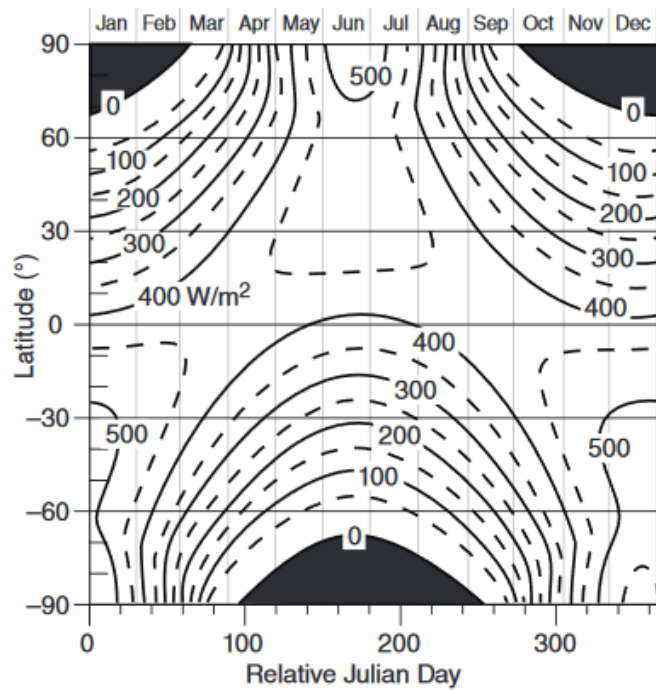

Figure A.1. Average daily insolation at the top of the Earth's atmosphere [6].

   However, passing through the atmosphere, the intensity on the surface decreases due to the interaction with the atmospheric constituents (absorption and scattering phenomena) [7]. The irradiance is also influenced by the solar zenith angle, the sky conditions (e.g. clouds), climate, daytime and season [7-13]. Earth's atmosphere receives an average of about 342 $W \cdot m^{-2}$ of solar energy, but only 70% are available on the surface [14].

   Worldwide overview of the annual average irradiance distribution on the ground-level for the period of 1991-1993 (daily average) is observed in Figure A.2. "Black dots" marked in the map correspond to the areas with great potential to provide energy [15]. The highest irradiance values are located near the equator (latitude equal to 0º).
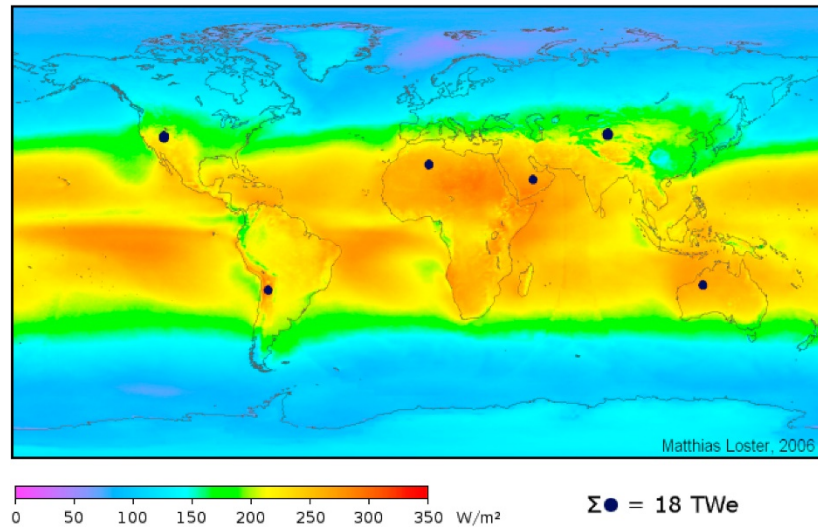
Figure A.2. Annual average irradiance (1991-1993) on a horizontal surface at ground-level [15].

Wald [7] reported the influence of the solar zenith angle on irradiance at the surface, without cloudiness (50 km of visibility from the ground-level) (Table A.1).

Table A.1. Total irradiance at the top of atmosphere and ground-level, and clearness index for different zenith angles (0º, 30º, and 60º) (adapted from [7]).

	Solar zenith angle (º)		
Irradiance (W·m^{-2})	0	30	60
Top of atmosphere	1354	1174	673
Ground-level	1045	885	464
Clearness index	0.77	0.76	0.69

Opálková *et al.* [16] measured the means of solar irradiance on a horizontal plane at the city of Ostrava (Czech Republic). Figure A.3 represents the daily profile of the 10 min means irradiance in three days with different sky conditions. The daily profile on a sunny day exhibits broadband, and a large band was also observed on the partly cloudy day but with variable irradiance. As expected, the cloudy day presents the lowest irradiance values.
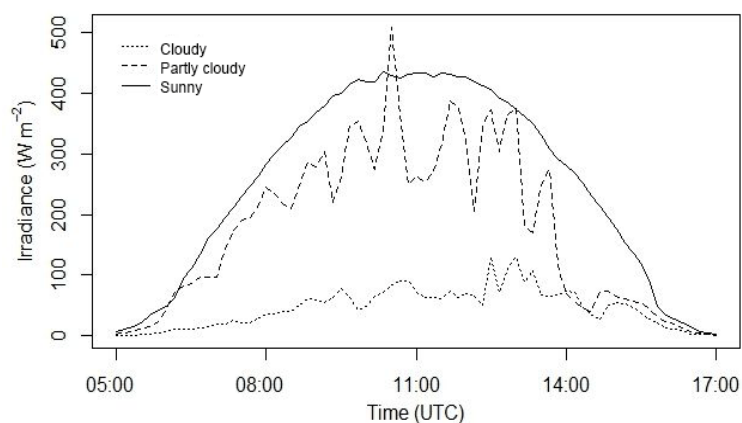
Figure A.3. Daily profile of the 10 min broadband irradiance recorded on ground-level at three different days (cloudy, partly cloudy, and sunny).

The static experiments on the MIL-125(Ti)_NH_2 were performed with the irradiance range of 250-850 $W \cdot m^{-2}$. Initially, the column was positioned along 8.7 cm distant of xenon lamp and the initial material temperature was recorded (T) (Figure A.4). The column was previously saturated with water in helium (50%) corresponding approximately to the minimum average relative humidity recorded in August (53%), during 1971 and 2000 in Portugal [17].
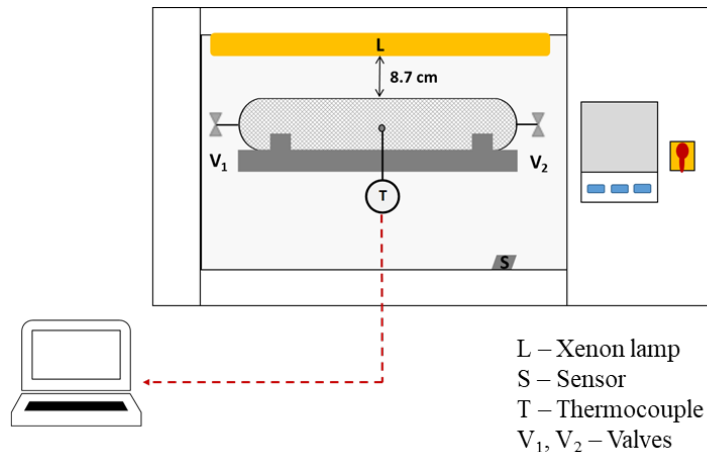
Figure A.4. Solar simulator schema of static experiments.

Figure A.5 displays the equilibrium temperature inside the column along with the rise of solar irradiance. As expected, the temperature of the material increases linearly with the gradual irradiance raise.
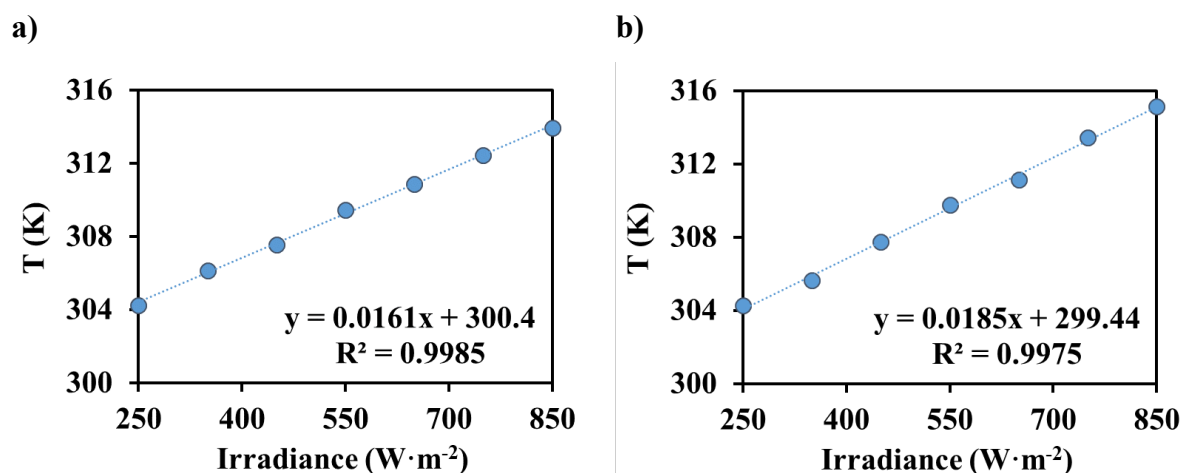
a)

b)

Figure A.5. Column temperature in function of solar irradiance with an initial temperature of (a) 297.6 K and (b) 297.0 K.

However, due to the distance between the lamp and column, possible loss of irradiance may occurred. To circumvent this possible loss, the column was positioned near the xenon lamp (Figure 3.18 – Chapter 3) and the same experiment was repeated. The initial temperature inside the column was of 297 K, while 305.2 K corresponds to the temperature inside the solar simulator. As in the experiments reported before, the material temperature was recorded along the time until attained the equilibrium (Figure A.6). At 250 W·m^{-2}, the equilibrium temperature was about 339 K, while at 350 W·m^{-2} the temperature measured was 349.3 K. For higher irradiance, the temperature measuring was not possible due to the experimental limitations at high temperatures (maximum equipment temperature = 373 K). As expected, along with the increase of the irradiance, the temperature recorded in the material increases.
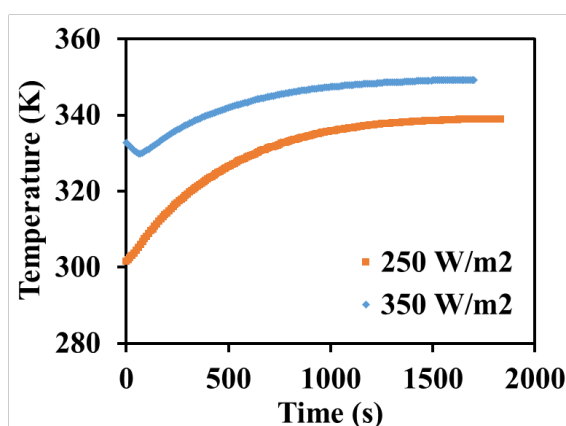

Figure A.6. Equilibrium temperature for irradiance of 250 and 350 W·m^{-2}.

References

1.   Landsberg, J. and P. Sands, *Chapter 2 - Weather and Energy Balance*, in *Terrestrial Ecology*. 2011, Elsevier. p. 13-48.

2.   Renné, D.S., *2 - Resource assessment and site selection for solar heating and cooling systems*, in *Advances in Solar Heating and Cooling*, R.Z. Wang and T.S. Ge, Editors. 2016, Woodhead Publishing. p. 13-41.

3.   Badescu, V., *Modeling Solar Radiation at the Earth's Surface: Recent Advances*. 2014: Springer Publishing Company, Incorporated.

4.   Kleissl, J., *Solar Energy Forecasting and Resource Assessment*. 2013: Academic Press.

5.   Kalogirou, S.A., *Chapter 2 - Environmental Characteristics*, in *Solar Energy Engineering (Second Edition)*, S.A. Kalogirou, Editor. 2014, Academic Press: Boston. p. 51-123.

6.   Stull, R., *Practical Meteorology: An Algebra-based Survey of Atmospheric Science*. 2016: Sundog Publishing, LLC.

7.   Wald, L., *Basics in Solar Radiation at Earth Surface*. 2018.

8.   Fennel, W. and T. Neumann, *Chapter 5 - Physical–Biological Interaction*, in *Introduction to the Modelling of Marine Ecosystems (Second Edition)*, W. Fennel and T. Neumann, Editors. 2015, Elsevier: Boston. p. 153-216.

9.   Pecenak, Z.K., et al., *Simulating irradiance enhancement dependence on cloud optical depth and solar zenith angle.* Solar Energy, 2016. **136**: p. 675-681.

10.   Luoma, J., J. Kleissl, and K. Murray, *Optimal inverter sizing considering cloud enhancement.* Solar Energy, 2012. **86**(1): p. 421-429.

11.   Yordanov, G.H., T.O. Saetre, and O. Midtgård, *100-millisecond Resolution for Accurate Overirradiance Measurements.* IEEE Journal of Photovoltaics, 2013. **3**(4): p. 1354-1360.

12.   Li, D.H.W. and S. Lou, *Review of solar irradiance and daylight illuminance modeling and sky classification.* Renewable Energy, 2018. **126**: p. 445-453.

13.   Kabir, E., et al., *Solar energy: Potential and future prospects.* Renewable and Sustainable Energy Reviews, 2018. **82**: p. 894-900.

14.   Hart, M., *Hubris: The Troubling Science, Economics, and Politics of Climate Change.* First Edition ed. 2015: Compleat Desktops. 614.

15.   Loster, M. *Total Primary Energy Supply - From Sunlight.* 2010   02/01/2020]; Available from: h[ttps://www.ez2c.de/ml/solar_land_area/.](https://www.ez2c.de/ml/solar_land_area/.)

16.   Opálková, M., et al., *A database of 10 min average measurements of solar radiation and meteorological variables in Ostrava, Czech Republic.* Earth Syst. Sci. Data, 2018. **10**(2): p. 837-846.

17.   Instituto Português do Mar e da Atmosfera (IPMA). *Portal do Clima.* [cited 2020; Available from: http://portaldoclima.pt/en/.

APPENDIX B

Dynamic adsorption experiments under different conditions are presented. The breakthrough curves were performed to corroborate the behaviour of saturated dynamic adsorption experiments. The water breakthrough curve on Al-Fum presented in Figure B.1 followed the protocol of Experiment 1 (Chapter 6) but with water vapor being transported by a helium stream at 22% RH. The breakthrough curve was performed to select the best fitting parameters of CMMS model (Table 5.4 – Chapter 5). As expected, the breakthrough curve followed the same dynamic present at 50% RH (Figure 6.1 – Chapter 6) and is according to the H_2O adsorption equilibrium isotherm (Figure 5.8). As in Figure 6.1, both types of fitting parameters (Fitting 1 and Fitting 2) are not suitable to validate the experimental results obtained on Al-Fum adsorbent.
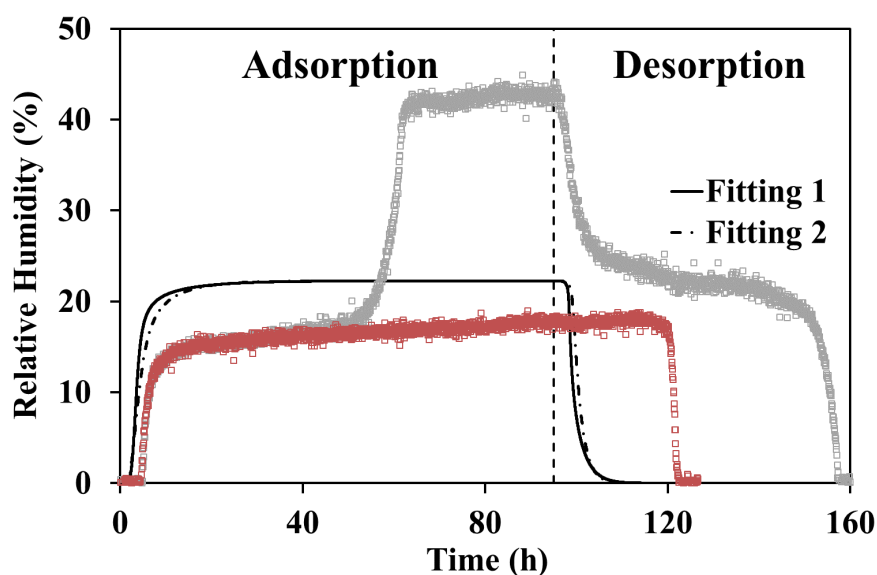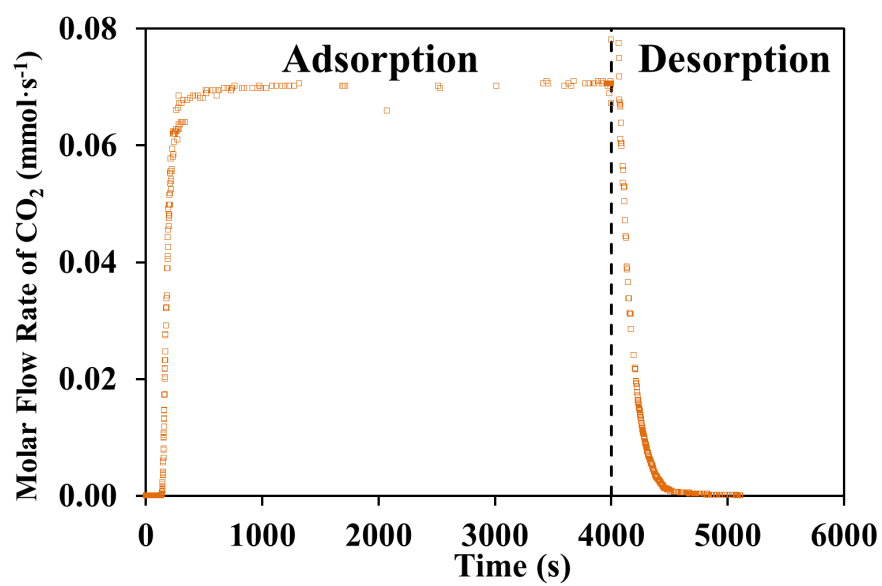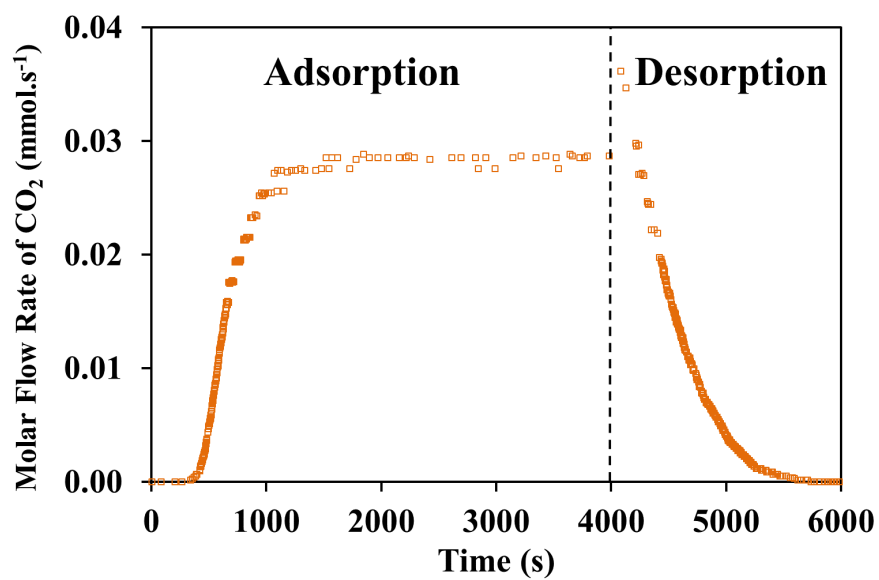

Figure B.1. Water vapor adsorption-desorption breakthrough curve obtained on Al-Fum with saturated helium (22% RH) at 298 K (Points represent experimental data and dashed line represents the beginning of the regeneration step).

The CO_2 breakthrough experiments on MIL-160(Al) followed the Experiment 6 protocol (Chapter 6). In Figure B.2b) the composition of CO_2:He ratio in the adsorption step was equal to 20:80. In Figure B.2c) the same composition was used and the helium stream was changed by nitrogen stream.
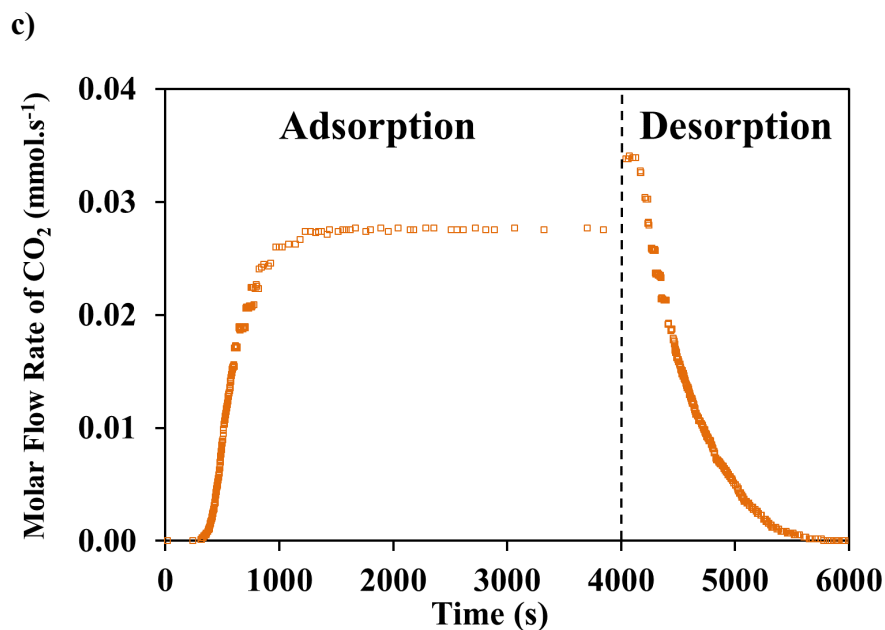
a)

b)

c)

Figure B.2. Carbon dioxide breakthrough curves of binary mixture of (a) dry He with CO_2 (50:50), (b) dry He with CO_2 (80:20), and (c) dry N_2 with CO_2 (80:20), on MIL-160(Al) at 298 K. (Points represent experimental data and dashed line represents the beginning of the regeneration step).

Figure B.3a) corresponds to CO_2 breakthrough experiments on MIL-160(Al) using CO_2 as water vapour carrier (Experiment 2 protocol) and Figure B.3b) is the CO_2 breakthrough curve resulted after adsorbent pre-saturation with water (Experiment 5 protocol). Both experiments show rapid desorption of CO_2 in the presence of water corroborating the strong water adsorption.
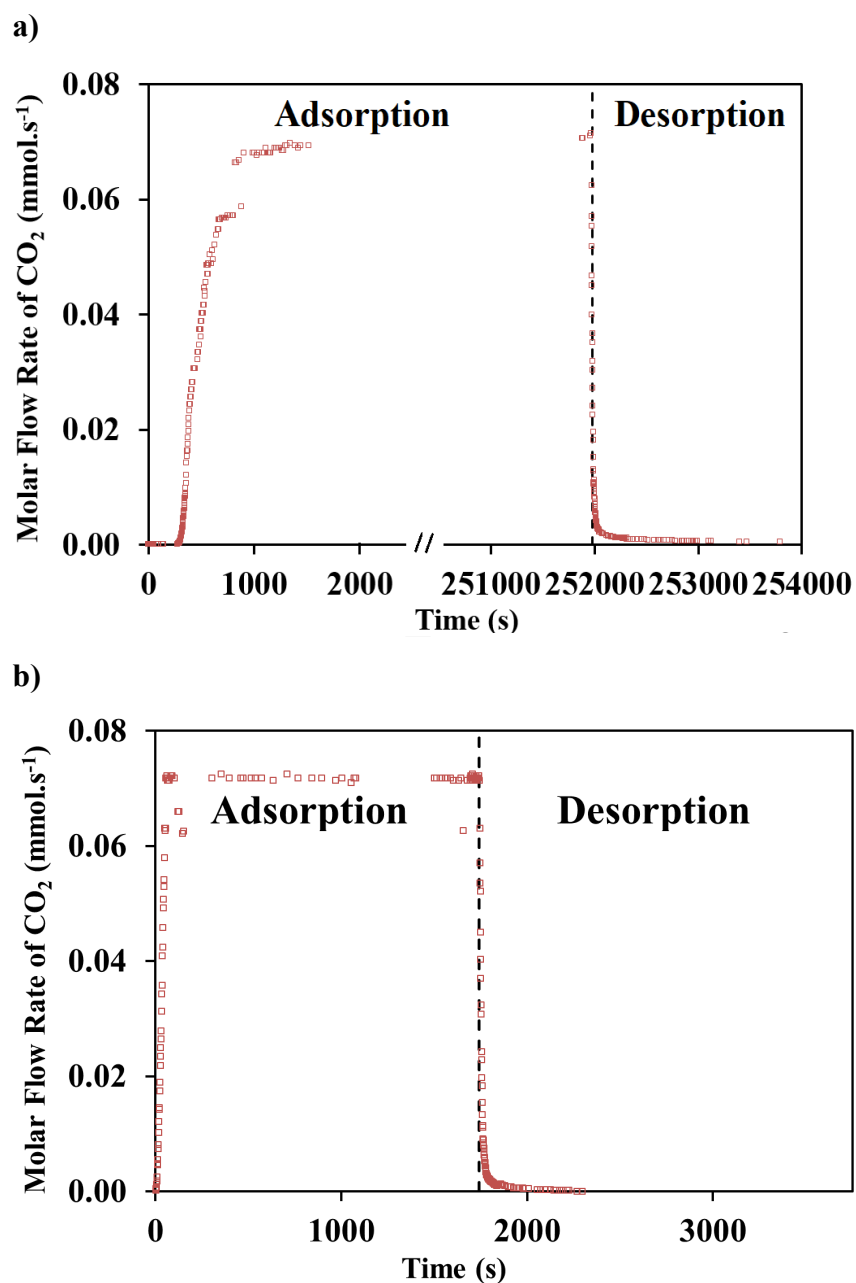
a)

b)

Figure B.3. Carbon dioxide breakthrough curves of (a) dry He with CO_2 saturated, and (b) after adsorbent pre-saturation with water on MIL-160(Al) at 298 K. (Points represent experimental data and dashed line represents the beginning of the regeneration step).

The CO_2 breakthrough curve present in Figure B.4 results from the procedure of Experiment 6 (Chapter 6).
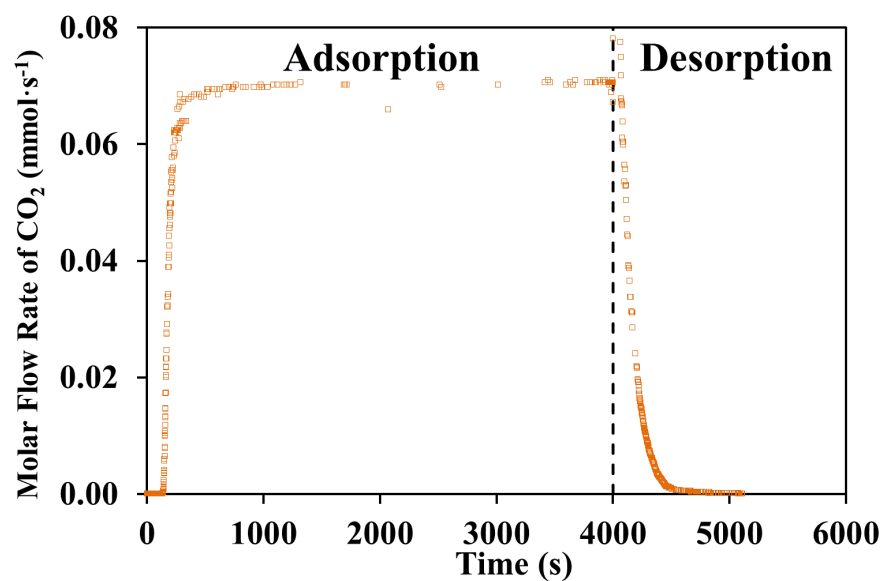
Figure B.4. Carbon dioxide breakthrough curve of binary mixture of (a) dry He with CO_2, on MIL-125(Ti)_NH_2 at 298 K. (Points represent experimental data and dashed line represents the beginning of the regeneration step).

As observed on MIL-160(Al), the strong water adsorption is visible on CO_2 breakthrough curves on MIL-125(Ti)_NH_2 (Figure B.5) where CO_2 molecules are unable to compete with water molecules.

a)

b)

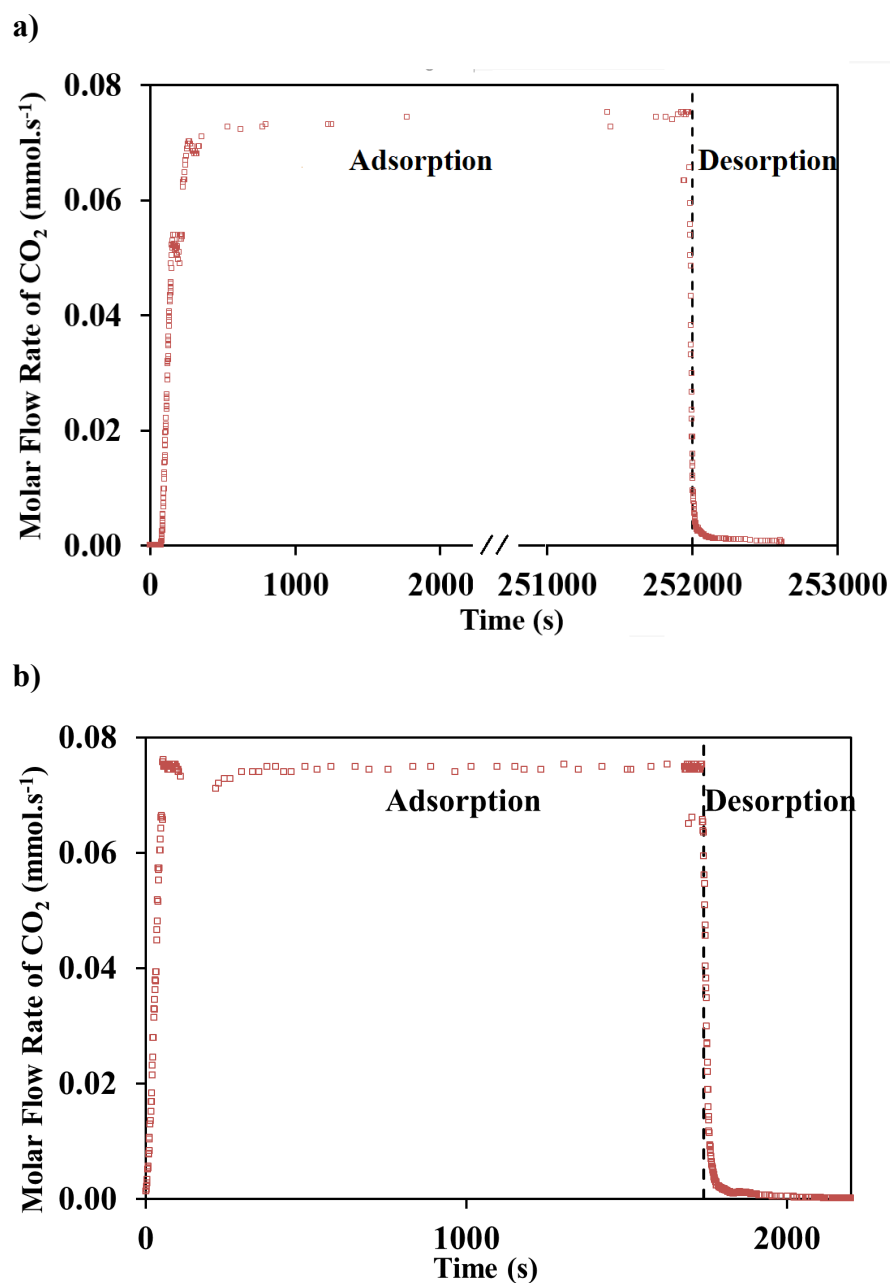Figure B.5. Carbon dioxide breakthrough curves of (a) dry He with CO_2 saturated, and (b) after adsorbent pre-saturation with water on MIL-125(Ti)_NH_2 at 298 K. (Points represent experimental data and dashed line represents the beginning of the regeneration step).